

<b>OCRWM</b>	<b>MODEL COVER SHEET</b>	1. QA: QA Page 1 of 316
--------------	--------------------------	----------------------------

2. Type of Mathematical Model:

Process Model     
  Abstraction Model     
  System Model

Describe Intended Use of Model:

The models and associated analyses documented in this report provide drift degradation input, including rockfall data, for various calculations, models, and analyses. The users of the output data provided in this document include the Specialty Analyses & Waste Package Design Department, the Total System Performance Assessment Department, the Disruptive Events Department, the Ambient and Thermal Drift Seepage Department, the Subsurface Department, and the Preclosure Safety Analysis Department.

3. Title:

**Drift Degradation Analysis**

4. DI (including Rev. No. and Change No., if applicable):

**ANL-EBS-MD-000027 REV 02**

5. Total Attachments:	6. Attachment Numbers - No. of Pages in Each:
18	I-4, II-18, III-28, IV-26, V-26, VI-16, VII-4, VIII-6, IX-12, X-6, XI-34, XII-2, XIII-6, XIV-22, XV-44, XVI-12, XVII-6, XVIII-20

	Printed Name	Signature	Date
7. Originator:	Dwayne C. Kicker (lead)	<i>[Signature]</i>	6/27/03
8. CSO:	K. Michael Cline	<i>[Signature]</i>	6/27/03
9. Checker:	Holly H. Miller (lead)	<i>[Signature]</i>	6/27/03
10. QER:	Judith E. Gebhart	<i>[Signature]</i>	6/27/03
11. Responsible Manager/Lead:	<del>Dennis Thomas</del> Daniel A. Thomas	<i>[Signature]</i>	6-27-03
12. Responsible Manager:	Thomas W. Doering	<i>[Signature]</i>	6-27-03

13. Remarks:

The preparer and checker for each section in this report are identified as follows:

Section or Attachment	Preparer	Checker
I through 5, 9, 10, I, V, VI	Dwayne Kicker	Holly Miller
6.1, II, XV	Dwayne Kicker	Ming Lin
6.2, III, XIII, XVII	Junghun Leem	Ming Lin
6.3, 6.4, IV, VII through XII, XIV, XVI, XVIII	Ming Lin	Junghun Leem
6.5 through 6.8, 8	Dwayne Kicker	Junghun Leem
7	Mark Board	Ming Lin

Robert Lung (USBR) and Michael Fahy (USGS) provided technical support in the development of Section 6.1 and Attachment II.

David Buesch (USGS) provided technical support in the development of Section 6.1 and Attachment XV.

Branko Damjanac (Itasca) provided technical support in the development of Sections 6.3, 6.4 and 7.

Carlos Carranza-Torres (Itasca) provided technical support in the development of Section 6.2 and Attachment III.

David Potyondy (Itasca) provided technical support in the development of Section 7.6.

John Kemeny (Univ. of Arizona) provided technical support in the development of Attachment IV.

2. Title: Drift Degradation Analysis	
3. DI (including Rev. No. and Change No., if applicable): ANL-EBS-MD-000027 REV 02	
4. Revision / Change Number:	5. Description of Revision/Change:
00	Initial issue.
00 / 01	The technical product cover sheet was changed to indicate that this document reports the development and use of a model. Section 6.5 on model validation was added. The report was changed to include results for 75°-azimuth emplacement drifts and to provide additional results for emplacement drifts with no backfill. The Document Input Reference System (DIRS) information was removed from document and made part of the records package. The numbering of the attachments has been changed to reflect removal of the DIRS information. Attachment VI is now Attachment I. Table 2 was modified. The description of the use of software routines in Section 3 was changed. The data in Tables 14, 15, 20, 21, 23, 24, and Figure 17 were corrected. Additional attachments were added to document the field observation of key blocks in the Cross-Drift, and to document natural analogues for the seismic effect on rock fall.
01	The Tptpln fracture geometry inputs to DRKBA were revised to be consistent with the developed fracture geometry data in ANL-EBS-GE-000006. Output information for the Tptpln was revised throughout the report. The data and information presented in the supporting calculation, CAL-EBS-MD-000010 REV 00, has been updated and merged with this report. Therefore, this revision supersedes calculation CAL-EBS-MD-000010 REV 00. Additional seismic analyses have been included in Attachment V. Information supporting the analysis of drift degradation features, events, and processes (FEPS) has been added in Section 6.6. Information supporting the resolution of applicable Nuclear Regulatory Commission (NRC) key technical issues has been added in Section 6.7. A brief discussion of the impacts of the small-trace length fracture data on drift degradation has been added in Section 7.2. Attachments VIII through XI were added to include the information that was previously provided in calculation CAL-EBS-MD-000010 REV 00 (note that data for the Tptpln unit has been updated in these attachments). Drift profile figures were moved from Section 6.4.3 to Attachment XII. The calculation of mean input data based on source DTNs identified in Section 4.1 was added as documented in Attachment XIII. An assessment of the joint plane representation in the DRKBA rock fall model was added in Attachment XIV to provide additional bases for Assumption 5.1.
(Continued on next page)	



INTENTIONALLY LEFT BLANK

## EXECUTIVE SUMMARY

Degradation of underground openings as a function of time is a natural and expected occurrence for any subsurface excavation. Over time, changes occur to both the stress condition and the strength of the rock mass due to several interacting factors. Once these factors contributing to degradation are characterized, the effects of drift degradation can typically be mitigated through appropriate design and maintenance of the ground support system. However, for the emplacement drifts of the geologic repository at Yucca Mountain, it is necessary to characterize drift degradation over a 10,000-year time period, which is well beyond the functional period of the ground support system. This document provides an analysis of the amount of drift degradation anticipated in repository emplacement drifts for discrete events and time increments extending throughout the 10,000-year regulatory period for postclosure performance. This revision of the drift degradation analysis was developed to support the license application and fulfill specific agreement items between the U.S. Nuclear Regulatory Commission (NRC) and the U.S. Department of Energy (DOE).

The earlier versions of *Drift Degradation Analysis* (Revisions 0 and 1) relied primarily on the Discrete Region Key Block Analysis (DRKBA) numerical code, which provides for a probabilistic key-block assessment based on realistic fracture patterns determined from field mapping in the Exploratory Studies Facility at Yucca Mountain. Note that a key block is defined as a critical block in the surrounding rock mass of an excavation, which is removable and oriented in an unsafe manner such that it is likely to move into an opening unless support is provided. However, the use of the DRKBA code to determine potential rockfall data at the repository horizon during the postclosure time period has several limitations and areas for improvement:

- The DRKBA code can not explicitly apply dynamic loads due to seismic ground motion.
- The DRKBA code can not explicitly apply loads due to thermal stress.
- The DRKBA code, which determines structurally controlled key-block failure, is not applicable for stress controlled failure in the lithophysal units.

To address these limitations, additional numerical codes have been included that can explicitly apply seismic and thermal loads, providing significant improvements to the analysis of drift degradation and extending the validity of drift degradation models.

## KEY COMPONENTS OF REPOSITORY ROCKFALL MODELING

**Rock Mass Characterization**—The repository horizon is located in both lithophysal (lower lithophysal [Ttptll] and upper lithophysal [Ttptul] zones) and nonlithophysal (middle nonlithophysal [Ttptmn] and lower nonlithophysal [Ttptln] zones) rock units in the Topopah Spring Tuff. These two rock types are expected to have fundamentally different modes of failure under dynamic loading and will require different analysis methods. The nonlithophysal rocks, which comprise roughly 15 percent of the emplacement area, are hard, strong, jointed rock

masses, whereas the lithophysal rocks, which comprise approximately 85 percent of the emplacement area, are relatively deformable with lower compressive strength.

The geologic structure and rock strength defines the failure mode in the Tptpmn. The failure mode in the Tptpmn is due to gravity drop of rock blocks resulting from stress-induced yield in either the intact rock or the joint surfaces. The analysis of the failure mechanism is complicated somewhat by the fact that the jointing in the Tptpmn is of short continuous trace length and is discontinuous in nature, thus forming fewer kinematically removable blocks. This type of jointing results in an inherently stronger rock mass as opposed to typical “blocky” rock masses where the block structure is well defined by multiple, continuous joint sets.

The Tptpll, on the other hand, is characterized by about 20 percent lithophysal cavities by volume. This unit has abundant small-scale fractures between lithophysae that result in the relatively weaker nature of the material. Rock mass failure in the Tptpll is controlled by the transient ground motion-induced stress concentrations that occur around the excavation. The mode of failure is primarily via tension from rarefaction of vertically traveling compression waves.

**Seismic Ground Motion**—Site-specific ground motions have been determined based on results from a probabilistic seismic hazard analysis. For a suite of ground motion measures, the probabilistic seismic hazard analysis determined the annual probability that various levels of ground motion would be exceeded. For an annual probability of exceedance of interest, a site response model modifies the ground motion from the probabilistic seismic hazard analysis by taking into account the effect of local site materials. Peak ground velocity determined from the site response model is used to develop seismic time histories (typically 15 three-component sets) for postclosure rockfall analysis. The time histories are developed such that observed randomness among time histories, for a given peak ground velocity, is maintained. The time histories thus appropriately reflect variability in ground motion estimation for Yucca Mountain.

**Thermal Stress**—Once the waste packages are placed within the emplacement drifts, heat will be released as a part of the process of the radioactive materials in the waste packages becoming less radioactive over time. This heat will transfer to the rock mass and thermally induced stresses will potentially be generated by thermal expansion of the rock mass. Thermal stresses at any location depend on the proximity and timing of waste emplacement, the amount of heat generated, the age of the waste, packaging and emplacement configuration, and the thermal-mechanical properties of the rock mass. Thermal stresses are time-dependent and are calculated over the 10,000-year regulatory period for postclosure performance.

**Time-Dependent Degradation of Rock Strength**—The rock mass surrounding the emplacement drifts may undergo over-stressing from thermal heating or time-dependent damage associated with static fatigue resulting from stress corrosion mechanisms. This damaged material may result in a slow unraveling (lithophysal rock) or block fallout (nonlithophysal rock). In the nonlithophysal rocks, static fatigue failure of roughness along fracture surfaces is possible and could result in gravitationally induced block failures. Static fatigue of hard rocks typically is associated with stress levels on the order of 80 percent or greater of the uniaxial compressive strength. This means that fatigue failure would presumably initiate along asperities on fracture surfaces, reducing the effective friction angle along the fracture surfaces. In the case of the

lithophysal rocks, the compressive stress concentrations along the immediate rib springline of the emplacement drifts will be at or near the uniaxial compressive strength so static fatigue failure is a distinct possibility.

### **ROCKFALL MODELING OF NONLITHOPHYSAL TUFF**

A nonlithophysal rockfall model was developed using the three-dimensional discontinuum code, 3DEC. This model includes the development of fracture patterns generated from multiple sampling from a synthetic rock mass volume that contains a realistic fracture population based on field mapping data. Site-specific ground motion time histories appropriate for both the preclosure and postclosure time periods are included in the model.

Degradation in the nonlithophysal units is primarily controlled by geologic structure. Preclosure ground motion results in minor drift damage due to rockfall. It should be noted that all results presented in this report are based on unsupported drift openings. The rockfall estimate during the preclosure period should be conservative, because the rockfall models assume the absence of ground support, while ground support will in fact be included to prevent rockfall. While postclosure ground motion also results in relatively minor drift damage due to rockfall, there are localized areas of rock failure sufficient to cover the drip shield.

Thermal-mechanical analyses were conducted using both a base-case set of thermal properties and a sensitivity case considering the values for thermal conductivity and specific heat one standard deviation smaller than the mean. There was no rockfall predicted at any time for the thermal only scenario (i.e., no seismic loading) for all cases analyzed. When thermal stresses were considered in combination with the stresses resulting from postclosure seismic ground motion, it is clearly shown that thermal loading significantly reduces amount of rockfall.

Drift stability due to the effect of time-dependent rock joint degradation is assessed based on a reduction of joint cohesion and friction angle. The reduced joint strength parameters are estimated to be in the range of the residual state with joint cohesion reduced to zero and the joint friction angle reduced to 30°. Dilation angle is also reduced to zero considering that the asperities on fracture surfaces had been sheared off. The degraded joint strength and dilational properties were applied for several selected cases, including the worst cases (cases with the most rockfall), the typical case, and the no rockfall case observed with postclosure seismic ground motion. While a slight increase in rockfall is predicted for the degraded state, joint strength degradation has a minor impact on drift stability.

### **ROCKFALL MODELING OF LITHOPHYSAL TUFF**

A lithophysal rockfall model was developed using the two-dimensional discontinuum code, UDEC. In this model, the rock mass is represented as an assembly of polygonal, elastic blocks in which the bond strength of the blocks is calibrated such that the overall mechanical behavior of the mass is consistent with the material model developed for the lithophysal rock. The lithophysal rockfall model allows for the formation of fractures between blocks (i.e., the formation of internal fracturing), separation, and instability (under action of gravity) of the rock mass around the drift. Site-specific ground motion time histories appropriate for both the preclosure and postclosure time periods are included in the model. The transient temperature

field around the repository was calculated using 90 and 70 percent ventilation efficiency. Two cases of thermal properties of rock mass and their effect on temperatures and induced stresses were considered. The analysis was done for six categories of rock mass qualities, which represent the variability expected on the repository level.

Degradation in the lithophysal units is primarily controlled by stress conditions. The analyses show that the drifts are stable after excavation with fracturing extending for 0.5 m in the drift walls. No rockfall is predicted due to heating for any of the six rock mass categories irrespective of the considered ventilation efficiency (70 or 90 percent) and the selection of rock mass thermal properties. Preclosure ground motion causes some rockfall for category 6, which is extremely poor rock quality. There is no significant rockfall due to preclosure ground motion in rock mass categories 1 through 5. However, if an earthquake hits the repository after 80 years of preclosure heating (time when temperature around the drifts peaks), rockfall is induced in rock mass category 1. Again, it should be noted that the modeled rockfall in the Tptpll is based on unsupported drift openings. The absence of ground support in the lithophysal rockfall model leads to a conservative rockfall estimate during the preclosure period, since the preclosure ground support will be designed to prevent rockfall.

Postclosure ground motions cause drift collapse irrespective of rock mass quality or particular case of ground motion. The extreme conditions of drift deterioration due to rock mass strength degradation were analyzed. Cohesive strength (cohesion and tensile strength) was gradually reduced to zero and resulting rockfall was monitored. The model was set to achieve conservative conditions of bulking of the caved rock mass (i.e., such that larger vertical pressures are imposed). The resulting vertical pressures of the rock on the drip shield are, with few exceptions, in the range between 150 kN/m<sup>2</sup> and 200 kN/m<sup>2</sup>.

## **RESOLUTION OF TECHNICAL ISSUES REGARDING ROCKFALL**

The drift degradation models and analyses documented in this report address the requirements of NRC/DOE agreement items regarding rockfall and related issues to support the resolution of NRC's key technical issue on Repository Design and Thermal-Mechanical Effects.

## CONTENTS

	<b>Page</b>
EXECUTIVE SUMMARY .....	5
ACRONYMS.....	23
1. PURPOSE.....	25
1.1 BACKGROUND.....	26
1.2 OBJECTIVES.....	27
1.3 SCOPE OF MODEL DOCUMENTATION.....	27
1.4 ANALYSIS/MODEL APPLICABILITY AND LIMITATIONS.....	28
2. QUALITY ASSURANCE.....	29
3. USE OF SOFTWARE.....	31
3.1 QUALIFIED COMPUTER SOFTWARE.....	31
3.2 OTHER SOFTWARE.....	32
4. INPUTS.....	33
4.1 DATA AND PARAMETERS.....	33
4.1.1 Joint Geometry Data.....	33
4.1.2 Joint Mechanical Properties Data.....	39
4.1.3 Intact Rock Physical and Mechanical Properties Data.....	39
4.1.4 Rock Mass Properties Data.....	40
4.1.5 Seismic Ground Motion Data.....	41
4.1.6 Rock Thermal Properties Data.....	41
4.1.7 Repository Layout Information.....	41
4.1.8 Matrix and Fracture Hydrologic Properties Data.....	41
4.2 CRITERIA.....	42
4.3 CODES AND STANDARDS.....	42
5. ASSUMPTIONS.....	43
5.1 THERMAL-MECHANICAL CALCULATION.....	43
5.1.1 Simultaneous Emplacement.....	43
5.1.2 Ventilation Heat Removal Ratio.....	43
5.1.3 Thermal Expansion.....	44
5.2 ROCKFALL MODELING.....	44
5.2.1 Joint Position Parameter in DRKBA.....	44
5.2.2 Block Size Distribution for Potential Rockfall in Lithophysal Units.....	44
5.3 GROUND SUPPORT.....	45
6. MODEL DISCUSSION AND ANALYSIS RESULTS.....	47
6.1 ROCK MASS CHARACTERISTICS OF REPOSITORY HOST HORIZON.....	47
6.1.1 Regional Geology.....	47
6.1.2 Lithostratigraphy at the Repository Horizon.....	50
6.1.3 Geotechnical Characterization.....	52

**CONTENTS (Continued)**

	<b>Page</b>
6.1.4 Discussion of Engineering Characteristics of Rock Mass Important to Geomechanical Performance .....	53
6.1.5 Field Observation of Key Blocks.....	63
6.1.6 Generation of Representative Rock Volumes Using FracMan.....	66
6.2 THERMAL-MECHANICAL CALCULATION.....	83
6.3 ROCKFALL IN THE NONLITHOPHYSAL UNITS .....	92
6.3.1 Three-Dimensional Discontinuum Analysis of Jointed Rock Mass for Wedge-Type Rockfall.....	92
6.3.2 Consideration of Intensely Fractured Zone.....	148
6.3.3 Impact of Small-Scale Fractures on Rockfall in Nonlithophysal Units.....	155
6.3.4 Drift Profile and Block Geometry Prediction in Nonlithophysal Units.....	160
6.4 ROCKFALL IN THE LITHOPHYSAL UNITS .....	166
6.4.1 Two-Dimensional Discontinuum Analysis of Lithophysal Rock Mass .....	167
6.4.2 Lithophysal Rock Mass Degradation.....	187
6.4.3 Investigation of Potential Key Blocks in Lithophysal Units .....	199
6.4.4 Drift Profile Prediction and Degraded Rock Mass Characteristics in Lithophysal Units.....	203
6.5 UNCERTAINTIES AND LIMITATIONS .....	204
6.6 DRIFT DEGRADATION FEATURES, EVENTS, AND PROCESSES.....	206
6.7 DOCUMENTATION OF ALTERNATIVE CONCEPTUAL MODELS.....	209
6.8 RESOLUTION OF KEY TECHNICAL ISSUES.....	210
7. VALIDATION.....	215
7.1 INTRODUCTION .....	215
7.2 MODEL VALIDATION LEVEL AND CRITERIA FOR VALIDATION .....	217
7.2.1 Level I Validation .....	217
7.2.2 Validation Criteria .....	218
7.3 MECHANICAL MATERIAL MODEL FOR LITHOPHYSAL ROCKS AND SELECTION OF INPUT PARAMETERS .....	220
7.3.1 Description of the Lithophysal Rocks.....	220
7.3.2 Model Requirements for Drift Degradation Prediction .....	222
7.4 LABORATORY AND FIELD DATABASE FOR CONSTITUTIVE MODEL DEVELOPMENT AND MODEL VALIDATION .....	223
7.4.1 Database.....	223
7.4.2 Subdivision of Properties into Categories for Design and Performance Assessment Studies.....	227
7.5 STRATEGY FOR DEVELOPMENT OF A MECHANICAL MATERIAL MODEL FOR LITHOPHYSAL ROCKS.....	229
7.5.1 Continuum-Based Approach to Representing Rock Masses .....	229
7.5.2 Discontinuum Approach to Representing Rock Masses.....	230
7.5.3 Strategy for Discontinuum Material Model Development .....	230
7.6 VALIDATION OF THE PARTICLE FLOW CODE (PFC) - A MICROMECHANICAL MODEL REPRESENTATION OF THE MECHANICAL BEHAVIOR OF LITHOPHYSAL ROCK.....	232

**CONTENTS (Continued)**

	<b>Page</b>
7.6.1 The PFC Model.....	232
7.6.2 Comparison of PFC Model Results Against Compression and Tensile Laboratory Tests on Cores.....	232
7.6.3 Calibration of PFC Model Properties .....	235
7.7 DEVELOPMENT AND VALIDATION OF A DRIFT-SCALE MODELING METHOD FOR LITHOPHYSAL ROCK USING THE UDEC PROGRAM .....	244
7.7.1 Qualification of the UDEC Program.....	244
7.7.2 Justification for a Two-Dimensional Isotropic Model of the Lithophysal Rock.....	245
7.7.3 Rock Mass Properties for Model Calibration .....	245
7.7.4 Model Calibration .....	245
7.7.5 Validation Strategy .....	252
7.7.6 Conclusions from UDEC Validation - Comparison to Criteria.....	276
7.7.7 UDEC Model Limitations.....	277
7.8 3DEC MODEL VALIDATION FOR REPRESENTATION OF NONLITHOPHYSAL ROCK.....	281
7.8.1 Introduction.....	281
7.8.2 Validation of the FracMan Model.....	281
7.8.3 3DEC Model Validation .....	285
7.8.4 Model Validation by Corroboration with Alternative Numerical Model .....	292
7.8.5 Model Validation by Expert Technical Review.....	293
7.8.6 Conclusions and Comparison to Validation Criteria .....	294
8. CONCLUSIONS.....	295
8.1 SUMMARY.....	295
8.2 ASSESSMENT.....	297
8.3 RECOMMENDATIONS.....	297
9. INPUTS AND REFERENCES.....	299
9.1 DOCUMENTS CITED.....	299
9.2 CODES, STANDARDS, REGULATIONS, AND PROCEDURES.....	307
9.3 SOFTWARE.....	308
9.4 SOURCE DATA, LISTED BY DATA TRACKING NUMBER .....	308
9.5 DEVELOPED DATA, LISTED BY DATA TRACKING NUMBER.....	314
10. ATTACHMENTS.....	315

INTENTIONALLY LEFT BLANK

## FIGURES

	<b>Page</b>
1. Drift Degradation Analysis.....	25
2. Simplified Lithostratigraphic Column of Paintbrush Group and the Rock Units that Form the Repository Host Horizon .....	48
3. Geology of the Central Block at Yucca Mountain and Location of the Exploratory Studies Facility (ESF), Including the ECRB Cross-Drift .....	49
4. Lithostratigraphic Features Related to Lithophysae and Fractures.....	50
5. Schematic Illustration of the Structure of the Topopah Spring Tuff.....	54
6. Fractures and Lithophysal Abundance in the ECRB Cross-Drift from Stations 0+00 to 27+00.....	55
7. Fracture Trace Length from Detailed Line Surveys as a Function of (a) Stationing Along the ECRB Cross-Drift and (b) Frequency Within Lithostratigraphic Units.....	56
8. Illustrative Example of a Full Periphery Geologic Map from the ESF, Ttpmnm.....	57
9. Fractures in Wall of the ECRB Cross-Drift in the Ttpmnm .....	58
10. Low-Angle Vapor-Phase Partings in Nonlithophysal Units in the ESF .....	59
11. Comparison of Lithophysae and Fracturing in the Ttpmnl and Ttpmnl .....	60
12. Lithophysae, Spots, and Clasts of Ttpmnl in Panel Map 1493 Located on the Right Rib from Stations 14+93 to 14+96.....	62
13. Calculated Porosity of Lithophysal Cavities, Rims, Spots, Matrix-Groundmass, and the Total Porosity in the Ttpmnl Exposed along the ECRB Cross-Drift .....	63
14. Illustration of a Typical Key Block and Associated Fracture Planes .....	64
15. Evidence of Key-Block Occurrence in the ECRB Cross-Drift, Station 11+55 .....	65
16. Opening Profile at ESF Main Loop Station 60+24.70 (Steel Set #1272, Ttpmnm Lithostratigraphic Unit) Based on Field Survey Data (dimensions in meters) .....	66
17. Relationship Between Trace Length and Radius .....	69
18. Ttpmnl Pole Plot Showing Great Circles for all Ttpmnl Fractures .....	71
19. Trace Length Distribution of the Ttpmnl Fractures (>45°) .....	72
20. FracMan Input Sheet for the Ttpmnl .....	73
21. Comparison of Full Periphery Geologic Maps from the Ttpmnl in the ECRB Cross- Drift with Simulated Full Periphery Geologic Maps from the FracMan Cube.....	75
22. Comparison of the Observed Ttpmnl Fracture Poles to the FracMan Fracture Poles .....	76
23. Comparison of the Observed Trace Length Distribution (Scaled by Two Thirds) to the FracMan Radii Distribution for Ttpmnl .....	77
24. Evaluation of Constant Intensity for Ttpmnl .....	77
25. Pole Plot of Ttpmnm Detailed Line Survey Data from the ESF Main Loop and ECRB Cross-Drift.....	78
26. FracMan Input sheet for the Ttpmnm .....	79
27. Comparison of Full Periphery Geologic Maps from the Ttpmnm in the ECRB Cross- Drift with Simulated Full Periphery Geologic Maps from the FracMan Cube.....	80
28. Comparison of the Observed Trace Length Distribution (Scaled by Two Thirds) to the FracMan Radii Distribution for Ttpmnm .....	81
29. Comparison of the Observed Ttpmnm Fracture Poles to the FracMan Fracture Poles .....	82
30. Heat Decay Curves for Thermal Calculations .....	86
31. Temperature History at the Drift Crown Due to the Linear Heat Load Presented in Figure 30 .....	86

**FIGURES (Continued)**

	<b>Page</b>
32. Comparison of Temperature Histories at Tunnel Crown for Case 1 Calculated Using NUFT and FLAC3D.....	87
33. Comparison of Stresses Around the Drift Between the FLAC and FLAC3D Predictions After 10 Years of Heating.....	88
34. Comparison of Stresses Around the Drift Between the FLAC and FLAC3D Predictions After 100 Years of Heating.....	88
35. Comparison of Stresses Around the Drift Between the FLAC and FLAC3D Predictions After 1000 Years of Heating.....	89
36. Comparison of Temperature Histories at Tunnel Crown for Case 1 Calculated Using NUFT and FLAC3D (for the Edge of the Repository).....	90
37. Comparison of Stresses Around the Drift Between the FLAC and FLAC3D Calculations for Edge of the Repository After 10 Years of Heating.....	90
38. Comparison of Stresses Around the Drift Between the FLAC and FLAC3D Calculations for Edge of the Repository After 100 Years of Heating.....	91
39. Comparison of Stresses Around the Drift Between the FLAC and FLAC3D Calculations for Edge of the Repository After 1000 Years of Heating.....	91
40. 3DEC Model Geometry and Cross-Sections.....	95
41. Illustration of Free-Field Boundaries in 3DEC Model.....	97
42. Examples of Ground Velocity Time Histories (H1) with Truncated Duration for Analysis.....	100
43. Comparison of Input Seismic Wave and Recorded Velocities in 3DEC Model.....	106
44. Illustration of the Simulation of Rockfall Impact to the Drip Shield 3DEC Simulation #55, $1 \times 10^{-6}$ Ground Motion # 12, at $t = 6.6$ sec.....	107
45. Time Histories for Normal and Shear Stress at Fracture Contact Coordinate: 2.046, 0.341, -3.271 (3DEC Simulation #21, $1 \times 10^{-6}$ Ground Motion #10).....	107
46. Normal and Shear Stress Path at Fracture Contact Coordinate: 2.046, 0.341, -3.271 (3DEC Simulation #21, $1 \times 10^{-6}$ Ground Motion #10).....	108
47. Definition of Impact Angle and Drip Shield Block Local Coordinate System.....	110
48. Histogram for Block Mass ( $1 \times 10^{-6}$ Annual Probability of Exceedance Hazard).....	111
49. Histogram for Relative Impact Velocity ( $1 \times 10^{-6}$ Annual Probability of Exceedance Hazard).....	111
50. Histogram for Impact Angle ( $1 \times 10^{-6}$ Annual Probability of Exceedance Hazard).....	112
51. Histogram for Impact Momentum ( $1 \times 10^{-6}$ Annual Probability of Exceedance Hazard).....	112
52. Histogram for Impact Energy ( $1 \times 10^{-6}$ Annual Probability of Exceedance Hazard).....	113
53. Comparison of Input Seismic Wave and Recorded Velocities in 3DEC Model for $1 \times 10^{-7}$ Annual Probability of Exceedance Ground Motion (H1).....	114
54. Illustration of the Simulation of Rockfall Impact to the Drift Shield (3DEC Simulation #55, $1 \times 10^{-7}$ Ground Motion # 12, at $t = 6.6$ sec).....	115
55. Time Histories for Normal and Shear Stress at Rock Bridge Contact Coordinate: 2.451, 2.749, -0.350 (3DEC Simulation #78, $1 \times 10^{-7}$ Ground Motion #7).....	115
56. Normal and Shear Stress Path at Rock Bridge Contact Coordinate: 2.451, 2.749, -0.350 (3DEC Simulation #78, $1 \times 10^{-7}$ Ground Motion #7).....	116
57. Histogram for Block Mass ( $1 \times 10^{-7}$ Annual Probability of Exceedance Hazard).....	117

**FIGURES (Continued)**

	<b>Page</b>
58. Histogram for Relative Impact Velocity ( $1 \times 10^{-7}$ Annual Probability of Exceedance Hazard) .....	118
59. Histogram for Impact Angle ( $1 \times 10^{-7}$ Annual Probability of Exceedance Hazard) .....	118
60. Histogram for Impact Momentum ( $1 \times 10^{-7}$ Annual Probability of Exceedance Hazard).....	119
61. Histogram for Impact Energy ( $1 \times 10^{-7}$ Annual Probability of Exceedance Hazard).....	119
62. Comparison of Input Seismic Wave and Recorded Velocities in 3DEC Model for $5 \times 10^{-4}$ Annual Probability of Exceedance Ground Motion (H1) .....	122
63. Illustration of the Simulation of Rockfall Impact to the Drift Shield (3DEC Simulation for $5 \times 10^{-4}$ Preclosure Run 16, at $t = 3.01$ sec).....	123
64. Time Histories for Normal and Shear Stress at Fracture Contact Coordinate: -5.106, 0.681, -5.306 (3DEC $5 \times 10^{-4}$ Preclosure Simulation 19) .....	123
65. Normal and Shear Stress Path at Fracture Contact Coordinate: -5.106, 0.681, -5.306 (3DEC $5 \times 10^{-4}$ Preclosure Simulation 19) .....	124
66. Histogram for Block Mass ( $5 \times 10^{-4}$ Annual Probability of Exceedance Hazard) .....	125
67. Histogram for Impact Velocity ( $5 \times 10^{-4}$ Annual Probability of Exceedance Hazard) .....	125
68. Histogram for Impact Angle ( $5 \times 10^{-4}$ Annual Probability of Exceedance Hazard) .....	126
69. Histogram for Impact Momentum ( $5 \times 10^{-4}$ Annual Probability of Exceedance Hazard).....	126
70. Histogram for Impact Energy ( $5 \times 10^{-4}$ Annual Probability of Exceedance Hazard).....	127
71. Stress Paths in the Drift Wall: Case 47 .....	129
72. Stress Paths in the Drift Roof: Case 47.....	129
73. Stress Paths in the Drift Wall: Elastic Model .....	130
74. Stress Paths in the Drift Roof: Elastic Model .....	130
75. Stress Paths in the Drift Wall: Case 47, Thermal Sensitivity Case 2 .....	132
76. Stress Paths in the Drift Roof: Case 47, Thermal Sensitivity Case 2 .....	132
77. Rockfall vs Time of Shaking for $1 \times 10^{-6}$ Ground Motion Set 4, Case 58 .....	136
78. Rockfall vs Time of Shaking for $1 \times 10^{-6}$ Ground Motion Set 12, Case 55 .....	137
79. Rockfall vs Time of Shaking for $1 \times 10^{-6}$ Ground Motion Set 8, Case 47 .....	138
80. Calibration of Nonlithophysal Rock Mass Material Properties .....	142
81. Minor Spalling for Intact Block (70 MPa unconfined compressive strength) Subject $1 \times 10^{-6}$ Ground Motion Set 5 .....	142
82. Severe Spalling for Intact Block (70 MPa unconfined compressive strength) Subject $1 \times 10^{-6}$ Ground Motion Set 4 .....	143
83. Minor Spalling for Intact Block (100 MPa unconfined compressive strength) Subject $1 \times 10^{-6}$ Ground Motion Set 4 .....	143
84. Cross-Section of the Four Model Dimensions Selected for Sensitivity Study .....	145
85. Blocks Accumulated Above the Drip Shield Without Implementing Block Deletion Algorithm, Fracture Modeling Region #8, $1 \times 10^{-6}$ Ground Motion Set #14.....	146
86. Blocks Accumulated Above the Drip Shield Without Implementing Block Deletion Algorithm, Fracture Modeling Region #16, $1 \times 10^{-6}$ Ground Motion Set #2.....	147
87. Photo Showing the Intensely Fractured Zone in ESF Main Drift.....	148
88. Fracture Analysis for the Intensive Fracture Zone .....	149
89. FLAC3D Model Mesh and Fracture Orientation.....	150
90. Yield State Prediction - Preclosure Ground Motion at 28 Seconds.....	151

**FIGURES (Continued)**

	<b>Page</b>
91. In-Plane Shear Stress Contours - Preclosure Ground Motion at 28 Seconds .....	152
92. Principal Stress Tensor - Preclosure Ground Motion at 28 Seconds .....	152
93. Yield State Prediction - Postclosure Ground Motion at 2 Seconds .....	153
94. In-Plane Shear Stress Contours - Postclosure Ground Motion at 2 Seconds .....	153
95. Principal Stress Tensor - Postclosure Ground Motion at 2 Seconds .....	154
96. Stress Path at Roof Under Preclosure Seismic Motion .....	154
97. Stress Path at Roof Under Postclosure Seismic Motion .....	155
98. Histogram Fracture Traces in Panels 11+15 and 11+30 .....	157
99. Pole Plots for the Filtered Small-Scale Fractures .....	158
100. Block Size Distribution Predicted from DRKBA Analyses .....	159
101. Drift Profile for $1 \times 10^{-7}$ Hazard Level, Worst Case .....	161
102. Drift Profile for $1 \times 10^{-7}$ Hazard Level, 75 Percentile Case .....	162
103. Drift Profile for $1 \times 10^{-6}$ Hazard Level, Worst Case .....	163
104. Drift Profile for $1 \times 10^{-6}$ Hazard Level, 75 Percentile Case .....	164
105. Drift Profile for $5 \times 10^{-4}$ Hazard Level, Worst Case .....	165
106. Geometry and Initial Conditions of the UDEC Model .....	169
107. Dynamic Model, Initial and Boundary Conditions: Initial Static Simulation .....	171
108. Dynamic Model Boundary Conditions for Dynamic Simulation .....	171
109. Horizontal Velocity, Component 1 for Ground Motion 4 .....	172
110. Geometry of the Model after Simulation for Preclosure Ground Motion (Probability $5 \times 10^{-4}$ ): Rock Mass Categories 1 and 6 .....	173
111. Elastic Stress Paths in the Drift Wall due to Preclosure Ground Motion: Category 1 .....	174
112. Elastic Stress Paths in the Drift Roof due to Preclosure Ground Motion: Category 1 .....	174
113. Elastic Stress Paths in the Drift Wall due to Preclosure Ground Motion: Category 5 .....	175
114. Elastic Stress Paths in the Drift Roof due to Preclosure Ground Motion: Category 5 .....	175
115. Geometry of the Model after Simulations for Postclosure Ground Motions (Probability $1 \times 10^{-6}$ ): Realizations 1 through 6 from Table 37 .....	177
116. Elastic Stress Paths in the Drift Wall due to Postclosure Ground Motion No. 1: Category 1 .....	178
117. Elastic Stress Paths in the Drift Roof due to Postclosure Ground Motion No. 1: Category 1 .....	178
118. Elastic Stress Paths in the Drift Wall due to Postclosure Ground Motion No. 1: Category 5 .....	179
119. Elastic Stress Paths in the Drift Roof due to Postclosure Ground Motion No. 1: Category 5 .....	179
120. Thermal-Mechanical Model Initial and Boundary Conditions .....	180
121. Thermally Induced Rockfall and Stresses After 80 and 10,000 years of Heating in Rock Mass Category 1 .....	182
122. Elastic Stress Paths in the Drift Wall due to Temperature History: Category 1 .....	183
123. Elastic Stress Paths in the Drift Roof due to Temperature History: Category 1 .....	183
124. Elastic Stress Paths in the Drift Wall due to Temperature History: Category 5 .....	184
125. Elastic Stress Paths in the Drift Roof due to Temperature History: Category 5 .....	184
126. Stress Paths in the Left Drift Wall due to Temperature History: Category 1 .....	185
127. Stress Paths in the Right Drift Wall due to Temperature History: Category 1 .....	185

**FIGURES (Continued)**

	<b>Page</b>
128. Stress Paths in the Drift Roof due to Temperature History: Category 1 .....	186
129. Rockfall and Fractures Induced Around a Drift by Preclosure Ground Motion After 80 Years of Heating in Rock Mass Categories 1 and 5 .....	187
130. Rockfall and Fractures Induced Around a Drift by Preclosure Earthquake After 80 Years of Heating (70 Percent Ventilation Efficiency) in Rock Mass Categories 1 and 5 .....	188
131. “Piping” Type of Caving Mechanism .....	190
132. Terzaghi Type of Caving Mechanism .....	190
133. Cave Height as a Function of Bulking Factor: Analytical Solution .....	192
134. Vertical Load on the Drip Shield as a Function of Bulking Factor: Analytical Solution .....	193
135. Failure Mechanism of a Deep Tunnel in Cohesionless Material .....	194
136. Piping Failure Mechanism Considered in the Continuum Model: Bulking Factor $B =$ $0.2$ .....	194
137. Terzaghi Failure Mechanism Considered in the Continuum Model: Bulking Factor $B = 0.1$ .....	195
138. Pressures on the Drip Shield Calculated from the Discontinuum Model: Case 4 .....	197
139. Evolution of the Cave as a Function of the Cohesive Strength: Case 4 .....	198
140. Size and Shape of the Cave for Cases 3, 4, and 5 .....	200
141. Stresses in the Rock Mass After Caving Shown at Two Scales .....	201
142. Summary of Vertical Load on the Drip Shield as a Function of Bulking Factor .....	202
143. Cross-Section of a Typical Simulated Lithophysal Rock Mass in 3DEC .....	203
144. (a) Matrix Fracturing in the Ttppll in 12-in-Diameter Core and (b) Lack of Fracturing in Matrix of Ttppl as Seen in the Wall of Alcove 8 off the ECRB Cross- Drift .....	221
145. Variation in Lithophysal Cavities in the Ttppll in the ECRB Cross-Drift from Top (Left) to Bottom of the Sub-Unit as Estimated by Tape and Angular Measurement Collected at 5-m Intervals .....	222
146. (a) Uniaxial Compression Strength Results for all Large Diameter Ttppl and Ttppll Core Samples from Batch 1 and 2 and Busted Butte and (b) Young’s Modulus Measurements Batch 1 and Batch 2 .....	224
147. Histogram of Estimated Porosities of Large Core Samples from Batch 1, Batch 2 and Busted Butte .....	225
148. Variation of Unconfined Compressive Strength as a Function of Estimated Lithophysal Porosity from Batch 1, Batch 2 and Busted Butte Ttppl and Ttppll Large Core Samples .....	226
149. Relationship of Uniaxial Compressive Strength to Young’s Modulus for All Batch 1 and 2 Large Core Samples of Ttppl and Ttppll .....	227
150. Schematic Illustration of Continuum (Left) and Discontinuum (Right) Approaches to Modeling Drift Stability .....	229
151. General Approach to Validation of Mechanical Material Model for Lithophysal Rocks .....	231
152. The Basic Mechanics of the PFC Program .....	233

**FIGURES (Continued)**

	<b>Page</b>
153. Relative Distributions of the Three Components of Lithophysal Tuff for (a) Real Material (Price et al. 1985) and (b) PFC Materials .....	235
154. PFC2D Unconfined Compressive Strength Test Specimens .....	236
155. PFC3D Unconfined Compressive Strength Test Specimens .....	237
156. PFC2D Simulation of Confined Compression of 2:1 L:D Samples of Nonlithophysal Material ( $n_v = 0$ ) Composed of Several Thousand Bonded Particles .....	238
157. PFC2D Simulation of Confined Compression of 2:1 L:D Samples of Lithophysal Material ( $n_v = 0.10$ ) Composed of Several Thousand Bonded Particles .....	239
158. PFC2D Simulation of Confined Compression of 2:1 L:D Samples of Lithophysal Material ( $n_v = 0.20$ ) Composed of Several Thousand Bonded Particles .....	240
159. PFC2D Simulation of Direct Pull Strength of 2:1 L:D Samples of Nonlithophysal and Lithophysal ( $n_v = 0.10$ and $0.20$ ) Composed of Several Thousand Bonded Particles .....	242
160. Young's Modulus Versus Void Porosity for Lithophysal Tuff and PFC Materials .....	243
161. Unconfined Compressive Strength Versus Void Porosity for Lithophysal Tuff and PFC Materials .....	243
162. Unconfined Compressive Strength Versus Young's Modulus for Lithophysal Tuff and PFC Materials .....	244
163. UDEC Lithophysal Rock Specimen Composed of Many Irregular Blocks with Roughly Equi-Dimensional Side Lengths .....	246
164. Micro Properties of the UDEC Voronoi Model .....	248
165. Numerical Experiment, Category 1: Stress-Strain Curves and Modes of Failure for Different Confinements and Loading Conditions .....	249
166. Numerical Experiment, Category 1: Failure Envelope .....	250
167. Numerical Experiment, Category 1: Volumetric Strain Versus Axial Strain for Different Confinements and Loading Conditions .....	251
168. UDEC Discontinuum Model of Failure of Lithophysal Tuff Specimen Under Uniaxial Compression .....	253
169. Predicted Failure Mode of UDEC Sample in Direct Tension Test .....	254
170. Observed Rock Mass Conditions at the Tunnel Springline in Lithophysal Rock in the ESF .....	255
171. Estimate of Rock Mass Fracturing and Stress State Under In Situ Loading Only, Depth of 300 m, Tptpll, Strength Category 1 (Low-Strength Characteristics) and 5 (High-Strength Characteristics) .....	257
172. Estimate of Rock Mass Fracturing as a Function of Overburden Between 250 m and 350 m, Tptpll, Strength Categories 1 and 6 (Low-Strength Characteristics) .....	258
173. Perspective View of Heated Drift Scale Test Showing Wing Heaters .....	259
174. Minor Superficial Slabbing in the Center of the Roof Span Observed During Thermal Overstressing of the Heated Drift Scale Test .....	260
175. UDEC Sample Calibration to Size-Effect Strength Data for an Approximate 1-m Sample Size, Tptpmn .....	261
176. Results from Heated Drift Analysis with 1997 Temperature Conditions .....	263
177. Results from Heated Drift Analysis with 1998 Temperature Conditions .....	264
178. Results from Heated Drift Analysis with 1999 Temperature Conditions .....	265

**FIGURES (Continued)**

	<b>Page</b>
179. Results from Heated Drift Analysis with 2000 Temperature Conditions.....	266
180. Results from Heated Drift Analysis with 2001 Temperature Conditions.....	267
181. Results from Heated Drift Analysis with 2002 Temperature Conditions.....	268
182. Problem Geometry of the Mechanical Response of a 5-m Diameter Tunnel in Jointed Rock Subjected to a Spherically Expanding Blasting Source.....	270
183. Radial Stress (Top) and Radial Velocity (Bottom) at the Centroid of the Future Tunnel Location in Problem 4 (Senseny 1993).....	272
184. Comparison of Predicted Tunnel Invert-Crown (Top) and Springline (Bottom) Closure for Problem 5 (Senseny 1993) .....	273
185. Comparison of Radial Stress Along Radial Lines at Peak Free Field Stress Arrival Time, Problem 5 (Senseny 1993).....	274
186. Comparisons of Exaggerated Tunnel Shapes ( $\times 10$ ) at Equilibrium, Problem 5.....	275
187. Block Size Effect: Behavior of the Rock Mass (Rock Mass Category 1, 300-m Overburden) Under Vertical and Horizontal Stress at Ratio of 2:1 .....	278
188. Effect of Voronoi Block Realization: Behavior of the Rock Mass (Rock Mass Category 1, 350-m Overburden) Under Vertical and Horizontal Stress at Ratio of 2:1.....	279
189. Direct Shear Test Results for a Rough, Sub-Horizontal Vapor-Phase Parting.....	286
190. Direct Shear Test Results for a Smooth, Sub-Vertical Cooling Joint.....	287
191. Perspective View of 3DEC Model of Direct Shear Test of Joint .....	288
192. Cross-Sectional View Through Model Showing Relative Shear Displacement of Joint Surfaces .....	289
193. Comparison of 3DEC Mohr-Coulomb Joint Constitutive Model to Laboratory Direct Shear Testing for Sample 643, Hole ERCB-GTEC-CS1250-13.....	290
194. Comparison of 3DEC Simulation of Direction Shear Testing of a Vapor-Phase Parting (see Figure 189) .....	291
195. Comparison of Rockfall Results from 3DEC and DRKBA.....	293

INTENTIONALLY LEFT BLANK

## TABLES

	<b>Page</b>
1. List of Qualified Software Supporting the Drift Degradation Analysis .....	31
2. Input Data and Parameters for the Drift Degradation Analysis.....	34
3. General Characteristics of Fracture Sets in the Middle Nonlithophysal Unit .....	56
4. Summary Statistics of the Tptpll Detailed Line Survey Data.....	72
5. Relative Proportions of Fractures from the Detailed Line Survey versus FracMan Output for the Tptpll .....	74
6. Comparison of Data from Detailed Line Survey and FracMan for the Tptpmn.....	78
7. Base-Case Material Properties for 3DEC Analysis .....	96
8. Boundary Conditions for 3DEC Analysis .....	96
9. Peak Ground Motion Parameters.....	99
10. Arias Intensity (m/sec) for Each Ground Motion Set.....	101
11. Seismic Analysis Duration and Complete Time History Duration.....	102
12. Combinations of Ground Motion and Fracture Modeling Region of 3DEC Analyses.....	103
13. Summary of 3DEC Rockfall Prediction for $1 \times 10^{-6}$ Annual Probability of Exceedance Hazard .....	108
14. Statistic Summary of the Rockfall Impact Parameters, $1 \times 10^{-6}$ Annual Probability of Exceedance Hazard .....	109
15. Summary of 3DEC Rockfall Prediction for $1 \times 10^{-7}$ Annual Probability of Exceedance Hazard .....	116
16. Statistic Summary of the Rockfall Impact Parameters, $1 \times 10^{-7}$ Annual Probability of Exceedance Hazard .....	117
17. Combinations of Ground Motion and Fracture Modeling Region of 3DEC Analyses.....	120
18. Summary of 3DEC Rockfall Prediction for $5 \times 10^{-4}$ Annual Probability of Exceedance Hazard .....	124
19. Statistic Summary of the Rockfall Impact Parameters, $5 \times 10^{-4}$ Annual Probability of Exceedance Hazard .....	124
20. Rockfall in Nonlithophysal Rock Due to $10^{-6}$ Ground Motion Combined with Thermal-Mechanical Effects: Base Case of Thermal Properties .....	133
21. Rockfall in Nonlithophysal Rock Due to $10^{-6}$ Ground Motion Combined with Thermal-Mechanical Effects: Thermal Properties One Standard Deviation Less Than Mean.....	133
22. Predicted Rockfall for Degradated Joints with Comparison to the Base Case.....	134
23. Comparison of Rockfall Prediction on Energy Content of Ground Motions .....	135
24. Impact of the Orientation of Horizontal Motions to the Rockfall Prediction.....	139
25. Three Categories of Joint Properties Used in the Sensitivity Study .....	140
26. Sensitivity of Joint Properties for Rockfall Prediction .....	140
27. Various Model Dimension for Sensitivity Study.....	144
28. Predicted Rockfall for Various Model Dimensions.....	144
29. Predicted Rockfall With and Without Block Deletion after Impact.....	147
30. Range of Fracture Traces in Panels 11+15 and 11+30.....	156
31. Block Volume (in cubic meter) Corresponding to Various Level of Predicted Cumulative Frequency of Occurrence.....	159
32. Summary of Results for DRKBA Comparative Analysis.....	159

**TABLES (Continued)**

	<b>Page</b>
33. Predicted Number of Rockfall and Volume for the Presented Drift Profile.....	166
34. Categories of the Lithophysal Rock Mass Selected for Analysis.....	167
35. Micro Properties in the Model with 0.2 m Block Size.....	168
36. Micro Properties in the Model with 0.3 m Block Size.....	168
37. Simulated Combinations of $10^{-6}$ Ground Motions and Rock Mass Categories.....	170
38. Summary of Loads on the Drip Shield after Drift Collapse Caused by Postclosure Ground Motion (Probability $1 \times 10^{-6}$ ).....	180
39. Summary of Pressures on the Drip Shield Calculated from the Continuum Model.....	195
40. Summary of Pressures on the Drip Shield Calculated from the Discontinuum Model.....	196
41. Summary of 3DEC Rockfall Prediction for Lithophysal Units.....	202
42. FEPs Addressed by This Model Report.....	207
43. Alternative Conceptual Models Considered.....	209
44. Repository Design and Thermal-Mechanical Effects Key Technical Issue Agreement Items Addressed in this Model Report.....	213
45. Suggested Range of Mechanical Properties Selected for Design and Performance Analyses.....	228
46. Code-to-Code Comparison Problems.....	270
47. Programs and Modeling Participants in the Benchmark Study.....	271
48. List of Attachments.....	315

## ACRONYMS

BSC	Bechtel SAIC Company, LLC
CHn1	Calico Hills and Lower Paintbrush non-welded
CHn2	Calico Hills and Lower Paintbrush non-welded
DOE	U.S. Department of Energy
DTN	data tracking number
EBS	engineered barrier system
ECRB	Enhanced Characterization of the Repository Block
ESF	Exploratory Studies Facility
FEPs	features, events, and processes
ICN	Interim Change Notice
KTI	key technical issue
LDTH	line-averaged heat source, drift-scale, thermohydrologic
LEFM	Linear Elastic Fracture Mechanics
NRC	U.S. Nuclear Regulatory Commission
PTn	Upper Paintbrush non-welded vitric
RMR	rock mass rating
RQD	rock quality designation
TCw	Tiva Canyon welded
Tptpll	Topopah Spring Tuff crystal poor lower lithophysal
Tptpln	Topopah Spring Tuff crystal poor lower nonlithophysal
Tptpmn	Topopah Spring Tuff crystal poor middle nonlithophysal
Tptpul	Topopah Spring Tuff crystal poor upper lithophysal
TSPA-LA	Total System Performance Assessment for the License Application
TSw1	Topopah Spring welded, lithophysal-rich
TSw2	Topopah Spring welded, lithophysal-poor
TSw3	Topopah Spring welded, vitrophyre
USBR	U.S. Bureau of Reclamation
USGS	U.S. Geological Survey
YMP	Yucca Mountain Project

**ACRONYMS (Continued)**

INTENTIONALLY LEFT BLANK

## 1. PURPOSE

The purpose of this report is to document the scientific analysis and modeling of the deterioration of the rock mass surrounding the emplacement drifts of the geologic repository at Yucca Mountain. Drift degradation has the potential to affect drip shield integrity, waste package integrity, and thermal-hydrologic environments within drifts. The results of this modeling and analysis activity will provide rockfall data to support structural analyses of the ground support system, the drip shield, and waste package. The drift degradation analysis also provides the changes in drift profile due to rockfall, which supports analyses of seepage into the emplacement drift during the period of compliance for postclosure performance. Figure 1 depicts the required inputs supporting the drift degradation analysis along with the primary users of the results of this study. This report has been developed in accordance with *Technical Work Plan for: Engineered Barrier System Department Modeling and Testing FY 03 Work Activities* (BSC 2003a).

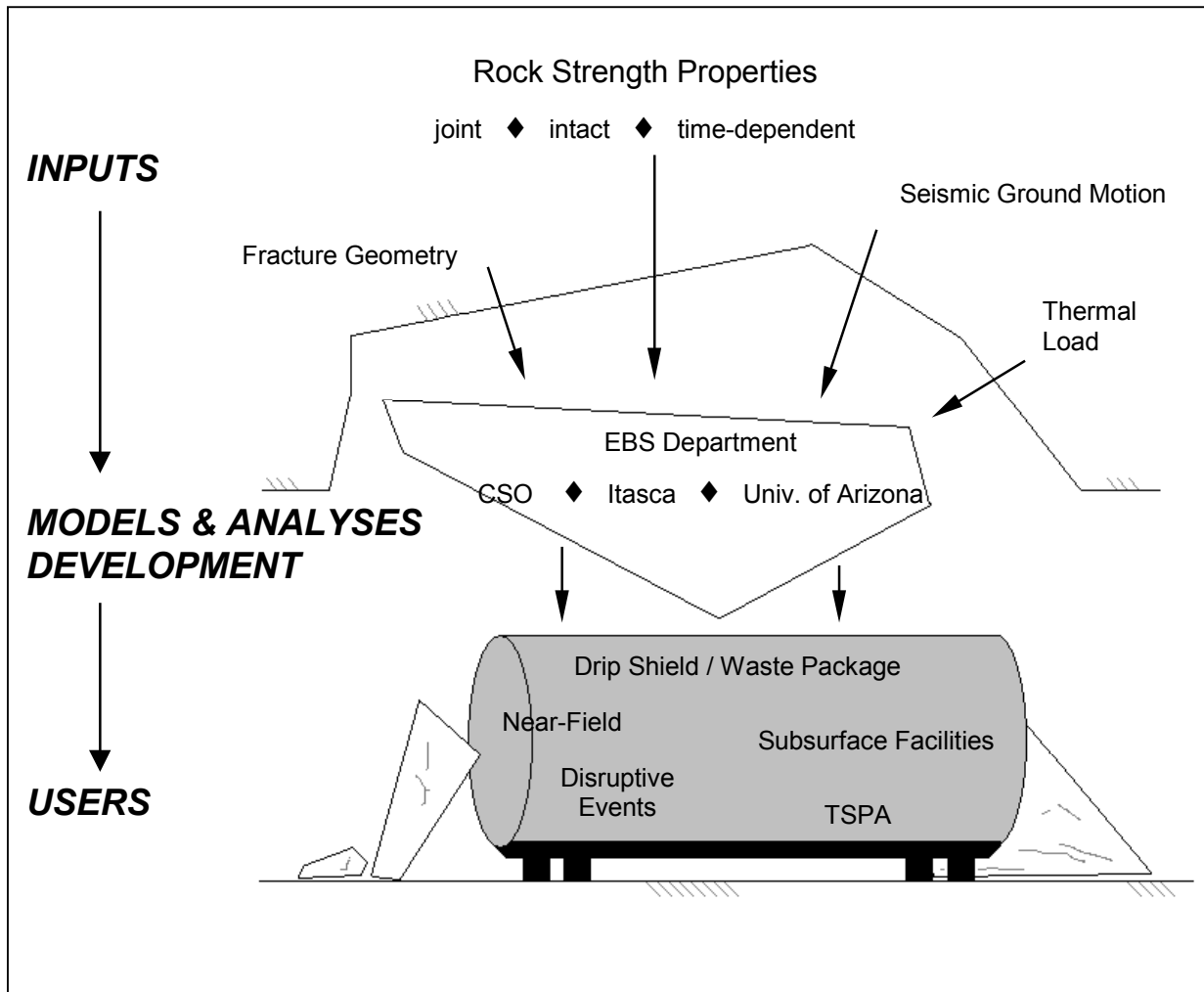


Figure 1. Drift Degradation Analysis

The drift degradation analysis includes the development and validation of rockfall models that approximate phenomenon associated with various components of rock mass behavior anticipated within the repository horizon. Two drift degradation rockfall models have been developed: the rockfall model for nonlithophysal rock and the rockfall model for lithophysal rock.

These models reflect the two distinct types of tuffaceous rock at Yucca Mountain. The output of this modeling and analysis activity documents the expected drift deterioration for drifts constructed in accordance with the repository layout configuration (BSC 2003b).

## 1.1 BACKGROUND

A probabilistic key-block analysis was initially proposed as part of the Exploratory Studies Facility (ESF) design confirmation activities. Key blocks are critical blocks in the surrounding rock mass of an excavation which are removable and oriented in an unsafe manner so that they are likely to move into an opening unless support is provided (Goodman and Shi 1985, pp. 98 and 99). The initial ESF design confirmation plans included an analysis of geotechnical mapping data from the ESF to identify the size of potential key blocks, assess specific key blocks occurring in the field, and conduct a stability analysis on these blocks, if necessary, to confirm the effectiveness of the existing ground support. Large key blocks are significant because they have the potential to increase ground support loads, and if disturbed by a seismic event, could potentially fail if the ground support is not adequate.

As part of the initial ESF design confirmation planning, technical literature sources were reviewed (see Attachment IV) for the purpose of determining the most appropriate approach to be used in the development of a key-block analysis for the Yucca Mountain Project (YMP). As a result, the Discrete Region Key Block Analysis (DRKBA) software was purchased. The DRKBA probabilistic approach is distinguished from traditional key-block analyses in that it assesses the maximum size of key blocks within a given number of simulations and also predicts the number of potential key blocks that will be formed within a referenced length of tunnel. The DRKBA approach also allows for a variety of tunnel and jointing configurations.

It was recognized that this key-block analysis has the potential to provide necessary information to support several key YMP documents, including the License Application. The potential users of the key-block analysis include the Specialty Analyses & Waste Package Design Department, the Total System Performance Assessment Department, the Disruptive Events Department, the Ambient and Thermal Drift Seepage Department, the Subsurface Department, and the Preclosure Safety Analysis Department.

The earlier versions of the Drift Degradation Analysis (Revisions 0 and 1) relied primarily on the DRKBA numerical code to develop a probabilistic key-block assessment based on realistic fracture patterns determined from field mapping in the ESF. However, the use of the DRKBA code to determine potential rockfall data at the repository horizon during the postclosure time period has several limitations and areas for improvement:

- The DRKBA code can not explicitly apply dynamic loads due to seismic ground motion.
- The DRKBA code can not explicitly apply loads due to thermal stress.
- The DRKBA code, which determines structurally controlled key-block failure, is not applicable for stress controlled failure in the lithophysal units.

To address the DRKBA limitations, additional numerical codes have been included that can explicitly apply seismic and thermal loads, providing significant improvements to the analysis of drift degradation and extending the validity of drift degradation models. This revision of the drift degradation analysis was developed to document these changes to support the submittal of a license application.

## **1.2 OBJECTIVES**

The specific objectives of the drift degradation analysis are:

- To model the jointed configuration of the rock mass surrounding the emplacement drift cavity.
- To provide a statistical description of block sizes formed by fractures around the emplacement drifts for the lithologic units of the repository host horizon.
- To estimate changes in drift profiles resulting from progressive deterioration of the emplacement drifts.
- To provide an estimate of the effects of time-dependent rock strength degradation.

## **1.3 SCOPE OF MODEL DOCUMENTATION**

Activities documented in this report involve developing models, using analytical methods, and performing calculations and statistical analyses to determine the expected quantities, locations, size distributions, and frequencies of rockfall, based on the repository layout configuration (BSC 2003b). Deteriorated drift profiles as a result of rockfall have been determined. This analysis has examined unsupported drifts, and applied static, thermal, and seismic loading conditions.

The drift degradation and stability models presented in this report were developed by the Engineered Barrier System (EBS) Department, with support provided by the Chief Science Officer, Itasca Consulting Group, Inc., the U.S. Geological Survey/U.S. Bureau of Reclamation (USGS/USBR) and the University of Arizona. The scope of model documentation required for analyzing the degradation anticipated in the repository emplacement drifts includes the following activities:

- Conduct a thermal-mechanical assessment of the repository block at Yucca Mountain to determine thermal stress inputs to the drift degradation models.
- Conduct a fracture degradation assessment to account for long-term strength degradation. This assessment provides strength degradation inputs to the drift degradation models.
- Develop a drift degradation structural model for nonlithophysal rock that includes thermal and seismic loading.
- Develop a drift degradation lithophysal model that includes thermal and seismic loading.

Revision 0 of this report included analyses with backfill as part of the baseline design. Since backfill is no longer part of the baseline design, the backfill results have not been included in this report. Revision 1 ICN 1 of this analysis considered various emplacement drift orientations, with the drift azimuth varied in appropriate increments to examine the effect of orientation on key block size and frequency. The results from this drift orientation study have not been included in this revision, and only the current emplacement drift orientation (BSC 2003b) has been considered in this report.

#### **1.4 ANALYSIS/MODEL APPLICABILITY AND LIMITATIONS**

The drift degradation results with seismic and thermal consideration, including the drift profiles, are applicable for 5.5-m-diameter emplacement drifts oriented at an azimuth of 72° in accordance with the repository underground layout configuration (BSC 2002a; BSC 2002b; BSC 2003b; BSC 2003c). The model results presented in this report are applicable for the lithophysal and nonlithophysal rock units of the repository host horizon. Uncertainties associated with the data available for model development are described in Section 6.5. The rockfall models presented in this report are valid for conditions anticipated within the repository over the 10,000-year regulatory period for both preclosure and postclosure performance, including increased loads due to seismic ground motion and thermal stress, and decreased rock strength due to time-dependent strength degradation. It should be noted that preclosure rockfall model validation is limited to a ground motion level with a  $5 \times 10^{-4}$  annual exceedance probability. Ground motions for lower probability preclosure levels (e.g.,  $1 \times 10^{-4}$  annual exceedance probability) have not been considered in this report.

## 2. QUALITY ASSURANCE

This report has been developed in accordance with AP-SIII.10Q, *Models*, as an implementing document of Work Package AEBM04, as described by *Technical Work Plan for: Engineered Barrier System Department Modeling and Testing FY03 Work Activities* (BSC 2003a).

There are no quality level assignments to individual items applicable to the development of this document in accordance with AP-2.22Q, *Classification Criteria and Maintenance of the Monitored Geologic Repository Q-List*. There are no evaluations from LP-SA-001Q-BSC, *Determination of Importance and Site Performance Protection Evaluations* that are directly applicable to the development of this document. All input data are identified and tracked in accordance with AP-3.15Q, *Managing Technical Product Inputs*.

All electronic data used in the preparation of this activity were obtained from the Technical Data Management System, as appropriate. Electronic data were controlled and managed per the technical work plan (BSC 2003a). To ensure accuracy and completeness of the information generated by this report access to the information on the personal computer used to develop this report is controlled with password protection. The personal computer files are stored on a network drive that is backed up daily per YMP standards. Upon completion of this work, all files are transferred to a CD-ROM, appropriately labeled, and verified by examining the file listing. Visual checks are conducted on printouts. The CD-ROM is transmitted to Document Control for transfer to the Records Processing Center. During the checking process, accuracy and completeness of the data retrieved and reported in this document is verified against the information placed in the Records Processing Center and YMP information databases, as applicable.

Output data/results developed in this report have been submitted to the Technical Data Management System in accordance with AP-SIII.3Q.

In addition to the procedures cited above, the following procedures are applicable to this document: AP-SI.1Q, *Software Management*, and AP-SIII.2Q, *Qualification of Unqualified Data and Documentation of the Rationale for Accepted Data*.

INTENTIONALLY LEFT BLANK

### 3. USE OF SOFTWARE

#### 3.1 QUALIFIED COMPUTER SOFTWARE

All controlled and baselined software used in the development of the drift degradation analysis is identified in Table 1. All software documented in this section is appropriate for the applications used in this drift degradation analysis. Each software item was obtained from Software Configuration Management in accordance with AP-SI.1Q, *Software Management*. All software was used only within the range of its validation as specified in the software qualification documentation, in accordance with AP-SI.1Q. All input and output files for each software item used in this analysis have been submitted to the Technical Data Management System as noted in Attachment I.

Table 1. List of Qualified Software Supporting the Drift Degradation Analysis

Software Title / Version	Software Tracking Number	Brief Description of Software Use
Universal Distinct Element Code (UDEC) Version 3.1	10173-3.1-00	UDEC was used to analyze the seismic and thermal effects on block movement in the lithophysal rock units (Section 6.4).
3-Dimensional Distinct Element Code (3DEC) Version 2.01	10025-2.01-00	3DEC was used to analyze the seismic and thermal effects on block movement in the nonlithophysal rock units (Section 6.3).
Fast Lagrangian Analysis of Continua (FLAC) Version 4.0	10167-4.0-00	FLAC was used in the thermal-mechanical calculation to define the distribution of stresses around the drifts due to the progressive heating of the repository area (Section 6.2).
Fast Lagrangian Analysis of Continua in 3 Dimensions (FLAC3D) Version 2.1	10502-2.1-00	FLAC3D was used in the thermal-mechanical calculation to define the distribution of stresses around the drifts due to the progressive heating of the repository area (Attachment III).
Particle Flow Code in 2 Dimensions (PFC2D) Version 2.0	10828-2.0-00	PFC2D was used to characterize rock mass behavior, including the analysis of long-term strength degradation (Section 7).
Particle Flow Code in 3 Dimensions (PFC3D) Version 2.0	10830-2.0-00	PFC3D was used to characterize rock mass behavior, including the analysis of long-term strength degradation (Section 7).
Discrete Region Key Block Analysis (DRKBA) Version 3.31	10071-3.31-00	DRKBA was used to analyze block development and failure in the nonlithophysal rock units (Attachment IV).
FracMan Version 2.511	10114-2.511-00	FracMan was used to replicate the fracture geometry observed in the ESF to develop a representative volume of jointed rock mass (Section 6.1.5).
Nonisothermal Unsaturated-Saturated Flow and Transport (NUFT) V3.0s	10088-3.0s-01	NUFT was used to simulate heat transfer around the emplacement drift (Section 6.2).
EarthVision V.5.1	10174-5.1-00	EarthVision was used to extract stratigraphic unit thickness and cross-sections from the Geological Framework Model (GFM2000) (Attachment XIII).

### 3.2 OTHER SOFTWARE

In addition to the above listed items, the standard functions of commercial off-the-shelf software, including both Microsoft Excel 97 SR-2 and Mathcad 2001i Professional, were also used. These software items were used to perform support calculation activities as described in Section 6.3, Section 6.4, and associated attachments. Attachment I provides a listing of all calculation files (Table I-1), including the location in this report where specific details of the calculation can be found. Microsoft Excel was used to calculate joint cohesion degradation, excavation orientation inputs, joint description input, and mean rock property values. Additionally, Microsoft Excel was used to process and summarize rockfall data and to provide graphical presentation of the block size distribution data. Mathcad was used to calculate joint cohesion degradation, joint description input parameters, and rock property values. Microsoft Excel 97 SR-2 and Mathcad 2001i Professional are exempted software applications in accordance with AP-SI.1Q, Section 2.1.1.

Attachments IV, V, IX, X, XI, XII, and XV have been provided with this report to document the use of standard functions of commercial-off-the-shelf software in sufficient detail to allow independent repetition of the software in accordance with AP-SIII.10Q Attachment III. Specifically, these attachments provide:

- The formula or algorithm used
- A listing of the inputs to the formula or algorithm
- A listing of the outputs from the formula or algorithm
- Narrative to describe the calculation(s).

These attachments document the following calculations:

- Calculation of joint parameter inputs to DRKBA (Attachment IV)
- Calculation of joint cohesion reduction for thermal and time-dependent effects in DRKBA analyses (Attachment IV)
- Calculation of the plane equations to describe the excavation opening as input to DRKBA (Attachment IV)
- Calculation of rock property values (Attachment V)
- Random selection of 3DEC modeling region (Attachment X)
- Calculation of rock block impact information from 3DEC analyses (Attachment XI)
- Conversion of FracMan fracture output to 3DEC input (Attachment XII)
- Calculation of descriptive statistics of lithophysal abundance and characteristics (Attachment XV).

DIPS Version 4.03 (DIPS V4.03, 30017 V4.03) was used solely for graphical presentation of fracture data in Sections 6.1, 6.3, and Attachment II, and is an exempted software application in accordance with AP-SI.1Q, Section 2.1.2.

## 4. INPUTS

### 4.1 DATA AND PARAMETERS

The geotechnical parameters include data and information collected either by field mapping or by laboratory testing. Input data include joint geometry data, joint mechanical properties data, intact rock physical and mechanical properties data, rock mass mechanical properties data, seismic ground motion data, rock thermal properties data, and repository layout information. These data and parameters are summarized in Table 2 and described below. Uncertainties in input data and parameters are discussed in Section 6.5.

#### 4.1.1 Joint Geometry Data

The development of joint geometry parameters is based on mapping data collected from the ESF, including the main loop (which is composed of the North Ramp, Main Drift, South Ramp) and the Enhanced Characterization of the Repository Block (ECRB) Cross-Drift. Qualified joint mapping data in the ESF were collected from the following lithologic units: the Topopah Spring Tuff crystal poor upper lithophysal zone (Ttpul), the Topopah Spring Tuff crystal poor middle nonlithophysal zone (Ttpmn), the Topopah Spring Tuff crystal poor lower lithophysal zone (Ttpll), and the Topopah Spring Tuff crystal poor lower nonlithophysal zone (Ttpln).

Mapping data from the ESF being used in the analysis includes both USGS/USBR full periphery geologic maps and the detailed line survey. Source DTNs for the full periphery geologic maps and the detailed line survey data are listed in Table 2.

**DRKBA Joint Geometry Inputs**—The DRKBA software uses joint geometry inputs provided by DTN: MO0008SPAFRA06.004, which is the Technical Product Output of *Fracture Geometry Analysis for the Stratigraphic Units of the Repository Host Horizon* (CRWMS M&O 2000a). These developed fracture data include joint set orientation, joint spacing, joint trace length, and joint offset from the detailed line survey. Fracture strike and dip data contained in the electronic files of the full periphery geologic maps were used to determine fracture set orientation, while fracture set spacing and trace length data were obtained from the detailed line survey. All fracture spacing information for the primary joint sets has been converted to “true spacing.” Details for the determination of fracture set orientations, the identification of joint sets, and fracture spacing and trace length data are provided in Attachment IV.

Subsequent studies by the USGS/USBR have generated data on “small-scale” fractures with trace lengths less than 1 m (DTN: GS990908314224.009). These data were collected at six locations in the Ttpmn (2 locations), Ttpll (3 locations), and Ttpln (1 location). These data are used in this analysis to provide an assessment of the impact of the small trace length fracture data on rockfall development (Section 6.3.3).

**3DEC Joint Geometry Inputs**—The 3DEC software uses source joint geometry inputs provided in Table 2. These inputs are then developed to produce a 100-m × 100-m × 100-m rock mass volume that contains a three-dimensional generation of fracture data derived from the field mapping data using a Poisson process (Section 6.1.5). Fractures are generated within this volume as circular disks with their size, dip, and dip direction determined based on field data.

Table 2. Input Data and Parameters for the Drift Degradation Analysis

Parameter		Value	Range	Source	Application	
Joint geometry	number of joint sets	See Table 4 (Tptpl) Table 6 (Tptpmn)  Attachment II, Table II-1 (Tptpul) Table II-3 (Tptpln)	See Section 6.1.6	GS971108314224.024	Rockfall Model for Nonlithophysal Rock (Section 6.3) (Attachment IV)  Rockfall Model for Lithophysal Rock (Section 6.4.3)	
	strike			GS971108314224.025		
				GS960708314224.008		
				GS000608314224.004		
				GS960708314224.010		
dip	GS971108314224.026	GS990908314224.009 MO0008SPAFRA06.004 GS971108314224.023 GS970808314224.008				
	GS960908314224.014					
	GS971108314224.028					
	GS970208314224.003					
	GS970808314224.010					
	GS960908314224.020					
	GS000608314224.006					
	GS960908314224.015					
	GS960908314224.016					
	GS960908314224.017					
	GS970108314224.002					
spacing	GS970208314224.004					
	GS970808314224.009					
	GS970808314224.011					
	GS990408314224.001					
	GS990408314224.002					
	GS990408314224.003					
	GS990408314224.004					
	GS990408314224.005					
	GS990408314224.006					
	Joint strength	Joint normal stress, $\sigma$ (MPa)	See Attachment V, Table V-3	See Attachment V, Table V-3	DTN: SNL02112293001.003 DTN: SNL02112293001.005 DTN: SNL02112293001.007	Rockfall Model for Nonlithophysal Rock (Section 6.3)
		Joint peak shear stress, $\tau_p$ (MPa)				
Joint dilation (deg)						
Joint normal stiffness, $K_n$ (MPa/m)		See Attachment V, Table V-4	See Attachment V, Table V-4			
Joint shear stiffness, $K_s$ (MPa/m)						

Table 2. Input Data and Parameters for the Drift Degradation Analysis (Continued)

Parameter		Value	Range	Source	Application
Intact rock strength for nonlithophysal rock	Young's modulus (GPa)	See Attachment V, Table V-5	See Attachment V, Table V-5	DTN: SNL02030193001.004 DTN: SNL02030193001.009 DTN: SNL02030193001.012 DTN: SNL02030193001.019 DTN: SNL02030193001.020 DTN: SNL02030193001.021 DTN: SNL02030193001.023 DTN: SNL02030193001.024 DTN: SNL02030193001.026	Rockfall Model for Nonlithophysal Rock (Section 6.3)
	Poisson's ratio				
	Tensile strength (MPa)	See Attachment V, Table V-6	See Attachment V, Table V-6		
	Ultimate Differential Strength (MPa)	See Attachment V, Table V-7	See Attachment V, Table V-7		
	Confining stress, $\sigma_3$ (MPa)				
Rock mass strength for lithophysal rock	Compressive strength (MPa)	See Attachment V, Table V-8 Figure V-3	See Attachment V, Table V-8 Figure V-3	DTN: SN0208L0207502.001 DTN: SN0211L0207502.002 DTN: SN0208F4102102.002 DTN: SN0212F4102102.004 DTN: SN0301F4102102.006 DTN: MO0301RCKPRPCS.001	Rockfall Model for Lithophysal Rock (Section 6.4)
	Young's modulus (GPa)				
	Poisson's ratio				
Rock mass strength for thermal-mechanical units	Q system input parameters from tunnel mapping in the ESF	RQD	See Attachment I, calculation file, <i>rock mass strength v1.xls</i> , worksheet "Spatial Data"	See Attachment I, calculation file, <i>rock mass strength v1.xls</i> , worksheet "Spatial Data"	DTN: GS950508314224.003 DTN: GS960908314224.020 DTN: GS000608314224.006 DTN: GS960908314224.015 DTN: GS960908314224.016 DTN: GS960908314224.017 DTN: GS970108314224.002 DTN: GS970208314224.004 DTN: GS970808314224.009 DTN: GS970808314224.011 DTN: GS970808314224.013 DTN: GS990408314224.003 DTN: GS990408314224.004 DTN: GS990408314224.005 DTN: GS990408314224.006
		$J_n$			
		$J_r$			
		$J_a$			

Table 2. Input Data and Parameters for the Drift Degradation Analysis (Continued)

Parameter		Value	Range	Source	Application	
Rock mass strength for thermal-mechanical units (continued)	Intact unconfined compressive strength for thermal-mechanical units, $\sigma_{ci}$ (MPa)	See Attachment I, calculation file, <i>rock mass strength v1.xls</i> , worksheet "Intact Strength"	See Attachment I, calculation file, <i>rock mass strength v1.xls</i> , worksheet "Intact Strength"	DTN: SNL02030193001.001	Thermal-Mechanical Calculation (Section 6.2)	
				DTN: SNL02030193001.002		
				DTN: SNL02030193001.003		
	DTN: SNL02030193001.004					
	DTN: SNL02030193001.005					
	DTN: SNL02030193001.006					
	DTN: SNL02030193001.007					
	DTN: SNL02030193001.008					
	DTN: SNL02030193001.012					
	DTN: SNL02030193001.013					
	DTN: SNL02030193001.014					
	DTN: SNL02030193001.015					
	DTN: SNL02030193001.016					
	DTN: SNL02030193001.018					
	DTN: SNL02030193001.019					
	DTN: SNL02030193001.020					
	DTN: SNL02030193001.021					
	DTN: SNL02030193001.022					
	DTN: SNL02030193001.023					
	DTN: SNL02030193001.024					
	DTN: SNL02030193001.026					
Rock mass strength in the Heated Drift	Q system input parameters from tunnel mapping in the Heated Drift alcove	<i>RQD</i>	See Attachment V, Table V-10	DTN: GS970608314224.007	Rockfall Model for Nonlithophysal Rock (Section 6.3)	
		$J_n$				
		$J_r$				
$J_a$						
Ultimate Differential Strength (MPa)	See Attachment V, Table V-11	See Attachment V, Table V-11	DTN: SNL02030193001.004			
Confining stress, $\sigma_3$ (MPa)			DTN: SNL02030193001.012			
			DTN: SNL02030193001.019			
			DTN: SNL02030193001.020			
			DTN: SNL02030193001.021			
			DTN: SNL02030193001.023			
			DTN: SNL02030193001.026			
Block strength for nonlithophysal rock	Intact unconfined compressive strengths for assessing sample size effect, $(\sigma_{ax})_u$ (MPa)	See Attachment V, Table V-14	See Attachment V, Table V-14	DTN: MO0301RCKPRPCS.001		Rockfall Model for Nonlithophysal Rock (Section 6.3)

Table 2. Input Data and Parameters for the Drift Degradation Analysis (Continued)

Parameter		Value	Range	Source	Application
Thermal conductivity (W/m°C)		See Attachment V, Table V-15	See Attachment V, Table V-15	DTN: SN0303T0503102.008 DTN: SN0208T0503102.007 BSC 2002c	Thermal-Mechanical Calculation (Section 6.2)
Rock specific heat (J/kg°C)		See Attachment V, Table V-16	See Attachment V, Table V-16	DTN: SN0303T0510902.002	
Thermal expansion (1/°C)		See Attachment V, Table V-17	See Attachment V, Table V-17	DTN: SNL01B05059301.006	
Heat decay curve		1.45 kW/m	—	<i>Repository Design, Repository/PA IED Subsurface Facilities</i> (BSC 2003d) BSC 2001a	
Rock density (kg/m <sup>3</sup> )	Thermal-Mechanical Units	See Attachment V, Table V-1	See Attachment V, Table V-1	DTN: SN0303T0503102.008 DTN: SN0208T0503102.007 BSC 2002c	Thermal-Mechanical Calculation (Section 6.2) Rockfall Model for Nonlithophysal Rock (Section 6.3) Rockfall Model for Lithophysal Rock (Section 6.4)
	Repository Horizon	See Attachment V, Table V-2	See Attachment V, Table V-2	DTN: SNL02030193001.027	Rockfall Model for Nonlithophysal Rock (Attachment IV)

Table 2. Input Data and Parameters for the Drift Degradation Analysis (Continued)

Parameter		Value	Range	Source	Application
In situ stress	Major principal stress, $\sigma_1$ (MPa) (vertical)	4.7	—	DTN: SNF37100195002.001 (The data can be accessed through the Records Processing Center Package #MOY-000901-07-10 [MOL.19970717.0008, pp. 15, 19, and 20] associated with this DTN.)	Thermal-Mechanical Calculation (Section 6.2)
	Intermediate principal stress, $\sigma_2$ (MPa) (horizontal)	2.9 Acting in the N15°E	$\pm 0.4$ MPa $\pm 14^\circ$		
	Minor principal stress, $\sigma_3$ (MPa) (horizontal)	1.7 Acting in the N75°W	$\pm 0.1$ MPa $\pm 14^\circ$		
Regional geology - stratigraphic thickness		See Attachment V, Table V-15	See Attachment V, Table V-15	DTN: MO0012MWDGFM02.002	
Repository layout		See Section 6.2	See Section 6.2	<i>Repository Design, Repository/PA IED Subsurface Facilities</i> (BSC 2003b; BSC 2003c) <i>Underground Layout Configuration</i> (BSC 2002a)	
Emplacement drift orientation		72° drift azimuth	—		
Emplacement drift diameter (m)		5.5	—	<i>Repository Design Project, Repository/PA IED Emplacement Drift Configuration</i> (BSC 2002b)	Rockfall Model for Nonlithophysal Rock (Section 6.3) Rockfall Model for Lithophysal Rock (Section 6.4)
Seismic ground motion	$5 \times 10^{-4}$ per year	See Section 6.3	See Section 6.3	DTN: MO0211TMHIS104.002	
	$1 \times 10^{-6}$ per year			DTN: MO0301TMHIS106.001	
	$1 \times 10^{-7}$ per year			DTN: MO0211AVTMH107.001	
Sampling of Stochastic Input Parameters		See Section 6.3.1.2.2 (Table 12) and Section 6.4.1.1 (Table 37)	See Section 6.3.1.2.2 (Table 12) and Section 6.4.1.1 (Table 37)	DTN: MO0301SPASIP27.004	
Lithophysal abundance		See Attachment XV	See Attachment XV	DTN: GS021008314224.002	Rockfall Model for Lithophysal Rock (Section 6.4)

The location of each fracture plane within the three dimensional space is also provided. Details for sampling within this rock mass volume to select fracture patterns for 3DEC modeling are provided in Section 6.3.1.2.2.

#### 4.1.2 Joint Mechanical Properties Data

Joint strength is characterized by cohesion, friction angle, dilation, and stiffness. Joint cohesion ( $C_j$ ) and friction angle ( $\phi_j$ ) values were developed in Attachment V based on laboratory shear strength test data from core specimens (Table V-3). Mean value and standard deviation are required as the inputs for the DRKBA and 3DEC structural analyses. The calculation of mean values in Attachment V (Section V.2) is consistent with *Yucca Mountain Site Geotechnical Report* (CRWMS M&O 1997, p. 5-143). Joint stiffness values ( $K_n$  and  $K_s$ ) are required as inputs for 3DEC, and are documented in Attachment V (Table V-4) based on laboratory shear strength test data from core specimens. Joint dilation data is provided based on the laboratory shear strength test data from core specimens (Attachment V, Table V-3). Note that for 3DEC analyses, dilation was conservatively selected to be zero, resulting in a higher estimation of rockfall (see Section 6.3.1.1).

#### 4.1.3 Intact Rock Physical and Mechanical Properties Data

The mean rock density value used in rockfall modeling (Sections 6.3 and 6.4) was calculated based on data from laboratory tests performed on rock cores from the North Ramp geotechnical and the systematic drilling boreholes (Attachment V, Table V-2). The saturated bulk density ( $\rho$ ) of 2.41 g/cc (Attachment V, Table V-2) for the Tptpln unit was used in each of the rockfall models in this analysis. This value is in agreement with the mean Tptpln saturated bulk density reported in *Yucca Mountain Site Geotechnical Report* (CRWMS M&O 1997, p. 5-26). That document also indicates that the mean density for the Tptpln unit is the highest mean value compared to other units of the repository horizon (i.e., the Tptpul, Tptpmn, Tptpll, and Tptpln) (CRWMS M&O 1997, pp. 5-25 and 5-26). The use of the mean density for the Tptpln unit to represent the density of all rock units in this analysis results in a larger mass of rock blocks, and is therefore conservative. The thermal-mechanical calculation (Section 6.2) uses density inputs grouped according to thermal-mechanical units. The calculation of mean density values for each thermal-mechanical unit is also documented in Attachment V (Table V-1).

Mean elastic rock properties from the TSw2 thermal-mechanical unit, including a Young's modulus ( $E$ ) of 33.03 GPa and a Poisson's ratio ( $\nu$ ) of 0.21, were used in this analysis for modeling nonlithophysal rock as calculated in Attachment V (Table V-5). Elastic rock properties were determined from laboratory tests performed on rock cores from the North Ramp geotechnical and the systematic drilling boreholes. The calculation of mean values in Attachment V is consistent with *Yucca Mountain Site Geotechnical Report* (CRWMS M&O 1997, pp. 5-26, 5-88, and 5-96). Intact bulk modulus ( $K$ ) and intact shear modulus ( $G$ ) for nonlithophysal rock were calculated based on the mean values of  $E$  and  $\nu$  as documented in Attachment V (Section V.3).

Tensile strength data for nonlithophysal rock were obtained from indirect tensile strength tests performed by the Brazilian Test method using core specimens (Attachment V, Table V-6). The mean tensile strength from this data is 11.56 MPa.

Triaxial strength data (Attachment V, Table V-7) are used to calculate intact cohesion and friction angle of the nonlithophysal rocks. The calculation of cohesion and friction angle is documented in Attachment V, resulting in a cohesion of 43.1 MPa and a friction angle of 46°.

#### **4.1.4 Rock Mass Properties Data**

##### **4.1.4.1 Strength of Lithophysal Rock**

Mechanical properties for lithophysal rock were determined based on available laboratory testing data on large rock cores from drilling in the ECRB Cross-Drift together with data from in situ slot testing in the ESF (Attachment V, Table V-8 and Figure V-3). Values of cohesion ( $C$ ), bulk modulus ( $K$ ), and shear modulus ( $G$ ) for lithophysal rock were calculated based on values of unconfined compressive strength ( $\sigma_c$ ), Young's modulus ( $E$ ), and Poisson's ratio ( $\nu$ ) as documented in Attachment V (Section V.4.1).

##### **4.1.4.2 Rock Mass Elastic Properties for Thermal-Mechanical Units**

The rock mass properties data used in this report include modulus of deformation and Poisson's ratio for each of the thermal-mechanical units (Table V-13). The rock mass properties data were calculated based on the intact rock data from laboratory testing identified in Table 2. The rock mass modulus of deformation data are provided for five rock mass categories representing the range of rock mass conditions encountered in ESF tunnels. The five rock mass categories correspond to 5 percent, 20 percent, 40 percent, 70 percent, and 90 percent probabilities of occurrence, and are provided to be consistent with geotechnical design analyses (BSC 2001b, Section 4.1.5). Mid-range values corresponding to a 40 percent probability of occurrence were used in this analysis, which provides an approximate estimate of the mean value. This data is appropriate for its use in the thermal-mechanical calculation (Section 6.2), which provides an assessment of the regional stresses anticipated within the rock mass. Poisson's ratio for the rock mass was determined to be equal to the Poisson's ratio from intact laboratory tests based on recent field testing (Attachment V, Table V-13).

##### **4.1.4.3 Rock Mass Properties for the Heated Drift in the ESF**

Rock mass properties for the Heated Drift are calculated using the Hoek-Brown failure criterion (Hoek et al. 2002) as documented in Attachment V (Section V.4.2). The inputs needed include rock mass classification data using the Q system as provided in Attachment V (Table V-10). Additionally, intact unconfined compressive strength ( $\sigma_{ci}$ ) is required input for the Hoek-Brown method, together with triaxial test data (Table V-11). The calculated rock mass properties using these data are provided in Attachment V (Table V-12).

##### **4.1.4.4 Block Strength of Nonlithophysal Rock**

The strength of large-scale intact rock block material (i.e., between joints) for nonlithophysal rock is calculated based on available size-effect laboratory compression test data from Price (1986). The size-effect data are presented in Attachment V (Table V-14). The approach for extrapolating this data to the block scale is documented in Attachment V (Section V.4.4).

#### 4.1.5 Seismic Ground Motion Data

Seismic ground motion time history data were provided for the following hazard levels:  $5 \times 10^{-4}$  per year,  $1 \times 10^{-6}$  per year, and  $1 \times 10^{-7}$  per year. Data tracking numbers (DTNs) for each of these ground motion levels are listed in Table 2. The ground motion data for the postclosure ground motion levels (i.e.,  $1 \times 10^{-6}$  and  $1 \times 10^{-7}$ ) each include 15 sets (three components) of time histories at the repository horizon. The sets were developed by scaling recorded motions such that their integrated peak particle velocities match expected point repository horizon particle velocities for the hazard level under consideration. Additionally, a desirable feature of the 15 sets is a magnitude distribution reflective of the horizontal component peak particle velocity deaggregation. This ensures a reasonable and defensible distribution of spectral shapes and time history durations. Conditioning on expected peak particle velocity alone was considered desirable as damage to underground structures is most strongly correlated with this point measurement, recognizing that underground (at-depth) spectral shapes are generally not identical to surficial or outcrop spectral shapes due to the effects of downgoing wavefields (DTN: MO0301TMHIS106.001).

The ground motion data for preclosure annual exceedance probabilities (i.e.,  $5 \times 10^{-4}$ ) consist of a single three-component set of time histories. This set was developed such that the response spectra of the time histories match the design response spectra for this hazard level at the repository horizon.

#### 4.1.6 Rock Thermal Properties Data

A regional thermal-mechanical calculation has been developed as part of this drift degradation analysis (Section 6.2), and uses the following thermal properties data (see Table 2 and Attachment V, Section V.5 for parameter values and source DTNs):

- Thermal conductivity (W/m<sup>°K</sup>)
- Rock specific heat (J/kg<sup>°K</sup>)
- Thermal expansion (/°C)
- Heat decay curve.

#### 4.1.7 Repository Layout Information

Repository layout information (Table 2), including emplacement drift diameter and azimuth, is provided by repository design and performance assessment information exchange drawings (BSC 2002b; BSC 2003b; BSC 2003c) and *Underground Layout Configuration* (BSC 2002a, Sections 5.1.4 and 8.7).

#### 4.1.8 Matrix and Fracture Hydrologic Properties Data

A temperature-history calculation has been developed as part of this analysis (Section 6.2) based on a 2-dimensional line-averaged heat source, drift-scale, thermohydrologic (LDTH) sub-model (DTN: LL000509112312.003) that was extracted from *Multiscale Thermohydrologic Model* (BSC 2001c). The calculation uses matrix and fracture hydrologic properties data from DTN: LB0205REVUZPRP.001 and DTN: LB0207REVUZPRP.002.

## 4.2 CRITERIA

This model report addresses acceptance criteria from Sections 2.2.1.3.2.2 and 2.2.1.3.2.3 of *Yucca Mountain Review Plan, Information Only* (NRC 2003) regarding the degradation and mechanical disruption of engineered barriers. Acceptance criteria from *Yucca Mountain Review Plan* include the following:

- AC1: System description and model integration are adequate.
- AC2: Data are sufficient for model justification.
- AC3: Data uncertainty is characterized and propagated through the model abstraction.
- AC4: Model uncertainty is characterized and propagated through the model abstraction.
- AC5: Model abstraction output is supported by objective comparison.

*Project Requirements Document* (Canori and Leitner 2003) contains the following criteria relevant to this report:

- PRD-002/T-014 “Performance Objectives for the Geologic Repository After Permanent Closure” (traceable to 10 CFR 63.113)
- PRD-002/T-015 “Requirements for Performance Assessment” (traceable to 10 CFR 63.114)

This report was therefore prepared to comply with subparts of the NRC high-level waste rule, 10 CFR Part 63. Relevant requirements for performance assessment from Section 114 of that document are:

Any performance assessment used to demonstrate compliance with Sec. 63.113 must: (a) Include data related to the geology, hydrology, and geochemistry ... used to define parameters and conceptual models used in the assessment. (b) Account for uncertainties and variabilities in parameter values and provide for the technical basis for parameter ranges, probability distributions, or bounding values used in the performance assessment. ... (g) Provide the technical basis for models used in the performance assessment such as comparisons made with outputs of detailed process-level models and/or empirical observations (e.g. laboratory testing, field investigations, and natural analogs).

## 4.3 CODES AND STANDARDS

There are no codes and standards applicable to this drift degradation analysis.

## 5. ASSUMPTIONS

The following assumptions have been used in this drift degradation analysis.

### 5.1 THERMAL-MECHANICAL CALCULATION

#### 5.1.1 Simultaneous Emplacement

*Assumption:* The thermal-mechanical calculation in this report assumes that generation of heat from the waste packages occurs simultaneously throughout the repository. The entire repository begins heating at the same time since sequential emplacement of waste packages has not been considered.

*Basis:* This assumption is necessary since design information is available only for the emplacement drift layout (BSC 2003b), but not for the emplacement schedule.

*Confirmation Status:* This assumption does not require further confirmation, since results from the thermal-mechanical calculation should be the most conservative based on this assumption (i.e., the assumption produces increased heat and greater stresses in the rock mass). Sequential emplacement may cause an additional internal stress between the emplacement drifts and the remaining drifts. This internal stress will be insignificant during the preclosure period, since majority of the heat load will be removed from the emplacement drifts due to ventilation (Section 5.1.2). The effects of the internal stress are expected to be minor during the postclosure period, since the waste packages will cool down significantly during the preclosure period, and the repository temperature is expected to be homogenized due to heat conduction between the drifts during the preclosure period. A range of temperatures have been considered in the rockfall analyses presented in this report (Sections 6.3.1.3 and 6.4.1.2), and the rockfall results are relatively insensitive to the temperature changes evaluated.

*Use in the Analysis/Model:* This assumption is used in the thermal-mechanical calculation of regional (repository-scale) and local (drift-scale) temperature and thermal stress (Sections 6.2, 6.3.1, and 6.4.1; Attachment III).

#### 5.1.2 Ventilation Heat Removal Ratio

*Assumption:* During the ventilated preclosure period, 90 percent of the decay heat output is removed from the emplacement drift system.

*Basis:* The basis of this assumption is provided from the preliminary calculations supporting a license application (BSC 2003e, Section 6.6).

*Confirmation Status:* No further confirmation is needed for this assumption, since sensitivity calculation regarding the heat removal ratio was conducted covering the heat removal ratio down to 70 percent (Section 6.2). The calculation showed that the results of rockfall analyses are not sensitive to heat removal ratio over this range.

*Use in the Analysis/Model:* This assumption is used in all the preclosure thermal-mechanical calculations except the ventilation sensitivity calculation (Sections 6.2, 6.3.1, and 6.4.1;

Attachment III). Because of this assumption it is accurate to model the preclosure period by simply reducing the decay heat output to 10 percent of its non-ventilated rate.

### **5.1.3 Thermal Expansion**

*Assumption:* Thermal expansion values used in the underlying layers (CHn1 and CHn2) under the repository units (Tsw2) are assumed to be equal to the those for the repository layers.

*Basis:* This assumption is necessary since the test data from core samples are limited.

*Confirmation Status:* This assumption does not require further confirmation since temperature increase in the underlying layers is insignificant and thermally induced stresses are negligible.

*Use in the Analysis/Model:* This assumption is used in all the thermal-mechanical calculation throughout the report (Sections 6.3.1 and 6.4.1; Attachment III).

## **5.2 ROCKFALL MODELING**

### **5.2.1 Joint Position Parameter in DRKBA**

*Assumption:* The positioning parameter required as joint parameter input is assumed to be the offset measured from the center of the trace length to the scan line of the detailed line survey.

*Basis:* This is the best available way to represent the positioning parameter since the determination of the true positioning parameter requires the three dimensional information of the joint plane that is not available.

*Confirmation Status:* This assumption does not require further confirmation. This approach is considered conservative because the offset measured from the one dimensional scan line is smaller than the true offset in three dimensional space (the probability of forming a key block is higher with a smaller offset value). The DRKBA rockfall results are used for confirmation only. This assumption does not impact the rockfall output documented in this report.

*Use in the Analysis/Model:* This assumption is used in Section 6.3.3 and Attachment IV.

### **5.2.2 Block Size Distribution for Potential Rockfall in Lithophysal Units**

*Assumption:* Block size distribution is assumed as a function of inter-lithophysal fracture density and lithophysae spacing.

*Basis:* This assumption is needed since the size of rock particles that are created from the lithophysal rocks is estimated from geologic and empirical evidence.

*Confirmation Status:* This assumption does not require further confirmation. The relatively abundant uniformly distributed lithophysae combined with fracturing fabric provide natural breaking surfaces. Observation in the ECRB Cross-Drift for block sizes on the order of a few inches in diameter supports this assumption (Attachment XV).

*Use in the Analysis/Model:* This assumption is used in Section 6.4.

### 5.3 GROUND SUPPORT

*Assumption:* It is assumed that ground support is not installed in the emplacement drifts. All rock blocks predicted in this model report are therefore blocks that fail in an unsupported opening.

*Basis:* When using the DRKBA software to analyze block development, this assumption is necessary due to the limitation of the DRKBA program. The assumption will lead to a conservative prediction of key blocks for the preclosure period (i.e., more blocks will be predicted to fail in the model that would otherwise be supported and remain stable with ground support) and is considered adequate for the postclosure period.

*Confirmation Status:* This assumption does not require further confirmation. Ground support will degrade and eventually fail during the postclosure period. Not including ground support is realistic for the postclosure period. Not including the ground support in the preclosure analyses presented in this report produces a conservative estimate of drift degradation for the preclosure period.

*Use in the Analysis/Model:* The assumption is used throughout this document.

INTENTIONALLY LEFT BLANK

## 6. MODEL DISCUSSION AND ANALYSIS RESULTS

This section documents the models and analyses conducted to predict the postclosure drift degradation resulting from thermally induced stresses, seismically induced rockfall, and possible static fatigue mechanisms.

The potential exists for rockfall to occur as a result of shaking induced by earthquakes. The models and analyses described in this section quantify possible seismically induced rockfall (and, ultimately, drip shield and waste package mechanical damage) over the 10,000 year regulatory postclosure period. Geologic mapping is used to define a “synthetic” or representative rock mass that is sampled randomly to create possible rock masses in which the tunnel is simulated. Numerical models (two- or three-dimensional, depending on the lithology in question), with input geometry and properties based on the geologic variability, are used to make rockfall estimates for ground motion levels whose amplitude is based on the probability of occurrence in terms of annual exceedance frequency. For each annual exceedance frequency, a number of probabilistically based, site-specific ground motions have been developed and used to provide the transient boundary conditions to the models. The resulting rockfall, in terms of the tonnage of the maximum size rock particle, total tonnage for a given simulated length of tunnel, and the velocity of rock particles, has been determined.

The rock mass surrounding the excavations may undergo damage from thermally induced stresses or time-dependent damage associated with static fatigue resulting from stress corrosion mechanisms. This damaged material may result in a slow unraveling (Tptpll) or block fallout (Tptpmn) mode of failure with some extent of drift filling. The effect of thermal stress on rock failure extent has been examined using the numerical techniques discussed in the subsequent sections.

Time-dependent degradation (i.e., rockfall from a tunnel or other unsupported excavation over long time periods) is not currently well understood, particularly in hard, strong rocks. It is expected that time-related rockfall will be more prominent in heavily fractured rocks such as the Tptpll, and will be related to the ratio of induced stress to rock mass strength. The goal of the analyses presented in this section is to provide a reasonable estimate of the propensity for yield and rockfall as a function of the induced stress levels and time.

### 6.1 ROCK MASS CHARACTERISTICS OF REPOSITORY HOST HORIZON

The purpose of this section is to provide a background discussion of rock mass characteristics that are important in understanding fundamental rock mass behavior. Specific rock mass parameters that are input to the rockfall models developed in this report are identified in Sections 6.3 and 6.4. Two systems of stratigraphic nomenclature are used in this report: thermal-mechanical (Ortiz et al. 1985) and lithostratigraphic (Buesch et al. 1996). Correlation between these two systems is provided in Figure 2.

#### 6.1.1 Regional Geology

Yucca Mountain lies in southern Nevada, in the Great Basin, which is part of the Basin and Range structural/physiographic province. In the Yucca Mountain area, pre-Tertiary rocks

(consisting of a thick sequence of Proterozoic and Paleozoic sedimentary rocks) underlie approximately 1000 to 3000 m of Miocene volcanic rocks (Gibson et al. 1990).

The Miocene volcanic sequence exposed at Yucca Mountain includes units of the Paintbrush and Timber Mountain Groups (Sawyer et al. 1994) and the entire section dips 5 to 10 degrees east (Day et al. 1998). The Paintbrush Group consists of pyroclastic rocks and lavas that originate from the Claim Canyon caldera (approximately 6 km north of the study area) and are from 12.7 to 12.8 million years old (Byers et al. 1976; Sawyer et al. 1994). The Paintbrush Group includes a sequence of four formations, the Tiva Canyon, Yucca Mountain, Pah Canyon, and Topopah Spring Tuffs, each of which consist primarily of large-volume, pyroclastic-flow deposits with minor amounts of pyroclastic-fall deposits (Byers et al. 1976; Christiansen et al. 1977; Broxton et al. 1993; Buesch, et al. 1996) (Figure 2). At Yucca Mountain, two of these formations, the Topopah Spring and Tiva Canyon Tuffs, are voluminous, mostly densely welded, compositionally zoned, outflow sheet, pyroclastic-flow deposits (also referred to as ignimbrites) that grade upward from rhyolite composition to quartz latite composition (Lipman et al. 1966; Byers et al. 1976; Schuraytz et al. 1989). The formations of the Paintbrush Group are interbedded with bedded tuffs, which consist of thinner pyroclastic-flow and pyroclastic-fall deposits, and locally a few lava flows (Byers et al. 1976; Christiansen et al. 1977; Broxton et al. 1993; Buesch, et al. 1996; Day et al. 1998). The 11.45 to 11.6 million year old rocks of the Timber Mountain Group were erupted from Timber Mountain caldera complex and consist of the Ammonia Tanks and Rainer Mesa Tuffs (Sawyer et al. 1994) and interbedded tuffaceous rocks and lava flows.

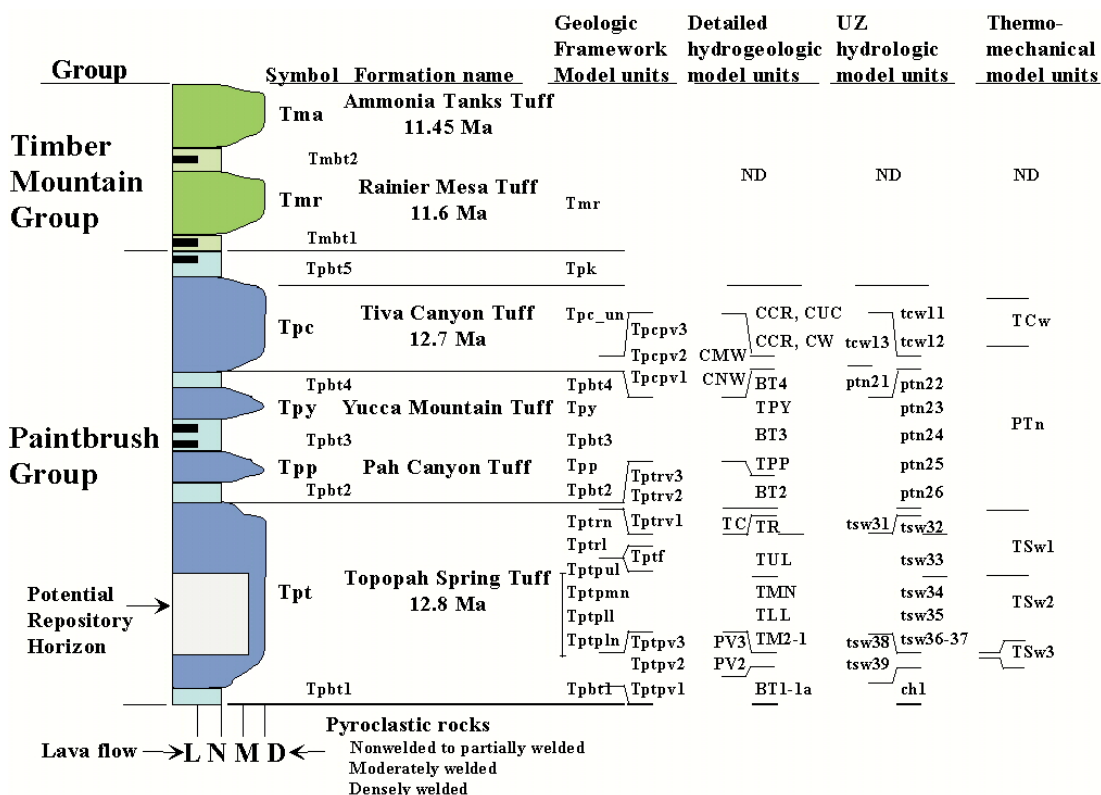


Figure 2. Simplified Lithostratigraphic Column of Paintbrush Group and the Rock Units that Form the Repository Host Horizon

The central block of Yucca Mountain is bounded by the Yucca Wash to the north, by the Solitario Canyon fault to the west, and the Bow Ridge fault to the east (Figure 3). Alluvium-filled structural valleys, consisting mostly of alluvial fan deposits (fluvial and colluvial sediments) and some thin eolian deposits, lie adjacent to the Bow Ridge and Solitario Canyon faults on the east and west sides, respectively. The Yucca Mountain area is cut by steeply dipping, north-south-striking normal faults which separate the Tertiary volcanic rocks into blocks one to four kilometers wide (Scott 1990; Day et al. 1998). Both the Solitario Canyon and Ghost Dance faults dip steeply toward the west, and displacement, amount of brecciation, and number of associated splays vary considerably along their trace (Scott and Bonk 1984; Day et al. 1998). The Solitario Canyon fault has normal down-to-the-west displacement of about 260 m in the vicinity of the repository block (Mongano et al. 1999, p. 60). The Ghost Dance fault is in the central part the repository block and is a generally north-striking normal fault zone, with down to the west displacement. The Sundance fault is located in the north-central portion of the repository block. It is a northwest-striking, east-dipping normal fault with a maximum cumulative down-to-the-northeast displacement of 6 to 11 m (Day et al. 1998). Numerous smaller faults and fault zones are present throughout the repository block, generally north-trending with offsets less than 5 m (Mongano et al. 1999).

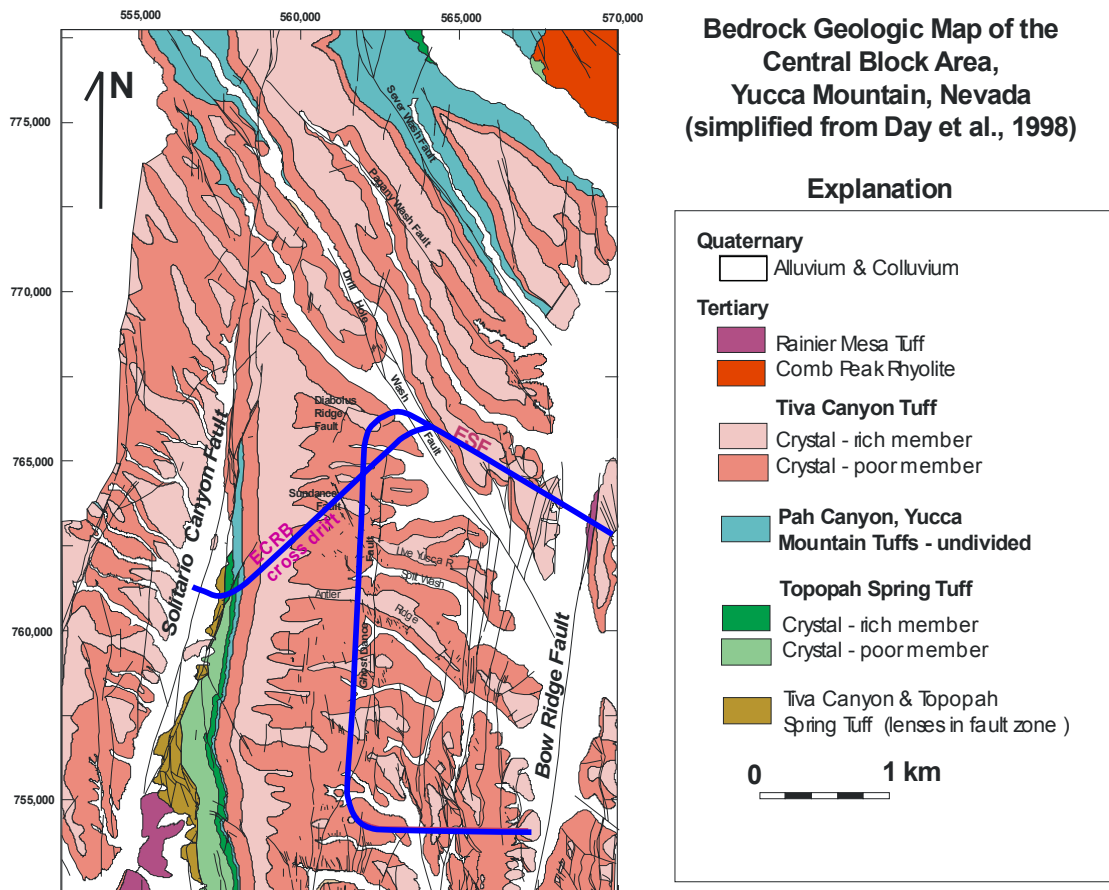
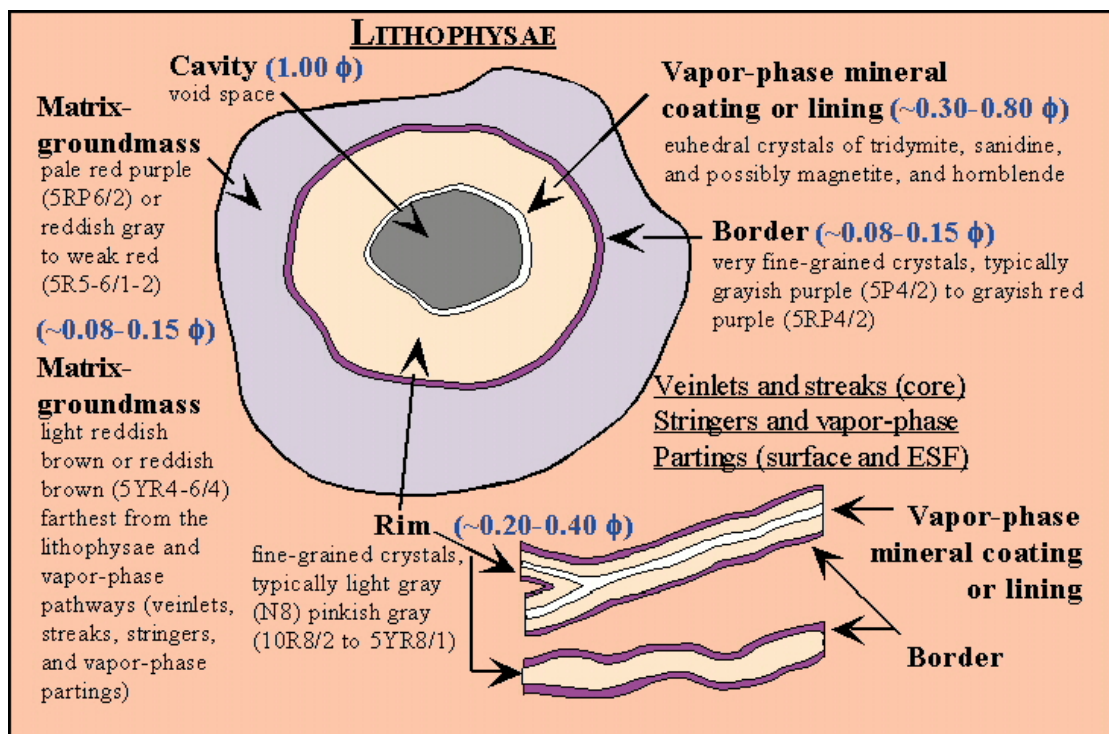


Figure 3. Geology of the Central Block at Yucca Mountain and Location of the Exploratory Studies Facility (ESF), Including the ECRB Cross-Drift

## 6.1.2 Lithostratigraphy at the Repository Horizon

All of the rocks of the repository host horizon lie within the Topopah Spring Tuff, specifically within the crystal-poor member, and geochemically these rocks have a very uniform composition of rhyolite (Peterman and Cloke 2002). The repository host horizon includes rocks from the lower part of the upper lithophysal zone (Ttpul) of the TSw1 thermal-mechanical unit, and all of the TSw2 thermal-mechanical unit, including the middle nonlithophysal zone (Ttpmn), the lower lithophysal zone (Ttpll), and the lower nonlithophysal zone (Ttpln) (Figure 2). These lithostratigraphic units are described in this section and are based on Mongano et al. (1999) unless otherwise indicated.

In the densely welded and crystallized rocks of the Topopah Spring Tuff, the zones and many of the subzones are identified on the basis of the abundance, size, and distribution (or lack thereof) of lithophysae, cavities in the rock formed during welding from the accumulation of the vapor phase. Lithophysae, spots (which are similar to the rims on lithophysae, but there is no cavity), and many fractures have similar characteristics such as rims, borders, and possibly vapor-phase mineral coatings (Figure 4).



NOTES: Porosity values for the matrix-groundmass are by Flint (1998), and the values for rims, borders, and vapor-phase mineral coatings are estimates by Buesch (2003a). The nomenclature for color (e.g., pale red purple is 5RP6/2) is based on soil color charts (Munsell Color Company 1994).

Figure 4. Lithostratigraphic Features Related to Lithophysae and Fractures

**Ttpul**—The crystal-poor upper lithophysal zone (Ttpul) is exposed in both the ESF main loop and ECRB Cross-Drift. In the ESF main loop, the upper lithophysal zone is exposed from Stations 17+97 to 27+20, 63+08 to 64+55, 67+91 to 68+47, and 71+68 to 73+02. The ECRB

Cross-Drift begins in the upper central portion of the zone and it exposes rocks of the middle and lower portions of the zone from Stations 0+00 to 10+15. The upper portion of the upper lithophysal zone is also exposed in the hanging wall of the eastern strand of the Solitario Canyon fault zone from Stations 25+90 to 26+57.5. The unit is densely welded, crystallized, lithophysal, and has various amounts of vapor-phase corrosion and mineralization. The rock contains 1 to 5 percent crystal fragments, 0 to 5 percent lithic fragments, 0 to 15 percent pumice fragments, 3 to 60 percent lithophysae, and 40 to 92 percent matrix-groundmass. The matrix-groundmass is a variable mix of pale to grayish red-purple (5RP5-7/1-2 to 5RP4/2) and light brown (5YR6/3-4) to pale reddish brown (10R5/4) and pale red (5-10R6/2) crystallized material. The matrix-groundmass contains 3 to 50 percent, white to very light gray (N-9 to N6) to grayish pink (5-10R8/2-1), spots, veinlets, streaks, rims on fractures, stringers, and vapor-phase partings of crystallized materials.

**Ttpmn**—The crystal-poor middle nonlithophysal zone (Ttpmn) is exposed in both the ESF main loop and ECRB Cross-Drift. The ESF main loop is excavated in the middle nonlithophysal zone from Stations 27+21 to 57+29, from 58+78 to 63+08, and from 70+58 to 71+68. The middle nonlithophysal zone contains an intensely fractured zone exposed in the ESF main loop from Stations 42+00 to 51+50 (Albin et al. 1997). This intensely fractured zone has been treated separately in the analyses presented in this report. The ECRB Cross-Drift exposes the middle nonlithophysal zone from Stations 10+15 to 14+44. In general, the rocks are densely welded, crystallized, and have various amounts of vapor-phase corrosion and mineralization. The rock contains 1 to 2 percent crystal fragments, 1 to 5 percent lithic fragments, 1 to 15 percent pumice fragments, 0 to 3 percent lithophysae, and 76 to 97 percent matrix-groundmass. The matrix-groundmass has two main colors that appear to result from variations in the types of crystallization, but locally there are gradations between these two types that form a heterogeneous mix of colors and crystallization products. One type of rock is a mix of grayish orange-pink (5YR7/2), grayish red (5R4/2), and grayish red-purple (5RP4-5/2) crystallized rock that locally has small veinlets and stringers. The other type of rock is pale brown (5YR6/2), light brown (5YR6/3-4) and moderate brown (5YR4/3), grayish brown (5YR6/1) or pale red (5-10R6/2). The matrix-groundmass contains 0 to 25 percent, white (N9), very light gray (N8), and light gray (N7) to grayish pink (5R8/2) spots, veinlets, streaks, rims on fractures, stringers, and vapor-phase partings of crystallized materials. Smooth, high-angle fractures are typical of the zone, but it also contains some low-angle, continuous shears and cooling joints. Another feature characteristic of the Ttpmn is the presence of concentrations of vapor-phase minerals along vapor-phase partings and these features appear as low-angle continuous partings subparallel to the dip of the unit. The lithophysae-bearing subzone (Ttpmn2) described by Buesch et al. (1996) occurs in the ECRB Cross-Drift and has 1 to 3 percent lithophysae (Mongano et al. 1999), but this subzone does not occur in the Main Drift of the ESF (Mongano et al. 1999; Buesch and Spengler 1998).

**Ttpll**—The crystal-poor lower lithophysal zone (Ttpll) is exposed in both the ESF main loop and ECRB Cross-Drift. The ESF main loop exposes the uppermost few meters of the lower lithophysal zone from Stations 57+29 to 58+78. The lower lithophysal zone is exposed along the ECRB Cross-Drift from Stations 14+44 to 23+26. The rocks are densely welded, crystallized, lithophysal, and have various amounts of vapor-phase corrosion and mineralization. The rocks are composed of 1 to 2 percent crystal fragments, 1 to 5 percent lithic fragments (locally 12 to 15 percent), 0 to 7 percent pumice fragments (locally 10 to 35 percent), 5 to 30 percent

lithophysae (locally 1 to 5 percent), and 56 to 93 percent matrix-groundmass. The matrix-groundmass is a mottled mix of pale red (5R6/2, 5R5/2, 10R6/2-3) and pale to light brown (5YR6/2; 5YR6/3; 5YR6/4), and moderate brown (5YR4-5/4), with variable amounts of pale to grayish red-purple (5RP5-7/1-2 to 5RP4/2), and locally it is dusky yellowish brown (10YR3/2). The matrix-groundmass contains 3 to 20 percent (locally 15 to 40 percent), grayish orange-pink (5YR7/2) or pinkish gray (5R8/2; 10R8/2) to light or very light gray (N7; N8) spots, veinlets, streaks, rims on fractures, stringers, and vapor-phase partings of crystallized materials. Lithophysae vary in size from a few centimeters to greater than 1 meter in diameter.

**Tptpln**—The crystal-poor lower nonlithophysal zone (Tptpln) is not exposed in the ESF main loop, but is exposed in the ECRB Cross-Drift from Stations 23+26 to 25+85. The rocks are densely welded, crystallized pyroclastic-flow material and typically are composed of 1 to 2 percent crystal fragments, 3 to 7 percent lithic fragments, 3 to 20 percent pumice fragments, 0 to 5 percent lithophysae, and 66 to 93 percent matrix-groundmass. Rocks of the lower nonlithophysal zone vary from a heterogeneous mix of grayish red and grayish orange pink (5YR7/2) matrix-groundmass to comparatively homogeneous pale red, light brown, pale brown, or grayish brown (5YR6/4) matrix-groundmass. Veinlets, streaks, and stringers form a minor component of the rock in some portions of the unit. In proximity to the Solitario Canyon fault zone, the unit is brecciated and altered. In this area, the breccia matrix varies from moderate reddish brown to grayish orange pink. Some breccia clasts adjacent to the fault plane are very light gray.

### 6.1.3 Geotechnical Characterization

Geotechnical data were collected based on two empirical rock mass classification systems: the Norwegian Geotechnical Institute rock quality system (Q system) (Barton et al. 1974) and the Geomechanics Rock Mass Rating system (RMR system) (Bieniawski 1989). Ratings are assigned to a five-meter length of tunnel using both rock classification systems. The use of this relatively short rating length may have the disadvantage of introducing variations in some evaluated parameters which may be expected to be stable; yet it has the advantage of capturing expected variations in more unstable parameters. For example, considering the Q system, one might assume the number of joint sets would be constant over a long reach of tunnel. Using a five-meter rating length permits evaluation of the actual occurrence of a particular joint set; therefore the rating value for the number of joint sets may vary within a ten-meter reach of tunnel. On the other hand, the five-meter rating length permits a description of the changes in fracture frequency represented by the rock quality designation (RQD). Overall, the five-meter rating length emphasizes changes in rock quality from one length to the next. When longer reaches of the tunnel or various stratigraphic units are compared, differences in the trends of the five-meter ratings and differences in the average ratings are meaningful. The geotechnical characterization of lithostratigraphic units is described in this section and is based on Mongano et al. (1999).

**Tptpul**—The Tptpul (Stations 0+00 to 10+15 and Stations 23+26 to 25+85), the longest reach of the ECRB Cross-Drift, has the lowest RQD rating (36 [poor]), yet the highest Q system rating (14 good). Its RMR value (57 fair) equals the RMR value of the Tptpll. Its lithophysae content ranges from 10 to 40 percent by volume. These cavities average 10 cm in diameter. Fractures are difficult to distinguish, with an average of only one joint set. No key blocks are expected to

form within this unit; however, there are occasionally some horizontal cooling joints. It has 11 faults, 1 fault zone, and 25 shears or shear zones.

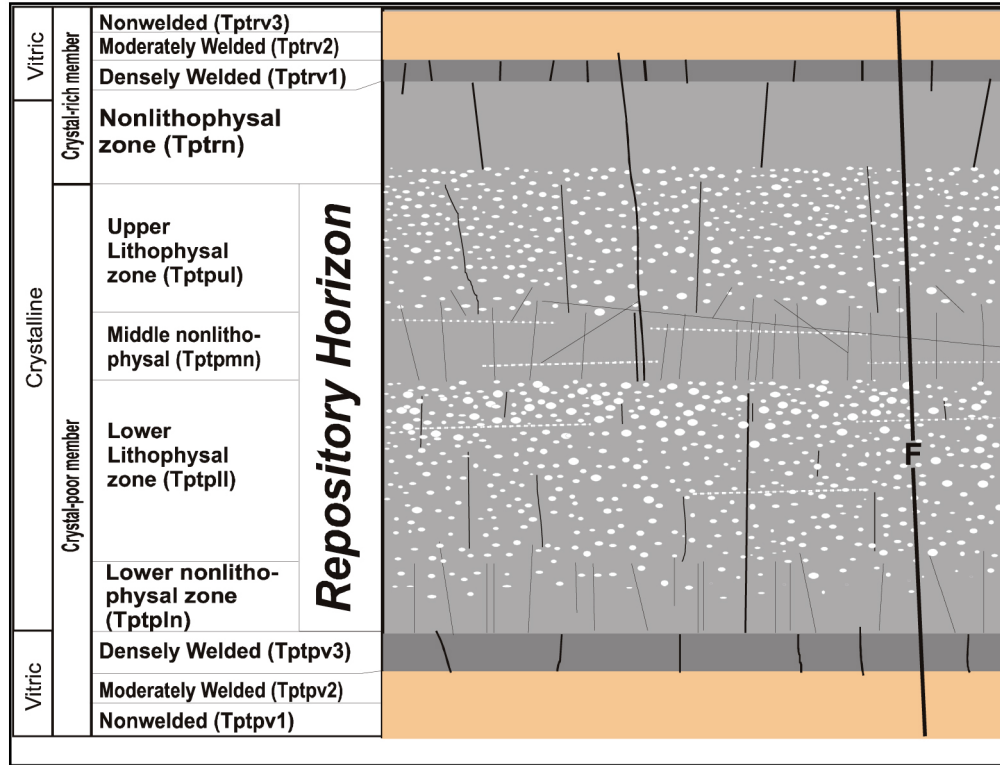
**Tptpmn**—The Tptpmn (Stations 10+15 to 14+44) has a mean horizontal RQD rating of 60 (fair), including lithophysae, and 62 (fair), excluding lithophysae. The projected Q rating from the predictive report agrees with this assessment. The RMR system rates the Tptpmn and the Tptpln as the highest, with a rating of 60 (fair). The unit is generally characterized by less than 3 percent lithophysae by volume. The Tptpmn has 430 meters of exposure in the ECRB Cross-Drift and has the least amount of fault/shear activity with a total of 1 fault zone, 6 faults, and 13 shears. It has an average of three to three+ random joint sets. The horizontal joint sets, or vapor-phase partings, cause the formation of key blocks at Stations 10+80 to 11+55 and Stations 13+10 to 13+15.

**Tptpll**—The Tptpll (Stations 14+44 to 23+26) has a horizontal RQD rating of 42 (poor). Its tunnel-calculated Q rating is 7.9 (fair), the lowest in the ECRB Cross-Drift. The RMR system estimates for this unit at 57 (fair). The Tptpll is generally characterized by lithophysae of 5 to 30 percent by volume and range in size from 5 to 130 cm. The larger lithophysal cavities tend to be irregular or ellipsoidal features that exhibit prismatic fracturing. The unit has an average of two+ random joint sets; however no key-block problems are apparent. The Tptpll has 4 faults and 30 shears exposed in 882 meters of rated tunnel.

**Tptpln**—The Tptpln (Stations 23+26 to 25+85) has the best horizontal RQD ratings: 62 (fair), including lithophysae, and 67 (fair), excluding the lithophysal cavities. Its tunnel-calculated Q rating is 12.3 (good). The RMR system rates this unit a 60 (fair). This unit is characterized by generally less than three percent lithophysal cavities by volume. It has an average of three joint sets, with no significant key-block occurrences. The Tptpln has 6 faults and 36 shear or shear zones.

#### **6.1.4 Discussion of Engineering Characteristics of Rock Mass Important to Geomechanical Performance**

The structure of the rock mass plays what is perhaps the most important role in defining the structural response of the repository to thermal and mechanical loading. In particular, the fracture geometry and properties and the amount of lithophysal porosity are the primary geologic structures of importance. Extensive geotechnical mapping of fractures has been performed in the entire ESF main loop and the ECRB Cross-Drift (CRWMS M&O 1998a; Mongano et al. 1999). Figure 5 shows a schematic of the Topopah Spring Tuff illustrating the general occurrence of fracturing and lithophysae in the various zones of the formation. The occurrence of fractures and lithophysae are roughly inversely proportional. This is illustrated schematically in Figure 5 and demonstrated quantitatively in Figure 6, where the fracture density (fractures with trace length greater than 1 m), determined from detailed line mapping (i.e., the detailed line survey), and the approximate percentage of lithophysal porosity in the ECRB Cross-Drift are shown. The density of fractures with trace length greater than 1 m is significantly larger in the Tptpmn and Tptpln (20-35 fractures/10 m), as compared to 5 fractures/10 m or less in the Tptpul and Tptpll.



00266DC\_003a.ai

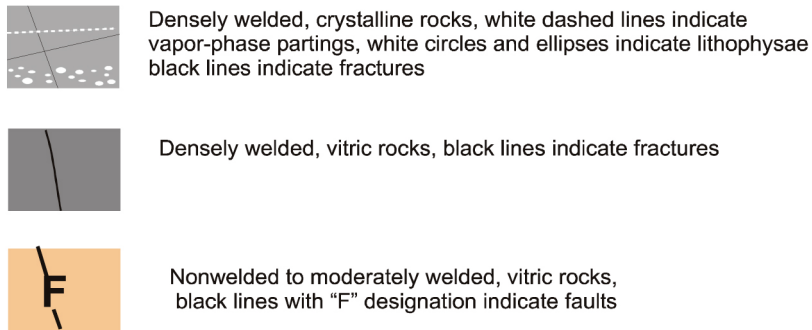
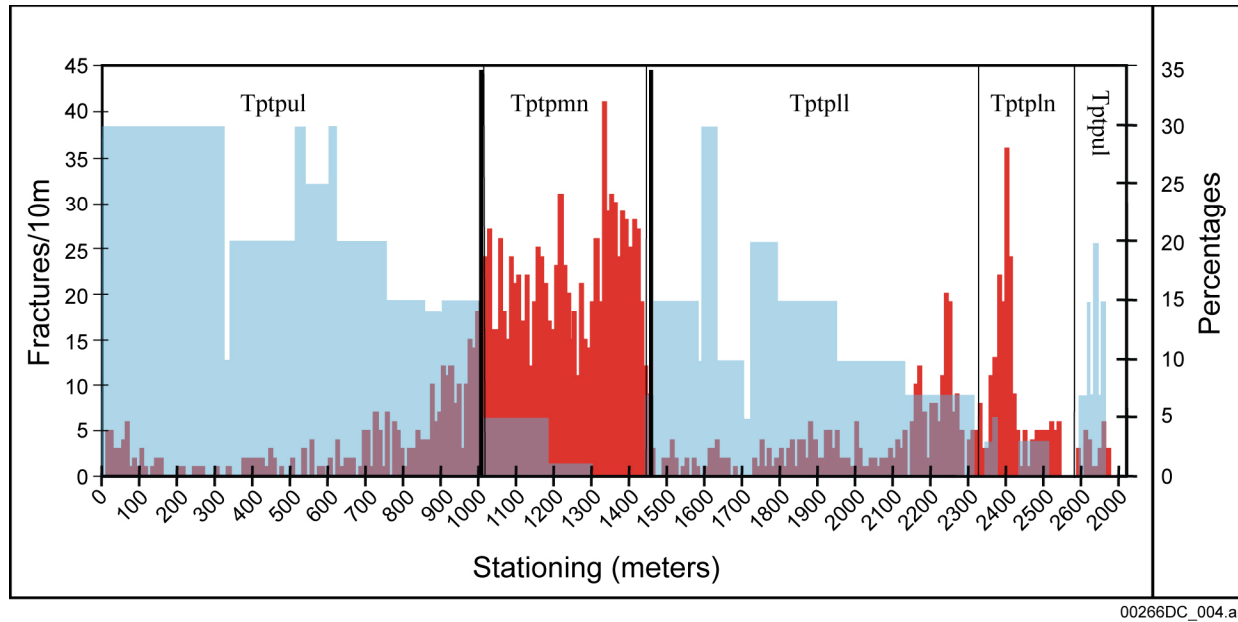


Figure 5. Schematic Illustration of the Structure of the Topopah Spring Tuff



Fracture frequency/ Lithophysal %

Source: Mongano et al. 1999

Figure 6. Fractures and Lithophysal Abundance in the ECRB Cross-Drift from Stations 0+00 to 27+00

### 6.1.4.1 Fracturing

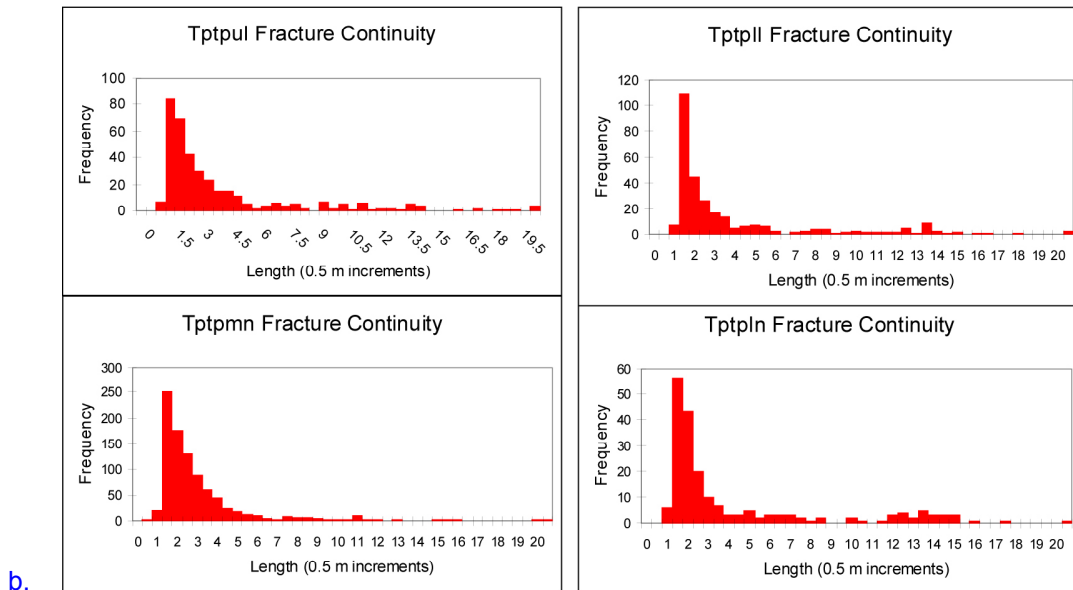
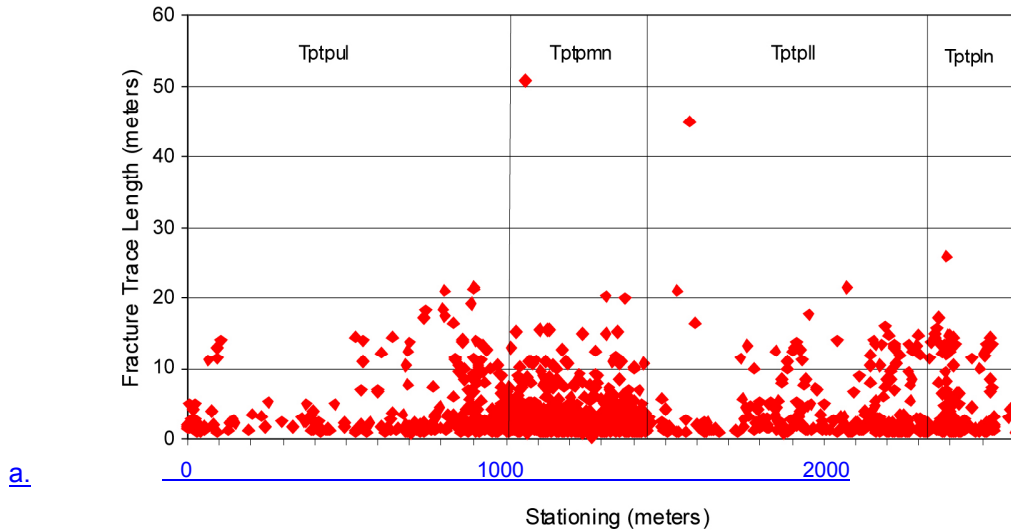
The discussion of fracturing presented in this section is based on Mongano et al. (1999). Full periphery geologic mapping and detailed line surveys (consisting of a description of orientation, trace length, small and large scale roughness and end terminations for all fractures with trace lengths of greater than or equal to one meter) were performed in all drifts. The database consists of over 35,000 entries and is recorded in CAD drawings as well as spreadsheets. There are, in general, four sets of fractures in the Tptpmn with the characteristics identified in Table 3.

The fractures have relatively short continuous trace lengths (Figure 7), with ends often terminating either against other fractures or in solid rock, leaving a solid rock “bridge” between joint tracks. Full periphery geologic maps that logged all fracture traces with length greater than one meter were created behind the tunnel boring machine as the ESF main loop and the ECRB Cross-Drift were driven. A typical full periphery geologic map showing all fractures is shown in Figure 8. Figure 9 shows the discontinuous nature of the fractures in each set. This figure shows a photograph typical of the wall of the ECRB Cross-Drift within the Tptpmn. The fracture traces were painted during the detailed line mapping (Figure 9). Each fracture termination was logged as being against another fracture, within solid rock, or continuous. The photo shows the common occurrence of fractures that terminate in solid rock (T-junctions) as opposed to continuous structures (arrowheads). The sub-vertical fractures, in particular, often have curved surfaces with large-amplitude (dozens of centimeters) asperities and wavelength of meters. Fractures often terminate in solid rock with discontinuous interconnection to adjacent joint tracks or against other joints.

Table 3. General Characteristics of Fracture Sets in the Middle Nonlithophysal Unit

Set	Mean Azimuth/Dip	Mean Spacing (m)	Mean Trace Length (m)	Comment
1	122/84	0.5	2.3	Rough to smooth, planar
2	195/85	1.48	1.9	Smooth but curved
3	306/09	4.2	2.7	Vapor-phase partings, rough, cohesive with coating minerals, planar
4	random	-	1.7	Random fractures with generally flat to moderate dip

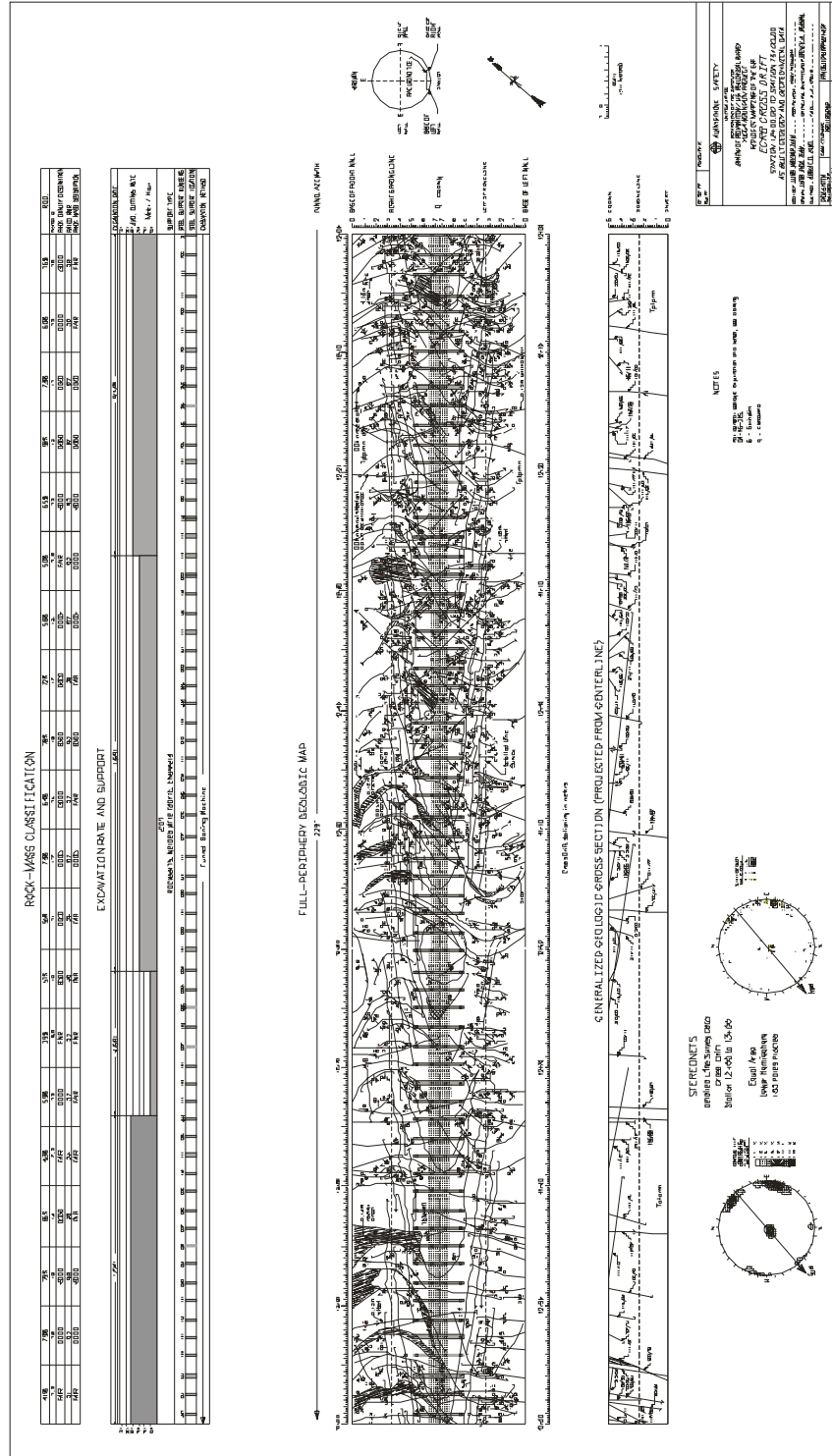
Source: Mongano et al. 1999



00266DC\_005.ai

Source: Mongano et al. 1999

Figure 7. Fracture Trace Length from Detailed Line Surveys as a Function of (a) Stationing Along the ECRB Cross-Drift and (b) Frequency Within Lithostratigraphic Units



DTN: GS990408314224.004

NOTE: The purpose of this figure is to illustrate the geologic structure contained on a full periphery geologic map. The annotated information on this figure is not intended to be legible. An enlarged, legible map is available through the source DTN.

Figure 8. Illustrative Example of a Full Periphery Geologic Map from the ESF, Ttpm



00266DC\_007.ai

NOTE: T-junctions on fractures indicate terminations; arrowheads show continuous features.

Figure 9. Fractures in Wall of the ECRB Cross-Drift in the Ttpmnn

The sub-horizontal vapor-phase partings (Figure 10) are relatively continuous structures seen throughout the Ttpmnn. These continuous, but anastomosing fractures are sub-parallel to the dip of the rock unit, and are filled with concentrations of vapor-phase minerals (primarily tridymite and cristobalite). The surfaces are rough on a small scale and, as a result of the mineral filling, they have cohesion (unlike the sub-vertical fractures).

The nature of the fracture geometry is extremely important to estimates of the stability of the rock mass, particularly under seismic shaking, as well as to estimates of the support function and level of required ground support. Most rock mass classification schemes are based on experience of rock masses with continuous joint sets that create regular, blocky masses (e.g., Hoek 2000). In the Ttpmnn, the relatively short trace lengths and non-persistent joints create relatively few kinematically removable blocks. This sparseness is evidenced by the fact that only a very small number of rock blocks have actually been removed in the ECRB Cross-Drift. Those blocks removed actually occurred under the action of the tunnel boring machine or were scaled out of the back and walls.

Short-length fractures (less than 1-m trace length), coupled with the lithophysae, are the most important features that govern stability in the Ttppll, since they impact the rock mass strength as described in Section 7.4. Whereas the Ttppl tends to have little small-scale inter-lithophysal fracturing (Figure 11a), the Ttppll has abundant fracturing. Figure 11b, from the upper portion of the Ttppll, shows the intensive fracturing that exists between lithophysae. The fractures, which exist throughout the Ttppll, have a primary vertical orientation, and have lateral spacing of a few centimeters.

Small-scale fracture traverses in the Ttppll confirm the close spacing and short trace lengths of fractures in this zone. The average spacing, from a combined 18 meters of traverse, is

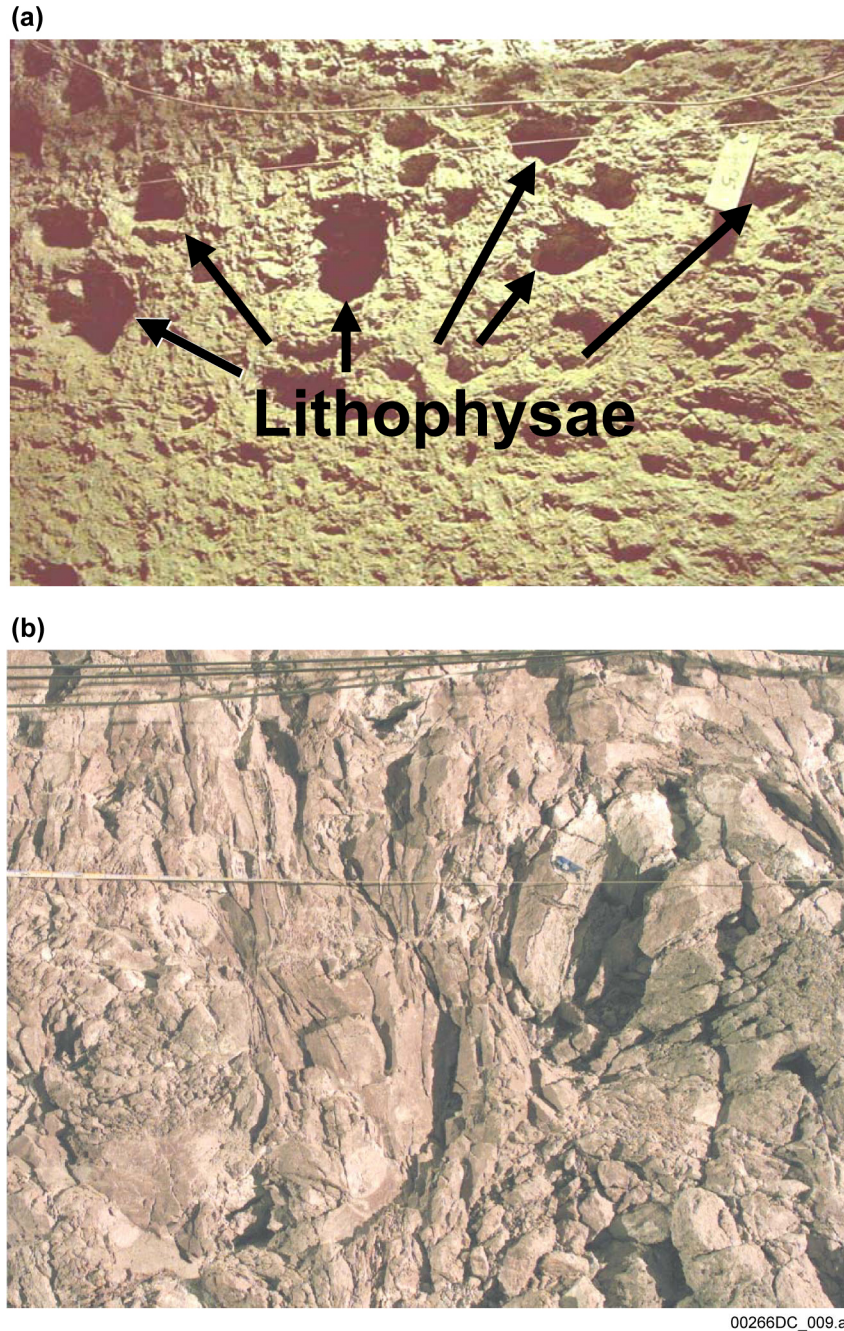
0.05 meters and an average trace length of 0.29 meters (DTN: GS990908314224.009). The intensity and short trace lengths of fractures in this zone creates a texture that severely limits the potential block size in this zone. By comparing the detailed line survey (fracture >1m) and the small-scale surveys, this intensity is clearly due to small-scale fractures (<1m trace length). The detailed line survey sampled almost 880 meters of tunnel in the ECRB Cross-Drift. There are 300 fractures recorded over this run of tunnel that have a trace length greater than 1 meter. The small-scale survey in the Tptpll can be combined into 18 meters of horizontal sampling. There are 376 fractures recorded over this 18 meters of sampling.

In some cases, it is difficult to distinguish whether these fractures have been disturbed by mining, or induced by in situ stresses, or whether they are newly created by mining along a weakness fabric in the rock. However, it is clear that the middle portion of the Tptpll has a ubiquitous fracture fabric that is most evident when large diameter core is removed from boreholes (see Figure 144a). The core, although competent, has numerous fractured surfaces that break into small blocks when stressed. Lithophysae and occasional horizontal fractures tend to create blocks with dimensions on the order of about 10 cm or less on a side. Thin section analyses of the fracturing in the Tptpll and the Tptpmn show rims on many of the fracture surfaces within the rock mass away from the tunnel wall, indicating there are numerous natural fractures (i.e., not mining-induced) and were formed during the cooling process (Buesch 2003b).



00266DC\_008.ai

Figure 10. Low-Angle Vapor-Phase Partings in Nonlithophysal Units in the ESF



NOTES: The Tptpul (a) is characterized by a relatively few fractures in the matrix-groundmass between lithophysae whereas the Tptpll (b) has abundant, natural, short-length fractures that interconnect lithophysae. Spacing of the fractures in the Tptpll is generally less than 5 cm.

Figure 11. Comparison of Lithophysae and Fracturing in the Tptpul and Tptpll

#### 6.1.4.2 Lithophysae

Although the character of the lithophysae varies between the Tptpul and Tptpll as shown in Figure 11, the mineralogy of the matrix material within both of these units is the same as in the nonlithophysal units.

Compositionally and mineralogically the rocks in lithophysal and nonlithophysal zones are similar, but there can be variations in the amounts of quartz, cristobalite, and tridymite; however, the main difference is in the abundance of lithophysae and features formed by crystallization in the presence of the vapor phase (rims, spots, etc.). The upper and lower lithophysal zones share many characteristics, but there are also numerous distinctions (Mongano et al. 1999), and these general characteristics are as follows.

The lithophysae in the Ttpul:

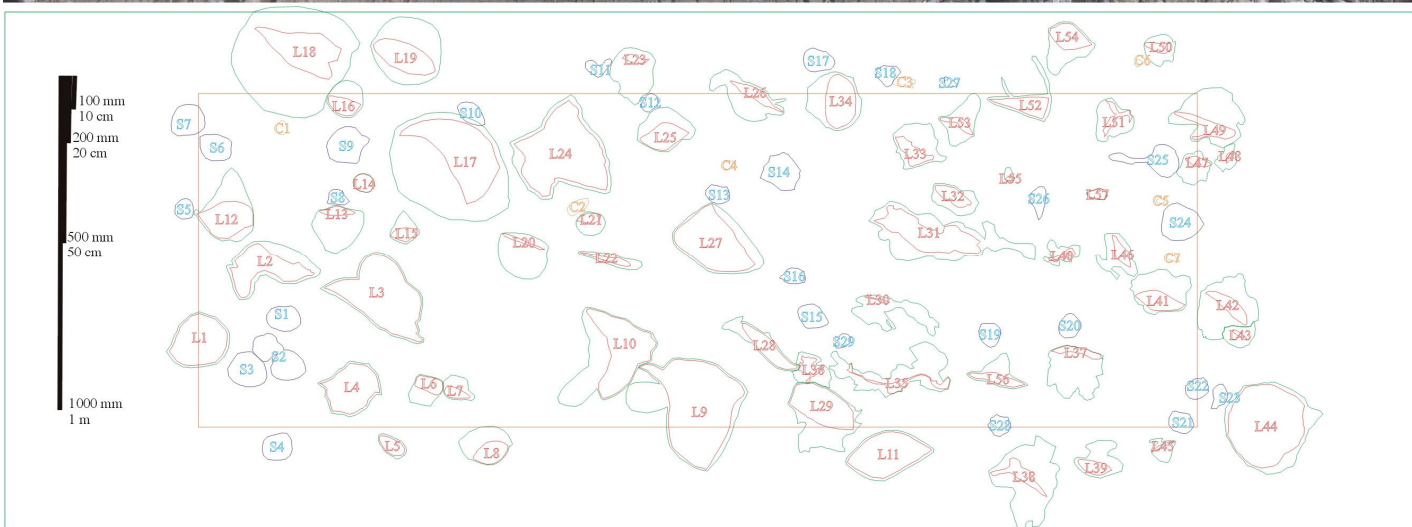
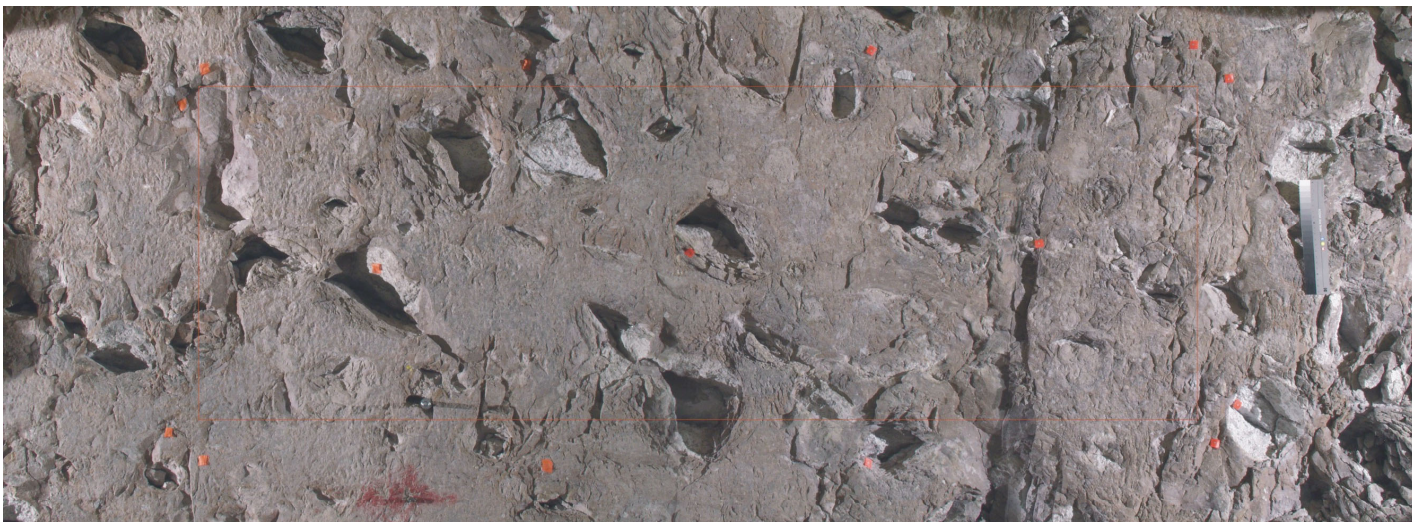
- Tend to be smaller (roughly 1 to 10 cm in diameter) compared to the Ttppl
- Are more uniform in size and distribution within the unit compared to the Ttppl
- Vary in infilling and rim thicknesses
- Have a volume percentage that varies consistently with stratigraphic position
- Are stratigraphically predictable.

The lithophysae in the Ttppl:

- Are highly variable in size, from less than 1 cm to 1.8 m in size
- Have shapes that are highly variable and are described as simple (elliptical cross-sections and spherical to ellipsoidal shapes), irregular, cusped, merged (two or more lithophysae joined into one large one), and extension-crack lithophysae
- Have infilling and rim thickness that vary greatly with vertical and horizontal spacing
- Have volume percentages that vary consistently with stratigraphic position
- Are stratigraphically predictable.

With the large amount of the repository located in the lower lithophysal zone, a detailed study of the lithostratigraphic features in the lower lithophysal zone exposed in the ECRB Cross-Drift has recently been completed (DTN: GS021008314224.002). The data package documents the distributions of size, shape, and abundance of lithophysal cavities, rims, spots, and lithic clasts, and these data can be displayed and analyzed as (1) local variations, (2) along the tunnel (a critical type of variation), and (3) as values for the total zone. A detailed description of lithophysal abundance and lithophysal characteristics is provided in Attachment XV.

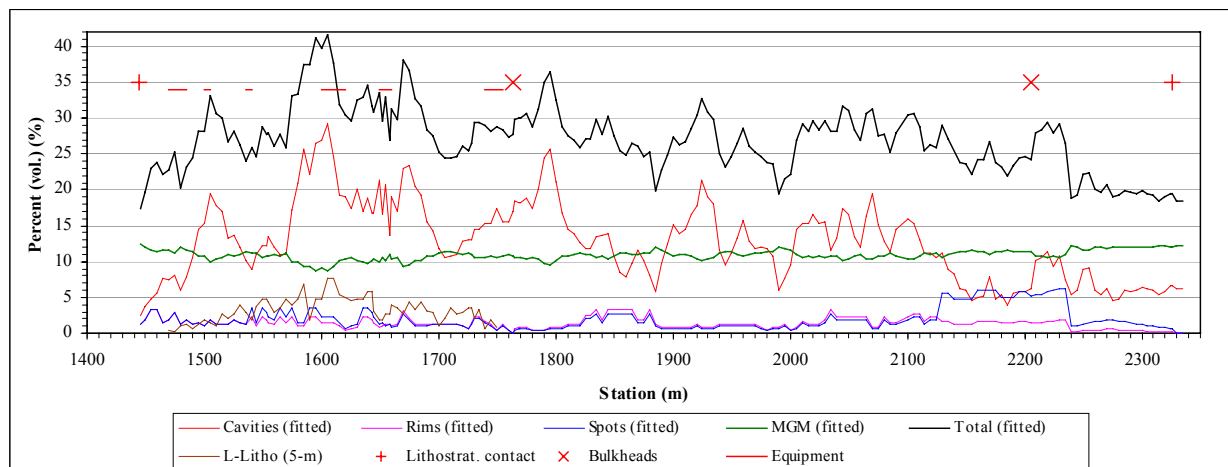
In addition to the along-the-tunnel variation in the abundance of features such as lithophysae, there are variations in the sizes, shapes, and distances between features. These types of variations are most easily observed with panel map data (Figure 12). Locations of the panel maps were positioned to capture representative variations in the rocks along the tunnel. Additional details on the development of these panel maps are provided in Attachment XV.



NOTE: Lithophysae have red “L” identifiers with cavities outlined in red and rims in green. Spots have blue “S” identifiers with cyan outlines. Lithic clasts have orange “C” identifiers with gold outlines.

Figure 12. Lithophysae, Spots, and Clasts of Tptpl in Panel Map 1493 Located on the Right Rib from Stations 14+93 to 14+96

Using the approach described in Attachment XV, the total porosity of the component features of the lithophysal rock mass (i.e., the porosity of the lithophysal cavities, rims, and spots) has been calculated. The porosity variation along the ECRB Cross-Drift is shown in Figure 13, with total porosity typically ranging from 20 to 35 percent.



NOTE: Porosity of the 5-m averaged large-lithophysae inventory is not included in the total.

Figure 13. Calculated Porosity of Lithophysal Cavities, Rims, Spots, Matrix-Groundmass, and the Total Porosity in the TptplI Exposed along the ECRB Cross-Drift

### 6.1.5 Field Observation of Key Blocks

Key blocks are critical blocks in the surrounding rock mass of an excavation which are removable and oriented in an unsafe manner so that they are likely to move into an opening unless support is provided (Goodman and Shi 1985, pp. 98 and 99). The failure of a key block opens up the excavation surface for further potential failures by subsequent blocks. Key blocks are formed by the intersection of three or more planes of structural discontinuities as shown in Figure 14. Key blocks in the 5-m-diameter ECRB Cross-Drift are first evident in the crown at about Station 10+50 in the Tptpmn unit (note that metric stationing is used throughout the ESF, i.e. Station 10+50 is located 1050 m from the start of the tunnel). Most of the key blocks in this region are of minor size and typically fall immediately after excavation prior to ground support installation. Key blocks are possible in this area because of the increased presence of the plane of weakness (i.e., a vapor-phase parting) in the near horizontal orientation that intersects with two opposing near vertical joint planes. Fallout from these key blocks during excavation is typical of the rock in the middle nonlithophysal zone (Tptpmn) of the TSw2 thermal-mechanical unit. The largest resultant void is possibly 0.5 cubic meters at approximately Station 11+55 as shown in Figure 15. No unstable key blocks were observed in the field. Documentation of key blocks observed in the ECRB Cross-Drift is provided in Attachment VI.

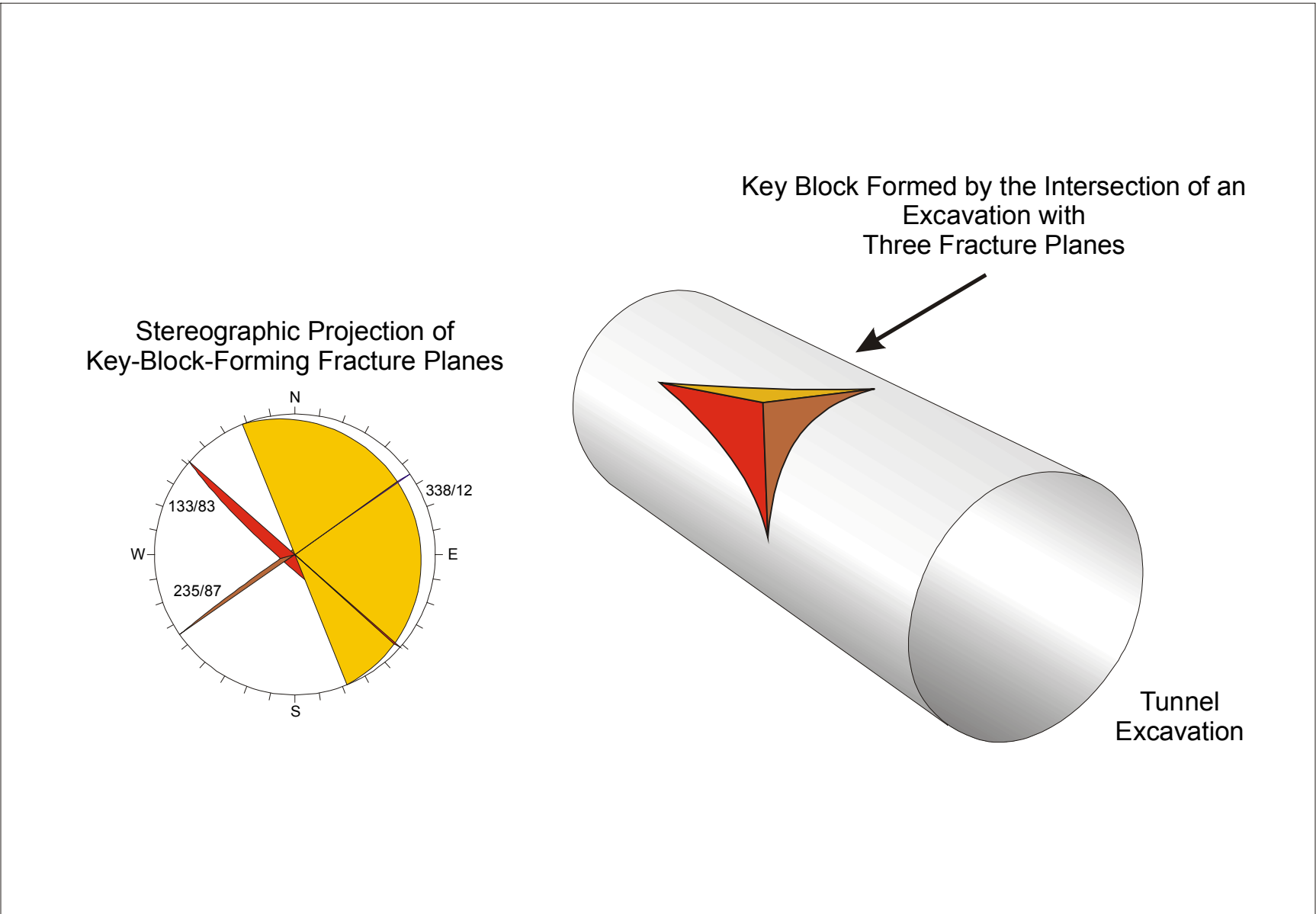


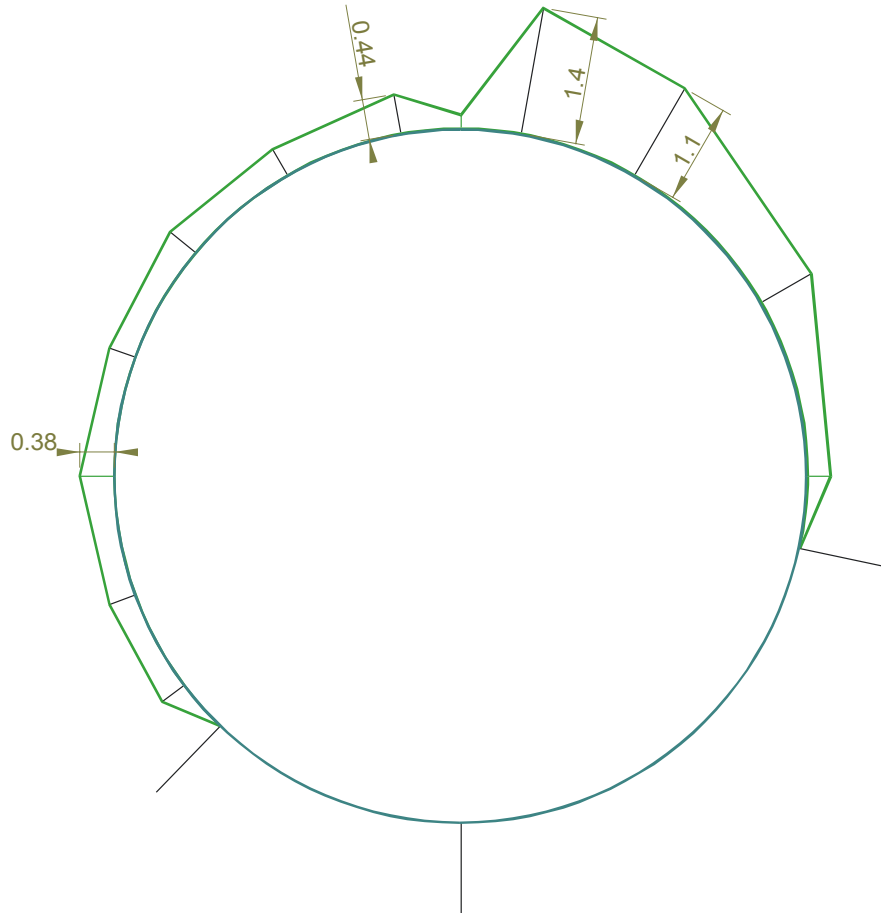
Figure 14. Illustration of a Typical Key Block and Associated Fracture Planes



Figure 15. Evidence of Key-Block Occurrence in the ECRB Cross-Drift, Station 11+55

While ground-support monitoring in the ESF main loop has provided long-term evidence indicating stable rock support performance, there are several sections in the ESF where excessive raveling and block fall-out have occurred. These typically correspond to the “3.01X” areas, and most often occurred in fault zones and in the TCw and TSw2 thermal-mechanical units. The 3.01X areas refer to sections of the ESF main loop that were constructed under Section 3.01X of the subsurface general construction specification (BSC 2002d, p. 17). The specification indicates that special actions may be necessary to continue excavation in the event that adverse ground conditions prevent normal tunnel boring machine operations. The location of 3.01X

areas is provided by *South Ramp 3.01.X Area Ground Support Analysis* (CRWMS M&O 1999, Section 1). A typical opening profile in a 3.01X area is shown in Figure 16. This profile is indicative of the worst case ground conditions in the Tptpmn lithologic unit of the ESF main loop.



Source: CRWMS M&O 1999, p. 29

Figure 16. Opening Profile at ESF Main Loop Station 60+24.70 (Steel Set #1272, Tptpmn Lithostratigraphic Unit) Based on Field Survey Data (Dimensions in Meters)

### 6.1.6 Generation of Representative Rock Volumes Using FracMan

As input to rockfall modeling, a representative FracMan simulation of the actual fracture network is constructed based on standard detailed line survey and full periphery geologic map data. These data consist of fractures with trace lengths of a meter or greater. The premise to this simulation is that a 100-meter on a side cube results in a representative fracture network. The fractures are simulated, and their location, orientation and size are inputs for the rockfall analyses. Individual 100-meter cubes are constructed for each lithostratigraphic unit. The Tptpll and Tptpmn units are presented in this section representing lithophysal and nonlithophysal rock, respectively, within the repository. Details for the analysis of other lithostratigraphic units (i.e., the Tptpul and Tptpln) are provided in Attachment II.

The timing of fracture formation in the field fundamentally determines the geometry of the fracture network by controlling the truncations and thereby the lengths of each subsequent fracture generation. First forming are vapor-phase partings, which are low-angle discontinuities (dips less than 45°) with vapor-phase mineralization, along with long, smooth, high-angle discontinuities with vapor-phase mineralization. These fractures tend to be long and only slightly truncated. Next, but still early in the cooling process of the pyroclastic flow deposits, smaller truncated fractures are formed. These smaller fractures are moderate to high angle and can have, or not have, vapor-phase mineralization. Smaller fractures commonly have the same orientations as the longer, high-angle fractures, and are distinguished based on their length.

The detailed line survey data are used to define the inputs for FracMan. The sampling is a combination of a limited area and line survey. Because of this there is a sampling bias. The Terzaghi correction (Terzaghi 1966) is a bias correction for a line survey and is therefore is inappropriate in detail for the sampling that was used to collect the data. In this analysis no correction factor is needed because FracMan uses the same sampling method for the synthetic fractures as was used in the collection of the observed data. In other words the same bias encountered in collecting the observed data is sampled in the synthetic data allowing a valid comparison without correcting the observed.

Construction of the FracMan network starts with the low-angle features. Because these features form first in the cooling process their truncation by other features is minimal. The truncation probability value (i.e., the probability that a fracture which intersects another fracture will be terminated against that fracture) for these features used in FracMan is 5 percent. To continue the construction of the FracMan network, the remaining fractures, having a dip greater than 45° are separated into two classes. The first class includes those fractures that formed about the same time as the vapor-phase partings. These fractures are referred to as cooling joints and have long trace lengths with some truncation occurring against the vapor-phase partings and themselves. The truncation probability value used in FracMan is 10 percent. The second class includes the fractures that have a shorter trace length. These fractures are considered to be later cooling and tectonic fractures. These fractures are generated into a network comprised of vapor-phase partings and long, high-angle cooling fractures and are truncated more severely than the earlier fractures. The truncation probability value used in FracMan is 70 percent.

This construction is significantly different from a construction with sets solely identified on the basis of orientation. However, observations of mineralization and truncation relations (Mongano et al. 1999) suggest that the current sequential construction is more appropriate to generate a representative rock volume. This construction does not create a replicate of the actual fracture geometries observed in the limited sampling afforded by the detailed line survey and the full periphery geologic map. The objective is to provide a generalized, representative fracture network for evaluation of the rock mass as a whole. The output from FracMan is a fracture network whose geometry is conditioned from a careful evaluation of the detailed line survey and full periphery geologic map data. Special geologic features are not represented in this effort. For example, in a 100-meter segment of tunnel mapping there may be a 15-meter section that shows an increased amount of fractures from a given set. The developer may decide to represent this zone by developing a specific distribution for this occurrence. However, for this report an average geometry is used to describe the simulation since the fracture network developed does not represent a specific section of the mapped area, but is representative of the general condition

of the rock mass. Not enough data exists to develop a simulation that represents every geologic variation in the rock mass. To avoid giving the impression of zones which display anomalous geometries in each lithostratigraphic unit, these zones are averaged into the simulation when the decision is made that adding this input helps represent the rock mass correctly with the data that is available. Because this output is not a replicate, a single constant fracture intensity is imposed for each set in each lithostratigraphic unit. Plots of cumulative fracture number against tunnel station display a constant slope for the most part along the sampled tunnel. Where the intensity is not constant, it is displayed as a change of slope in these plots. Further discussion appears later in this section.

Correct fracture size is critical to the construction of a representative network. Unfortunately, the radius of a fracture cannot be measured from a surface sampling of the fracture network. If all fractures are considered circular disks, then the centers of those disks do not have to coincide with the sampling surface. The observed trace length is then typically not the disk diameter; it is usually something less because the centers of the fracture disks do not coincide with the sample surface.

In order to get an intuitive feel for the radius distribution and how it relates to the observed trace length distribution consider the following: a single fracture of radius  $R$  oriented perpendicular to the sampling plane. If the fracture intersects the plane the observed trace length can vary from 0.0 to  $2.0R$ .

As shown in Figure 17, the trace length is a function of the distance from the sampling plane and the fracture radius, and is defined based on standard geometric relationships:

$$T = 2(R^2 - z^2)^{0.5} \quad (\text{Eq. 1})$$

The mean observed trace length  $T_m$  is then

$$T_m = \frac{1}{R} \int_0^R 2(R^2 - z^2)^{0.5} dz \quad (\text{Eq. 2})$$

$$T_m = \pi R/2 \text{ or } R = T_m 2/\pi \quad (\text{Eq. 3})$$

indicating that the mean fracture radius is about 2/3 of the mean trace length observed.

This means that the expected distribution of trace lengths is equal to the distribution of the intersecting fractures times a constant factor  $\pi/2$ . In a log-log plot multiplication of a power law by a constant does not change the slope, so that the scaling exponent of trace lengths is the same as the scaling exponent of the radius distribution of intersecting fractures.

The radii distributions are compared to a distribution formed from the trace lengths observed multiplied by two-thirds to adjust the trace lengths to approximate radii. This is not a perfect adjustment because the dip of the fractures as well as their persistence will influence the number "two-thirds." The trace lengths are observed with a sampling surface or detailed line survey. Additional effects may be present when comparing the radii in the 100-meter cube with the

surface or line sampling. Individual plots of these distributions are included in each of the following sections for the lithostratigraphic units. Overall, the fits are good to excellent.

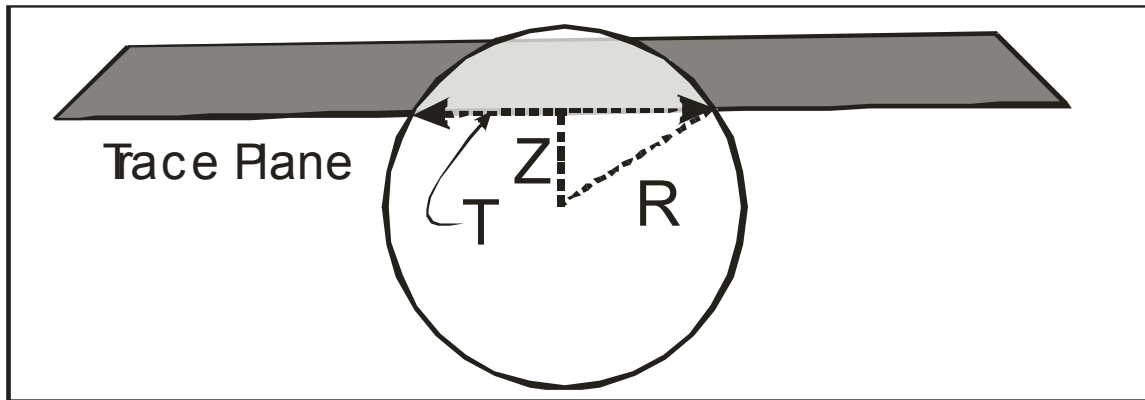


Figure 17. Relationship Between Trace Length and Radius

Finally, with the sequence of formation determined and the length distribution selected, orientation is evaluated to further subdivide the fractures into sets. This division is based on analysis of stereonet pole plots. All fractures with a dip  $> 45^\circ$  are used for this analysis because the orientations of the longer fractures and the shorter fractures are coincident. Once this is accomplished, the actual inputs for FracMan are developed.

The following is a brief description of the inputs required to begin the generation of simulated fracture geometries. The fracture geometry data for each lithostratigraphic unit are converted to the parameters needed for FracMan. An input sheet for FracMan is then developed for each lithostratigraphic unit. The input values are derived for this report from the detailed line survey data. The trend and plunge of the poles are used to set the mean orientations for each of the sets. The dispersion ( $k$ ) is set by visually evaluating the pole plot of the detailed line survey data for each set. The FracMan radius needed is estimated as two thirds of the minimum trace length for each set. The two remaining input values, termination percent and intensity, are initially developed by making qualitative estimates from the full periphery geologic maps. As development of the simulation progresses these values are refined to generate a representative simulation of the fracture geometries for each lithostratigraphic unit.

Several comparisons are made to confirm that the results of the FracMan output are giving a simulated fracture geometry that resembles the actual rock mass. The first comparison after the generation is to compare the relative proportions of the fractures in each set comparing the proportions from FracMan to the detailed line survey fractures. The results of this comparison are presented through the following sections for each lithostratigraphic unit.

The next comparison is between the detailed line survey data pole plots and the FracMan data pole plots. Correct selection of the mean orientation as well as the correct dispersion, the “ $k$ ” value, is key to getting an acceptable distribution of poles on the stereonet. The results of this comparison are presented through the following sections for each lithostratigraphic unit. For each pair of stereonets for each lithostratigraphic unit, data from the FracMan realization and the observed detailed line survey data show good to excellent comparisons for both the mean

orientation and dispersion about the mean. Comparison of the stereonets of poles to fractures is limited because FracMan is not creating a replicate but merely a reasonable model from the observed data. The observed data display more scatter than the FracMan realization but it is a sufficient representation of the observed. The observed data are from detailed line survey mappings that may have limitations.

The goal of the orientation comparison is therefore to represent the major sets with reasonable conformance to the observed mean orientations and the observed spread or dispersion about the mean. Not every fracture observed will be displayed in the FracMan realizations.

More fractures will be displayed in the 100-m on a side FracMan cube than are observed in the detailed line survey data. The detailed line survey data is sampling a small surface area compared to even the full periphery geologic map and considerably less fractures are observed than are present in the 100-m cube. The primary comparison to make between the rock mass geometry and the FracMan geometry is to compare full periphery geologic maps. The FracMan geometry allows for the same kind of sampling as the original data. For each of the following sections a direct comparison is presented to confirm the FracMan geometry resembles the observed geometry. Intensity controls the number of fractures and the check for intensities relies on the comparison of FracMan full periphery geologic maps to the observed full periphery geologic maps for validation. If the intensity from the FracMan full periphery geologic maps and the observed full periphery geologic maps are similar then the validation is considered satisfactory.

Fracture intensity measures are classified based upon the dimension of the measurement region and the dimension of the fracture measure. P stands for persistence and the measures are  $P_{ij}$ . For example,  $P_{32}$  is the fracture area (dimension 2) divided by the region volume (dimension 3). The number of fractures (dimension 0) per unit length (dimension 1) is  $P_{10}$ . Spacing, S, is  $P_{10}^{-1}$ .

The general relationship between the fracture intensity  $P_{32}$  and the mean fracture spacing, S, along a line is given by Dershowitz and Herda (1992):

$$P_{32} = C/S = C P_{10} \tag{Eq. 4}$$

where C is a constant that depends on the orientation distribution of the fractures. Dershowitz and Herda (1992) suggested a range of expected values between 1.0 and 3.0 and a value of 2.0 for a uniform distribution of orientations.

The equations have been derived for the simplified case where the orientation distribution is constant. For different orientation distributions then the equation becomes inaccurate for large variations about the mean pole orientation. The main equation then becomes

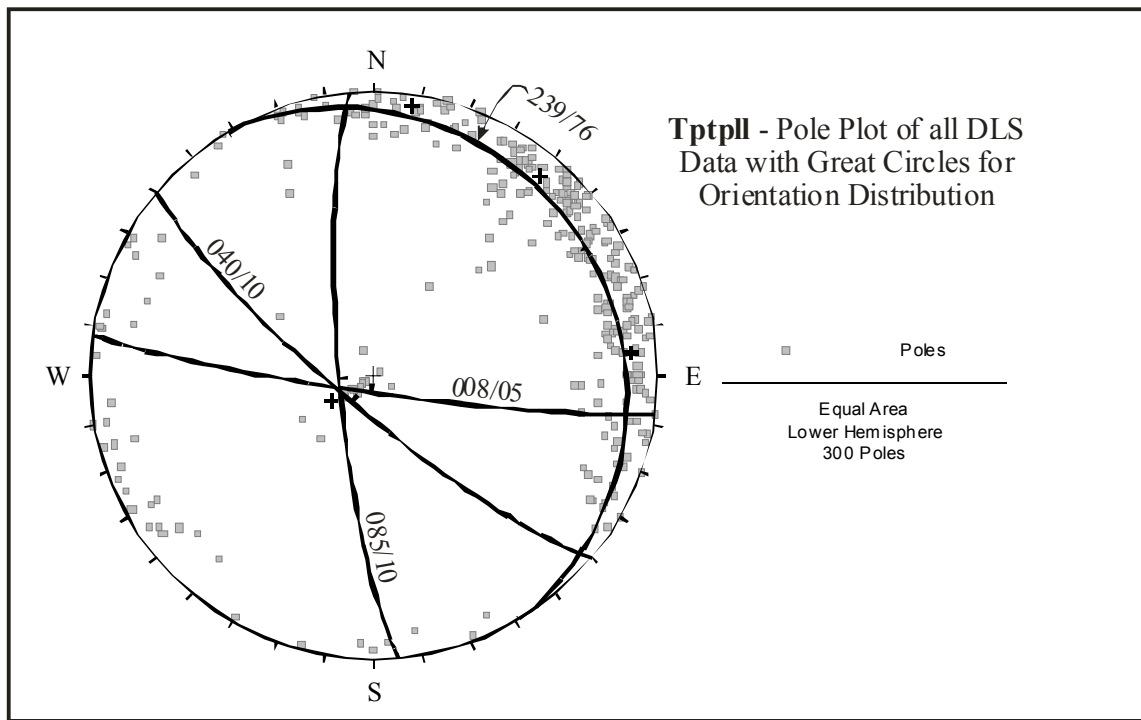
$$P_{32} = \frac{C}{d \cdot \left( \frac{1}{\int_0^\pi \sin(\theta) f(\theta) d\theta} \right)} \tag{Eq. 5}$$

where  $d$  is the inter-fracture distance along a line, and  $f(\theta)$  is the orientation probability density function.

In this report, the FracMan model uses a constant  $P_{32}$  for each set of fractures, which is based on the consideration that there is no spatial heterogeneity in intensity. There are a few discrete changes in intensity observed in the detailed line survey and full periphery geologic map data but for the most part the “average” intensity is constant as depicted by a linear cumulative fracture number versus stationing plot for each of the lithostratigraphic units. The validation for this approach is the comparison of the full periphery geologic map observed with the FracMan full periphery geologic map. These are in agreement for the overall intensity.

### 6.1.6.1 Inputs and Results for the Tptpll

To begin the analysis of the Tptpll, the observed vapor-phase partings are identified in the detailed line survey data. This is done by sorting the observed data with respect to dip and identifying those fractures which have a dip of less than 45 degrees. For the Tptpll there are 20 vapor-phase partings. The mean pole orientation is 239/76. Figure 18 shows the Great Circle for the mean orientation of the vapor-phase partings. The poles for the other sets are also plotted.

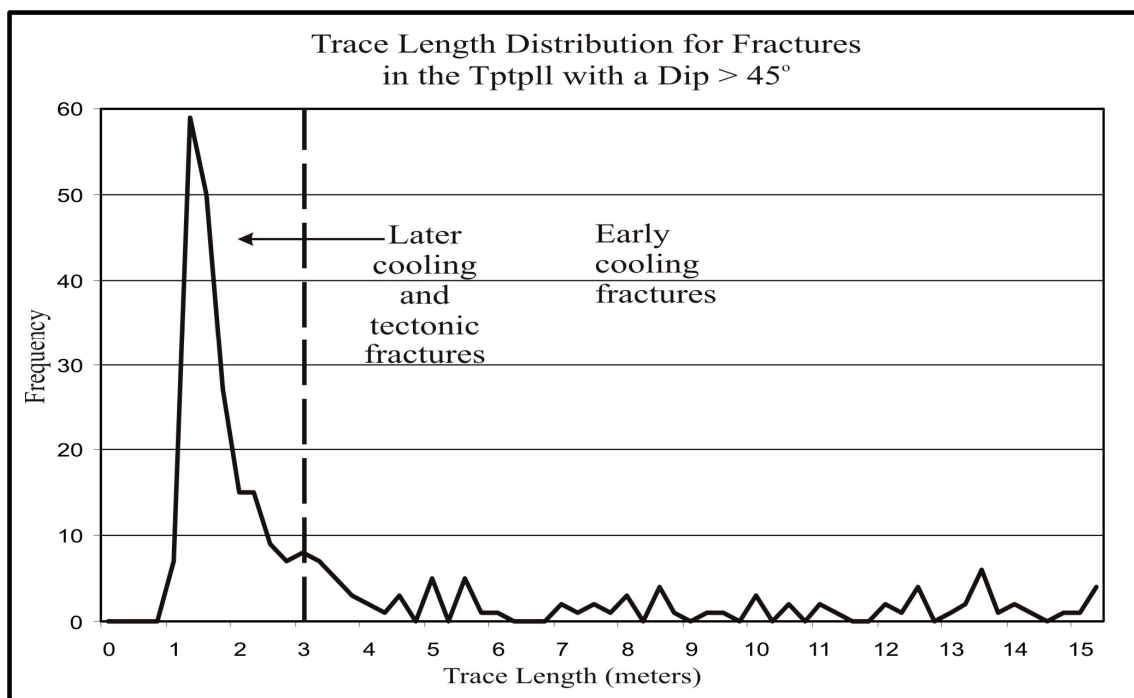


DTN: GS990408314224.001  
GS990408314224.002

Figure 18. Tptpll Pole Plot Showing Great Circles for all Tptpll Fractures

The remaining fracture trace lengths are plotted on a histogram and the trace length distribution is evaluated. The distribution is polymodal. A break is defined to separate the long fractures from the short fractures. For the Tptpll, this break occurs at approximately 3 meters (Figure 19). The distribution of poles for both the cooling and later cooling/tectonic fractures is shown in Figure 18. The set attributes developed from the detailed line survey are provided in Table 4.

In Figure 20, the values used as input to the FracMan simulation are shown. Table 5 is a direct comparison of the observed detailed line survey data with the FracMan output with respect to the number of fractures in each set as well as the proportions of the total in each set. The proportions of fracture types are very important to establish a representative FracMan network. The actual number of fractures is not relevant because the sampling areas are not comparable.



DTN: GS990408314224.001  
GS990408314224.002

Figure 19. Trace Length Distribution of the Tptpll Fractures (>45°)

Table 4. Summary Statistics of the Tptpll Detailed Line Survey Data

Set	Strike & Dip (Trend & Plunge)	Trace Length (mean)	Number of Fractures
Vapor-Phase Partings	329/14 (239/76)	7.2m	20
1 <sup>st</sup> Generation Cooling Joints	130/80 & 175/80 (040/10 & 085/10)	9.5m	71
2 <sup>nd</sup> Generation Cooling and Tectonic Joints	130/80, 175/80, 278/85 (040/10, 085/10, 008/05)	1.6m	209

DTN: GS990408314224.001; GS990408314224.002

NOTE: Strike and dip values were determined graphically using the steronet shown in Figure 18.

The most critical comparison is presented in Figure 21. This is the direct comparison between an actual full periphery geologic map from the ECRB Cross-Drift to a synthetic full periphery geologic map from FracMan. The synthetic full periphery geologic map is not a replicate, but based on professional expertise and judgment, the FracMan full periphery geologic map is adequately similar to the observed full periphery geologic map both for intensity and lengths.

Project Ttptll Task Drift Degradation Date 01-24-03 Modeler Lung-Fahy  
 Seed #: 0725 Fracmeter Unit: 50 Truncation mode Region View Center 0,0,0  
 Direction \_\_\_\_\_ Scale \_\_\_\_\_ % displayed 100 Orientation = Pole or Dip Pole # frac sides 6

Frac Set	Model Type	Generation Region & Dimension	Orientation TR,PI	Dist. Type	k dispersion	Size eqv. Radius	Dist. type	Mean SD	Max. Min.	Elongation	Aspect Ratio	Termin %	Intensity
1	Baecher	100x100x100	239/76	Fisher	70	1.30	Power (3.1)			NA	NA	5	0.02
2	Baecher	100x100x100	040/10	Fisher	70	1.80	Power (3.1)			NA	NA	10	0.05
3	Baecher	100x100x100	085/10	Fisher	70	1.53	Power (3.1)			NA	NA	10	0.02
4	Baecher	100x100x100	040/10	Fisher	100	0.60	Power (3.1)			NA	NA	70	0.035
5	Baecher	100x100x100	085/10	Fisher	100	0.60	Power (3.1)			NA	NA	70	0.007
6	Baecher	100x100x100	008/05	Fisher	100	0.60	Power (3.1)			NA	NA	70	0.002

NN factor \_\_\_\_\_ NN export: \_\_\_\_\_ WZ inten: \_\_\_\_\_ WZ parall: \_\_\_\_\_ WZ large: \_\_\_\_\_ WZ close \_\_\_\_\_ Frac Dim (LL,FB)(.5-5.) \_\_\_\_\_  
 Zone Thick \_\_\_\_\_ Fracs \_\_\_\_\_ # iterations \_\_\_\_\_ Frac Dim (POCS) \_\_\_\_\_ Ampl Shaper Fac (POCS) \_\_\_\_\_ Box Frac Dim \_\_\_\_\_ Spherical/Exp \_\_\_\_\_  
 Variogram \_\_\_\_\_ Semivariogram Sill \_\_\_\_\_ Corr Length \_\_\_\_\_

\_\_\_\_\_.FDT (binary, cant port to non DOS computers, cannot be edited in std word processing )  
 \_\_\_\_\_.BAB (babylonian ASCII version of FDT, only frac. data stored. Can be ported to non DOC computers. No std word processing.)  
 \_\_\_\_\_.DCM (Std ASCII version of FDT. Only frac data stored. Can be ported to most computers. Can be edited by std. Word processing. Large files)  
 \_\_\_\_\_.SAM (ASCII) \_\_\_\_\_ .ORS (ASCII) \_\_\_\_\_ .PCS (ASCII, for conditioned data)  
 \_\_\_\_\_.F2D (ASCII, frac trace data)

DTN: GS990408314224.001  
 GS990408314224.002

NOTES: The parameter, "k dispersion" is determined visually by comparing simulated stereonet to observed stereonet. The parameter, "size eqv. radius" is the mean radius (m). The power law distribution is used for the parameter, "dist. type." The power law is selected since the fracture process generally follows power law physics, such that the number of fractures greater than a given length (x) is proportional to 1/x raised to the power law exponent. The parameter, "intensity" is selected to maintain the proportion of fractures in each set.

Figure 20. FracMan Input Sheet for the Ttptll

Table 5. Relative Proportions of Fractures from the Detailed Line Survey Versus FracMan Output for the Tptpll

Detailed Line Survey			FracMan		
Feature	Number of fractures	Proportion	Feature	Number of Fractures	Proportion
Vapor-Phase Partings	20	6%	Vapor-Phase Partings	647	7%
1 <sup>st</sup> Generation Cooling Joints	71	24%	1 <sup>st</sup> Generation Cooling Joints	2494	25%
2 <sup>nd</sup> Generation Cooling and Tectonic Joints	209	70%	2 <sup>nd</sup> Generation Cooling and Tectonic Joints	6738	68%
Total	300	100%	Total	9879	100%

DTN: GS990408314224.001; GS990408314224.002

The orientation comparison is presented in Figure 22. Pole plots for the detailed line survey data and the FracMan output are compared to ensure that the clusters from the detailed line survey are correctly simulated in FracMan. For the Tptpll this comparison demonstrates that the FracMan output is adequately similar to the observed data. The means are similar and the spread of the data about the mean is similar. Not all observed fractures are simulated because the FracMan output has less scatter and is not a replicate.

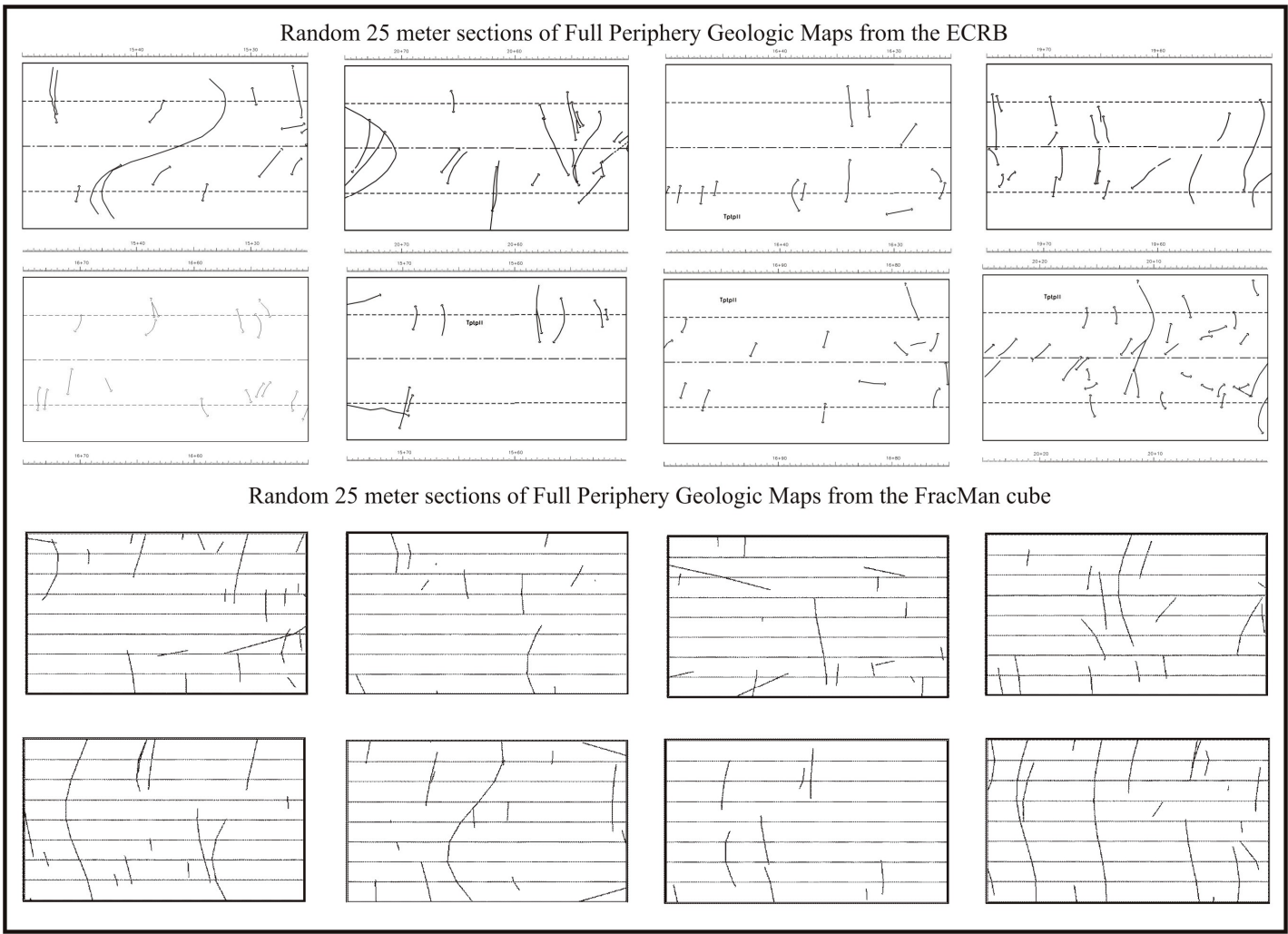
Figure 23 provides confirmation that the radius distribution of fractures from FracMan matches reasonably well with the observed trace lengths. Figure 24 shows that fracture intensity, that is the slope, is nearly constant until approximately Station 21+50. At this point a sequence of small offset faults occurs causing the intensity to increase.

#### 6.1.6.2 Inputs and Results for the Tptpmn

The analysis for the Tptpmn uses a classical approach to identify sets based on orientation. The classical approach uses orientation only to identify the sets (Mongano et al. 1999; CRWMS M&O 2000a). Four sets are defined in the Tptpmn; the great circles for these sets are displayed in Figure 25.

Although this development is different from those for the other lithostratigraphic units, the geometry resulting from FracMan is representative. The detailed line survey data are used to condition FracMan to develop representative fracture trace lengths and spacings. The same comparisons of detailed line survey and FracMan output apply to this realization. Table 6 displays the mean orientation of the sets, a comparison of average radius converted to diameter and average trace length, and intensity (average spacing) from FracMan and average spacing from the detailed line survey.

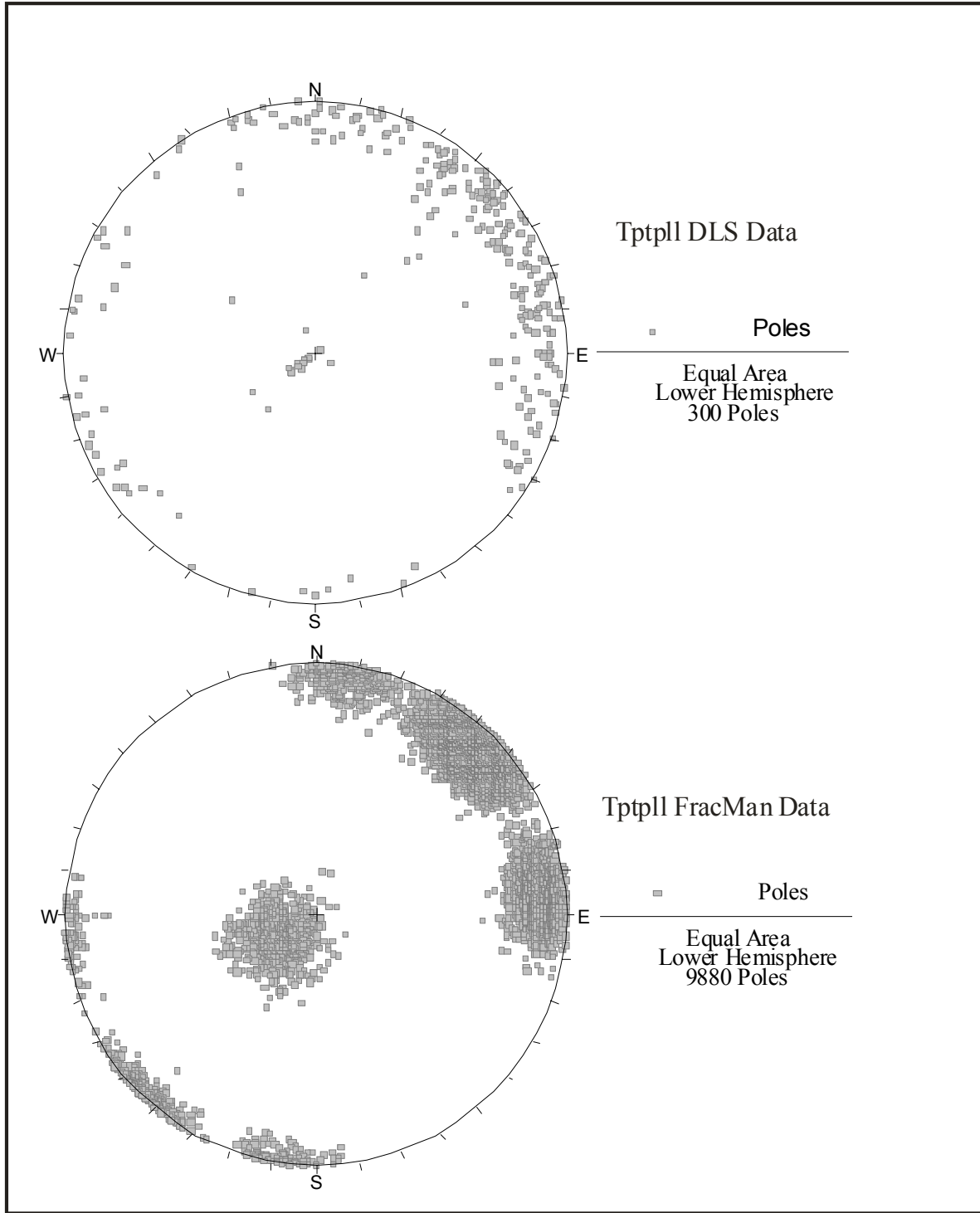
The input sheet for the Tptpmn is shown in Figure 26. The most important comparison is presented in Figure 27. This is a direct comparison between an actual full periphery geologic map from the ECRB Cross-Drift to a synthetic full periphery geologic map from FracMan. Again, the realization from FracMan is not a replicate. The comparison is made to evaluate intensity and length with a sampling method identical to the observed sampling. In this case, the sampling is a full periphery geologic map. Based on the professional expertise and experience, the FracMan full periphery geologic map is acceptably conditioned to be visually similar to observed full periphery geologic maps for the Tptpmn.



DTN: GS990408314224.004, GS990408314224.005  
GS990408314224.006.

NOTES: The purpose of this figure is to illustrate the geologic structure contained on a full periphery geologic map. The annotated information on this figure is not intended to be legible.

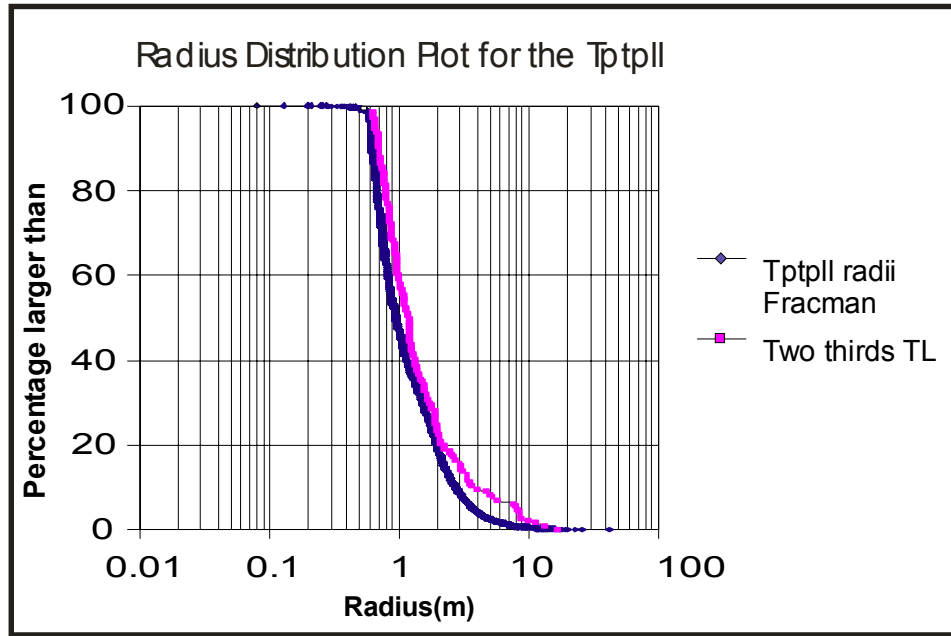
Figure 21. Comparison of Full Periphery Geologic Maps from the TptplI in the ECRB Cross-Drift with Simulated Full Periphery Geologic Maps from the FracMan Cube



DTN: GS990408314224.001  
 GS990408314224.002

NOTE: The FracMan data is representative of the entire rock mass, and is not a replicate of the detailed line survey data. Therefore, the number of poles in FracMan is expected to be much greater than the detailed line survey data. The location of the poles should agree, which is shown by this figure.

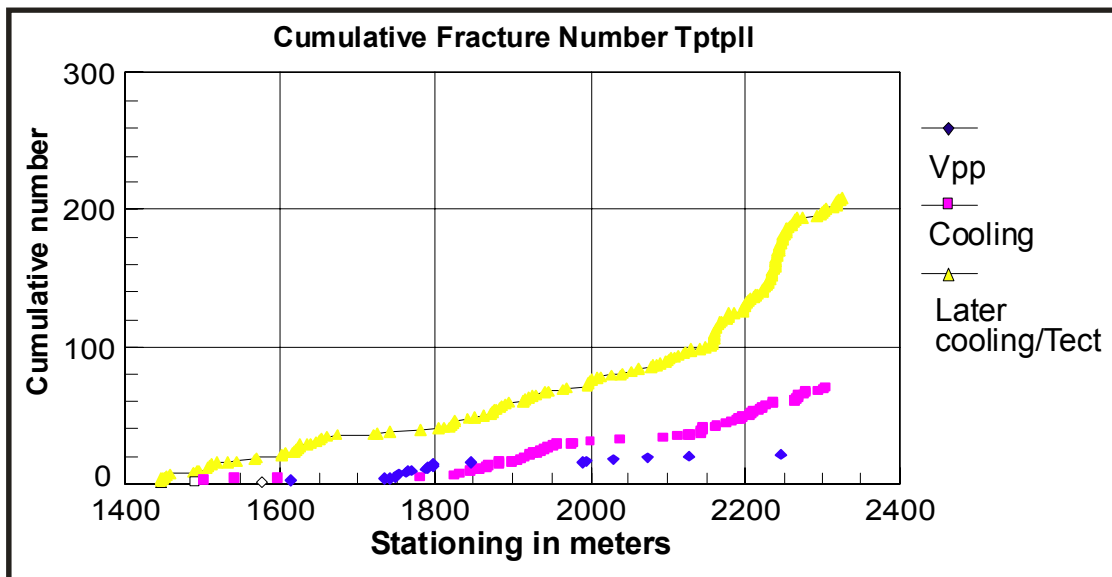
Figure 22. Comparison of the Observed Tptpl Fracture Poles to the FracMan Fracture Poles



DTN: GS990408314224.001  
GS990408314224.002

NOTE: This figure compares fracture radii from FracMan to observed trace length data scaled by two-thirds. This is based on the relationship between fracture trace length and radius (see Figure 17). The mean fracture radius should be about two thirds of the mean trace length observed.

Figure 23. Comparison of the Observed Trace Length Distribution (Scaled by Two Thirds) to the FracMan Radii Distribution for TptplI



DTN: GS990408314224.001  
GS990408314224.002

NOTE: Constant slope indicates constant intensity.

Figure 24. Evaluation of Constant Intensity for TptplI

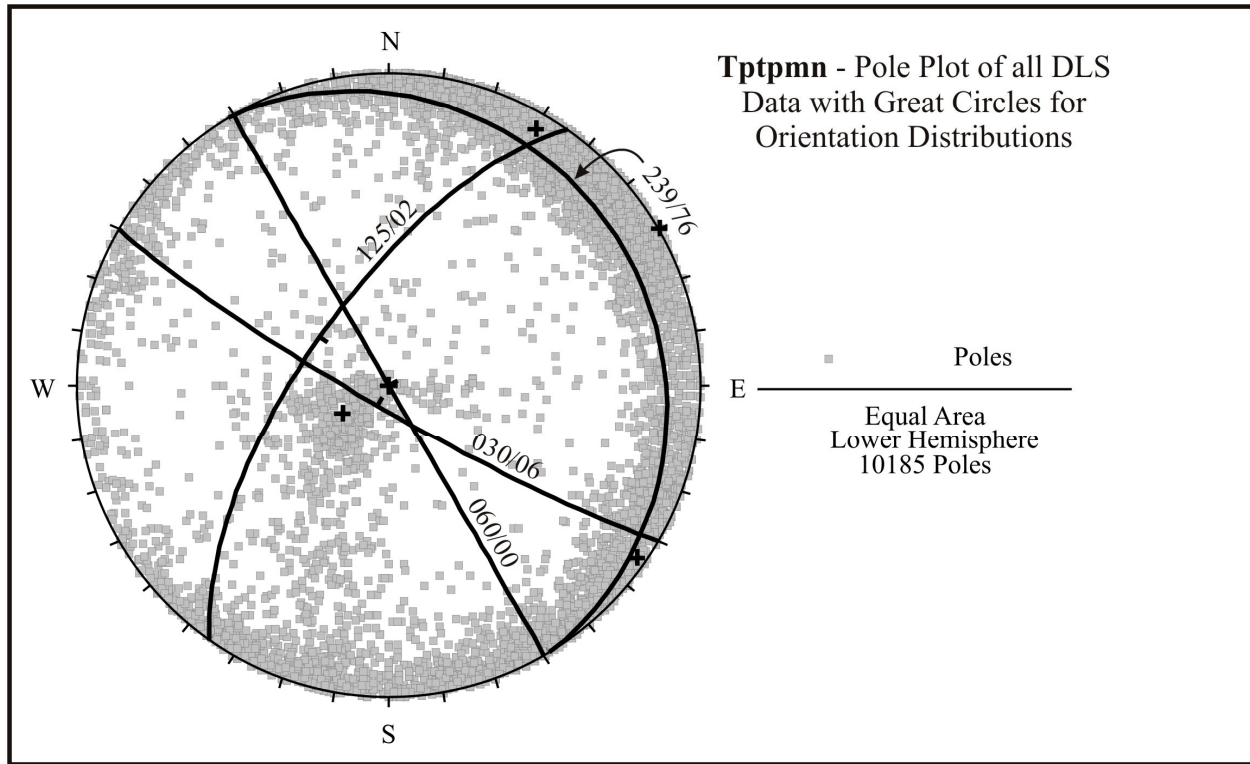


Figure 25. Pole Plot of Tptpmn Detailed Line Survey Data from the ESF Main Loop and ECRB Cross-Drift

Table 6. Comparison of Data from Detailed Line Survey and FracMan for the Tptpmn

Set Number	Orientation (Strike/Dip)	Proportions		Trace Length (m)		Spacing (m)	
		FracMan	DLS	FracMan	DLS	FracMan	DLS
Set 1	120/84	53%	55%	1.8	2.3	0.61	0.55
Set 2	215/88	20%	20%	1.5	1.9	1.61	1.48
Set 3	329/14	8%	7%	2.1	2.7	6.8	4.2
Random	Random	19%	18%	1.4	1.7	N/A	N/A

NOTES: DLS = detailed line survey. See Figure 25 for detailed line survey source DTNs. Strike and dip values were determined graphically using the steronet shown in Figure 25.

The orientation comparison is presented in Figure 28. Pole plots for the detailed line survey and FracMan are compared to ensure that the clusters from the detailed line survey are correctly simulated in FracMan. For the Tptpmn, the means and the spread about the means are adequately represented by the FracMan network. The comparison in Figure 29 confirms that a good conformance exists between the radii distribution from FracMan and the observed trace length distribution.

Project Ttpmnn Task Drift Degradation Date 07/02 Modeler Lung-Fahy  
 Seed #: 0725 Fracmeter Unit: 50 Truncation mode Region View Center 0,0,0  
 Direction \_\_\_\_\_ Scale \_\_\_\_\_ % displayed 100 Orientation = Pole or Dip Pole # frac sides 6

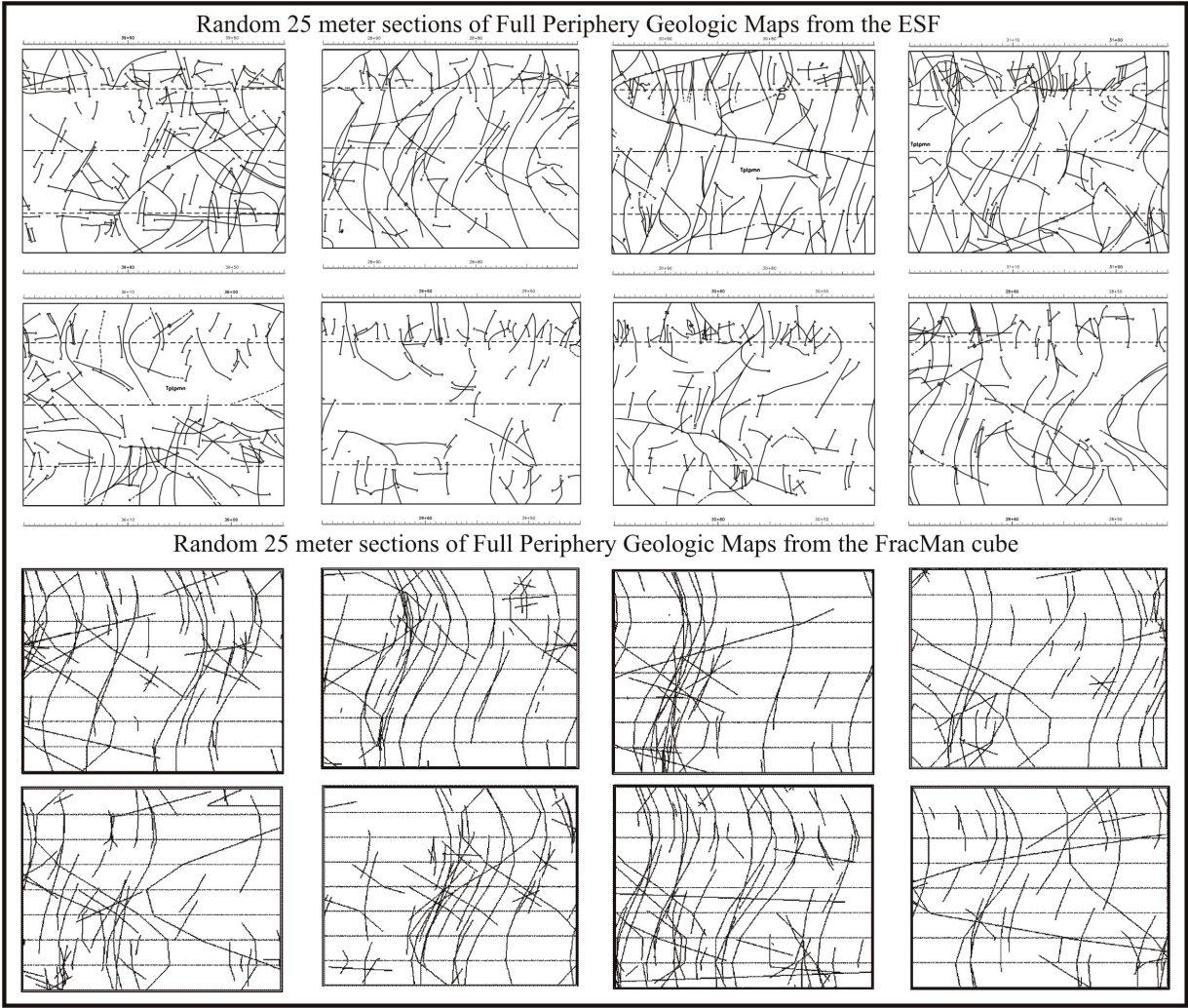
Frac Set	Model Type	Generation Region & Dimension	Orientation TR,PI	Dist. Type	k dispersion	Size eqv. Radius	Dist. type	Mean SD	Max. Min.	Elongation	Aspect Ratio	Termin %	Intensity
1	Baecher	100x100x100	030/06	Fisher	70	1.80	Power (3.1)			NA	NA	10	0.40
2	Baecher	100x100x100	125/02	Fisher	70	1.53	Power (3.1)			NA	NA	5	0.10
3	Baecher	100x100x100	239/76	Fisher	70	2.09	Power (3.1)			NA	NA	0	0.05
RND	Baecher	100x100x100	060/00	Fisher	05	1.35	Power (3.1)			NA	NA	5	0.07

NN factor \_\_\_\_\_ NN export: \_\_\_\_\_ WZ inten: \_\_\_\_\_ WZ parall: \_\_\_\_\_ WZ large: \_\_\_\_\_ WZ close \_\_\_\_\_ Frac Dim (LL,FB)(.5-5.) \_\_\_\_\_  
 Zone Thick \_\_\_\_\_ Fracs \_\_\_\_\_ # iterations \_\_\_\_\_ Frac Dim (POCS) \_\_\_\_\_ Ampl Shaper Fac (POCS) \_\_\_\_\_ Box Frac Dim \_\_\_\_\_ Spherical/Exp \_\_\_\_\_  
 Variogram \_\_\_\_\_ Semivariogram Sill \_\_\_\_\_ Corr Length \_\_\_\_\_

\_\_\_\_\_ .FDT (binary, can't port to non DOS computers, cannot be edited in std word processing)  
 \_\_\_\_\_ .BAB (babylonian ASCII version of FDT, only frac. data stored. Can be ported to non DOC computers. No std word processing.)  
 \_\_\_\_\_ .DCM (Std ASCII version of FDT. Only frac data stored. Can be ported to most computers. Can be edited by std. Word processing. Large files)  
 \_\_\_\_\_ .SAM (ASCII) \_\_\_\_\_ .ORS (ASCII) \_\_\_\_\_ .PCS (ASCII, for conditioned data)  
 \_\_\_\_\_ .F2D (ASCII, frac trace data)

NOTE: See Figure 25 for detailed line survey source DTNs. See Figure 20 for explanation of parameters.

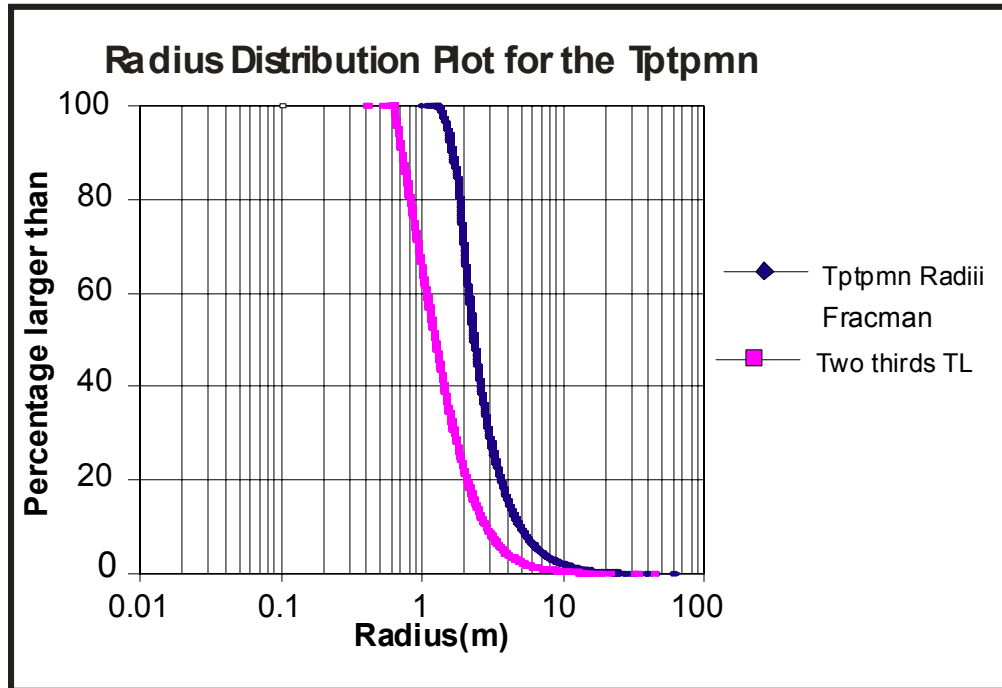
Figure 26. FracMan Input Sheet for the Ttpmnn



DTN: GS990408314224.004, GS000608314224.006  
GS960908314224.015, GS960908314224.016

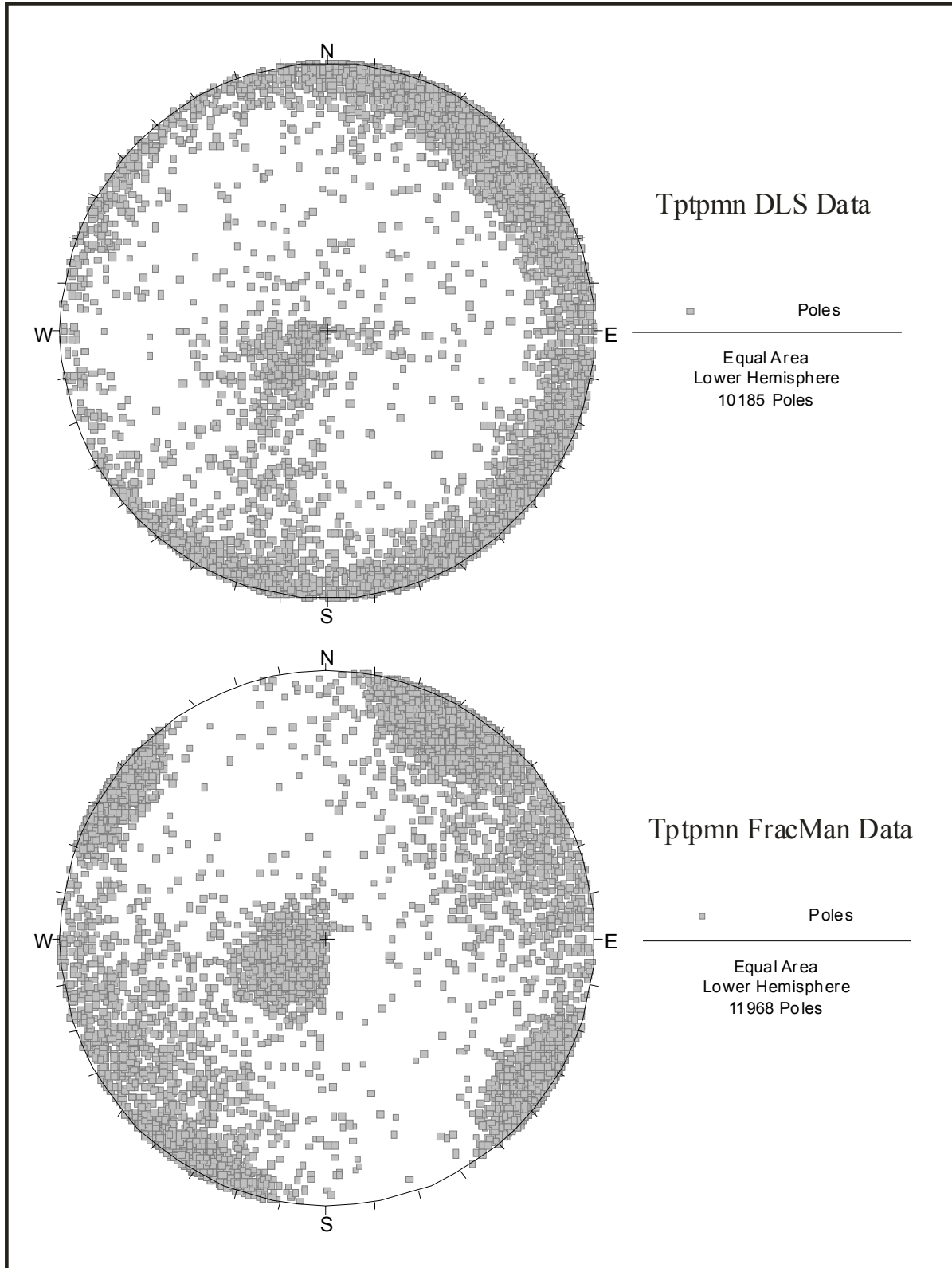
NOTES: The purpose of this figure is to illustrate the geologic structure contained on a full periphery geologic map. The annotated information on this figure is not intended to be legible.

Figure 27. Comparison of Full Periphery Geologic Maps from the Tptpmn in the ECRB Cross-Drift with Simulated Full Periphery Geologic Maps from the FracMan Cube



NOTES: See Figure 25 for detailed line survey source DTNs. This figure compares fracture radii from FracMan to observed trace length data scaled by two-thirds. This is based on the relationship between fracture trace length and radius (see Figure 17). The mean fracture radius should be about two thirds of the mean trace length observed.

Figure 28. Comparison of the Observed Trace Length Distribution (Scaled by Two Thirds) to the FracMan Radii Distribution for Tptpmn



NOTE: See Figure 25 for detailed line survey source DTNs.

Figure 29. Comparison of the Observed Tptpmn Fracture Poles to the FracMan Fracture Poles

## 6.2 THERMAL-MECHANICAL CALCULATION

Coupled thermal-mechanical processes in the rock mass surrounding the geologic repository at Yucca Mountain are examined in this section. This thermal-mechanical calculation investigates the temperature history throughout the preclosure and postclosure periods of the repository, and stress changes,  $\Delta\sigma_{ij}$ , due to temperature change, according to the following relation (Itasca 2002, Manuals/3DEC/Optional Features/Section 1: Thermal Option, Section 1.2.3):

$$\Delta\sigma_{ij} = \delta_{ij} 3K\alpha\Delta T \quad (\text{Eq. 6})$$

where  $\delta_{ij}$  is the Kronecker  $\delta$  (unit matrix),  $\alpha$  is the coefficient of thermal expansion ( $^{\circ}\text{C}^{-1}$ ),  $K$  is the bulk modulus (Pa), and  $\Delta T$  is the change in temperature ( $^{\circ}\text{C}$ ). The coupled thermal-mechanical calculation was conducted by two sets of calculations: the drift-scale (described in this section) and the coupled regional- and drift-scale calculations (described in Attachment III).

The drift-scale thermal-mechanical calculation consists of the temperature history (thermal) calculation and the thermal stress (mechanical) calculation. The thermal part of the drift-scale calculation was performed by the NUFT thermohydrology software simulating two-dimensional drift-scale thermal-hydrologic behavior. The temperature history results from the NUFT code were imported to the UDEC discrete-element software and the FLAC finite-difference software in order to calculate the thermal stress around the emplacement drift. UDEC and 3DEC (the three-dimensional equivalent of UDEC) were used to model the effects of the thermal stress and to conduct a rockfall analysis associated with the previous thermal stress calculation. Details of the thermal stress calculation and the rockfall analysis for nonlithophysal and lithophysal units are presented in Sections 6.3.1.3 and 6.4.1.2, respectively.

The drift-scale calculations (both thermal and mechanical) consider an infinite extent (perpendicular and in the direction of the drifts) of the repository; consequently, they are two-dimensional (a single drift included in the calculation), with a symmetry boundary condition on a plane halfway between the emplacement drifts. The coupled regional- and drift-scale thermal-mechanical calculation (Attachment III) was planned and conducted to support this drift-scale calculation by assessing repository-scale effects, including edge effects and the effects of finite repository size and depth on predicted temperatures and stresses. These calculations are three-dimensional, and analysis was carried out in two steps. First, the regional-scale thermal-mechanical calculation was used to determine temperature and stress changes on the scale of the entire mountain. In the next step, the drift-scale thermal-mechanical analysis was performed such that boundary conditions for temperature and stress fields (functions of time) were determined from the regional-scale calculation. Thus, this calculation did not use any simplifying assumptions (e.g., infinite extent of the repository) for the boundary conditions. Both components of the regional- and drift-scale thermal-mechanical calculations were performed using FLAC3D. Because the goal of the calculation was to support the drift-scale calculation, details of the calculation and results are presented in Attachment III. A comparison of temperatures and stresses as calculated by the drift-scale and the coupled regional- and drift-scale calculations is presented at the end of this section.

The thermal part of drift-scale calculation applies a two-dimensional LDTH sub-model, which is described in *Multiscale Thermohydrologic Model* (BSC 2001c). A non-backfilled and mean

infiltration version of the sub-model was extracted from the data submittals in DTN: LL000509112312.003. The LDTH sub-model, which was selected from the 31 LDTH sub-models in *Multiscale Thermohydrologic Model* (BSC 2001c), is L2C3 (coordinates: E170731, N234973). The L2C3 LDTH sub-model is used to compute temperature-history of the emplacement drift and surrounding areas throughout the preclosure and postclosure periods.

The L2C3 LDTH sub-model location selected has the following characteristics of interest (further details of the model can be found in *Multiscale Thermohydrologic Model* (BSC 2001c):

- Approximately the geometric center of the license application reference repository layout (BSC 2003b).
- The repository horizon is located approximately 281 m below the ground surface and 327 m above the water table. This elevation puts the repository horizon at approximately 1057 meters above sea level (DTN: LL000509112312.003).
- The repository horizon is located in the Tptpl with approximately 34 m of Tptpl above the repository horizon and 68 m of Tptpl below the repository horizon (DTN: LL000509112312.003).
- The mean infiltration conditions have surface infiltration rates of 12.0 mm/year during the first 600 years of emplacement (present day climate), 40.8 mm/year from 600 years to 2000 years (monsoonal climate), and 63.2 mm/year from 2000 years on (glacial transition climate) (DTN: LL000509112312.003).
- The ground surface temperature is fixed at 16.9°C, and the water table temperature is fixed at 29.2°C (DTN: LL000509112312.003).

In addition to the LDTH sub-model, updated thermal and hydrologic properties were used for the repository and non-repository rock units. The thermal and hydrologic properties are presented in Section 4.1.6 and 4.1.8, respectively. Details of the data preparation for input files of the LDTH sub-model are described in *Multiscale Thermohydrologic Model* (BSC 2001c).

Three major cases of the drift-scale thermal calculation were carried out, including:

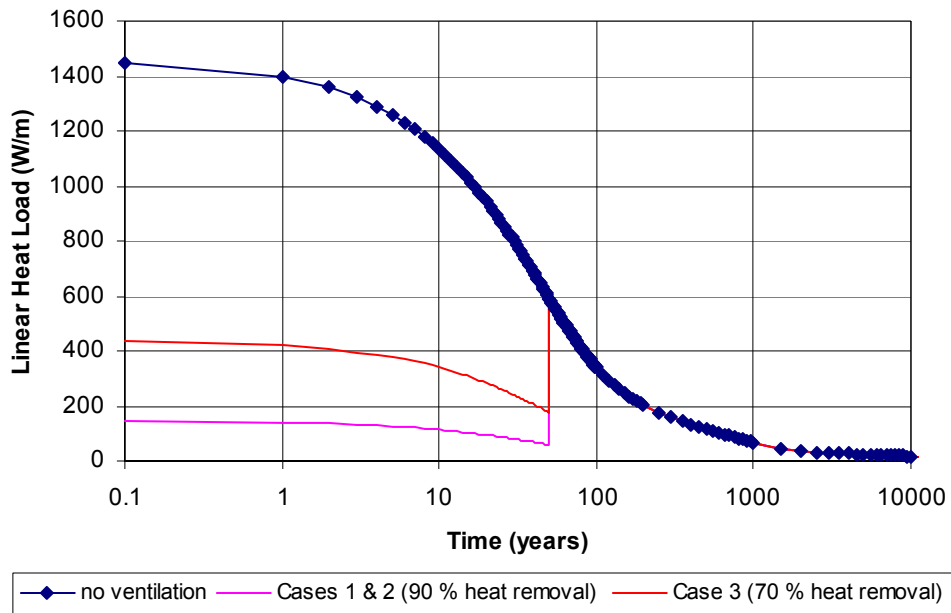
- Case 1: Base-case calculation with 1.45 kW/m initial heat load and 50 years preclosure ventilation (90 percent heat removal ratio, Section 5.1).

- Case 2: Sensitivity calculation for thermal properties of repository rock material (Tptpl) with 1.45 kW/m initial heat load, 50 years preclosure ventilation, and 90 percent heat removal ratio. Values of thermal conductivity and specific heat one standard deviation less than the mean values were used:
  - Thermal Conductivity (SN0208T0503102.007): 1.64 W/m-K (= 1.89 W/m-K – one standard deviation [0.25 W/m-K]) for wet conditions and 1.03 W/m-K (= 1.28 W/m-K – one standard deviation [0.25 W/m-K]) for dry conditions.
  - Heat Capacity: 811 J/kg-K (= 954 J/kg-K – one standard deviation [143 J/kg-K]).
- Case 3: Sensitivity calculation for heat removal ratio. 70 percent heat removal ratio was used for the preclosure ventilation (Section 5.1).

The heat capacity data used in all the three cases were preliminary data superseded by DTN: SN0303T0510902.002 (Table V-16). Therefore, an impact analyses was conducted regarding the preliminary data and presented in Attachment XVII. Heat capacity values for the range of  $T \leq 95^{\circ}\text{C}$  were utilized for the NUFT calculations (Table V-16). Since consideration of latent heat effects above the boiling point is built into the NUFT code, the high heat capacity value at the temperature range of 95 to  $114^{\circ}\text{C}$  (Table V-16) were not used in the NUFT thermal calculations.

Decay curves of the linear heat load used in all the calculation cases are presented in Figure 30. The original linear heat decay curve (no ventilation) was obtained from *Repository Design, Repository/PA IED Subsurface Facilities* (BSC 2003d). 90 percent of the constant ventilation heat removal ratio (Section 5.1) was applied for Cases 1 and 2, while 70 percent of constant heat removal ratio (Section 5.1) was used in Case 3.

Temperature histories at the drift crown for all the cases of the drift-scale thermal calculations are presented in Figure 31. The results exhibited the temperature increase from base case (Case 1) to sensitivity calculations (Cases 2 and 3). In particular, Case 3 showed a significant temperature increase at the preclosure period. The peak temperate for Case 1 was  $138^{\circ}\text{C}$  at around 75 years, while Cases 2 and 3 were  $161^{\circ}\text{C}$  and  $153^{\circ}\text{C}$  at around 75 years, respectively.



NOTES: The no ventilation curve is from BSC 2003d. Cases 1 and 2 use the 90 percent heat removal curve while Case 3 uses the 70 percent heat removal curve.

Figure 30. Heat Decay Curves for Thermal Calculations

**Temperature-History at Drift Crown**  
**1.45 kW/m linear heat load, 50 years pre-closure ventilation**

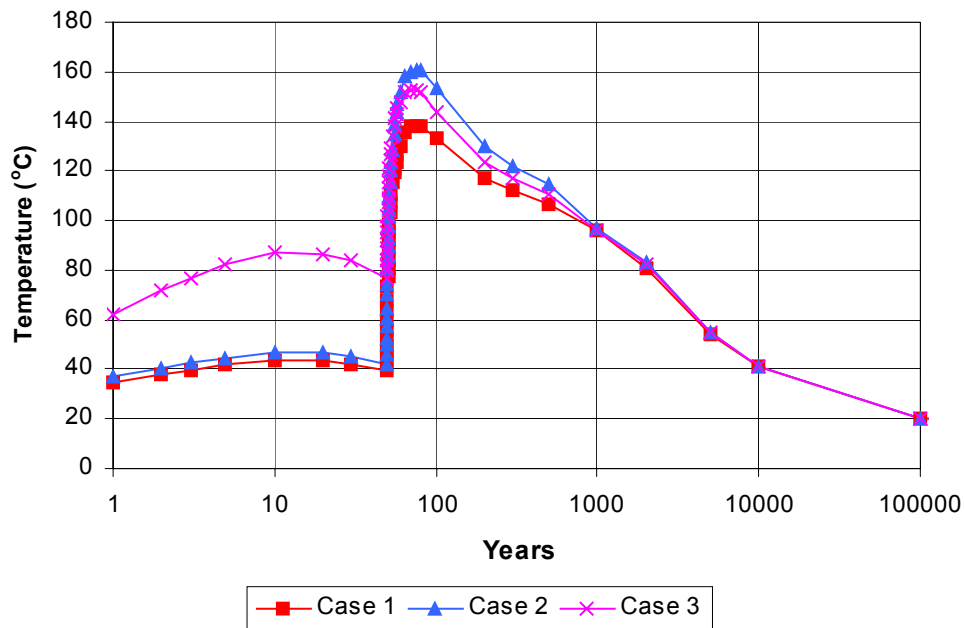


Figure 31. Temperature History at the Drift Crown Due to the Linear Heat Load Presented in Figure 30

A comparison of temperature histories in the drift crown for Case 1, as determined in the drift-scale calculation (NUFT) and the coupled regional- and drift-scale calculations (FLAC3D) for the conditions in the middle of the repository, is shown in Figure 32. The agreement between histories is quite good. With the exception of the state at 10,000 years after waste emplacement, the temperature differences between the two calculations are less than 10°C.

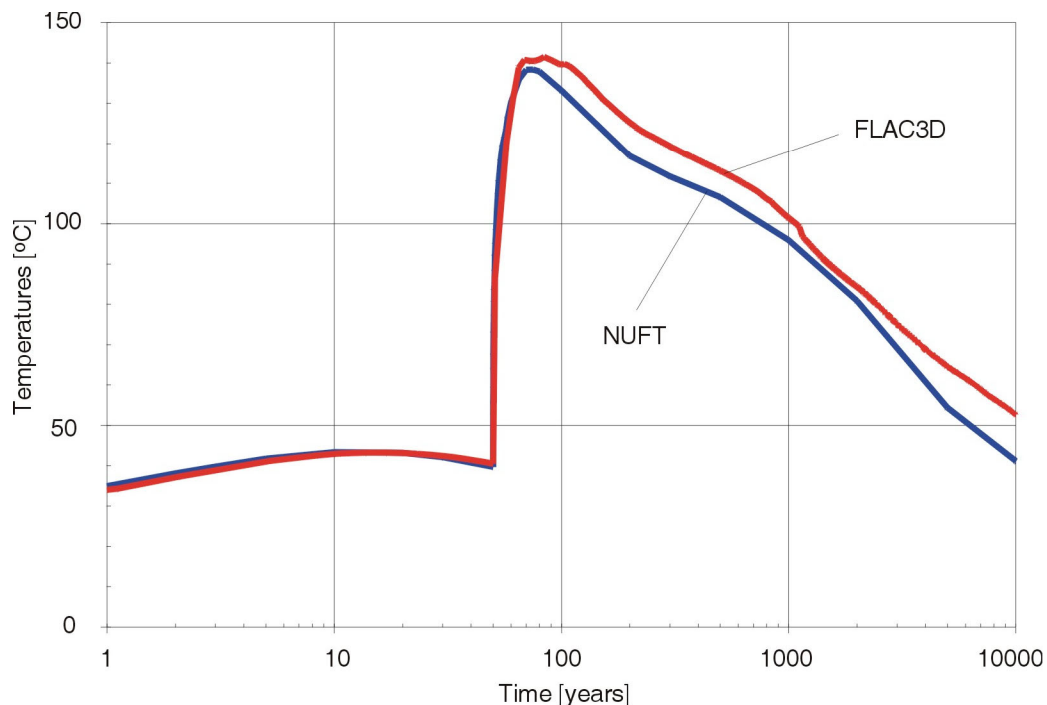


Figure 32. Comparison of Temperature Histories at Tunnel Crown for Case 1 Calculated Using NUFT and FLAC3D

Stresses in the drift wall and crown for conditions in the middle of the repository, as predicted by two calculations [drift-scale (FLAC) and coupled regional- and drift-scale (FLAC3D)], are shown for 10 years, 100 years, and 1000 years after waste emplacement in Figures 33, 34, and 35, respectively. FLAC results are presented from the calculation for lithophysal rock mass category 4 (discussed in Section 6.4), which has the same Young's modulus as the value used in the coupled regional- and drift-scale calculation. Agreement of the tangential stresses in the crown is excellent at all three times presented. As expected, the two-dimensional calculation (FLAC) predicts a slightly higher tangential stress in the crown after 1000 years of heating. The most significant difference between the two calculations is the vertical stress after 100 and 1000 years. The coupled regional- and drift-scale calculations (FLAC3D) show an increase in the vertical stress (in the wall after 100 years and 1000 years, but also throughout the repository horizon after 1000 years) because of the effect of the finite repository size and elastic restoring stresses caused by the heat-induced deformation. This effect could not be accounted for in the drift-scale calculation in which the average vertical stress is determined by the weight of the overburden. The drift scale calculation stress predictions are justified for use in the analysis of drift degradation, because the increase in the vertical stress in the wall (not accounted for in the two-dimensional calculation) is not significant.

Drift Degradation Analysis

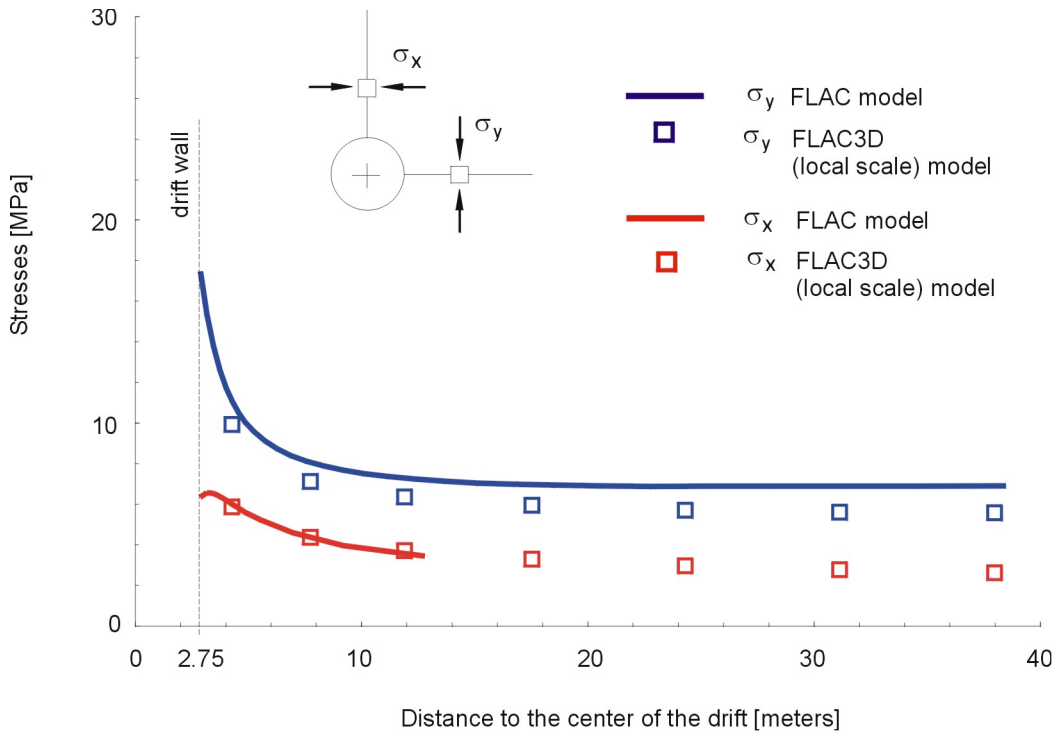


Figure 33. Comparison of Stresses Around the Drift Between the FLAC and FLAC3D Predictions After 10 Years of Heating

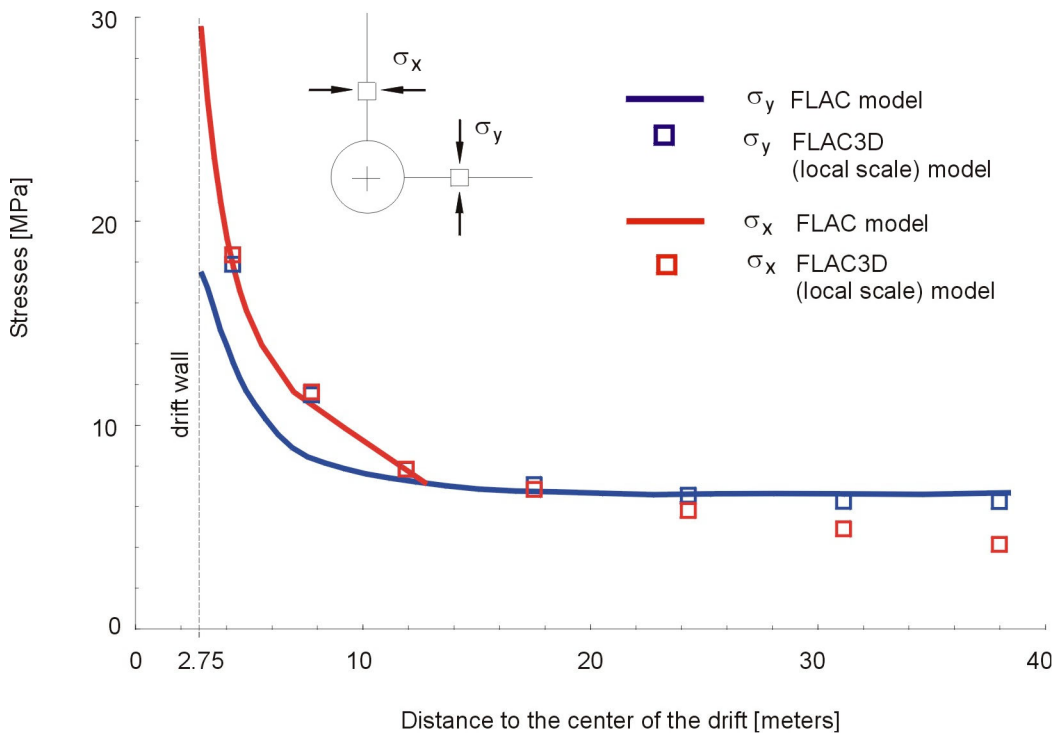


Figure 34. Comparison of Stresses Around the Drift Between the FLAC and FLAC3D Predictions After 100 Years of Heating

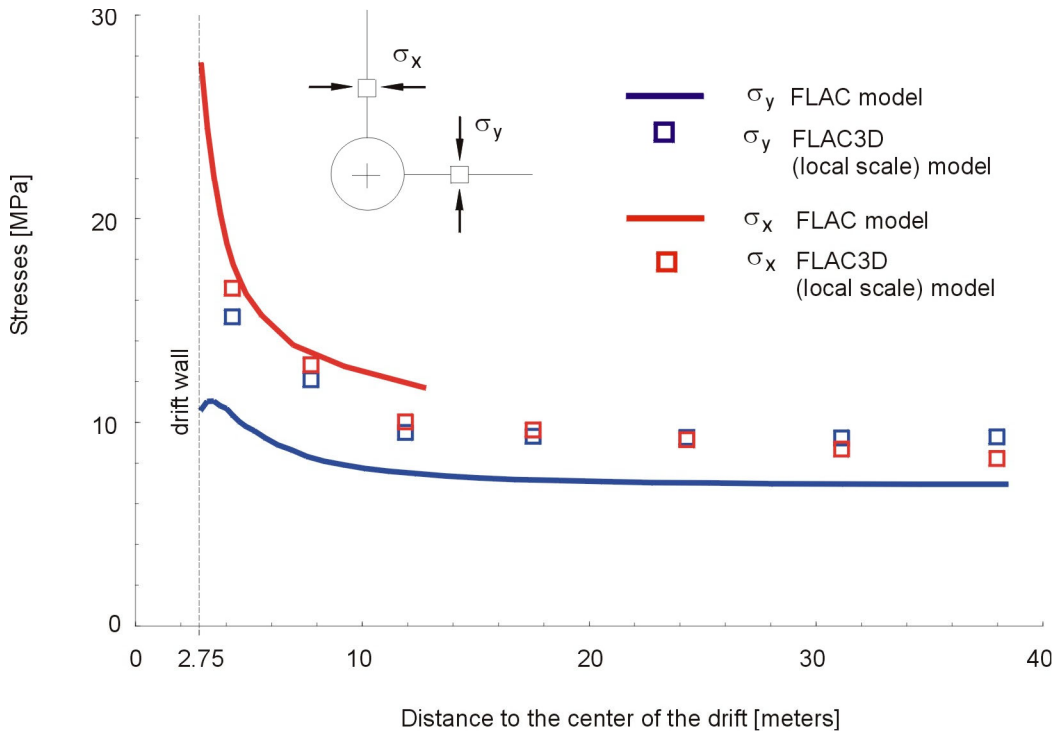


Figure 35. Comparison of Stresses Around the Drift Between the FLAC and FLAC3D Predictions After 1000 Years of Heating

The drift stability analysis presented in this report was carried out for temperature and stress conditions in the middle of the repository. However, the temperatures and stresses for the conditions at the edge of the repository are investigated using the coupled regional- and drift-scale (FLAC3D) calculations (the actual location considered and other details are described in Attachment III). The temperature history from the coupled calculations for the edge of the repository compared with the NUFT results for the center of the repository are shown in Figure 36. As expected, the temperatures at the edge of the repository will be smaller than temperatures in the middle of the repository.

The stress profiles around the emplacement drift located at the edge of the repository, 10, 100, and 1000 years after waste emplacement are shown in Figures 37 through 39. Stresses at the edge of the repository are, in general, smaller than in the middle of the repository. Smaller vertical stress at the repository edge is due to smaller overburden. However, the most significant difference between stress conditions at the edge and in the middle is in the horizontal stress 1000 years after waste emplacement. The horizontal stress is approximately 5 MPa smaller at the edge compared to the middle of the repository (Figure 38). After a heating time when the drifts start to thermally interact with each other, conditions of almost complete confinement (idealized in two-dimensional models by symmetry conditions on the plane half-way between the drifts) exist in the middle of the repository, leading to increased horizontal stresses. The confinement and temperatures at the edge are smaller (than in the middle of the repository) resulting in smaller horizontal stresses. It appears from these results that limiting the drift degradation analysis to thermally induced stresses in the middle of the repository is justified.

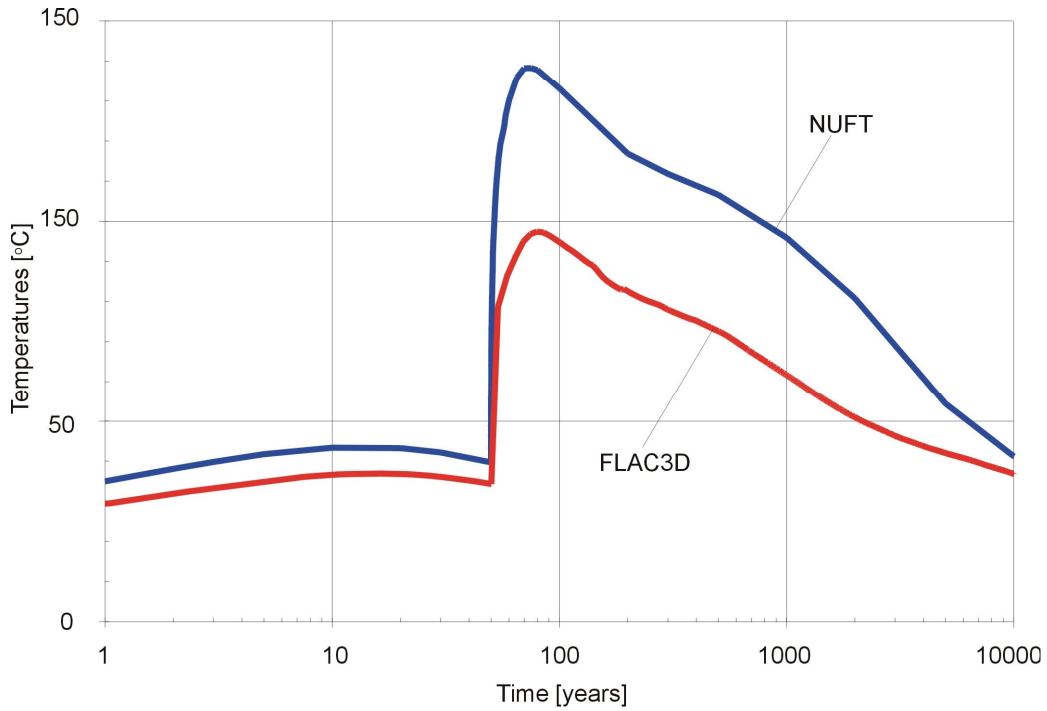


Figure 36. Comparison of Temperature Histories at Tunnel Crown for Case 1 Calculated Using NUFT and FLAC3D (for the Edge of the Repository)

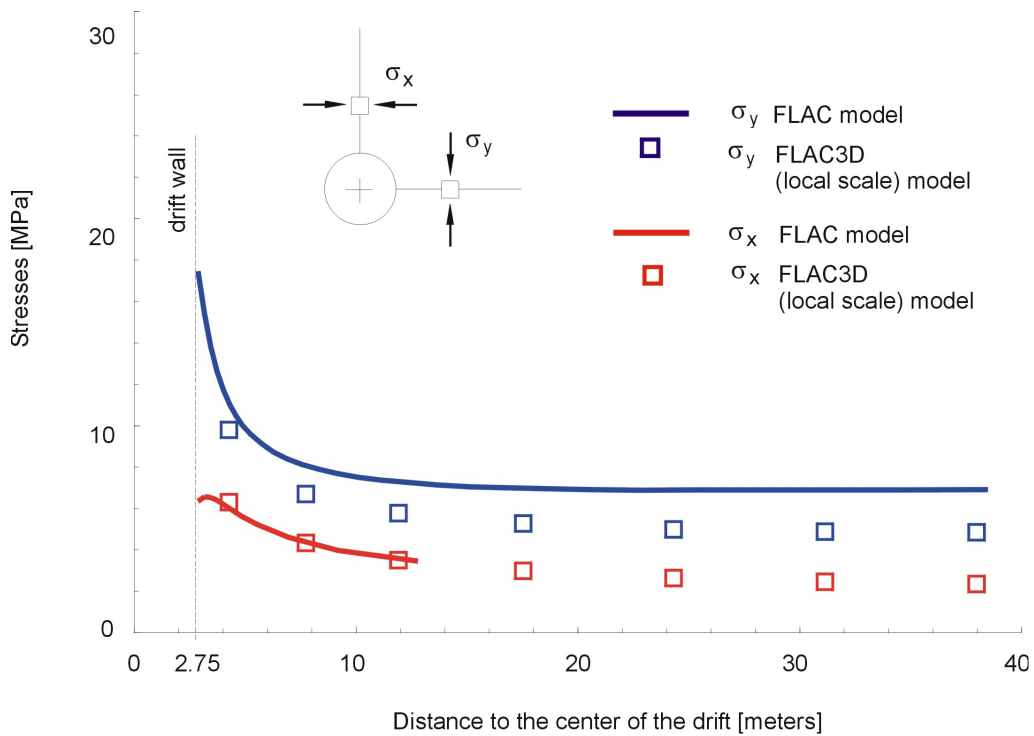


Figure 37. Comparison of Stresses Around the Drift Between the FLAC and FLAC3D Calculations for Edge of the Repository After 10 Years of Heating

Drift Degradation Analysis

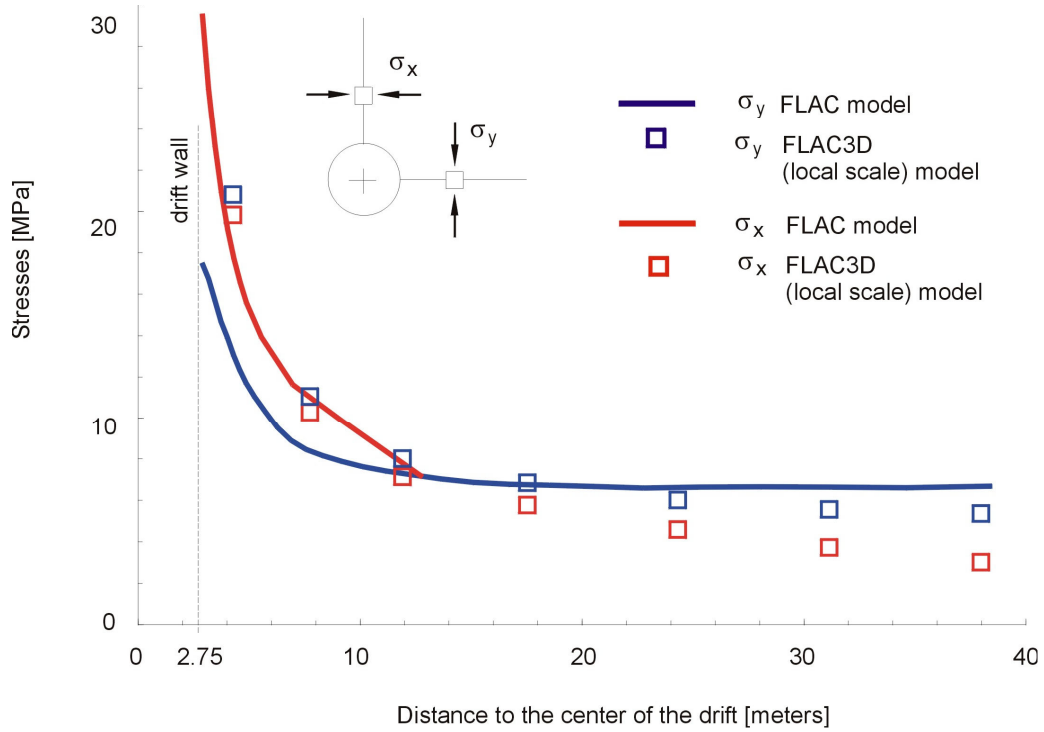


Figure 38. Comparison of Stresses Around the Drift Between the FLAC and FLAC3D Calculations for Edge of the Repository After 100 Years of Heating

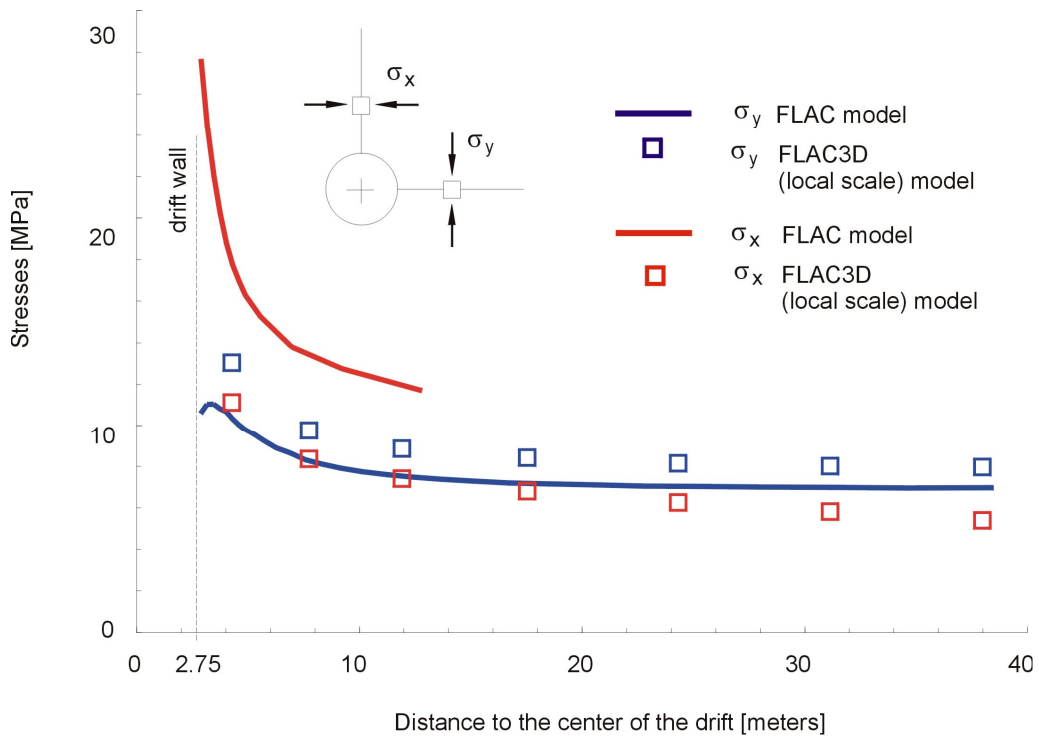


Figure 39. Comparison of Stresses Around the Drift Between the FLAC and FLAC3D Calculations for Edge of the Repository After 1000 Years of Heating

### **6.3 ROCKFALL IN THE NONLITHOPHYSAL UNITS**

The assessment of rockfall in the nonlithophysal units is mainly based on a three-dimensional discontinuum analysis (3DEC analysis). This analysis is adequate for the wedge-type failure in a jointed rock mass, which has been validated in Section 7.8.3. A description of this set of analyses and a presentation of the results are provided in Section 6.3.1. An intensely fractured zone was observed in the ESF main loop between Stations 42+00 and 51+50 (Albin et al. 1997, p. 58). A 3DEC analysis is not suited for such highly fractured rock. Therefore, a three-dimensional continuum analysis with a ubiquitous joint model (FLAC3D analysis) was adopted to account for the effect of the highly fractured and anisotropic behavior of the rock mass in this limited zone as described in Section 6.3.2. The aforementioned analyses consider only fractures with trace lengths greater than 1 m. The impact of small-scale fractures (less than 1-m trace length) for block forming is assessed using the key-block code DRKBA. A comparison of the results for including and excluding the small-scale fractures is provided in Section 6.3.3. The drift profile predictions considering wedge-type failure are provided in Section 6.3.4.

It should be noted that in previous versions of this document (Revisions 0 and 1), rockfall in the nonlithophysal units was based on a Discrete Region Key Block Analysis (DRKBA). In this report, DRKBA analyses primarily provide a confirmatory role in the assessment of drift degradation. DRKBA analyses are documented in Attachment IV.

#### **6.3.1 Three-Dimensional Discontinuum Analysis of Jointed Rock Mass for Wedge-Type Rockfall**

The three-dimensional discontinuum analysis is used for simulation of the mechanical behavior of the jointed rock mass in the nonlithophysal units for loading conditions with which stability response will be controlled by the fractures. The program 3DEC was selected for its capability of simulating jointed rock mass under both thermal and seismic loadings. The jointed rock mass is represented as a number of intact rock blocks that are separated by interface planes whose mechanical behavior is represented by a standard Coulomb slip criterion. The intact blocks are subdivided into tetrahedral finite difference zones and can be assigned suitable mechanical constitutive law (Itasca 2002). Due to the high intact rock strength in the nonlithophysal units, rock blocks are considered to behave elastically.

It is important in the 3DEC analysis to include field fracture geometric data for modeling the nonlithophysal units. Since the fractures within the Tptpmn are non-persistent in nature (with mean trace lengths in the range of 1-m to 2-m, which is smaller than the diameter of the tunnel), many fractures are of insufficient length to form a regular block. The fracture geometries used as input to 3DEC are derived from the FracMan simulations as discussed in Section 6.1.6. Modifications to the 3DEC program have been made to accommodate the FracMan output; namely, the discontinuous nature of the fractures. In the earlier versions of 3DEC fractures are modeled as continuous in nature and thus it was impossible to have a fracture that ends in solid rock. The program now includes the capability of various sets of property assignment logic within a contact; therefore, the finite trace length fractures from FracMan can be modeled by bonding all fracture contact points outside the fracture surface. In this manner, it is possible for the contacts to be given the equivalent properties of the solid rock (allow shear in the fracture plane) or to simply join the adjacent blocks to form a discontinuous fracture.

Other enhancements added to 3DEC for rockfall modeling include: (1) implement free field boundary as the quiet boundary for dynamic analysis with superposition of the P and S wave motions, and (2) partial density scaling for dynamic analysis. Descriptions for these enhancements are provided in Attachment VIII.

The coordinate systems adopted in FracMan and 3DEC are different; therefore, a conversion of the outputs from FracMan to inputs in 3DEC is provided in Attachment XII. To account for the stochastic nature of the jointed medium, a total of 76 fracture geometries were selected by generating random tunnel centroid locations within the 100-m-cube simulated FracMan rock mass. A representative tunnel volume, approximately two tunnel diameters around the tunnel centroid and 25 m in length, is created at each of these locations to contain fractures generated in FracMan. This volume is considered sufficient to contain the limits of damaged rock, and of sufficient length (approximately 5 times the tunnel diameter and over 10 times the mean trace lengths) to provide a representative volume of rockfall (see Figure 40 for 3DEC model region).

The combination of computer runs considering fracture geometry, seismic ground motion, material properties variation, and thermal loading scenario are immense. In order to complete the task in a timely fashion, several techniques were used to speed up the calculation. These techniques are described in Attachment VIII.

### 6.3.1.1 3DEC Model Set Up

Figure 40 shows the base-case 3DEC model geometry with fracture modeling region #36. The model is slightly larger than a 25-m  $\times$  25-m  $\times$  25-m cube with the tunnel oriented at 75° azimuth. The region with detailed fractures imported from FracMan is one diameter at the side of the tunnel and two diameters on top of the tunnel. Three cross-section views are included in Figure 40 to illustrate the fractures and blocks around the excavation. Rock mass that does not form blocks is shown with green color, while distinct blocks are identified as areas with different colors. Some of the fractures shown in the cross-section views are artificial which were generated during the block cutting process or to facilitate mesh generation. The dimension of the model is selected to optimize the time required for analysis and the ability of the model to predict rockfall accurately. Sensitivity of the model dimension to the outcome of rockfall prediction is provided in Section 6.3.1.6. The drip shield is represented as a stiff block fixed to the invert of the drift. The drip shield block is placed to collect information on the locations and relative velocities of the rockfall impact.

Input properties for the distinct block 3DEC model involve both the fracture and block (intact) properties. Table 7 lists the base-case properties used in 3DEC. A linear elastic model is used for the block material, whereas Coulomb slip criterion is used to present joint mechanical behavior. A linear elastic model is used as the intact block constitutive model for the 3DEC analysis. This approach is used to obtain a conservative (i.e., increased) estimate of the block volume. Breaking and spalling of the rock inside the blocks are expected considering the large amplitude of seismic waves for postclosure ground motions. This mechanism is addressed in Section 6.3.1.6 with a two-dimensional discontinuum model representing the rock mass (UDEC analysis). Although the low dipping vapor-phase parting consists of higher cohesive material, a single set of joint mechanical properties are used for all joints for conservatism (i.e., more rockfall will be produced). Coulomb slip criterion is also used for the intact bridges between

adjacent fractures, as the intact cohesion and friction is assigned for the bridge strength. Sensitivity analyses of the joint strength properties, dilation angle, and joint stiffness were conducted to evaluate their impact to rockfall, the range of properties and their impacts to the analysis results are presented in Section 6.3.1.6.

The initial state of stress was included at the model consolidation stage. Based on the in situ stress measurement using the hydraulic fracturing technique (DTN: SNF37100195002.001), the vertical component of in situ stress is the major principal stress. The direction of the intermediate principal stress is N15°E with a ratio to major principal stress of 0.617, whereas the direction of the minor principal stress is N105°E with a ratio to major principal stress of 0.361. The vertical component of in situ stress (the major principal stress) is approximated as 7 MPa and the horizontal components (the minor and intermediate principal stresses) are simplified to be 3.5 MPa. The in situ stress for each emplacement drift will vary depending on the cover depth on top of the drift. The approximated values assigned for the in situ stress are adequate and insensitive to the results judging the magnitude of the induced seismic and thermal stress.

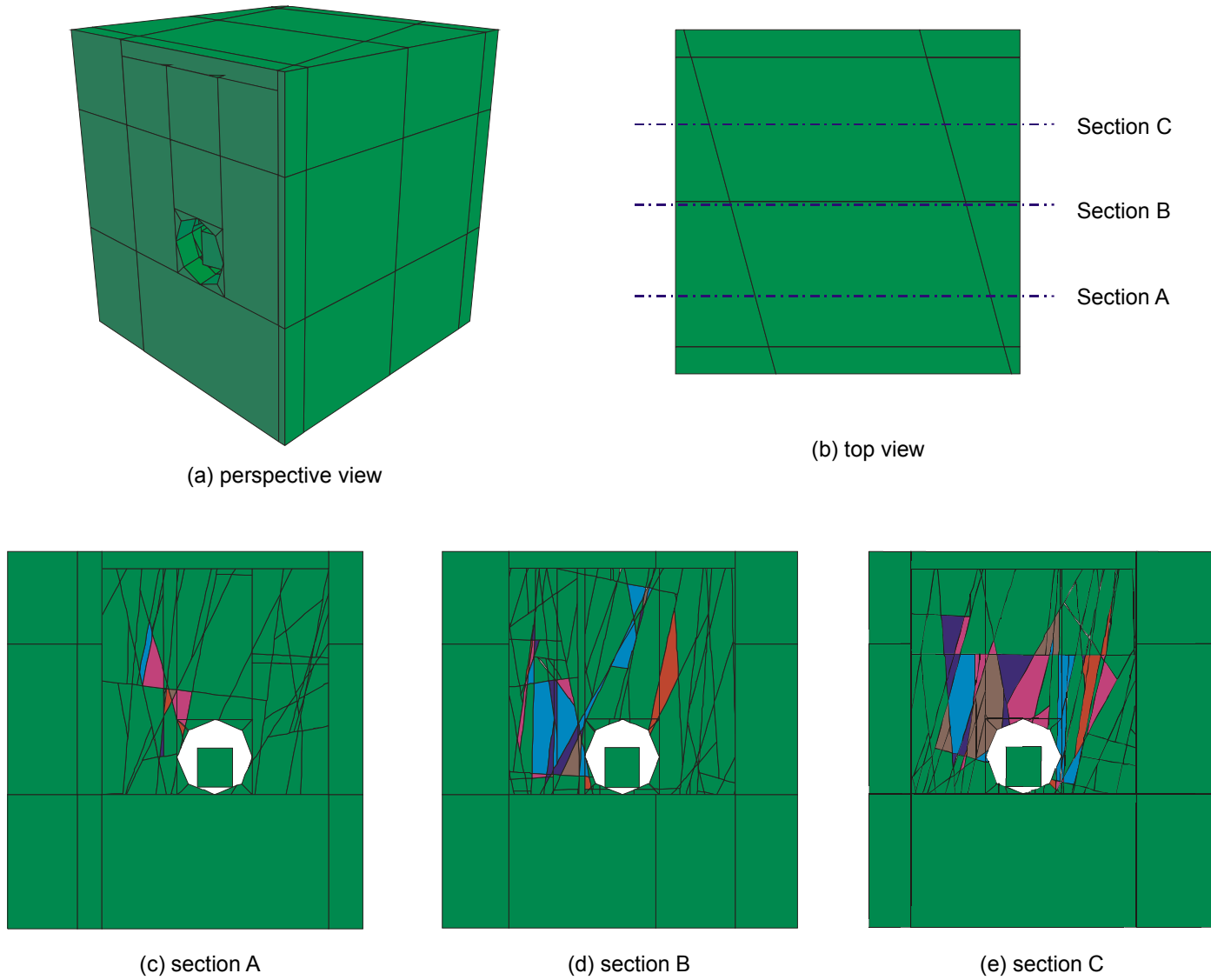


Figure 40. 3DEC Model Geometry and Cross-Sections

Table 7. Base-Case Material Properties for 3DEC Analysis

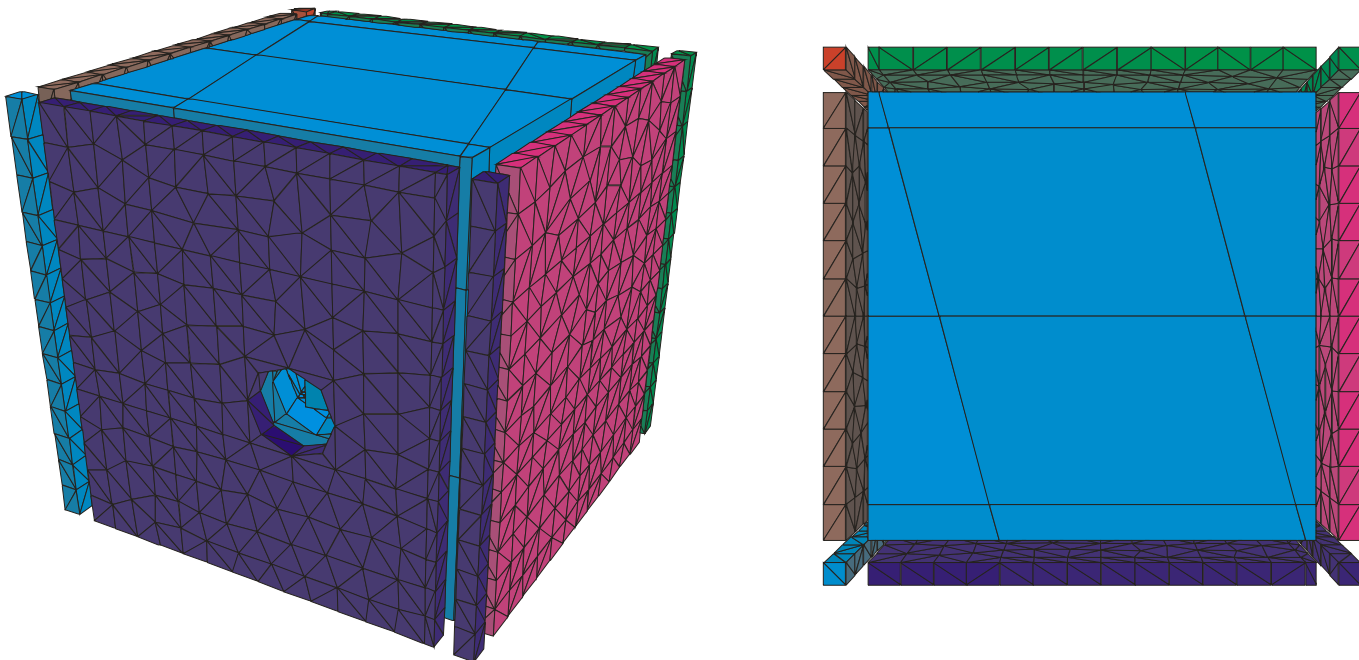
Joint strength properties	Joint cohesion (MPa)	0.1
	Joint friction (deg)	41
	Joint dilation (deg)	0
	Joint normal stiffness, $K_n$ (MPa/m)	5.0E+04
	Joint shear stiffness, $K_s$ (MPa/m)	5.0E+04
Intact rock deformation properties	Young's Modulus (GPa)	33.03
	Poisson's ratio	0.21
	Bulk modulus (GPa)	19.2
	Shear modulus (GPa)	13.6
Intact bridge strength properties	Cohesion (MPa)	47.2
	Friction angle (deg)	42
	Tensile strength (MPa)	11.56

NOTES: Values of cohesion and friction angle were derived from preliminary data with a slight deviation from the reported values in Attachment V (Section V.3). An impact analysis was conducted with no difference in the results for rockfall prediction as described in Attachment XVII. Joint dilation (Attachment V, Table V-3) is set to zero for the base-case analysis. With no dilation, joints are modeled as perfectly planar and smooth, resulting in a conservative (i.e., higher) estimation of rockfall.

The boundary conditions for various stages of the analysis are presented in Table 8. At the initial consolidation stage and the later thermal loading period, fixed velocity boundaries were used to ensure boundary effect does not affect the stress distribution around the opening. For the seismic analysis, non-reflecting boundary is used for both the top and bottom of the model, whereas free-field boundary is imposed at the perimeter of the model as shown in Figure 41. The free-field boundaries ensure that plane waves propagating upward suffer no distortion at the boundary. A description of the free-field boundary is provided in Attachment VIII. Dynamic loading was applied at the bottom of the model as a prescribed stress boundary, and propagated vertically upwards. The conversion of the ground motion velocity to input seismic stress is discussed in Section 6.4.1.1 (Equation 7).

Table 8. Boundary Conditions for 3DEC Analysis

Boundary	Initial Consolidation and Excavation Stage	Thermal Analysis Stage	Dynamic Analysis Stage
Lateral	Fixed at the direction normal to the face	Fixed at the direction normal to the face	Free-Field boundary
Bottom	Fixed at the vertical direction	Fixed at the vertical direction	Non-reflecting boundary
Top	Fixed at the vertical direction	Fixed at the vertical direction	Non-reflecting boundary



(a) Free-field Boundaries  
(perspective view)

(b) Free-field Boundaries  
(top view)

Figure 41. Illustration of Free-Field Boundaries in 3DEC Model

### 6.3.1.2 Seismic Consideration in Nonlithophysal Units

#### 6.3.1.2.1 Site Specific Ground Motions

Site-specific ground motions for three levels of annual probability of exceedance,  $5 \times 10^{-4}$ ,  $1 \times 10^{-6}$ , and  $1 \times 10^{-7}$ , are included in this study. The  $5 \times 10^{-4}$  ground motions are for preclosure consideration, while the  $1 \times 10^{-6}$  and  $1 \times 10^{-7}$  ground motions are for postclosure. The  $5 \times 10^{-4}$  preclosure level is provided for comparison to the postclosure levels. The  $5 \times 10^{-4}$  preclosure ground motions are not representative of all preclosure ground motions (see Section 1.4). For higher-frequency spectral accelerations (5 to 10 Hz) and an annual exceedance probability of  $5 \times 10^{-4}$ , results of the probabilistic seismic hazard analysis for Yucca Mountain indicate the ground motion hazard derives primarily from earthquakes in the magnitude range of 5.0 to 6.5 occurring at distances less than 15 km from the site. For lower-frequency spectral accelerations (1 to 2 Hz) at the same annual exceedance probability, the hazard shows, in addition to nearby sources, a significant contribution from earthquakes in the magnitude range of 7.0 to 8.0 occurring at an epicentral distance of about 50 km. For annual exceedance probabilities of  $1 \times 10^{-6}$  and  $1 \times 10^{-7}$ , nearby earthquakes in the magnitude range 5.5 to 7.0 are the dominant sources contributing to ground motion hazard at both higher and lower spectral accelerations.

A total of 15 sets of Point B ground motions (i.e., ground motions developed at repository horizon) were selected for each annual postclosure hazard level. The multiple sets ensure a reasonable distribution of spectral shapes and time history durations. For each set of ground motions, two horizontal components (H1 and H2) and one vertical component (V) of acceleration, velocity, and displacement are supplied. Figure 42 shows the H1 velocity time history for all three annual hazard levels. Only one ground motion was provided for the preclosure hazard level because of the deterministic-based approach for preclosure consideration. The amplitude of the peak ground acceleration, velocity, and displacement, and the seismic induced far field stress for one of the ground motion sets from each hazard level are provided in Table 9. This table is used to demonstrate the typical ground motion parameters for the three hazard levels considered. It is apparent that the preclosure ground motions have lower amplitude vibrations and hence lower induced stresses comparing with the postclosure ground motions. The peak values for each ground motion set provided for postclosure hazard level varies. For example, the peak ground velocity in the vertical component for  $1 \times 10^{-7}$  hazard level ground motion set #3 reaches 1634 cm/sec with an induced seismic stress of 155 MPa. The complete data sets of the ground motion are contained in the source DTNs listed in Table 2 (Section 4.1).

Arias Intensity (an estimate of energy delivered to structures) for each set of ground motions is listed in Table 10. A large variation of energy within the same hazard level is observed. All 15 sets of ground motions were combined with fracture patterns for probabilistic analysis. The combining of ground motion and fracture patterns is described in Section 6.3.1.2.2.

Table 9. Peak Ground Motion Parameters

Annual Hazard Level	Ground Motion Component	Peak Acceleration (g)	Peak Velocity (cm/sec)	Peak Displacement (cm)	Seismic Induced Stress Corresponding to Peak Velocity (MPa)
$5 \times 10^{-4}$	H1	0.19	19.00	12.86	1.09
	H2	0.18	17.72	12.37	1.02
	V	0.16	12.37	7.83	1.17
$1 \times 10^{-6}$ Ground Motion Set 1	H1	6.86	243.74	28.19	13.96
	H2	7.31	243.35	17.44	13.94
	V	10.46	229.79	14.26	21.79
$1 \times 10^{-7}$ Ground Motion Set 1	H1	16.28	535.26	58.68	30.67
	H2	14.79	428.42	58.72	24.55
	V	13.15	298.44	36.86	28.30

DTN: MO0211TMHIS104.002  
MO0301TMHIS106.001  
MO0211AVTMH107.001

NOTES: Seismic induced stress (column six) is calculated based on elastic wave equations (Itasca 2002, Manuals/3DEC/Optional Features/Section 2: Dynamic Analysis, Section 2.5).

In running the 3DEC seismic simulation, the duration of the seismic time histories was truncated to that portion of the records displaying the majority of the energy. Initially, records were truncated to a duration bracketed by the 5-percent and 95-percent points in the energy buildup as measured by the Arias Intensity. For each three-component set of ground motions, these points were determined for each component (H1, H2, and V) and then the earliest 5-percent point and the latest 95-percent point were used to define the duration for that set of ground motions. Because preliminary analyses showed that rockfall continued in some cases beyond the 95-percent energy buildup point, an additional 5 seconds was added to the duration used for all analyses. If the added 5 seconds exceeded the end of the time history, the end of the record was used. Table 11 presents the beginning and ending time for each set of ground motions and the consequent duration used for dynamic analysis. The table also shows the total duration of each set of time histories for comparison. The sensitivity of rockfall to the duration of seismic ground motion is examined in Section 6.3.1.6.

#### 6.3.1.2.2 Combinations of Ground Motion and Fracture Modeling Region

Rockfall is part of the seismic scenario calculations in support of the Total System Performance Assessment for the License Application. The analysis results provide inputs to the sequential calculations, such as drip shield structural response calculation and waste package vibratory ground motion calculation, for assessment of the structural integrity of drip shields and waste packages. To ensure that the ultimate performance measure of interest (i.e., failed patch area in the drip shield or waste package) can be tracked to the underlying uncertain inputs in a consistent fashion, a sampling strategy was developed to include a consistent set of pointers for the sampled parameters (i.e., ground motions and fracture modeling regions in rockfall analysis). A detailed description of the sampling strategy is provided in DTN: MO0301SPASIP27.004.

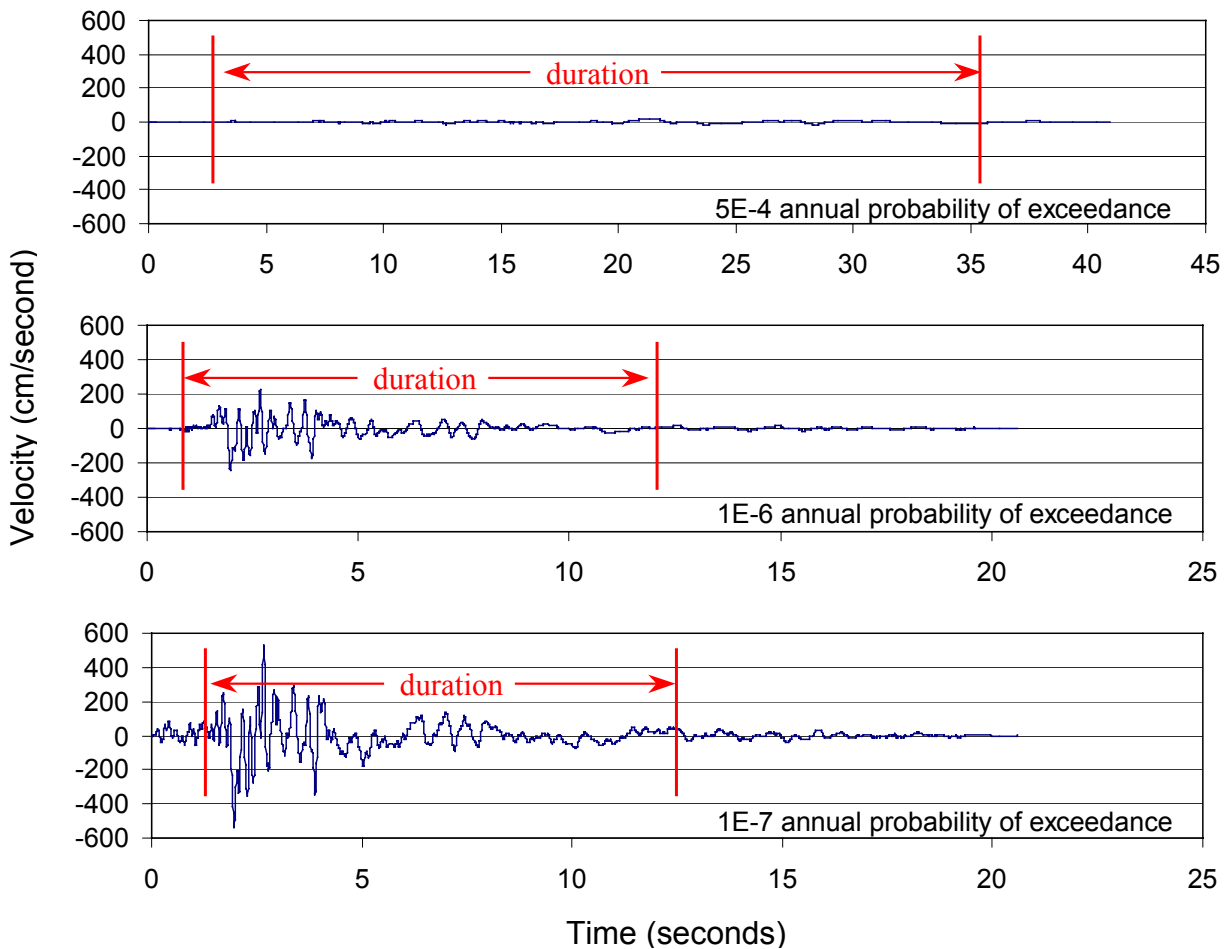


Figure 42. Examples of Ground Velocity Time Histories (H1) with Truncated Duration for Analysis

Table 10. Arias Intensity (m/sec) for Each Ground Motion Set

Annual Hazard Level	Ground Motion Set <sup>a</sup>	H1	H2	V	Total Sum
1×10 <sup>-6</sup> Annual Probability of Exceedance	1	246	304	482	1032
	2	229	229	471	928
	3	139	23	33	195
	4	179	176	282	638
	5	58	81	150	288
	6	42	160	71	272
	7	65	58	217	339
	8	65	35	213	312
	9	174	39	91	303
	10	94	186	615	894
	11	63	74	146	283
	12	97	40	117	254
	13	82	131	56	269
	14	43	386	206	636
	16	24	42	86	151
	1×10 <sup>-7</sup> Annual Probability of Exceedance	1	1128	1215	820
2		989	1202	2972	5163
3		577	735	971	2283
4		856	1052	1013	2921
5		373	568	205	1146
6		331	271	566	1168
7		303	291	3357	3951
8		343	524	437	1304
9		813	1691	3340	5844
10		282	125	409	816
11		272	214	321	808
12		277	284	332	893
13		469	815	881	2165
14		302	351	854	1507
16		112	72	244	428
5×10 <sup>-4</sup> Annual Probability of Exceedance			0.59	0.67	0.46

DTN: MO0211TMHIS104.002  
 MO0301TMHIS106.001  
 MO0211AVTMH107.001

NOTE: <sup>a</sup>A total of 17 sets of ground motions was developed for each postclosure level. Ground motion sets #15 and #17 were not used.

Table 11. Seismic Analysis Duration and Complete Time History Duration

Annual Hazard Level	Ground Motion Set <sup>a</sup>	Dynamic Analysis Start Time (sec)	Dynamic Analysis End Time (sec)	Dynamic Analysis Duration (sec)	Complete Time History Duration (sec)
1×10 <sup>-6</sup> Annual Probability of Exceedance	Set 1	0.85	12.06	11.21	20.60
	Set 2	0.59	13.13	12.54	26.00
	Set 3	1.74	10.04	8.29	39.99
	Set 4	1.37	19.96	18.59	26.11
	Set 5	2.01	15.31	13.30	30.32
	Set 6	2.36	14.96	12.60	41.63
	Set 7	4.05	16.26	12.21	16.26
	Set 8	1.14	10.99	9.85	29.95
	Set 9	0.79	13.18	12.39	29.98
	Set 10	1.60	15.84	14.25	29.92
	Set 11	2.14	15.27	13.13	39.94
	Set 12	1.40	18.60	17.20	39.98
	Set 13	1.91	22.01	20.10	39.95
	Set 14	7.23	26.51	19.28	48.12
1×10 <sup>-7</sup> Annual Probability of Exceedance	Set 1	1.28	12.47	11.19	20.60
	Set 2	0.80	12.40	11.61	20.60
	Set 3	1.75	9.73	7.98	19.99
	Set 4	1.48	22.29	20.81	26.11
	Set 5	1.69	17.35	15.66	19.99
	Set 6	2.44	15.57	13.13	19.99
	Set 7	3.55	16.26	12.71	16.26
	Set 8	1.21	11.48	10.27	20.60
	Set 9	0.76	13.00	12.24	29.98
	Set 10	1.67	14.58	12.90	19.98
	Set 11	2.08	15.30	13.22	20.60
	Set 12	2.17	20.66	18.50	39.98
	Set 13	1.90	24.53	22.64	39.95
	Set 14	5.37	28.94	23.57	40.00
Set 16	3.43	15.43	12.00	31.99	
5×10 <sup>-4</sup> Annual Probability of Exceedance		3.24	33.67	30.43	40.96

DTN: MO0211TMHIS104.002  
 MO0301TMHIS106.001  
 MO0211AVTMH107.001

NOTE: <sup>a</sup>A total of 17 sets of ground motions was developed for each postclosure level. Ground motion sets #15 and #17 were not used.

As described in Section 6.1, a 100-m cube was constructed for providing the fracture network required in 3DEC analysis. A random selection of 105 centroid locations was conducted. These 105 centroid locations combined with the 15 sets of ground motions served as the pointers for sampling. The process of random generation and the coordinate of the centroid locations in the 100-m cube are provided in Attachment X. A simple Latin Hypercube sampling scheme was used for the paring of ground motion and fracture modeling region (DTN: MO0301SPASIP27.004). Table 12 lists the 76 sets of analyses conducted for seismic consideration.

Table 12. Combinations of Ground Motion and Fracture Modeling Region of 3DEC Analyses

<b>3DEC Simulation Number</b>	<b>Ground Motion Time History Number</b>	<b>Fracture Modeling Region</b>
14	7	22
15	11	21
16	11	30
17	16	27
18	14	26
19	13	10
20	5	19
21	10	9
22	5	23
23	12	5
24	3	6
25	3	17
26	9	12
27	6	14
28	7	25
29	13	3
31	16	79
32	12	7
33	1	102
34	16	75
35	11	33
36	5	78
37	12	15
38	3	29
39	5	37
40	6	99
41	16	42
42	6	24
43	4	59
44	9	65
45	10	39
46	6	50
47	8	103
48	16	35
49	5	57
50	9	67
51	10	63
52	9	82
53	12	4
54	1	83
55	12	16
56	3	98
57	14	28

Table 12. Combinations of Ground Motion and Fracture Modeling Region of 3DEC Analyses (Continued)

58	4	8
59	2	74
60	11	80
61	12	81
62	12	71
63	11	96
64	14	49
65	7	20
66	3	62
67	9	41
68	6	69
69	10	11
70	2	54
71	8	104
72	16	36
73	6	53
74	8	94
75	14	92
76	14	68
77	10	48
78	7	18
79	3	1
80	1	93
81	14	84
82	12	91
83	13	90
84	13	2
85	1	100
86	16	13
87	2	73
88	11	43
89	7	72
90	11	105

DTN: MO0301SPASIP27.004

NOTES: 3DEC simulation numbers 14 through 29 are from the first sampling in the nonlithophysal zone provided by the source DTN. 3DEC simulation numbers 31 through 90 are from the second sampling in the nonlithophysal zone provided by the source DTN. Duplicate fracture modeling regions (i.e., synthetic fracture pattern numbers) occurring in both the first and second samplings were not used as part of the base case for rockfall modeling.

### 6.3.1.2.3 Results for Seismic Analysis Subjected to $1 \times 10^{-6}$ Annual Probability of Exceedance Ground Motions

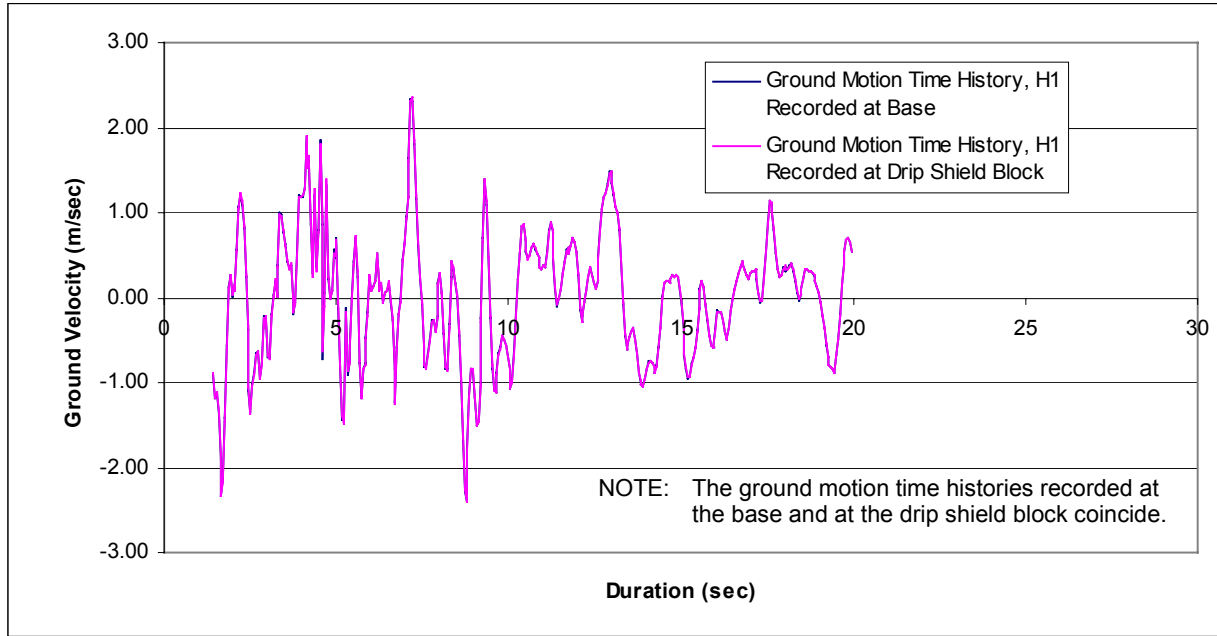
The results for a complete set of 3DEC analyses, as tabulated in Table 12, subjected to the postclosure hazard level of  $1 \times 10^{-6}$  annual probability of exceedance ground motions are presented in this section. Figure 43 compares the input ground motion for the first horizontal component (H1, Ground Motion Set 4) with the recorded velocities at the base of the model and at the center of the model. The results confirm the correct wave inputs and proper wave propagation in the 3DEC model. As described in Section 6.3.1.1, a drip shield block anchored at the invert is included in the model to record the information of the locations and relative velocities for the rockfall impact. Figure 44 shows a typical block impacting the drip shield in the 3DEC dynamic simulation. Note that fallen blocks are subsequently deleted after impacting the drip shield. The deletion is to facilitate the recording of all possible rockfall on the drip shield. If the blocks are not deleted for the heavy rockfall cases, the drip shield will be covered with fallen rocks so that some of the rockfall at the later part of seismic shaking will not impact the drip shield. The simulation without deletion of the rock block after the impact is presented in Section 6.3.1.6. The results indicate less rockfall impact without the deletion scheme.

Time histories of normal and shear stresses for joints close to the opening were recorded during the seismic shaking in the 3DEC model. Figure 45 shows typical normal and shear stress time histories at a fracture contact taken from 3DEC simulation #21 with ground motion set #10. Major seismic loading appears to occur at the duration of two to six seconds, consistent with the input ground motion. The stress path of this fracture contact is plotted against the Coulomb slip criterion, as shown in Figure 46. It is observed that shear slip started at around two seconds when the normal stress of the fracture drops to 1 MPa due to the extensile motion from seismic loading.

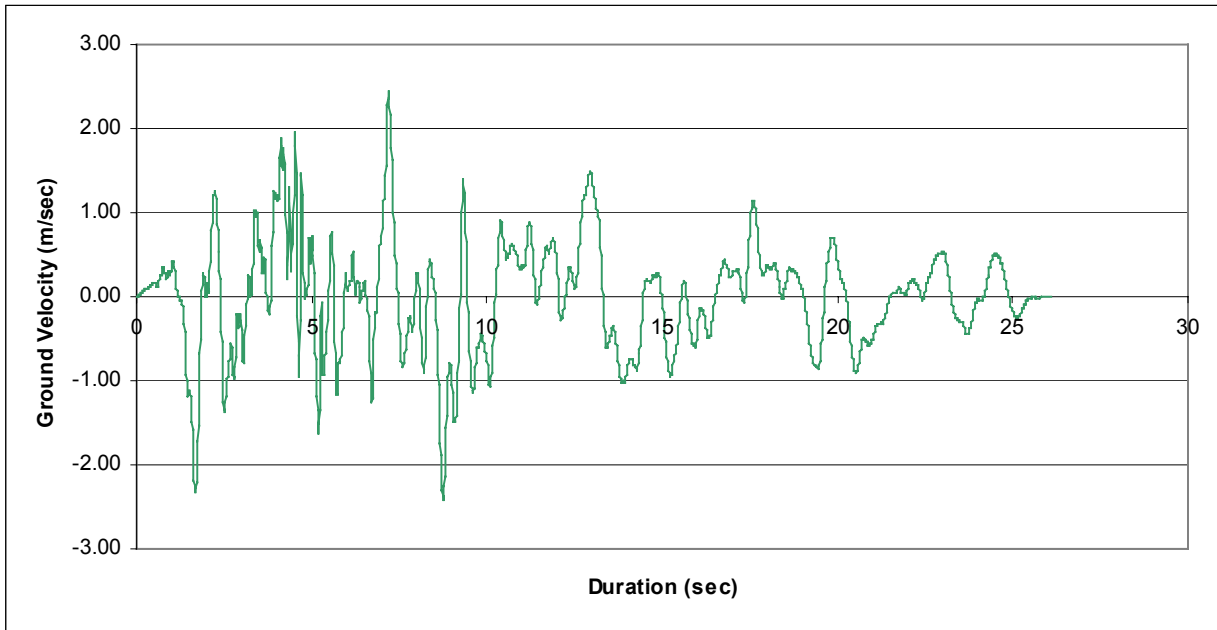
The results of the 76 3DEC simulations are summarized in Table 13. Approximately two thirds of the simulations predicted rockfall under seismic shaking. A total of 279 blocks have been identified from the analyses. The associated impact parameters for these blocks from the analyses include the following:

- Rock block volume falling on the drip shields (unit in  $m^3$ )
- Relative impact velocity of rock block to the drip shields (unit in meter/sec)
- Impact location.

Drift Degradation Analysis



(a) Recorded Velocities



(b) Input Seismic Wave

DTN: MO0301TMHIS106.001

Figure 43. Comparison of Input Seismic Wave and Recorded Velocities in 3DEC Model

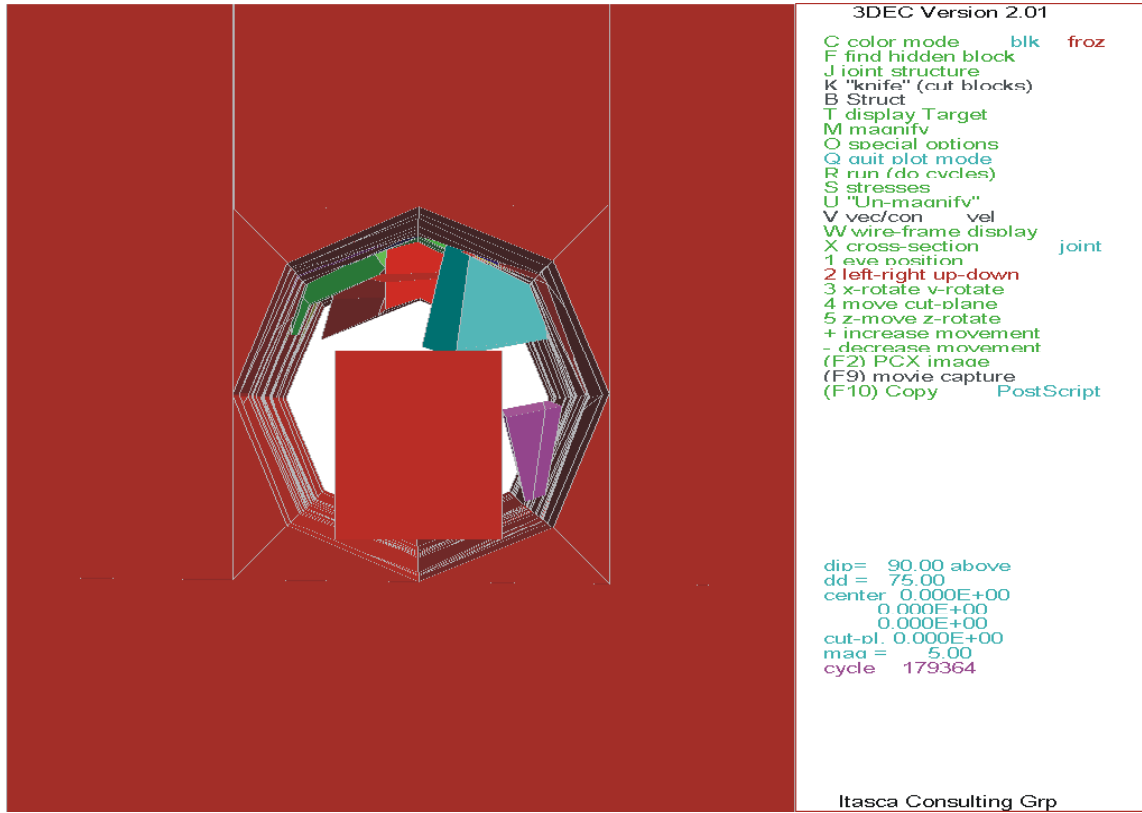


Figure 44. Illustration of the Simulation of Rockfall Impact to the Drip Shield 3DEC Simulation #55,  $1 \times 10^{-6}$  Ground Motion # 12, at t = 6.6 sec

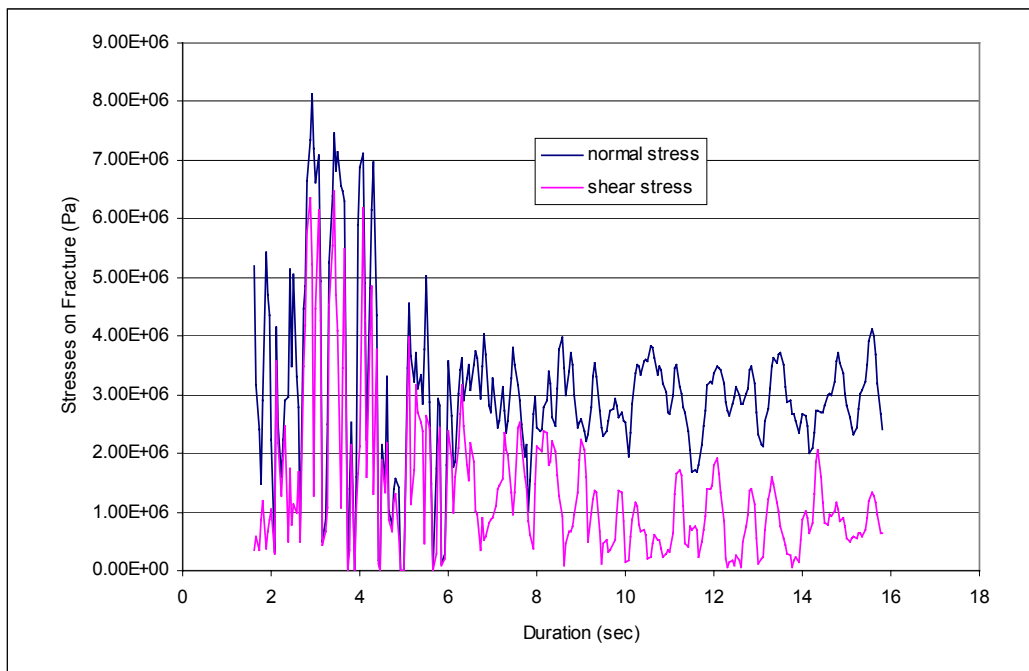


Figure 45. Time Histories for Normal and Shear Stress at Fracture Contact Coordinate: 2.046, 0.341, -3.271 (3DEC Simulation #21,  $1 \times 10^{-6}$  Ground Motion #10)

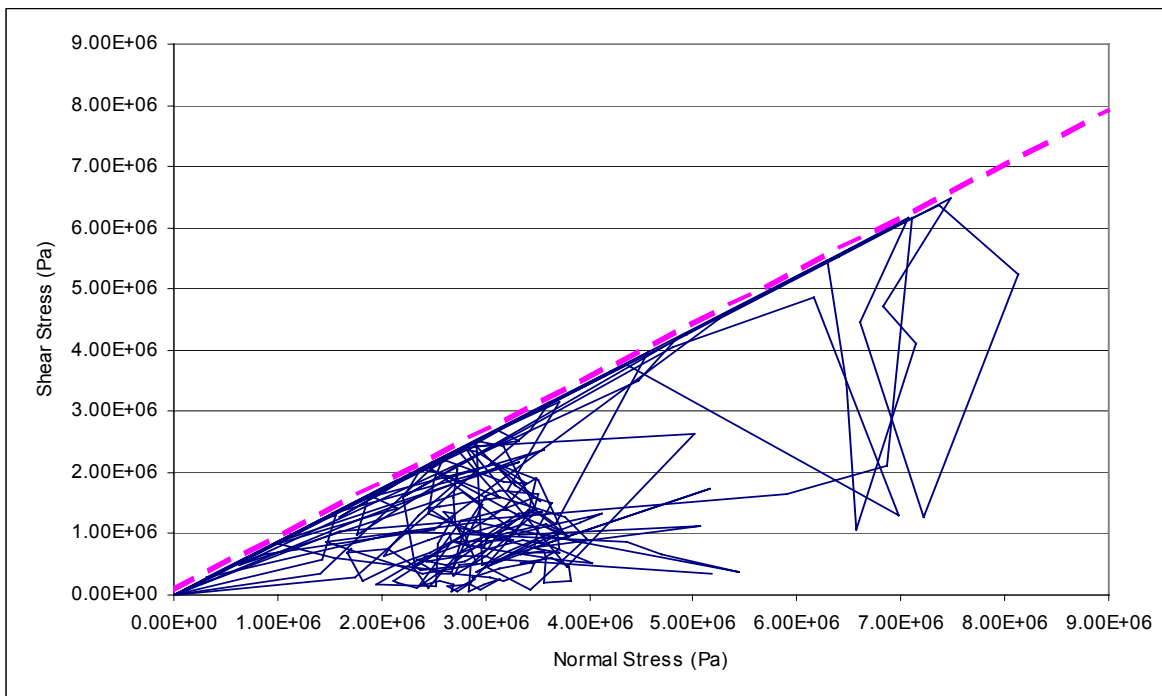


Figure 46. Normal and Shear Stress Path at Fracture Contact Coordinate: 2.046, 0.341, -3.271 (3DEC Simulation #21,  $1 \times 10^{-6}$  Ground Motion #10)

Table 13. Summary of 3DEC Rockfall Prediction for  $1 \times 10^{-6}$  Annual Probability of Exceedance Hazard

Simulations Completed	76
Number of Simulations Predicting No Rockfall	24
Total Number of Rockfall	281
Total Volume of Rockfall (m <sup>3</sup> )	101.8
Total Length of Drift Simulated (m)	1900
Number of Blocks per km	148
Volume of Rockfall per km (m <sup>3</sup> )	53.6

A detailed listing of the impact information for each recorded block is provided in Attachment XI. The impact locations are provided as the coordinates based on the drip shield local coordinate system (Figure 47). The distribution of the data for each parameter (i.e., block mass, relative impact velocity, impact angle, impact momentum, and impact energy) is presented using histograms (Figures 48 to 52). Also included in each histogram plot is the cumulative frequency of occurrence. Due to the gravity effect, most of the rockfall will occur in the range of 48° to 132° as confirmed in Figure 50. The impact momentum and impact energy, both functions of block mass and impact velocity, were calculated as the required outputs for drip shield structural response calculation. Summary statistics for these parameters are provided in Table 14. The maximum rockfall block mass predicted is 21.42 tonnes with median block size of 0.23 tonnes. The predicted results (Table 14) show large variance and high skewness with the exception of impact velocity, as confirmed by the shape of the histograms (Figures 48 to 52). The block mass, impact angle, impact momentum and impact energy show the trend of

exponential distribution with most of the data concentrated on the low end of the data range. The impact velocity shows a typical bell shape for the normal distribution. The distribution centers around 3 m/sec with a standard deviation of approximately 1.5 m/sec. The relative low impact velocities indicate that block fall-out is mainly due to free fall. Differential acceleration or energy trapping to induce high ejection velocity is not observed.

Table 14. Statistic Summary of the Rockfall Impact Parameters,  $1 \times 10^{-6}$  Annual Probability of Exceedance Hazard

	<b>Block Mass (tonnes)</b>	<b>Relative Impact Velocity (m/sec)</b>	<b>Impact Angle (degree)</b>	<b>Impact Momentum (kg*m/sec)</b>	<b>Impact Energy (Joules)</b>
Mean	0.87	3.39	132	2747	5267
Median	0.23	3.49	120	663	902
Standard Deviation	1.97	1.61	81	6209	12941
Skewness	6.04	0.04	1.12	6.23	7.52
Range	21.39	7.54	355	68836	163083
Minimum	0.02	0.02	5	4	0
Maximum	21.42	7.56	360	68840	163083
Sum	245.55	NA*	NA*	771861	1479888

NOTE: \*Not Applicable

#### **6.3.1.2.4 Results for Seismic Analysis Subjected to $1 \times 10^{-7}$ Annual Probability of Exceedance Ground Motions**

The results for a complete set of 3DEC analyses subjected to the postclosure hazard level of  $1 \times 10^{-7}$  annual probability of exceedance ground motions are presented in this section. Figure 53 compares the input ground motion for the first horizontal component (H1, Ground Motion Set 7) with the recorded velocities at the base of the model and at the center of the model. As for the case of  $1 \times 10^{-6}$  annual probability of exceedance hazard, the results confirm the correct wave inputs and proper wave propagation in the 3DEC model.

Figure 54 shows several large size blocks impacting drip shield in 3DEC dynamic simulation. Time histories of normal and shear stresses for joints close to the opening were also recorded during the seismic shaking of  $1 \times 10^{-7}$  annual probability of exceedance ground motions in 3DEC model. Shear failure similar to the case for  $1 \times 10^{-6}$  annual probability of exceedance ground motions, as shown in Figures 45 and 46, were observed for most of the fracture contacts around the opening. Figure 55 shows the normal and shear stress time histories at a rock bridge taken from 3DEC simulation #78 with ground motion set #7. The stress path of this bridge contact is plotted against the Mohr-Coulomb criterion with tension cut-off, as shown in Figure 56. A tensile stress pulse at around 8 seconds reaches the tensile strength of the intact material and subsequently fractures the rock bridge. The bridge contact shows no resistance to the tensile stress afterward.

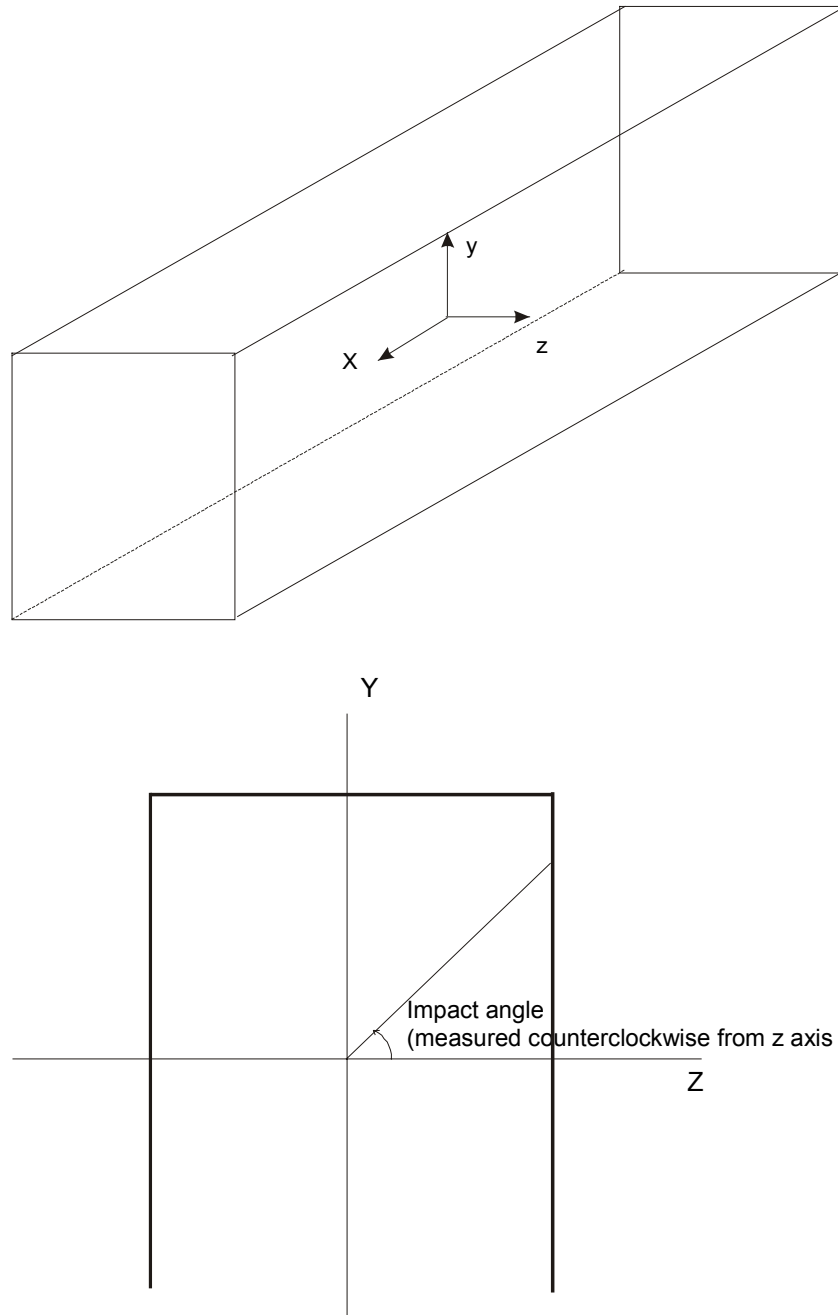


Figure 47. Definition of Impact Angle and Drip Shield Block Local Coordinate System

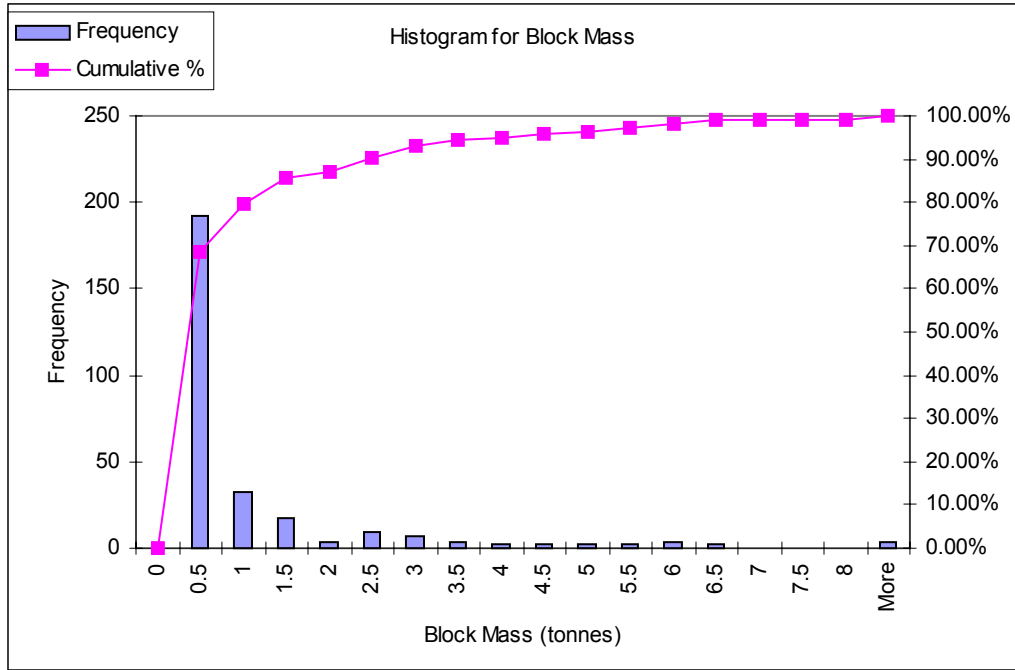


Figure 48. Histogram for Block Mass ( $1 \times 10^{-6}$  Annual Probability of Exceedance Hazard)

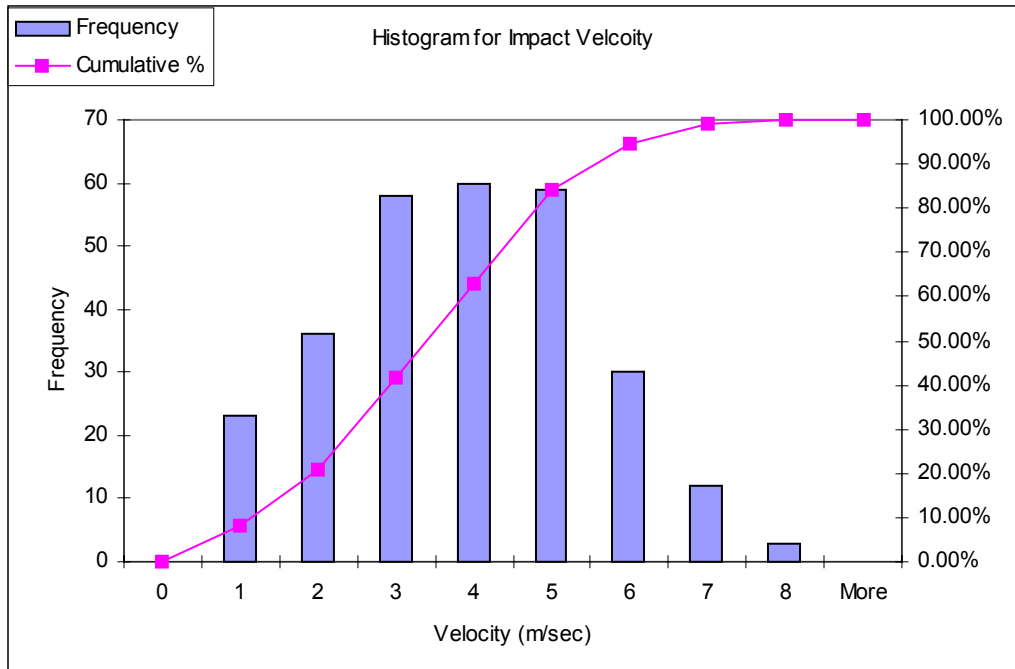


Figure 49. Histogram for Relative Impact Velocity ( $1 \times 10^{-6}$  Annual Probability of Exceedance Hazard)

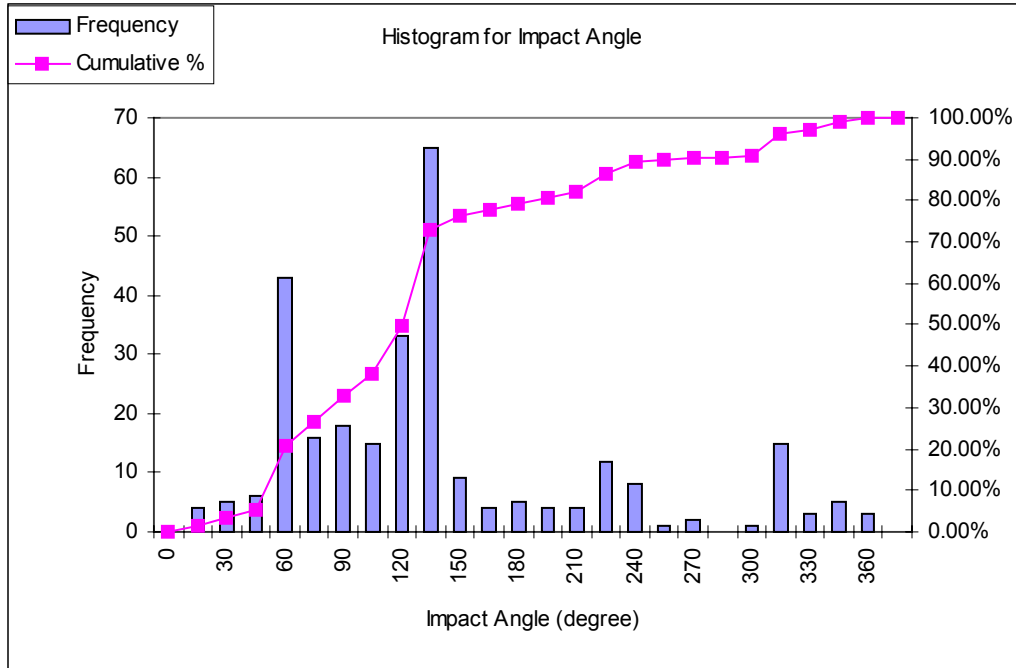


Figure 50. Histogram for Impact Angle ( $1 \times 10^{-6}$  Annual Probability of Exceedance Hazard)

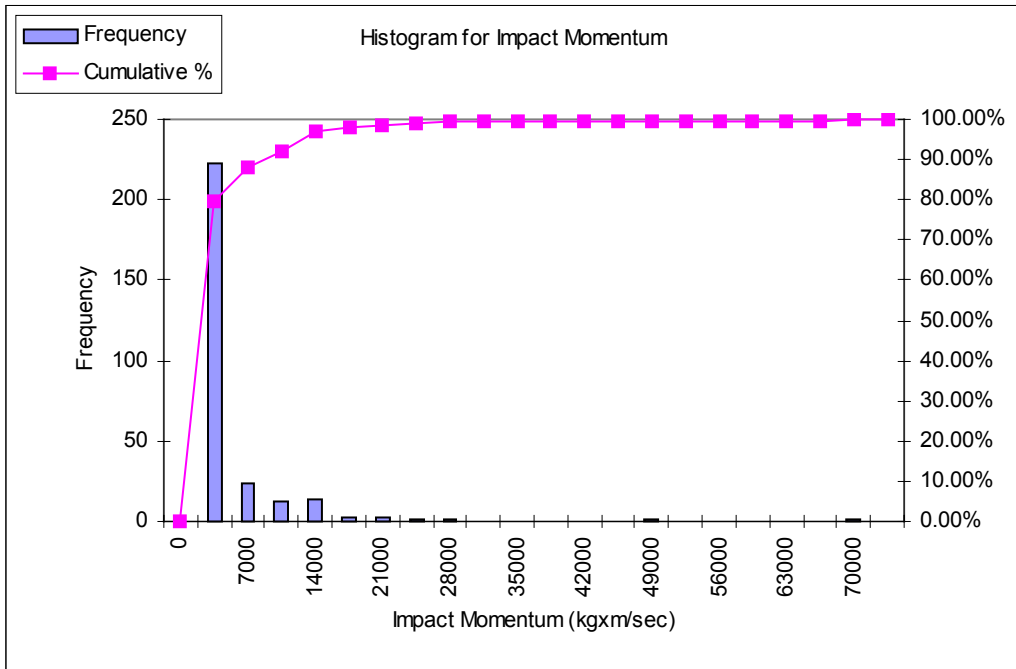


Figure 51. Histogram for Impact Momentum ( $1 \times 10^{-6}$  Annual Probability of Exceedance Hazard)

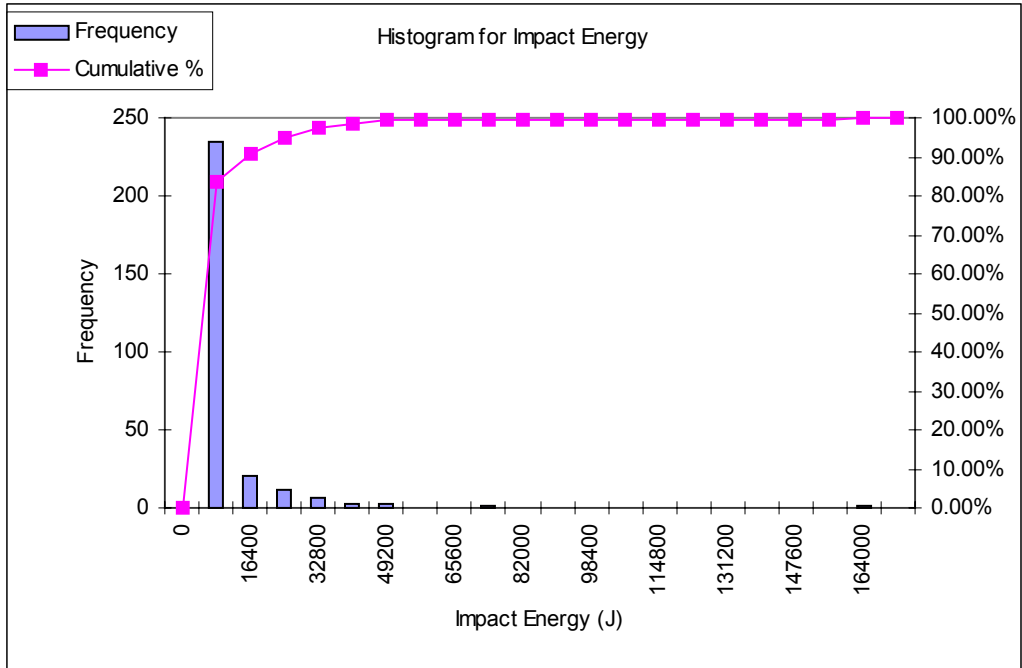
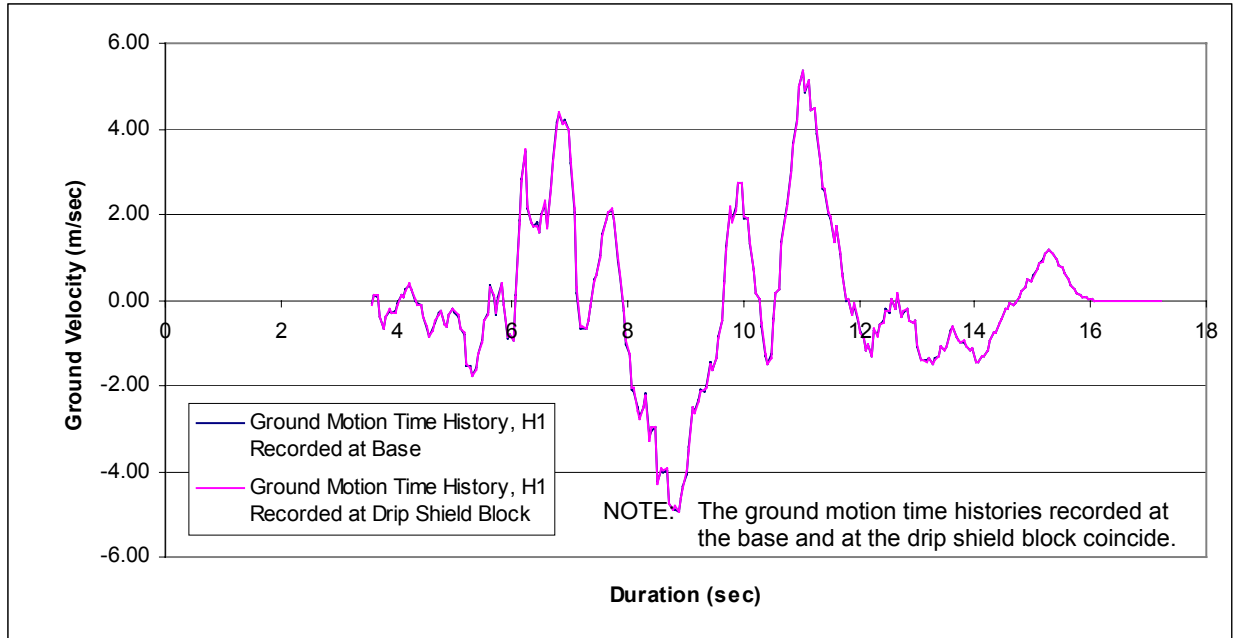
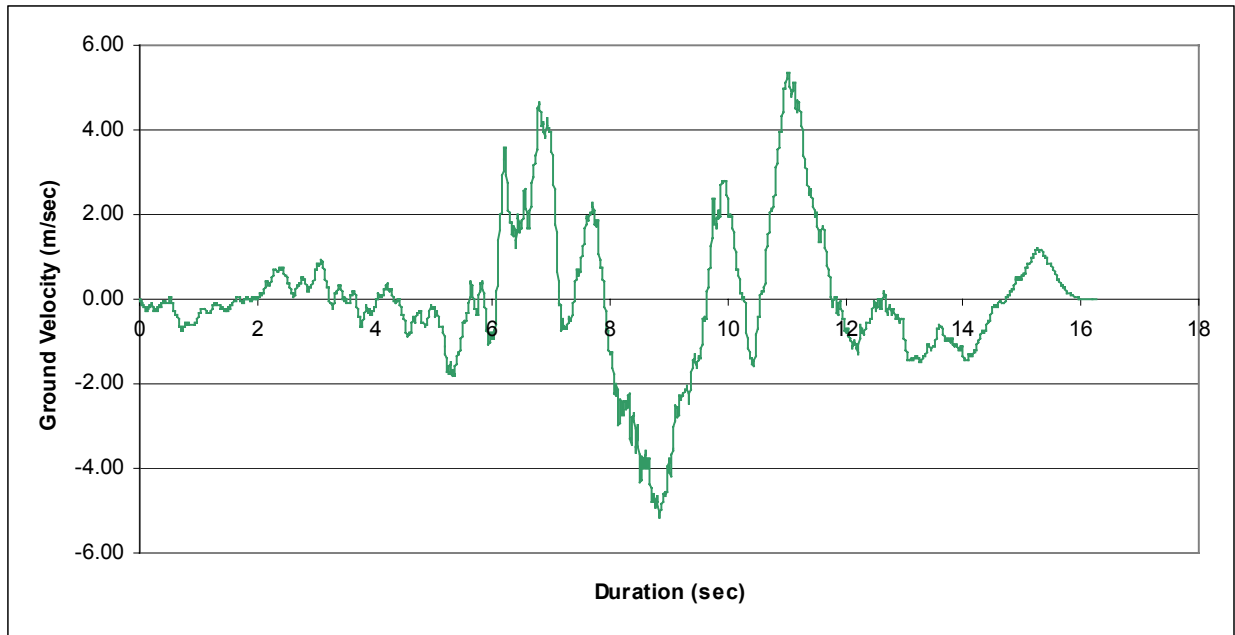


Figure 52. Histogram for Impact Energy ( $1 \times 10^{-6}$  Annual Probability of Exceedance Hazard)

Drift Degradation Analysis



(a) Recorded Velocities



(b) Input Seismic Wave

DTN: MO0211AVTMH107.001

Figure 53. Comparison of Input Seismic Wave and Recorded Velocities in 3DEC Model for  $1 \times 10^{-7}$  Annual Probability of Exceedance Ground Motion (H1)

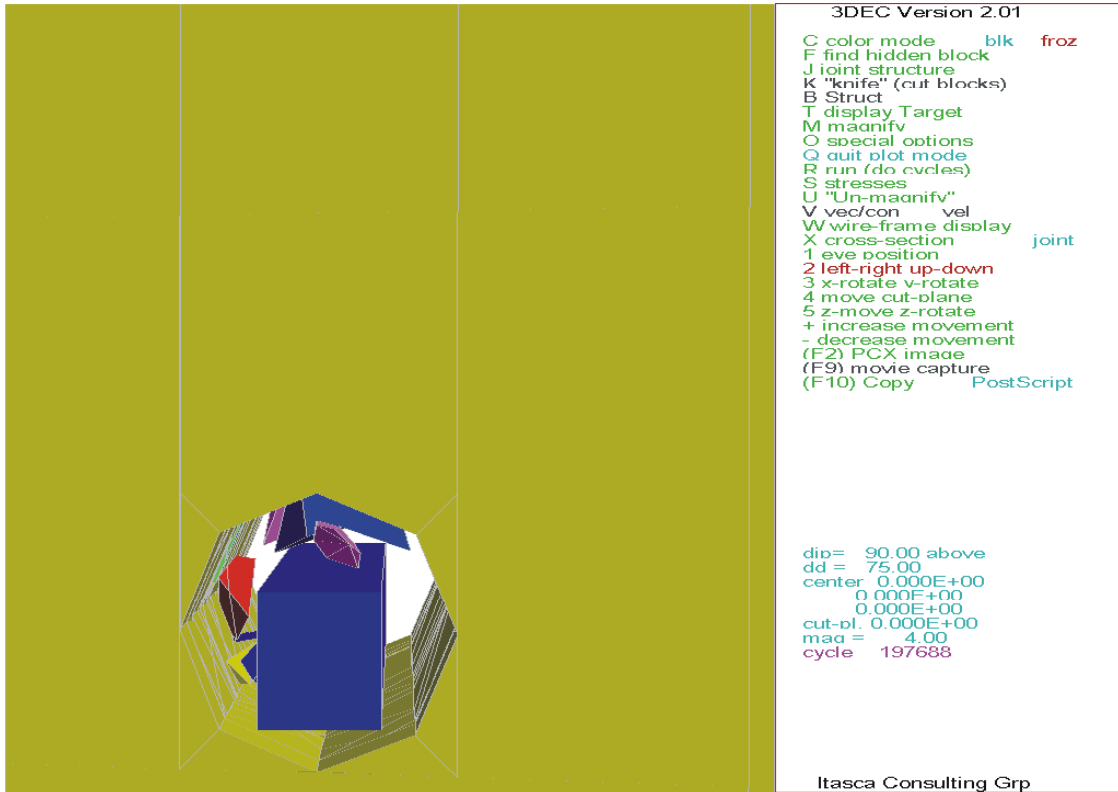


Figure 54. Illustration of the Simulation of Rockfall Impact to the Drift Shield (3DEC Simulation #55,  $1 \times 10^{-7}$  Ground Motion # 12, at t = 6.6 sec)

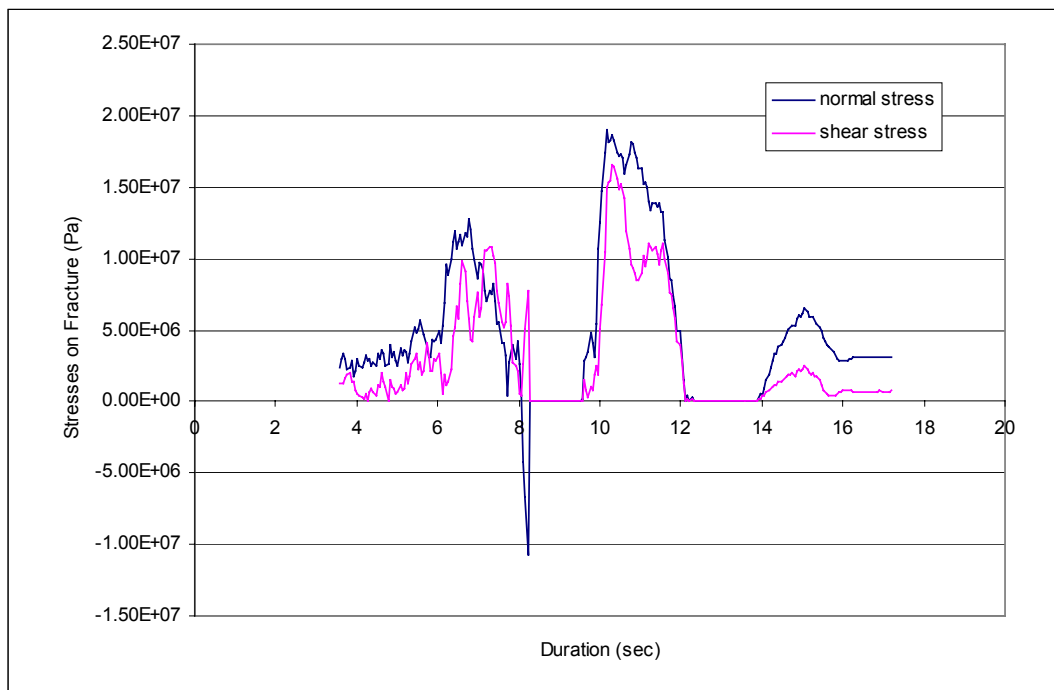


Figure 55. Time Histories for Normal and Shear Stress at Rock Bridge Contact Coordinate: 2.451, 2.749, -0.350 (3DEC Simulation #78,  $1 \times 10^{-7}$  Ground Motion #7)

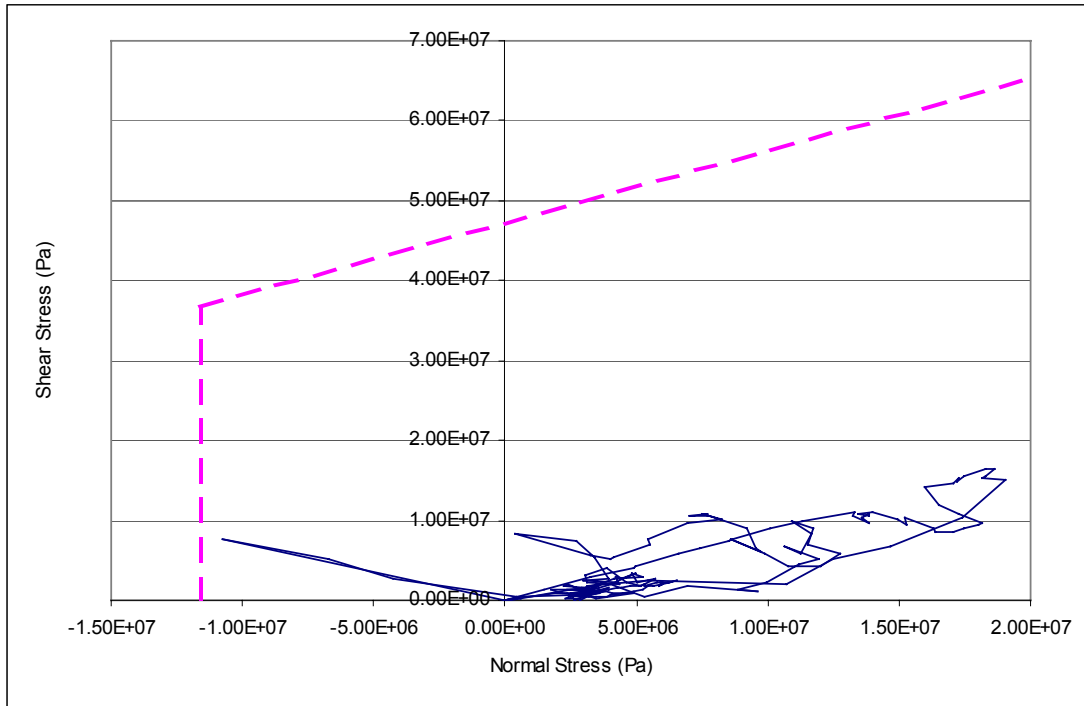


Figure 56. Normal and Shear Stress Path at Rock Bridge Contact Coordinate: 2.451, 2.749, -0.350 (3DEC Simulation #78,  $1 \times 10^{-7}$  Ground Motion #7)

The results of the 76 3DEC simulations are summarized in Table 15. Approximately 20 percent of the simulations predicted no rockfall under this level of seismic shaking. A total of 380 blocks have been identified from the analyses. A detailed listing of the impact information for each recorded block is also included in Attachment XI. Summary statistics for these parameters are provided in Table 16. The maximum rockfall block mass predicted is 21.42 tonnes, which is the same as predicted for the  $1 \times 10^{-6}$  annual probability of exceedance ground motions. The median block size is 0.23 tonnes, also the same as predicted for the  $1 \times 10^{-6}$  annual probability of exceedance hazard. The median impact momentum and energy predicted for rockfall impact onto drip shield for the  $1 \times 10^{-7}$  annual probability of exceedance hazard are approximately two times the values at  $1 \times 10^{-6}$  annual probability of exceedance hazard. Figures 57 to 61 present the histograms and the cumulative frequency of occurrence for the five impact parameters. The distribution of each parameter is similar to that for the  $1 \times 10^{-6}$  annual probability of exceedance hazard.

Table 15. Summary of 3DEC Rockfall Prediction for  $1 \times 10^{-7}$  Annual Probability of Exceedance Hazard

Simulations Completed	76
Number of Simulations Predicting No Rockfall	16
Total Number of Rockfall	380
Total Volume of Rockfall (m <sup>3</sup> )	151.2
Total Length of Drift Simulated (m)	1900
Number of Blocks per km	200
Volume of Rockfall per km (m <sup>3</sup> )	79.6

Table 16. Statistic Summary of the Rockfall Impact Parameters,  $1 \times 10^{-7}$  Annual Probability of Exceedance Hazard

	Block Mass (tonnes)	Relative Impact Velocity (m/sec)	Impact Angle (degree)	Impact Momentum (kg*m/sec)	Impact Energy (Joules)
Mean	0.96	5.03	139	4169	11459
Median	0.23	4.63	127	980	2440
Standard Deviation	2.04	2.78	87	8489	27461
Skewness	5.01	1.00	1.06	4.64	6.73
Range	21.39	17.67	356	89485	348170
Minimum	0.02	0.07	1	18	4
Maximum	21.42	17.74	357	89502	348174
Sum	364.58	NA*	NA*	1584186	4354385

NOTE: \*Not Applicable

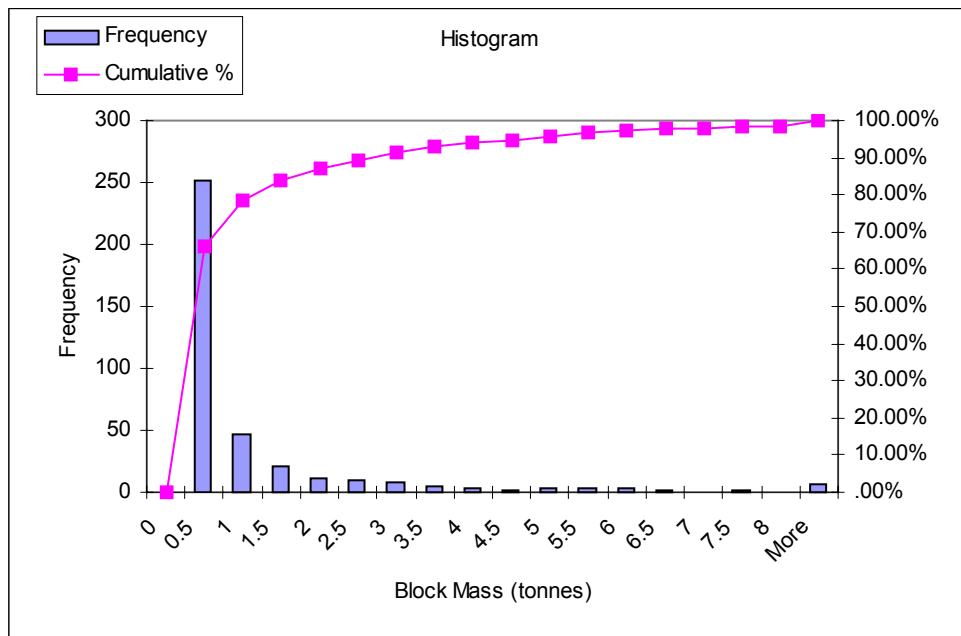


Figure 57. Histogram for Block Mass ( $1 \times 10^{-7}$  Annual Probability of Exceedance Hazard)

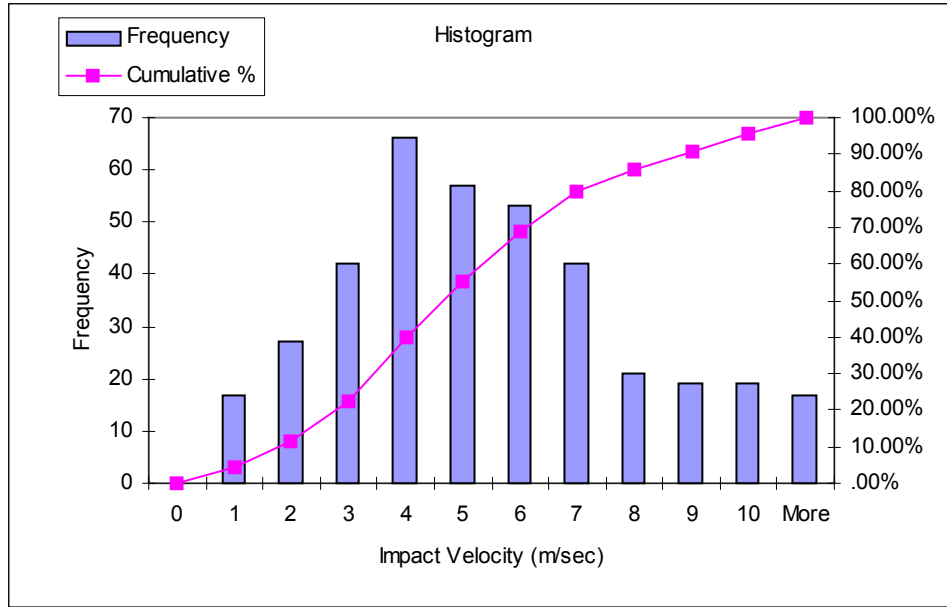


Figure 58. Histogram for Relative Impact Velocity ( $1 \times 10^{-7}$  Annual Probability of Exceedance Hazard)

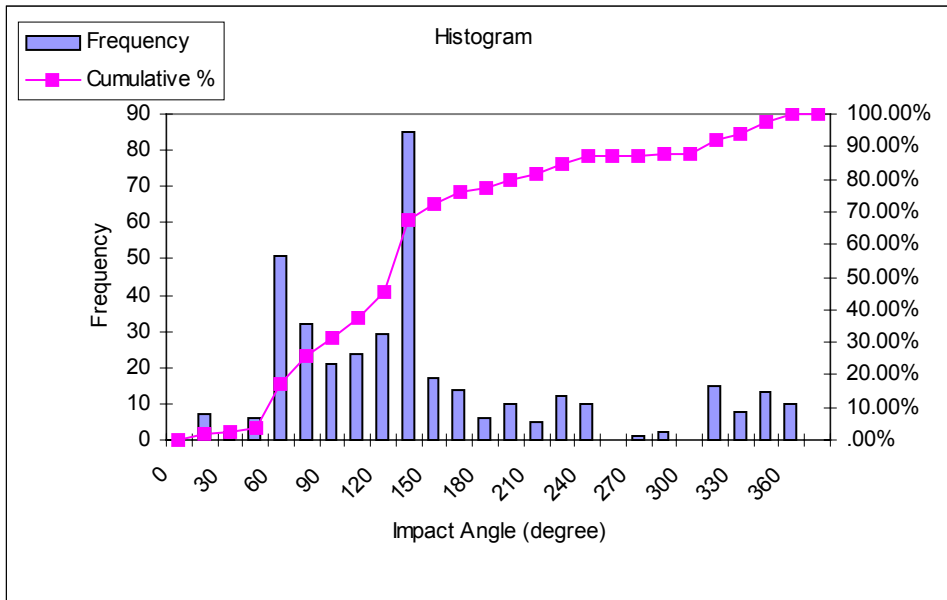


Figure 59. Histogram for Impact Angle ( $1 \times 10^{-7}$  Annual Probability of Exceedance Hazard)

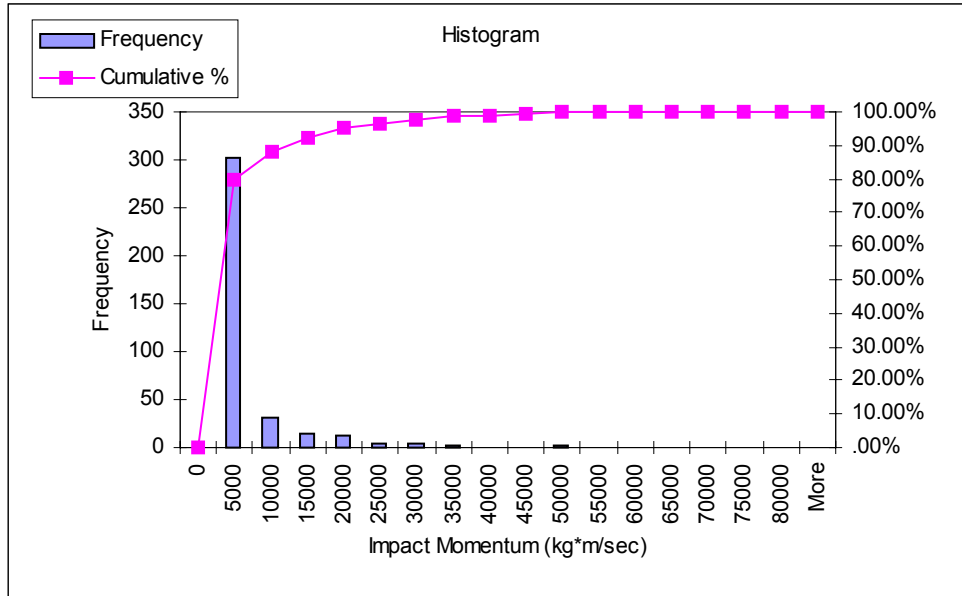


Figure 60. Histogram for Impact Momentum ( $1 \times 10^{-7}$  Annual Probability of Exceedance Hazard)

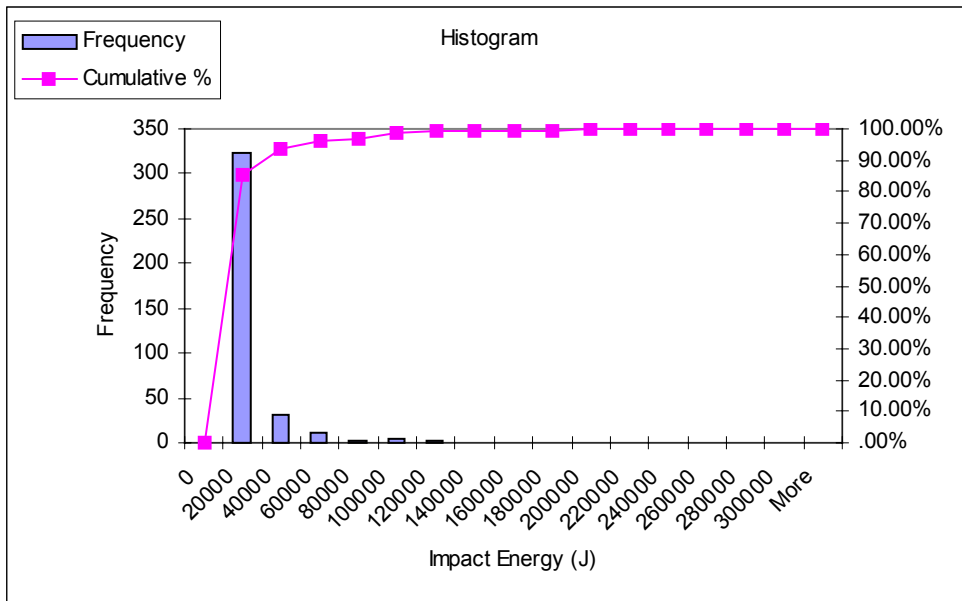


Figure 61. Histogram for Impact Energy ( $1 \times 10^{-7}$  Annual Probability of Exceedance Hazard)

### 6.3.1.2.5 Results for Seismic Analysis Subjected to $5 \times 10^{-4}$ Annual Probability of Exceedance Ground Motion

The results for the preclosure hazard level of  $5 \times 10^{-4}$  annual probability of exceedance ground motion are presented in this section. As described in Section 6.3.1.2.1, only a single set of ground motion is considered in the rockfall analysis for preclosure seismic level. Due to the much lower amplitude of ground motion considered for the preclosure hazard level and hence, much less rockfall hazard anticipated, only 25 runs were conducted for preclosure cases compared to 76 cases for postclosure cases. The rockfall simulation results for the cases with  $1 \times 10^{-6}$  annual probability of exceedance ground motions were used to select the 25 fracture modeling regions with most block fall predicted. Table 17 lists the corresponding fracture modeling regions for the 25 preclosure runs.

Table 17. Combinations of Ground Motion and Fracture Modeling Region of 3DEC Analyses

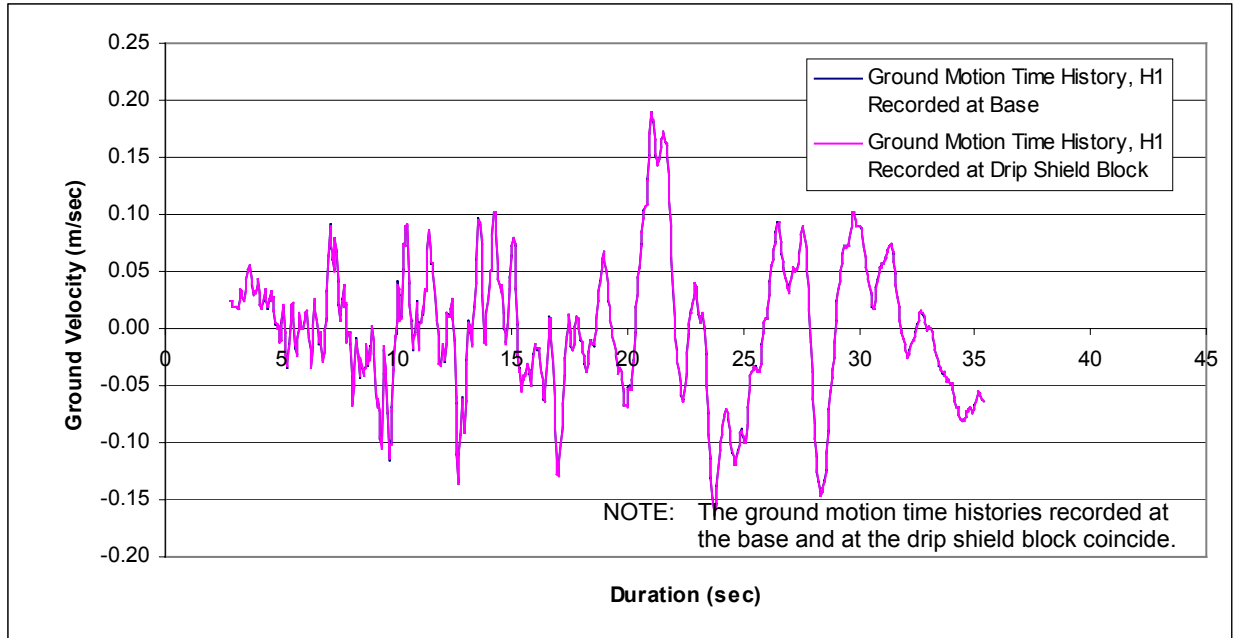
3DEC Simulation Number for Preclosure Runs	Fracture Modeling Region
1	8
2	16
3	33
4	39
5	59
6	93
7	11
8	14
9	100
10	19
11	5
12	7
13	49
14	63
15	62
16	78
17	57
18	79
19	36
20	82
21	15
22	92
23	48
24	9
25	2

Figure 62 compares the input ground motion for the first horizontal component with the recorded velocities at the base of the model and at the center of the model. The results confirm the correct wave inputs and proper wave propagation in the 3DEC preclosure seismic run. Figure 63 shows a typical block impacting a drip shield in the 3DEC dynamic simulation.

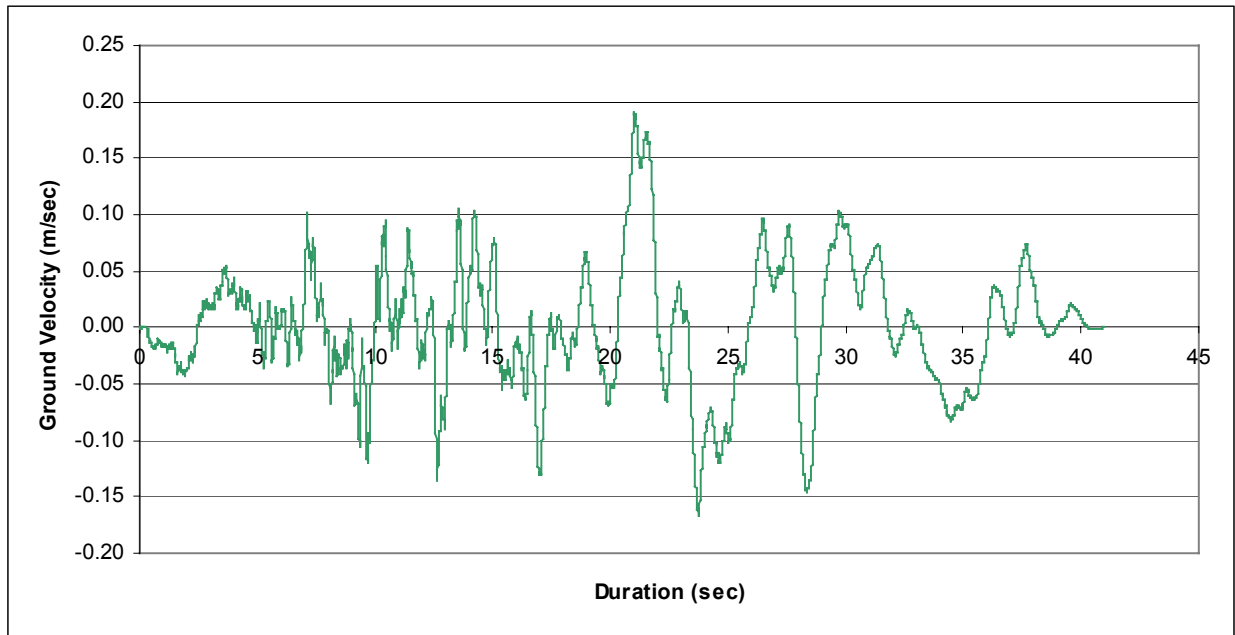
Time histories of normal and shear stresses for joints close to the opening were recorded during the seismic shaking in the 3DEC model. Figure 64 shows typical normal and shear stress time histories at a fracture contact taken from 3DEC simulation #19 for preclosure case. Very minor perturbation of both normal and shear stresses along fracture contact is observed. The stress path of this fracture contact is plotted against the Coulomb slip criterion (Figure 65). The stress state at the fracture contact is found to be well below the failure criterion.

The results of the 25 3DEC preclosure simulations are summarized in Table 18. Approximately half of the simulations predicted rockfall under seismic shaking. A total of 37 blocks were identified from the analyses. The rockfall density predicted in Table 18 should be considered as the high end of the prediction since the 25 simulations selected were the fracture model regions with most the blocks predicted in the postclosure runs.

The associated impact parameters due to rockfall on the drip shield are included in Attachment XI. Summary statistics for these parameters are provided in Table 19. The maximum rockfall block mass predicted for preclosure case is 2.89 tonnes with a median block size of 0.47 tonnes. Most of the parameters estimated are considerably smaller than predicted for postclosure cases. Figures 66 to 70 present the histograms and the cumulative frequency of occurrence for the five parameters. The relative low impact velocities, as shown in Figure 67, indicate that block fall-out is mainly due to free fall. Differential acceleration or energy trapping to induce high ejection velocity is not observed.



(a) Recorded Velocities



(b) Input Seismic Wave

DTN: MO0211TMHIS104.002

Figure 62. Comparison of Input Seismic Wave and Recorded Velocities in 3DEC Model for  $5 \times 10^{-4}$  Annual Probability of Exceedance Ground Motion (H1)

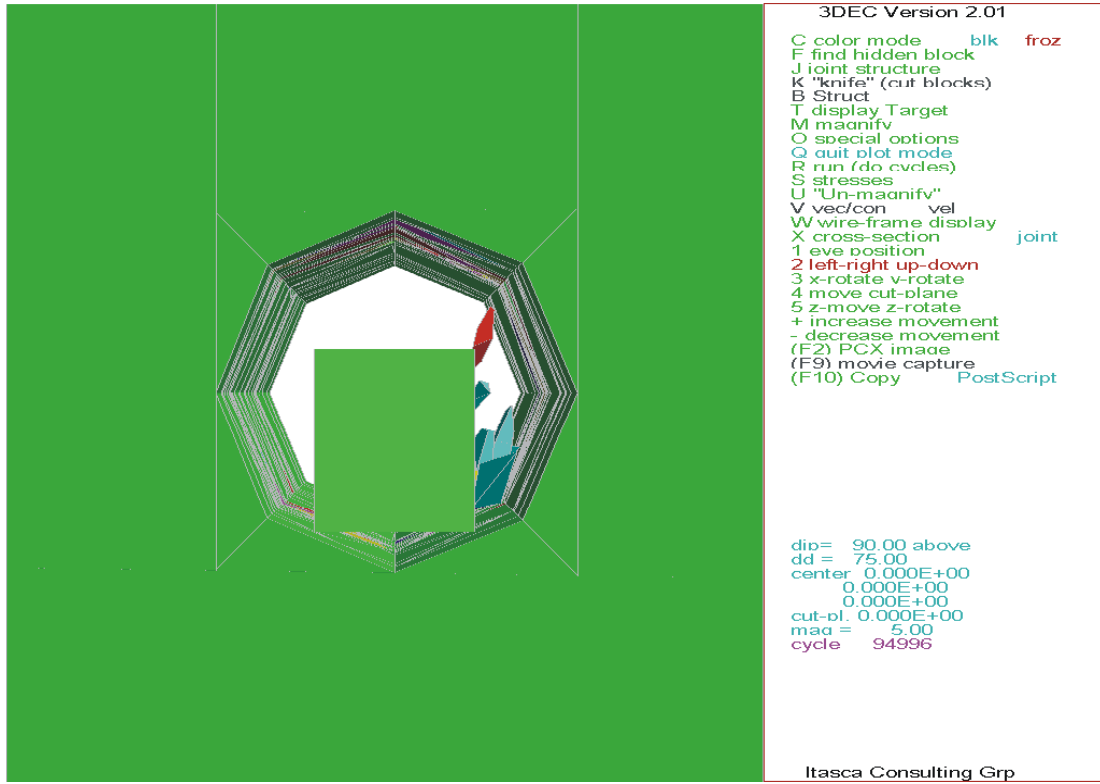


Figure 63. Illustration of the Simulation of Rockfall Impact to the Drift Shield (3DEC Simulation for  $5 \times 10^{-4}$  Preclosure Run 16, at  $t = 3.01$  sec)

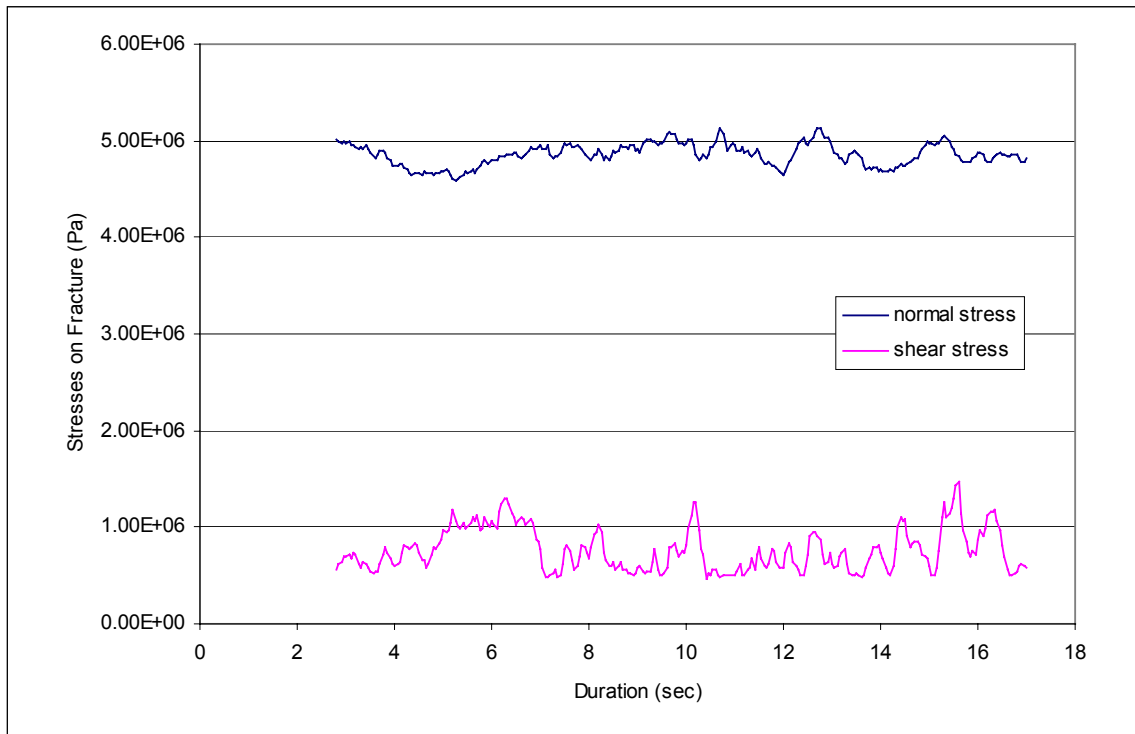


Figure 64. Time Histories for Normal and Shear Stress at Fracture Contact Coordinate: -5.106, 0.681, -5.306 (3DEC  $5 \times 10^{-4}$  Preclosure Simulation 19)

Drift Degradation Analysis

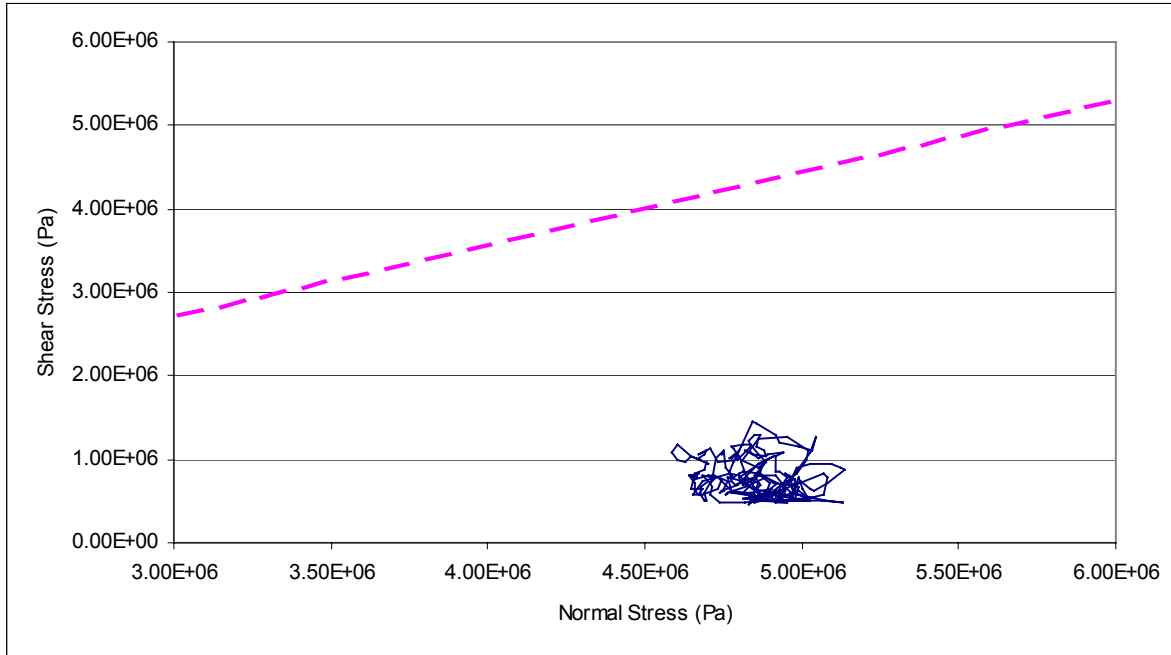


Figure 65. Normal and Shear Stress Path at Fracture Contact Coordinate: -5.106, 0.681, -5.306 (3DEC  $5 \times 10^{-4}$  Preclosure Simulation 19)

Table 18. Summary of 3DEC Rockfall Prediction for  $5 \times 10^{-4}$  Annual Probability of Exceedance Hazard

Simulations Completed	25
Number of Simulations Predicting No Rockfall	14
Total Number of Rockfall	37
Total Volume of Rockfall (m <sup>3</sup> )	7.3
Total Length of Drift Simulated (m)	625
Number of Blocks per km	59
Volume of Rockfall per km (m <sup>3</sup> )	4.8

Table 19. Statistical Summary of the Rockfall Impact Parameters,  $5 \times 10^{-4}$  Annual Probability of Exceedance Hazard

	Block Mass (tonnes)	Relative Impact Velocity (m/sec)	Impact Angle (degree)	Impact Momentum (kg-m/sec)	Impact Energy (Joules)
Mean	0.47	2.22	159	1101	1518
Median	0.17	2.08	131	175	237
Standard Deviation	0.73	1.11	82	1923	3081
Skewness	2.20	0.33	1.12	3.23	4.17
Range	2.87	4.98	309	10040	17493
Minimum	0.02	0.06	47	22	1
Maximum	2.89	5.05	355	10062	17494
Sum	17.51	NA <sup>a</sup>	NA <sup>a</sup>	40724	56169

NOTE: <sup>a</sup> Not Applicable

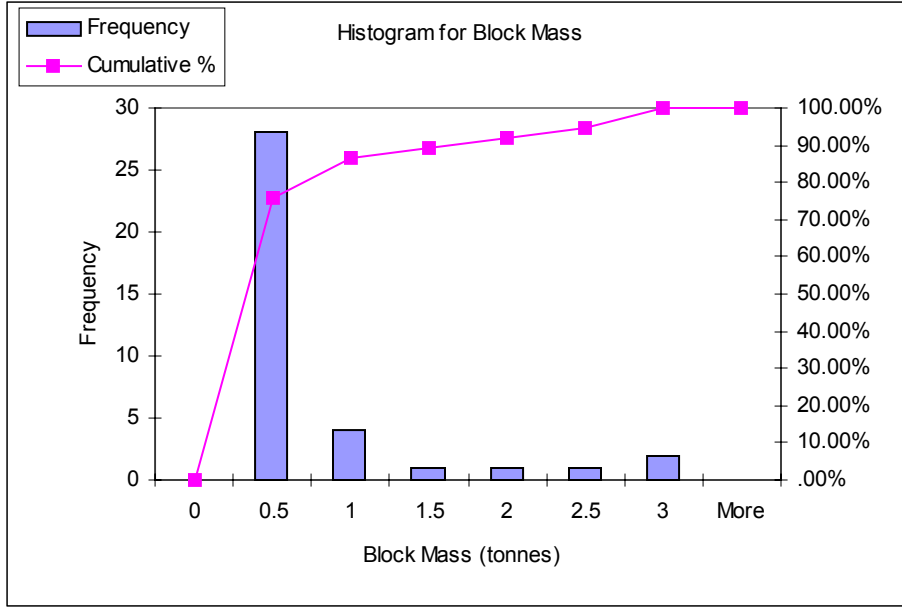


Figure 66. Histogram for Block Mass ( $5 \times 10^{-4}$  Annual Probability of Exceedance Hazard)

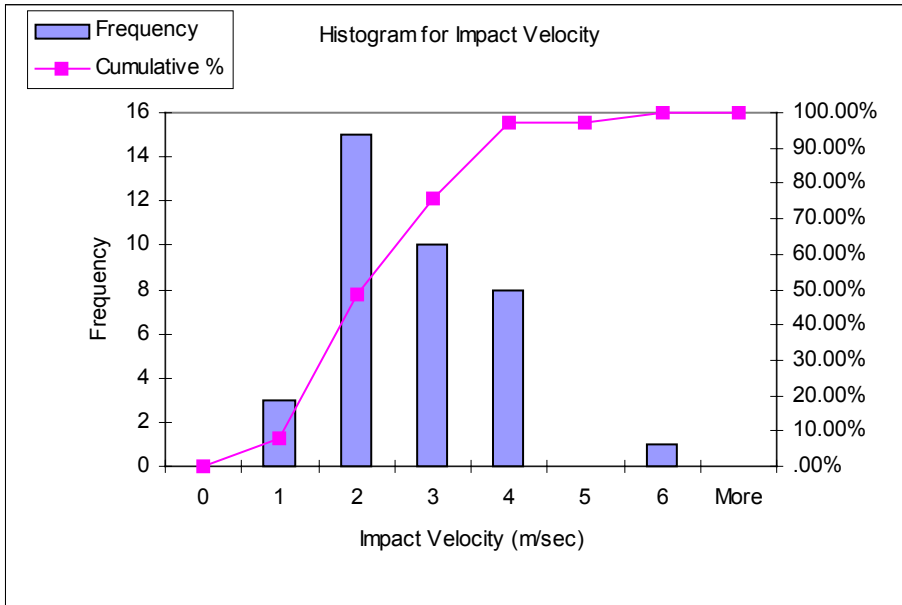


Figure 67. Histogram for Impact Velocity ( $5 \times 10^{-4}$  Annual Probability of Exceedance Hazard)

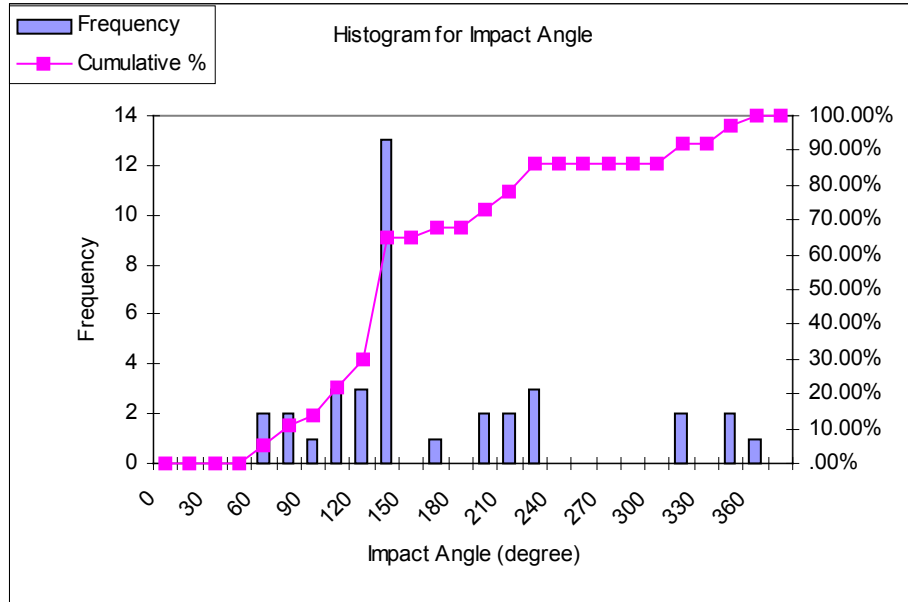


Figure 68. Histogram for Impact Angle ( $5 \times 10^{-4}$  Annual Probability of Exceedance Hazard)

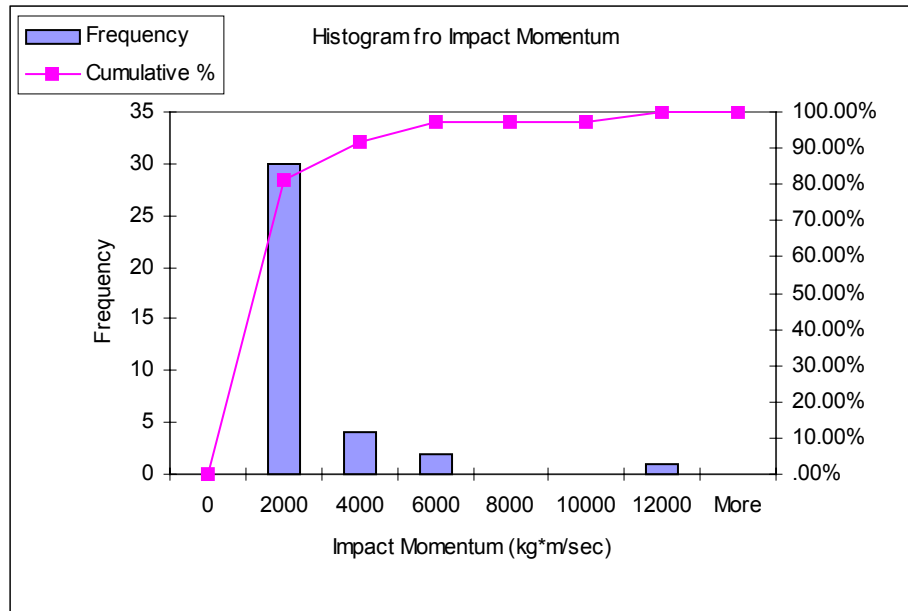


Figure 69. Histogram for Impact Momentum ( $5 \times 10^{-4}$  Annual Probability of Exceedance Hazard)

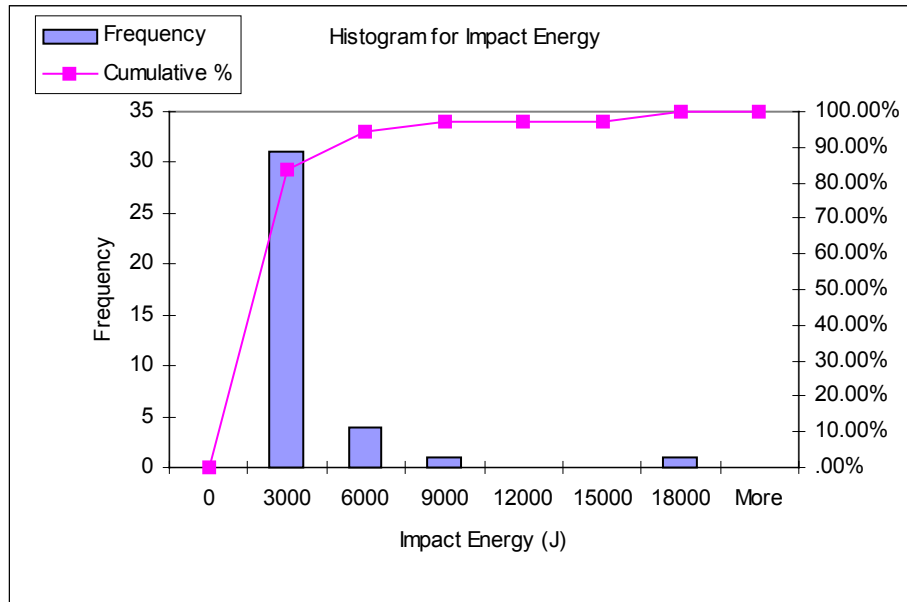


Figure 70. Histogram for Impact Energy ( $5 \times 10^{-4}$  Annual Probability of Exceedance Hazard)

### 6.3.1.3 Thermal Consideration in Nonlithophysal Units

The extensive analysis of drift stability in nonlithophysal units discussed in Section 6.3.1.2 has been conducted considering an in situ stress state perturbed by the excavation of the emplacement drifts only. The effects of the thermally generated stresses in the rock mass surrounding the repository were not taken into account. This section provides the results for the analyses including thermal consideration.

3DEC was not used for the thermal-mechanical analysis of the drift in the nonlithophysal units because it has a simplistic model of heat conduction based on analytic solutions, which deals with complicated boundaries in an approximate way. Instead, the analysis for the nonlithophysal units was done as a three-step process. Variation of temperatures throughout the rock mass due to heating was calculated using NUFT, which generated temperature fields for a number of times after waste emplacement. This implies that the mechanical models that use those temperature fields will be subjected to discrete temperature and, consequently, stress changes when moving from one temperature state to another. In reality, those changes are continuous. Because the mechanical models of drift stability are non-linear, their results are path-dependent. To ensure that the model results are not affected by discrete stress changes, the temperature increment was limited to around  $5^{\circ}\text{C}$ . It was difficult to perform thermal stress calculations in the 3DEC model because it is limited to a certain region around the drift. Also, the model axes are oblique relative to the drift axis, making it very difficult to extend the model to the plane of symmetry between the drifts, which is necessary for stress calculation due to heating. Therefore, the stress changes due to the temperature changes, as calculated by NUFT and described in Section 6.2, were calculated using the continuum code FLAC. In the next step, elastic stress states are imported from FLAC into 3DEC in a sequential manner. For each elastic stress change due to temperature change, 3DEC is first run elastically to equilibrium (all joints were elastic).

Subsequently, the finite strength was assigned to the joints, and the new equilibrium was determined.

Thermal-mechanical analysis was conducted for two sets of thermal rock mass properties (discussed in Section 6.2): (a) the base case, using the mean values of thermal conductivity and specific heat, and (b) the thermal sensitivity case, using the values for thermal conductivity and specific heat one standard deviation smaller than the mean. The values for the sensitivity case thermal properties are provided in Section 6.2.

The fracture modeling regions from the following combinations of fracture modeling region and  $1 \times 10^{-6}$  ground motion set were analyzed: (a) Cases 55 and 58 (most seismically induced rockfall), (b) Case 47 (typical rockfall), and (c) Case 87 (no rockfall). The corresponding fracture modeling regions and ground motions sets for those four cases are provided in Table 12. There was no rockfall due to heating only for any of the cases analyzed, neither for the base case of thermal properties, nor for the sensitivity case for thermal properties. The stress paths (shear stress versus normal stress) on the joints around the drift (in the wall and the roof) for the base-case thermal properties and case 47 are shown in Figures 71 and 72. For most of the points (particularly in the wall), the stress paths move away from the slip surface, indicating increasing block stability. The analysis is carried out considering the blocks to be elastic. In order to demonstrate that heating will not induce stress levels inside the blocks sufficient to cause damage, stress paths from the linearly elastic model (for nonlithophysal rock stiffness) are shown in Figures 73 and 74 relative to the Mohr-Coulomb yield surface (using an unconfined compressive strength of 70 MPa and a  $40^\circ$  friction angle). In both the wall and the roof, thermally induced stress variations are well within the elastic region. The approach of linear block behavior during thermal loading is justified. The effect of ground motions, in addition to thermal loading, is discussed in Section 6.3.1.4.

#### **6.3.1.4 Combined Seismic and Thermal Effect in Nonlithophysal Units**

The effect of the thermal stresses on seismic drift stability depends on how the stress state, throughout the rock mass and on the pre-existing joints, changes in the stress space relative to the failure surface. If the stress state (particularly in the vicinity of the drifts) predominantly moves away from the failure surface due to stress changes caused by heating, the rock mass becomes more stable and resistant to ground shaking. However, if the stress state predominantly moves towards the yield surface or reaches it (i.e., rock mass yields during the heating), there will be more rockfall caused by ground motion. It is difficult to determine a single index or condition that characterizes this effect in an integrated way for the entire rock mass.

Drift Degradation Analysis

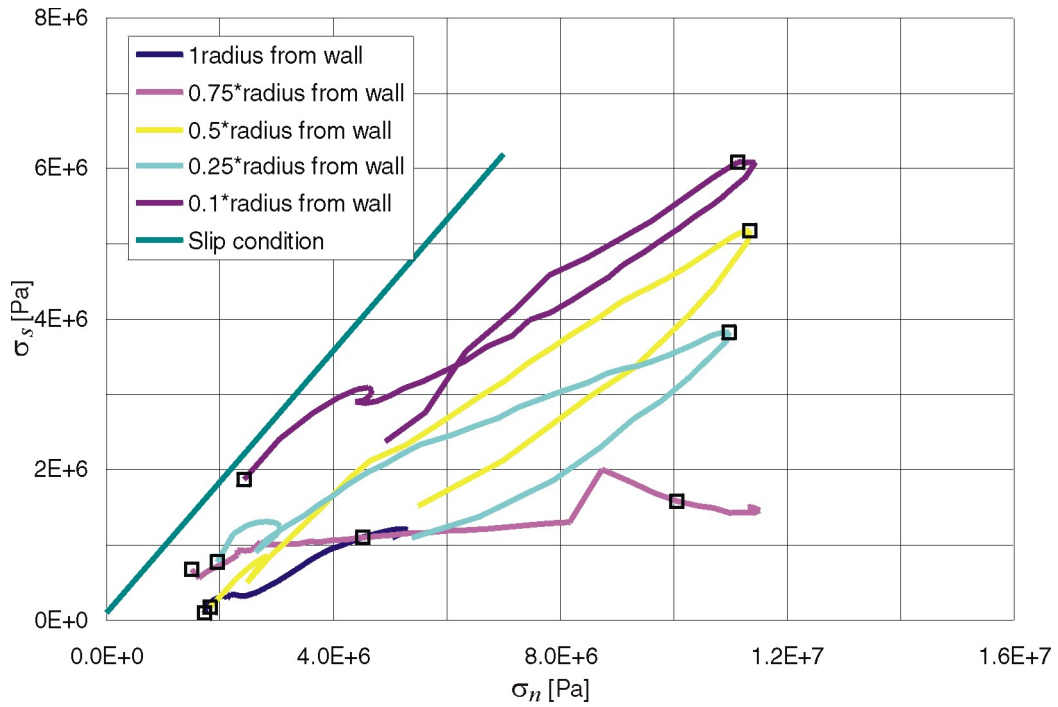


Figure 71. Stress Paths in the Drift Wall: Case 47

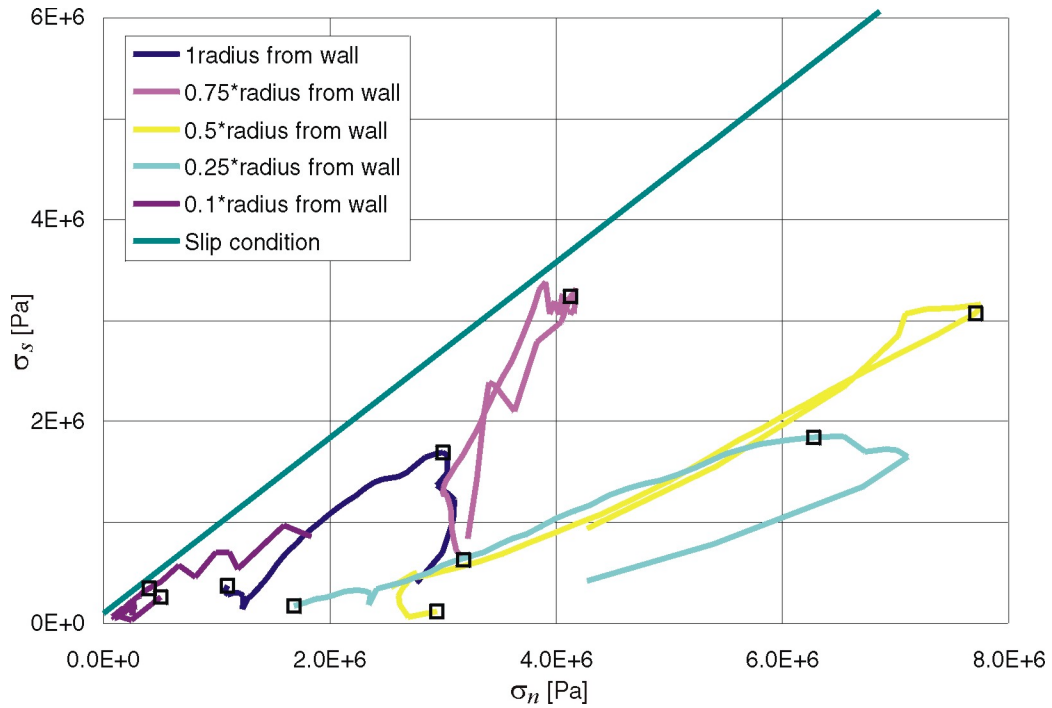


Figure 72. Stress Paths in the Drift Roof: Case 47

Drift Degradation Analysis

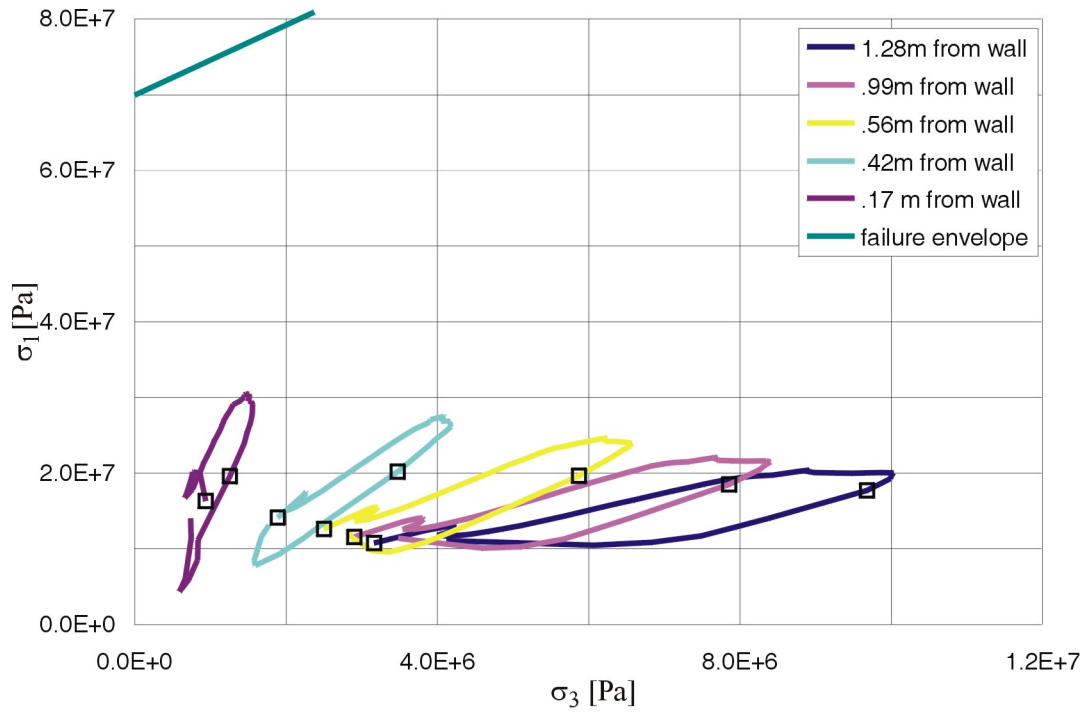


Figure 73. Stress Paths in the Drift Wall: Elastic Model

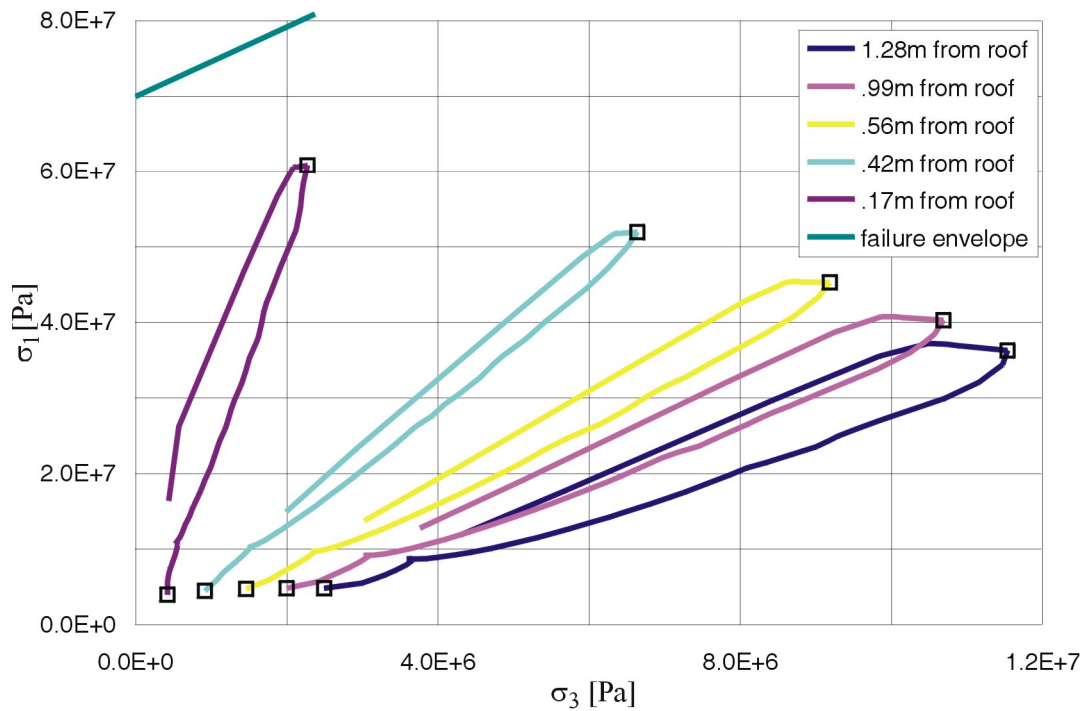


Figure 74. Stress Paths in the Drift Roof: Elastic Model

Temperatures around the emplacement drift will increase for a certain period of time after emplacement of the waste; however, as a result of decay of the released heat, the temperatures will also decrease. Consequently, the stress state around the repository during the regulatory period will be transient. A simplified approach was adopted in which rockfall caused by ground shaking was estimated for the “most critical” stress state during the regulatory period. Stress paths at a number of locations on the joints surrounding the drift were recorded during the temperature changes. The critical state (or time after waste emplacement) was determined by qualitative inspection of those stress paths. The model in the most critical state during the regulatory period was then subjected to a ground motion corresponding to  $1 \times 10^{-6}$  probability of annual occurrence.

The effect of seismic shaking combined with thermal-mechanical effects was considered for characteristic cases (combinations of fracture modeling regions and ground motions) presented in Section 6.3.1.3. As mentioned, stress paths at five points on joints in the wall and the roof of the drift, for the base case of thermal properties (shown in Figures 71 and 72), move away, in general, from the yield surface (particularly at the points in the wall shown in Figure 71). The critical state seems to be the in situ stress state (marked with a square at the beginning of each curve) for which extensive seismic stability analysis had been conducted. Another state of interest was the other extreme point on the stress path curves (also marked with a square), which, for case 47 represented in Figures 71 and 72, corresponds to 80 years after waste emplacement. Stress paths for the thermal sensitivity case (case 2) are presented in Figures 75 and 76.

The critical stress states for both the base and the thermal sensitivity cases are determined in a similar manner for other jointing cases. These states are indicated in Tables 20 and 21 (as “time of ground motion”), which also summarize total rockfall after shaking the models with specified ground motions. Clearly, heating significantly reduces the amount of rockfall. Also, the thermal sensitivity case results in higher temperatures and less rockfall than the base case. These results are consistent with the stress paths shown in Figures 71 and 72. The results of rockfall analysis in nonlithophysal units for in situ stress conditions are conservative since they over predict the number of unstable blocks and total volume of rockfall, because temperatures throughout the regulatory period will be larger than in situ temperatures.

### **6.3.1.5 Rock Joint Degradation in Nonlithophysal Units**

The rock mass surrounding the excavations may undergo over-stressing from thermal heating and/or time-dependent damage associated with static fatigue resulting from stress corrosion mechanisms. Another likely long-term effect includes the increasing amounts of moisture/air induced weathering along the joints close to the tunnels. This damaged and/or weathered material may result in block fallout in the nonlithophysal units.

# Drift Degradation Analysis

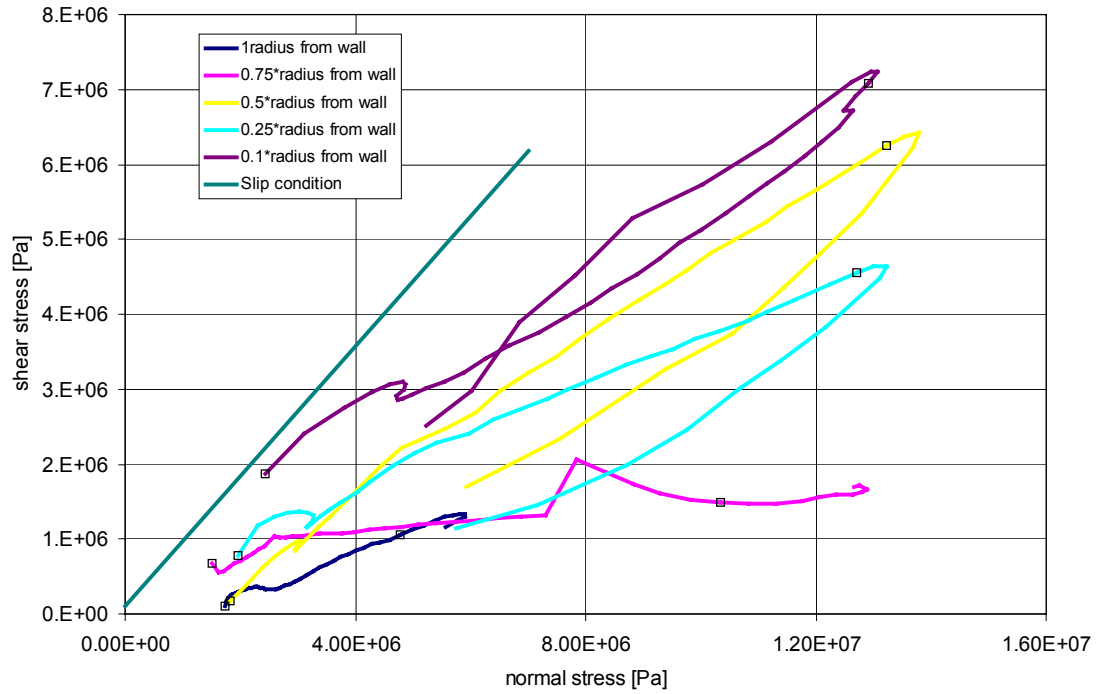


Figure 75. Stress Paths in the Drift Wall: Case 47, Thermal Sensitivity Case 2

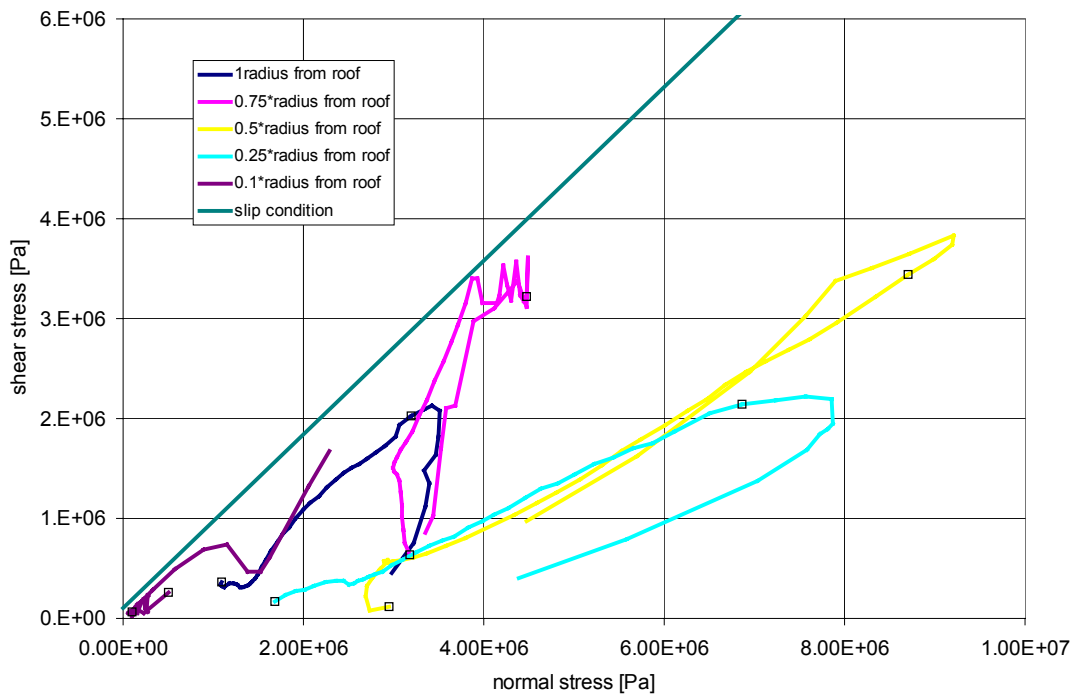


Figure 76. Stress Paths in the Drift Roof: Case 47, Thermal Sensitivity Case 2

Table 20. Rockfall in Nonlithophysal Rock Due to  $10^{-6}$  Ground Motion Combined with Thermal-Mechanical Effects: Base Case of Thermal Properties

Case	Ground Motion	Joint Pattern	Time of Ground Motion (year)	Number of Blocks	Rockfall Volume (m <sup>3</sup> )	Time of Earthquake (year)	Number of Blocks	Rockfall Volume (m <sup>3</sup> )
58	4	8	0	44	42.26	80	5	0.58
55	12	16	0	21	12.99	80	2	1.54
47	8	103	0	2	0.08	80	0	0.00
87	2	73	0	0	0.00	300	0	0.00

Table 21. Rockfall in Nonlithophysal Rock Due to  $10^{-6}$  Ground Motion Combined with Thermal-Mechanical Effects: Thermal Properties One Standard Deviation Less Than Mean

Case	Ground Motion	Joint Pattern	Time of Ground Motion (year)	Number of Blocks	Rockfall Volume (m <sup>3</sup> )	Time of Earthquake (year)	Number of Blocks	Rockfall Volume (m <sup>3</sup> )
58	4	8	0	44	42.26	70	5	0.59
55	12	16	0	21	12.99	80	0	0.00
47	8	103	0	2	0.08	70	0	0.00
87	2	73	0	0	0.00	70	0	0.00

Static fatigue of hard rocks typically is associated with stress levels on the order of 60 to 80 percent of the uniaxial compressive strength. Fatigue failure would presumably initiate along asperities on fracture surfaces, reducing the effective friction angle along the fracture surfaces. Uniaxial static fatigue tests on nonlithophysal rock from the Tptpmn are on going. The result of these tests will be an estimate of time to failure for stress levels at a given percentage of the uniaxial compressive strength. The data from static fatigue testing will be used as a basis for examination of its impact on shear strength of discontinuities.

Since the results from static fatigue testing are not available at this time, the drift stability due to the effect of rock joint degradation is assessed based on a conservative estimate of the reduction of joint cohesion and friction angle. The reduced joint strength parameters are estimated to be in the range of the residual state with joint cohesion reduced to 0 and the joint friction angle reduced to 30°. The reduced friction angle is a typical value for a smooth joint reported by Goodman (1980, p. 158) and is consistent with the direct shear test results (DTN: GS030283114222.001 [see Records Processing Center Package #MOY-030226-41-01 (MOL.20030226.0038 through MOL.20030226.0042, pp. 2-6) associated with this DTN.]). Dilation angle is also conservatively presumed to be zero considering the asperities on fracture surfaces had been sheared off, resulting in greater rockfall. The degraded joint strength and dilatational properties were applied in  $1 \times 10^{-6}$  seismic motion cases 58, 55, 47, and 87. These 4 cases represent the two worst cases, the median case, and the best case as reported in Section 6.3.1.2.3. The predicted number of rockfall and the total rockfall volume are presented in Table 22 with a comparison to the base case. While a slight increase in rockfall is predicted for the degraded state, joint strength degradation has a minor impact on drift stability in nonlithophysal rock.

Table 22. Predicted Rockfall for Degradated Joints with Comparison to the Base Case

Case	Degradated State (cohesion = 0, friction angle = 30°, dilation angle = 0°)		Base Case (cohesion = 0.1 MPa, friction angle = 41°, dilation angle = 0°)	
	Number of Blocks	Rockfall Volume (m <sup>3</sup> )	Number of Blocks	Rockfall Volume (m <sup>3</sup> )
Case 58 (fracture modeling region #8, 1×10 <sup>-6</sup> ground motion #4)	46	47.32	44	42.26
Case 55 (fracture modeling region #16, 1×10 <sup>-6</sup> ground motion #12)	25	12.81	21	12.99
Case 47 (fracture modeling region #103, 1×10 <sup>-6</sup> ground motion #8)	5	0.13	2	0.08
Case 87 (fracture modeling region #73, 1×10 <sup>-6</sup> ground motion #2)	0	0	0	0.00

### 6.3.1.6 Sensitivity Study of the Parameters

There are four major variable sets included in the three-dimensional discontinuum analysis: ground motions, joint geometrical properties, joint and intact mechanical properties, and thermal stress history. A total of 15 sets of ground motions were used for each hazard level in the postclosure consideration to ensure a reasonable distribution of spectral shapes and time history durations. Section 6.3.1 provides the description of the ground motions used. Results for the sensitivity study on the energy contents, duration, and orientation of horizontal motions in the 3DEC model to the rockfall prediction are presented in Section 6.3.1.6.1.

The variability of joint geometrical properties is incorporated in the application of FracMan to generate a 100-m cube fracture network. A total of 76 drift locations were selected from the 100-m cube fractured rock mass for the 3DEC analyses. Results from the analyses of 76 drift locations (or fracture modeling regions) cover the variability of joint geometrical properties.

The results presented in previous sections are based on the base-case material properties presented in Table 7. The impact of the variability of joint properties to rockfall prediction is described in Section 6.3.1.6.2. A linear elastic material is used as the intact block material for the base case. The likelihood of breaking and spalling of the intact rock subject to vibratory ground motions is discussed in Section 6.3.1.6.3.

Other sensitivity and uncertainty studies include model dimension and block deletion after impacting drip shield. These are addressed in Sections 6.3.1.6.4 and 6.3.1.6.5, respectively.

#### 6.3.1.6.1 Ground Motion Variation

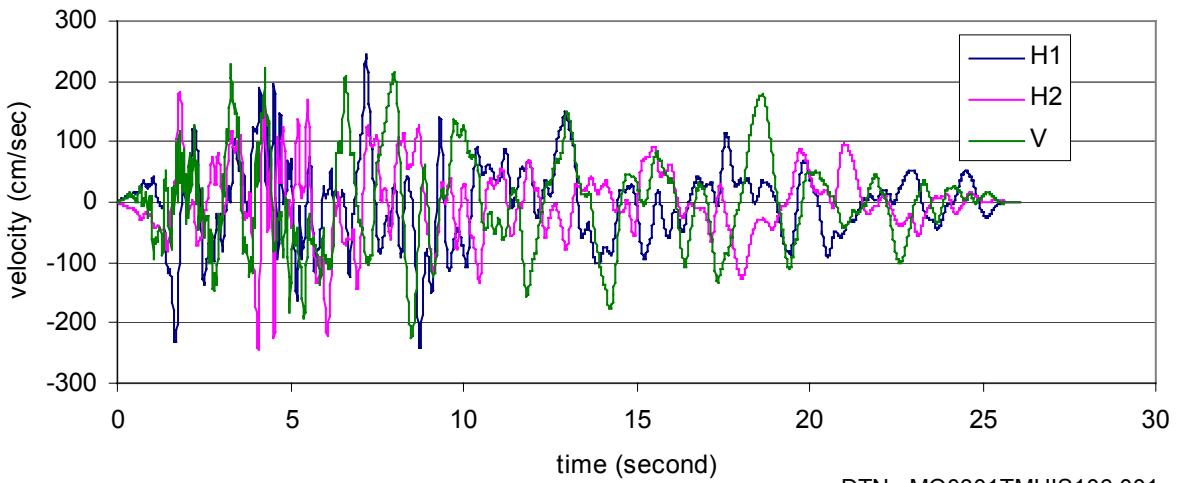
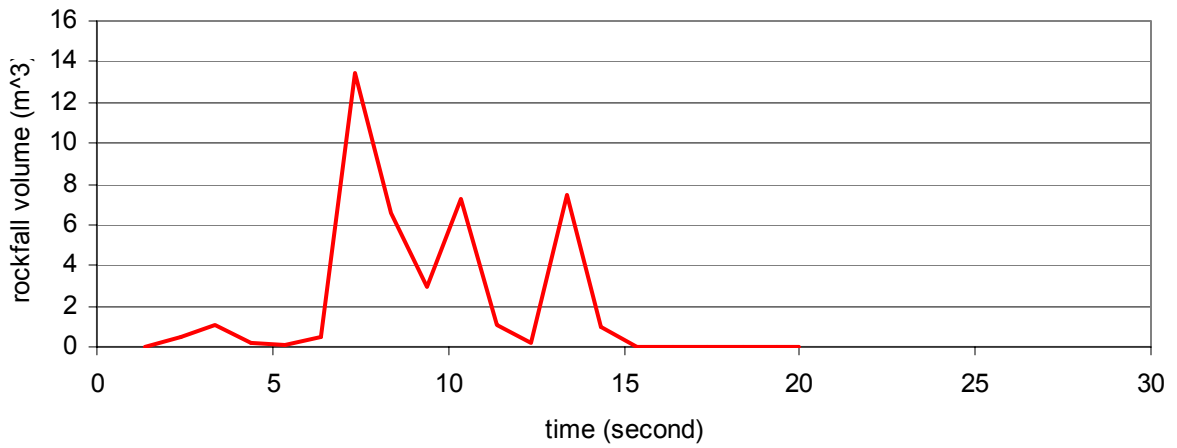
The effect of energy content to rockfall prediction was investigated using 12 fracture modeling regions versus ground motion pairs as shown in Table 23, with the associated sum of Arias Intensity for the three components listed beside the ground motion identifier. The 1×10<sup>-6</sup> ground motions were randomly selected in this study. The predicted number of rockfall and the total rockfall volume are presented in Table 23. Out of the 12 pairs, identical results were obtained for 7 pairs. The remaining 5 pairs show minor difference on rockfall prediction. More rockfall was predicted with higher energy for 3 pairs, however, contrary results were obtained for the

other 2 pairs. It appears that the energy content of the ground motion within the same level of annual probability of exceedance does not directly impact the amount of rockfall.

The duration truncation method of 5 to 95 percent plus 5 seconds energy bracket was used in the 3DEC analysis, as described in Section 6.3.1.2.1. Data for rockfall volume versus seismic shaking time was extracted to elucidate the effect of the duration to rockfall prediction. Figures 77 to 79 present the rockfall volume during the seismic shaking juxtaposed with the corresponding ground motions for 3 cases. In Case 58, shown in Figure 77 as the case with the most rockfall, the majority of the rockfall occurs in between 5 to 15 seconds of shaking. No rockfall was observed after 15 seconds. In Case 55, the case with the second largest volume of rockfall as shown in Table 24, blocks fall mainly in the first 10 seconds of shaking, with a minor rockfall occurring at around 18 seconds. Rockfall appears to be synchronized with the ground motions in this case. In Case 47, the median case in terms of rockfall volume, blocks fall at the first impulse of strong ground motion, but there is no rockfall for the remaining duration of the shaking. This is typical for most of the cases with minor rockfall. Based on the truncation method of 5 to 95 percent plus five seconds energy bracket, the duration appears to be adequate based on the above observation.

Table 23. Comparison of Rockfall Prediction on Energy Content of Ground Motions

Pair	Fracture Modeling Region	Ground Motion Set	Sum of Arias Intensity for Three Components of Ground Motion (m/sec)	Number of Rockfall	Total Rockfall Volume (m <sup>3</sup> )
1	1	3	195	0	0.000
	1	9	303	0	0.000
2	2	1	1032	1	0.323
	2	13	269	1	0.323
3	7	2	928	14	1.522
	7	12	254	10	1.106
4	8	4	638	44	42.257
	8	14	636	39	40.745
5	13	1	1032	0	0.000
	13	16	151	0	0.000
6	15	4	638	5	0.416
	15	12	254	6	0.579
7	16	2	928	21	14.109
	16	12	254	21	12.989
8	18	6	272	1	0.217
	18	7	339	1	0.217
9	20	4	638	0	0.000
	20	7	339	0	0.000
10	24	6	272	0	0.000
	24	16	151	2	0.301
11	28	8	312	0	0.000
	28	14	636	0	0.000
12	29	3	195	0	0.000
	29	8	312	0	0.000



DTN: MO0301TMHIS106.001

Figure 77. Rockfall vs. Time of Shaking for  $1 \times 10^{-6}$  Ground Motion Set 4, Case 58

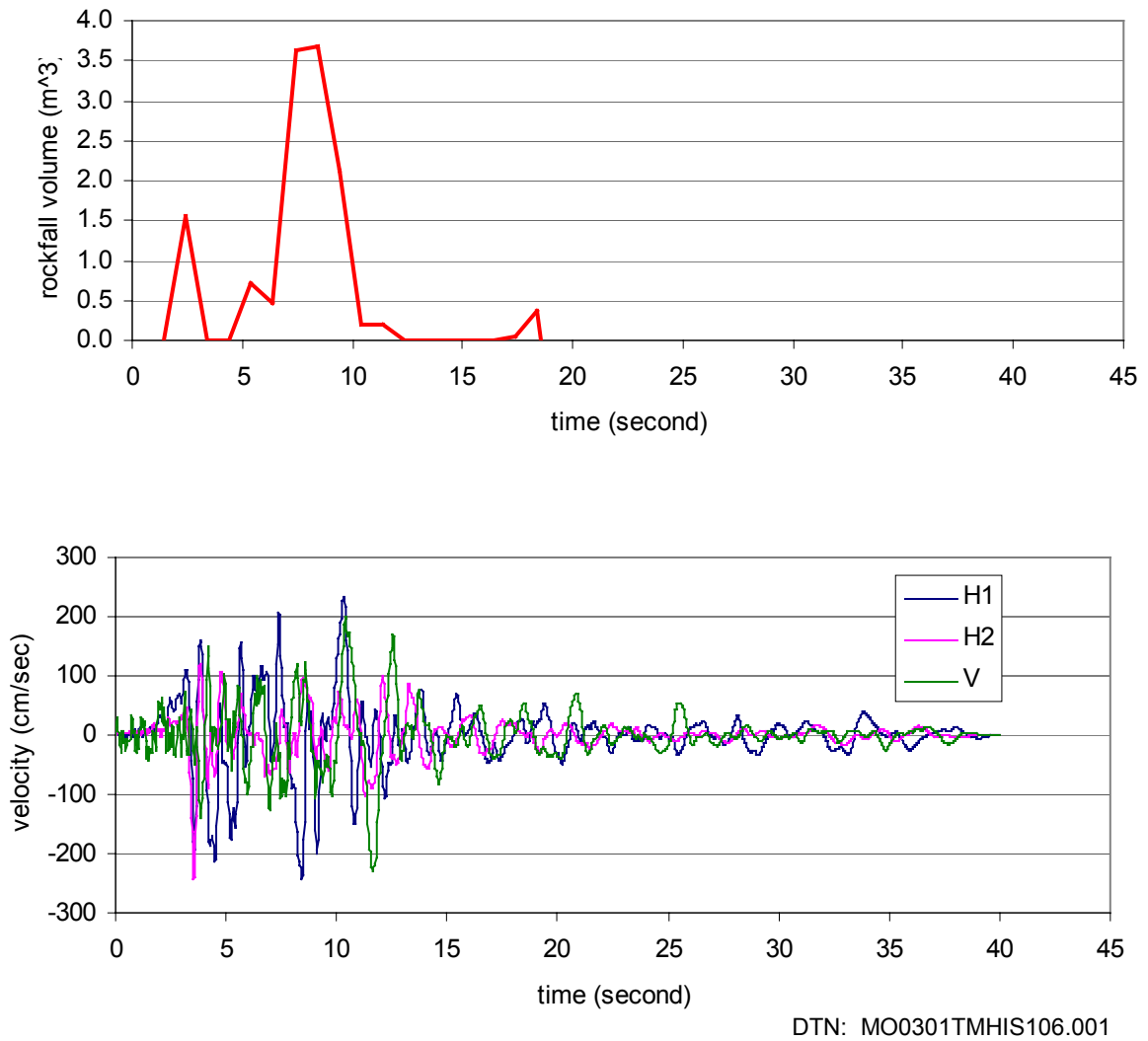


Figure 78. Rockfall vs. Time of Shaking for  $1 \times 10^{-6}$  Ground Motion Set 12, Case 55

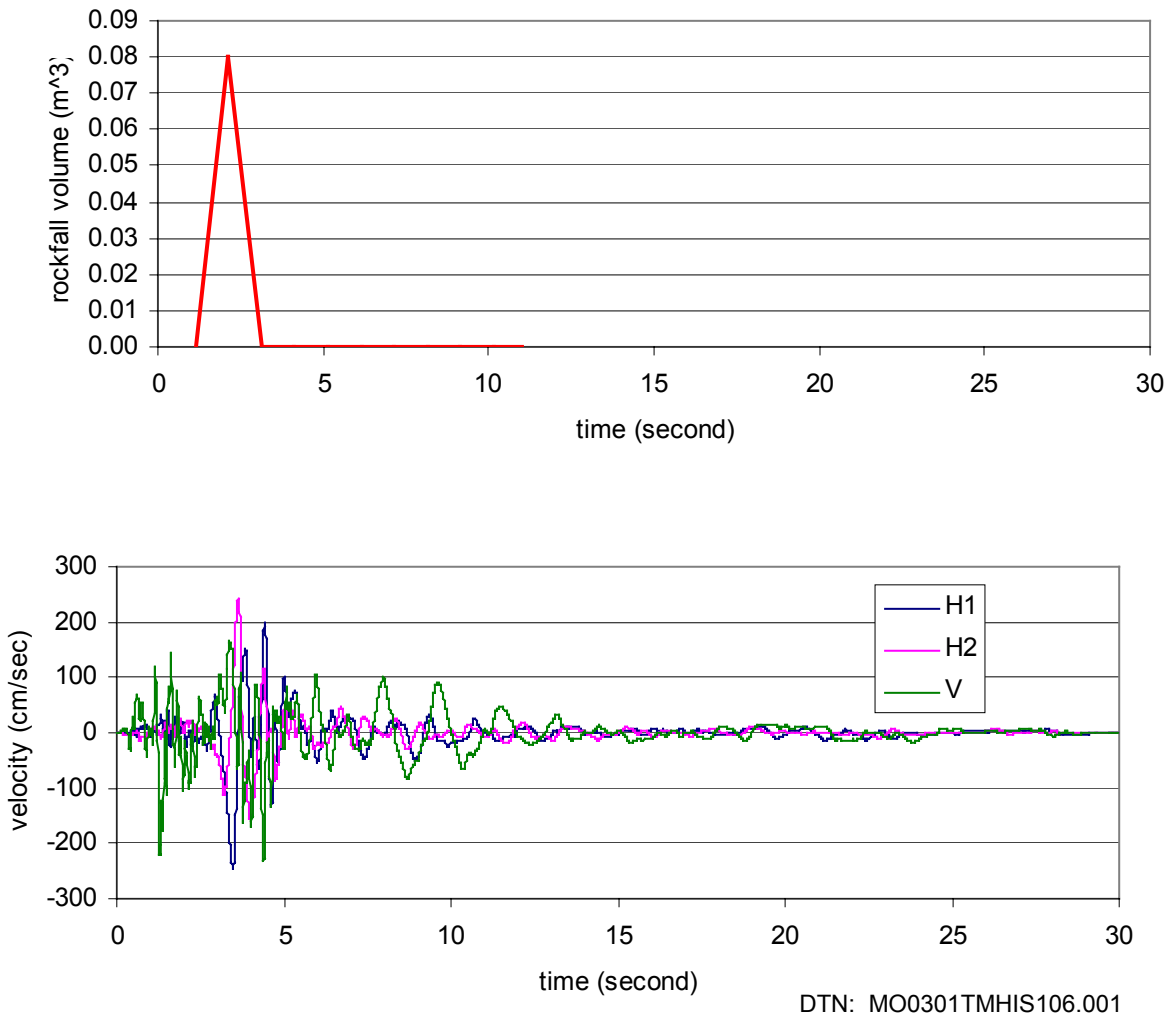


Figure 79. Rockfall Vs Time of Shaking for  $1 \times 10^{-6}$  Ground Motion Set 8, Case 47

The orientation of horizontal motions is conveniently specified as H1 parallel to the x-axis and H2 parallel to the z-axis (the North direction) in the 3DEC model (3DEC coordinate system is shown in Figure XII-1). An alternative approach with H1 parallel to the z-axis (North) and H2 parallel to the x-axis was used to check the sensitivity of the orientation. Table 24 presents the comparison of the predicted rockfall with the two approaches. The difference is minor in general, which is expected since the amplitudes of the peak motions are similar for the two horizontal components of the ground motion.

Table 24. Impact of the Orientation of Horizontal Motions to the Rockfall Prediction

Case	Fracture Modeling Region	Ground Motion Set	Original Approach (H2 as North)		Alternative Approach (H1 as North)	
			Number of Rockfall	Total Rockfall Volume (m <sup>3</sup> )	Number of Rockfall	Total Rockfall Volume (m <sup>3</sup> )
Case 58	8	4	44	42.26	46	46.13
Case 55	16	12	21	12.99	13	7.28
Case 35	33	11	34	10.27	39	12.27
Case 45	39	10	35	7.38	34	7.37
Case 27	14	6	5	3.48	0	0
Case 43	59	4	6	3.04	5	3.48
Case 80	93	1	4	2.74	5	2.89
Case 69	11	10	1	1.85	4	2.74
Case 85	100	1	5	1.76	4	1.33
Case 20	19	5	3	1.47	3	1.47

### 6.3.1.6.2 Joint Material Properties Variation

The base-case joint properties, listed in Table 7, were based on the rotary shear tests of the cored specimen as derived in Attachment V. Additional direct shear tests are in progress, and the preliminary results from these tests are used to provide the range of variation. With limited joint test results currently available and the fact that the use of rotary shear devices in rock mechanics is sparse, some of the parameters in the base case, such as cohesion and dilation angle, were scaled down from the testing results for conservatism, to allow for increased rockfall.

A range of joint properties, as shown in Table 25, was selected for the sensitivity study. The values were established based on the residual friction angle of 30° (see Section 6.3.1.5) and three tiers of dilation angles. The dilation angles were selected within the range of reported test results presented in Attachment V. Cohesion is conservatively set to 0. The joint stiffness values were taken from work by Barton (Duan 2003) based on the formulation of Barton-Bandis joint model (Barton and Choubey 1977) and the preliminary direct shear test data (DTN: GS030283114222.001). The joint normal stiffness value is reported to be in the range of 2 to 3 orders of magnitude higher than the shear stiffness value in *An Application of Rock Mass Characterization and Rock Joint Empirical Models at Yucca Mountain, to Assist in the Disposal Tunnel Design Studies* (Duan 2003). Numerical difficulty was encountered with the large difference in the normal and shear stiffness values in 3DEC modeling. The solution was to scale down the normal stiffness value to 20 times the shear stiffness value as listed in Table 25. The scaling value of 20 is based on the range of joint normal stiffness values observed in rotary shear tests (Table V-4). The maximum joint normal stiffness was estimated to be  $90 \times 10^4$  MPa/m in Table V-4, which is approximately 18 times the base-case shear stiffness ( $5 \times 10^4$  MPa/m). The value of 20 is considered adequate to provide the contrast of the values between normal and shear stiffness.

Four cases with various combinations of fracture model region and ground motion were selected for the sensitivity analysis of joint mechanical properties. These four cases represent the two worst cases, the median case, and the best case in terms of rockfall volume for  $1 \times 10^{-6}$  ground

motions (Sections 6.3.1.2.2 and 6.3.1.3). They were selected for the sensitivity analysis of joint mechanical properties. The results for the sensitivity of joint properties to the rockfall prediction are presented in Table 26. Of the three joint categories, Joint Category 1 predicts similar results as the base case. The effect of dilation angle to rockfall appears to be significant when comparing the base case with Joint Category 3 case. The base-case results are in general conservative (i.e., produce more rockfall), even comparing with Joint Categories 1 and 2 covering the probable low end of strength properties.

Table 25. Three Categories of Joint Properties Used in the Sensitivity Study

Joint Category	Joint Cohesion (Pa)	Joint Dilation Angle	Peak Friction Angle	Joint Normal <sup>a</sup> Stiffness (Pa/m)	Joint Shear <sup>a</sup> Stiffness (Pa/m)	Joint Normal Stiffness Used in 3DEC Analysis (Pa/m)
1	0	1.4	31.4	1.4E+12	2.5E+09	5.0E+10
2	0	4.4	34.4	1.2E+12	1.9E+09	3.8E+10
3	0	11	41	7.0E+11	1.7E+09	3.4E+10

NOTE: <sup>a</sup>Source: Duan 2003, attachment Tables 5.2 and 5.3.

Table 26. Sensitivity of Joint Properties for Rockfall Prediction

Fracture Model Region	1×10 <sup>6</sup> Ground Motion Set	Joint Property Category	Number of Rockfall	Total Rockfall Volume (m <sup>3</sup> )	Notes
8	4	Base Case	44	42.26	Case 58 in Section 6.3.1.3
8	4	Joint Category 1	46	47.54	
8	4	Joint Category 2	43	41.29	
8	4	Joint Category 3	34	22.00	
16	12	Base Case	21	12.99	Case 55 in Section 6.3.1.3
16	12	Joint Category 1	23	12.75	
16	12	Joint Category 2	25	13.44	
16	12	Joint Category 3	15	7.54	
103	8	Base Case	2	0.08	Case 47 in Section 6.3.1.3
103	8	Joint Category 1	0	0	
103	8	Joint Category 2	0	0	
103	8	Joint Category 3	0	0	
73	2	Base Case	0	0	Case 87 in Section 6.3.1.3
73	2	Joint Category 1	0	0	
73	2	Joint Category 2	0	0	
73	2	Joint Category 3	0	0	

### 6.3.1.6.3 Intact Rock Response to Vibratory Ground Motions

A linear elastic model is used to represent the intact block constitutive model for the 3DEC analysis to obtain a conservative (i.e., increased) estimate of the block volume, since breaking and spalling of the rock inside the blocks are expected considering the large amplitude of seismic waves for the postclosure ground motions. A two-dimensional discontinuum model representing the rock mass is used to evaluate the spalling mechanism in intact material at nonlithophysal

units. The rationale and justification of using two-dimensional distinct element code, UDEC, for spalling type of failure mechanism in lithophysal rock is provided in Section 6.4.1 and Section 7.7.4. The rock mass is represented as an assembly of polygonal, elastic blocks. The entire domain is discretized into blocks using Voronoi tessellations. This approach is not entirely suitable for the nonlithophysal rock mass with large amount of wedge-type failure, but is used to obtain a bounding estimate for rock spalling. Notice that many of the 3DEC dynamic simulations yield no block failure (Section 6.3.1.2), indicating that the rock mass is interconnected with rock bridges for these cases. This approach is more applicable for these cases.

The blocks used in the UDEC model do not represent the actual internal structure of the intact rock mass. They are used as a tool in the numerical model to simulate damage and fracturing of the intact rock. Joints in this model do not correspond to actual features. Calibration was conducted to ensure an assembly of Voronoi blocks behaves as an intact rock mass with material strength and stiffness consistent with nonlithophysal material properties reported in Attachment V. Calibration is done by numerical simulation of laboratory or field tests. The model parameters are varied until macro properties important for the drift stability analysis are matched with measurements from the actual tests. Stress-strain curves obtained from the numerical experiment for different conditions of confinement are shown in Figure 80. The model matches an unconfined compressive strength of 70 MPa and a Young's modulus of 24.5 GPa for the nonlithophysal rock mass material properties (Attachment V, Section V.4.4). Notice that the rock mass properties derived in Section V.4.4 for the nonlithophysal rock are based on available size-effect laboratory compression test data, such that the strength was selected as representative of the large-scale intact rock block material (the mean unconfined compressive strength of the Tptpmn core samples is approximately 170 MPa). An additional set of calibrated properties with unconfined compressive strength of 100 MPa was also obtained to cover the likely range of intact strength within the rock block. The two sets of unconfined compressive strength values provide the ranges of strength in between the intact and rock mass properties.

Other than the calibration against unconfined compressive strength test, the UDEC model also includes the consideration of the tensile test. The model is calibrated to match the tensile strength of 10 MPa, which is approximately 90 percent of the laboratory testing results (Attachment V, Table V-6). More detailed description of the calibration process and the limitation of the model are provided in Sections 6.4.1 and 7.7.4.

Figures 81 and 82 show two different responses of the intact material with unconfined compressive strength of 70 MPa subjected to  $1 \times 10^{-6}$  ground motion sets 4 and 5. Minor spalling is predicted for ground motion set 5 (Figure 81), whereas severe spalling is predicted for ground motion set 4 (Figure 82). However, if material strength is increased to 100 MPa, minor spalling, instead of severe spalling, is predicted even with  $1 \times 10^{-6}$  ground motion set 4 as shown in Figure 83.

Based on the UDEC analysis results, spalling is likely for the postclosure level ground motion. Spalling at nonlithophysal units is not expected for the preclosure ground motion. This is concluded from the preclosure seismic results for the lithophysal units as reported in Section 6.4.1.1 and the fact that the nonlithophysal intact strength is much higher than that of the

Drift Degradation Analysis

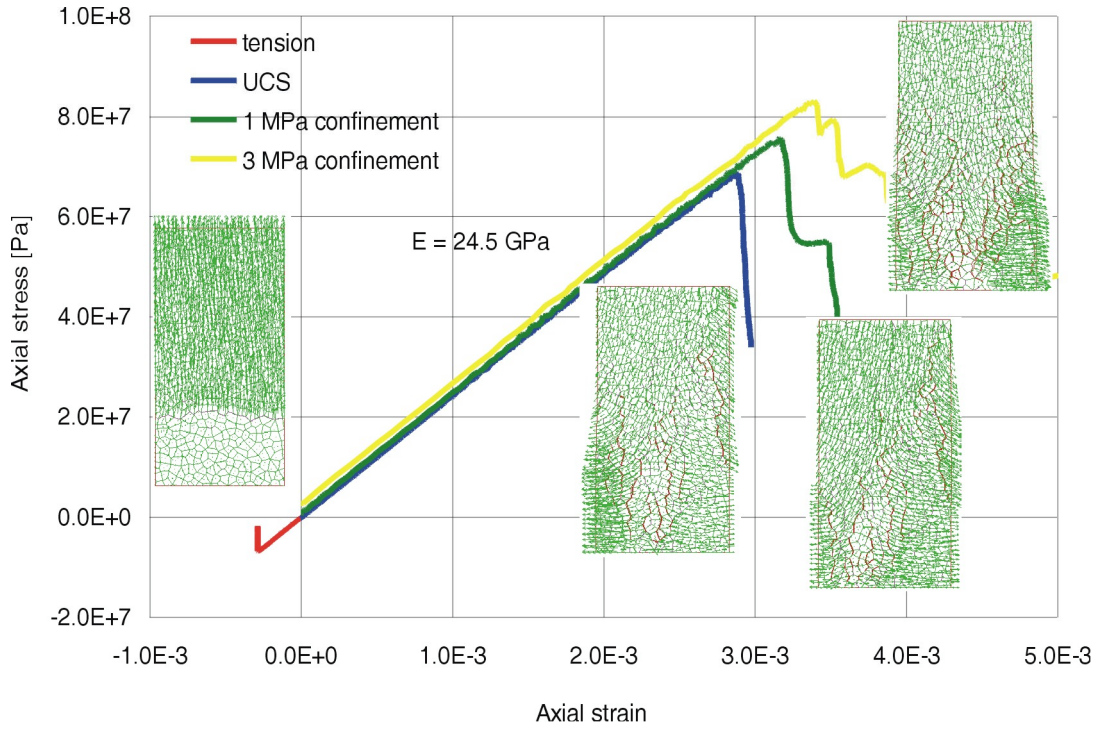


Figure 80. Calibration of Nonlithophysal Rock Mass Material Properties

Job Title :  
From File : Case5jointing7motion6final.sav

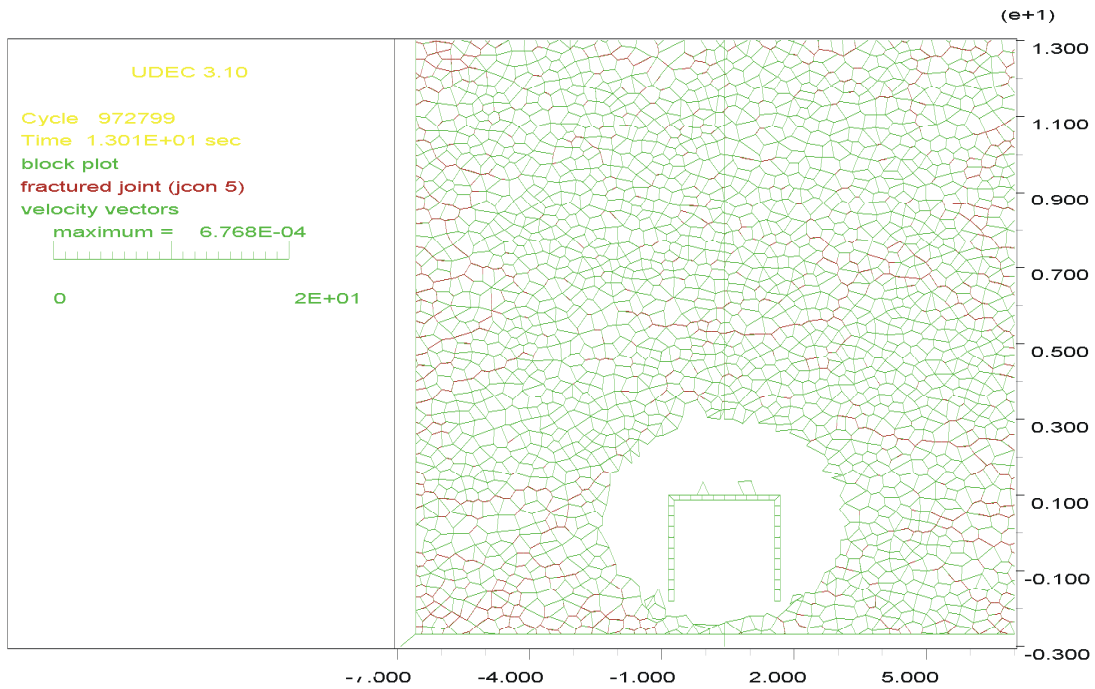


Figure 81. Minor Spalling for Intact Block (70 MPa unconfined compressive strength) Subject  $1 \times 10^{-6}$  Ground Motion Set 5

# Drift Degradation Analysis

Job Title :  
From File : Case8jointing7motion4final.sav

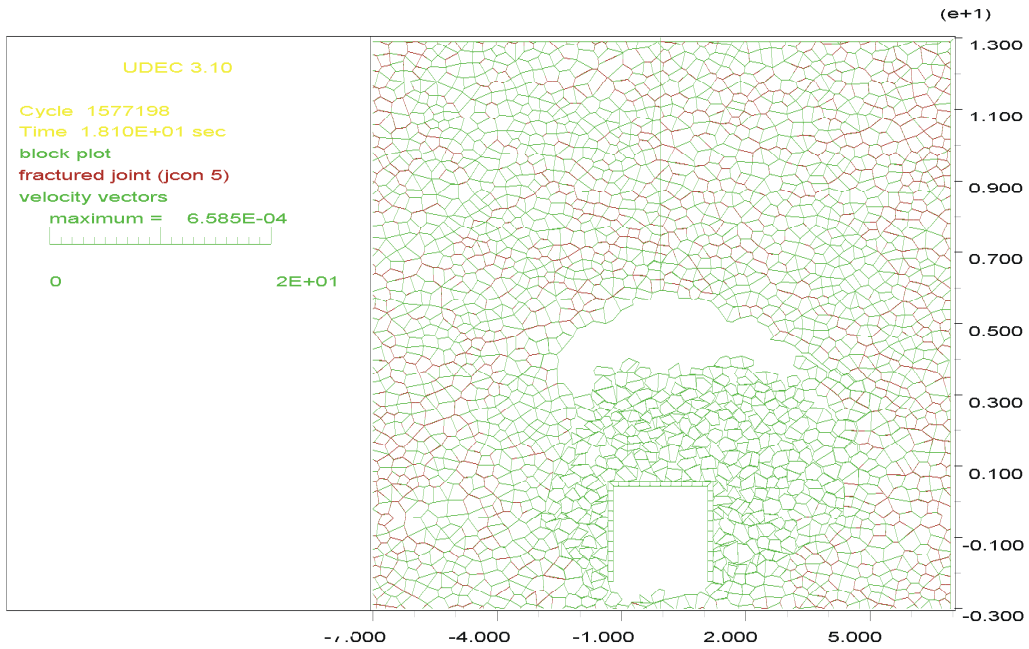


Figure 82. Severe Spalling for Intact Block (70 MPa unconfined compressive strength) Subject  $1 \times 10^{-6}$  Ground Motion Set 4

Job Title :  
From File : Up\_4.vel

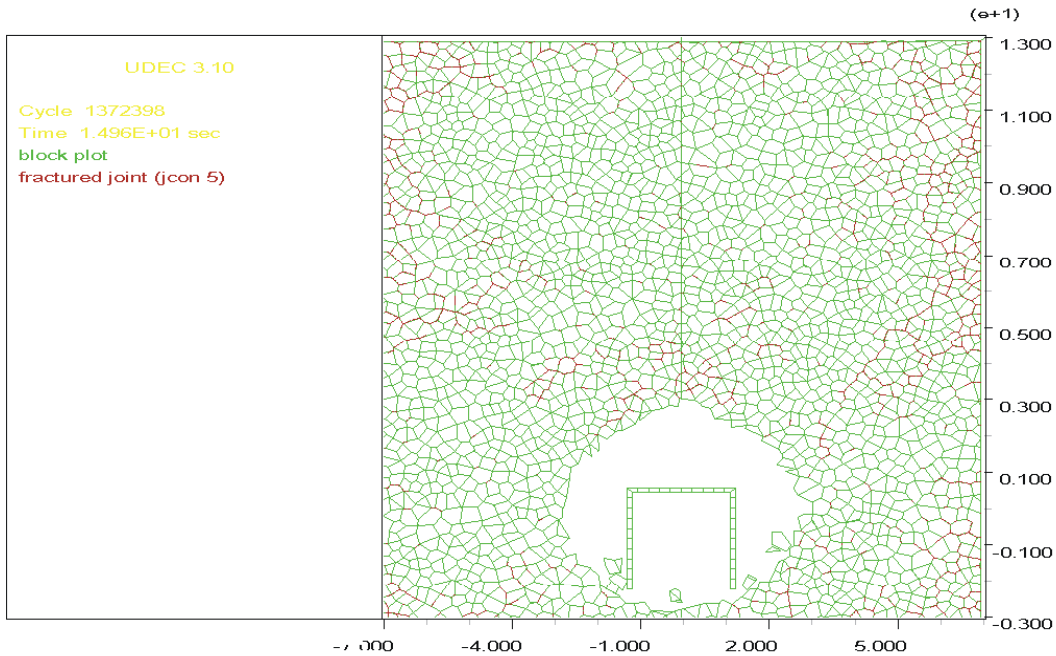


Figure 83. Minor Spalling for Intact Block (100 MPa unconfined compressive strength) Subject  $1 \times 10^{-6}$  Ground Motion Set 4

lithophysal rock. The analyses results presented in this section do not consider the impact of thermal stress. Thermal stress is found to have adverse effect on the spalling mechanism as presented in Section 6.4.1.2.

#### 6.3.1.6.4 Model Dimension

As described in Section 6.3.1.1, the 3DEC base-case model is slightly larger than a 25-m cube (the actual size: 25-m × 27.5-m × 25-m) with the tunnel oriented at 75° azimuth. The region with detail fractures imported from FracMan is one diameter at the side of the tunnel (dimension s) and two diameters on top of the tunnel for the base case (dimension t). Additional analyses with various modeling dimensions were conducted to investigate the sensitivity of model dimension to rockfall prediction. Table 27 lists the additional 3 model dimensions used for the sensitivity runs. The x-axis length (15° clockwise from the drift axis) remains constant at 25 m for all cases.

Table 27. Various Model Dimension for Sensitivity Study

Model Size	Model Dimension (m)	s <sup>a</sup> (m)	t <sup>b</sup> (m)
small	25×25×25	2.75	5.5
base case	25×27.5×25	5.5	11
large 1	25×33.75×30	8	16.5
large 2	25×38.75×37.5	11	22

NOTES: <sup>a</sup>s = horizontal distance away from the side wall.  
<sup>b</sup>t = vertical distance away from the roof.

Cases 58 and 55 of the  $1 \times 10^{-6}$  ground motion cases, the two worst cases for block prediction, were selected for the sensitivity study. Figure 84 shows the cross-sectional views of Case 58 (fracture modeling region 8) for the 4 various dimensions. The total distinct blocks generated in each model dimension are listed by each cross-section. The distinct blocks are the blocks that exist in the rock mass regardless of whether the blocks are kinematically or mechanically able to fall. As expected, the distinct blocks increase as the model dimension increases. The predicted rockfall for the 4 model dimensions are presented in Table 28. It is clearly shown that the small model underestimates the amount of rockfall, whereas the base case and the large models predict roughly the same amount of rockfall. The exception is the Case 58 large 1 model, which estimates about one-third less rockfall than the base case. In all, the base case appears to be adequate to provide a reasonable answer for rockfall.

Table 28. Predicted Rockfall for Various Model Dimensions

Model Size	Model Dimension	Case 55 (fracture modeling region 16, $1 \times 10^{-6}$ ground motion #12)		Case 58 (fracture modeling region #8, $1 \times 10^{-6}$ ground motion #4)	
		Number of Blocks	Rockfall Volume (m <sup>3</sup> )	Number of Blocks	Rockfall Volume (m <sup>3</sup> )
small	25×25×25	6	2.17	28	28.55
base case	25×27.5×25	21	12.99	44	42.26
large 1	25×33.75×30	18	13.22	31	26.2
large 2	25×38.75×37.5	21	14.04	49	51.59

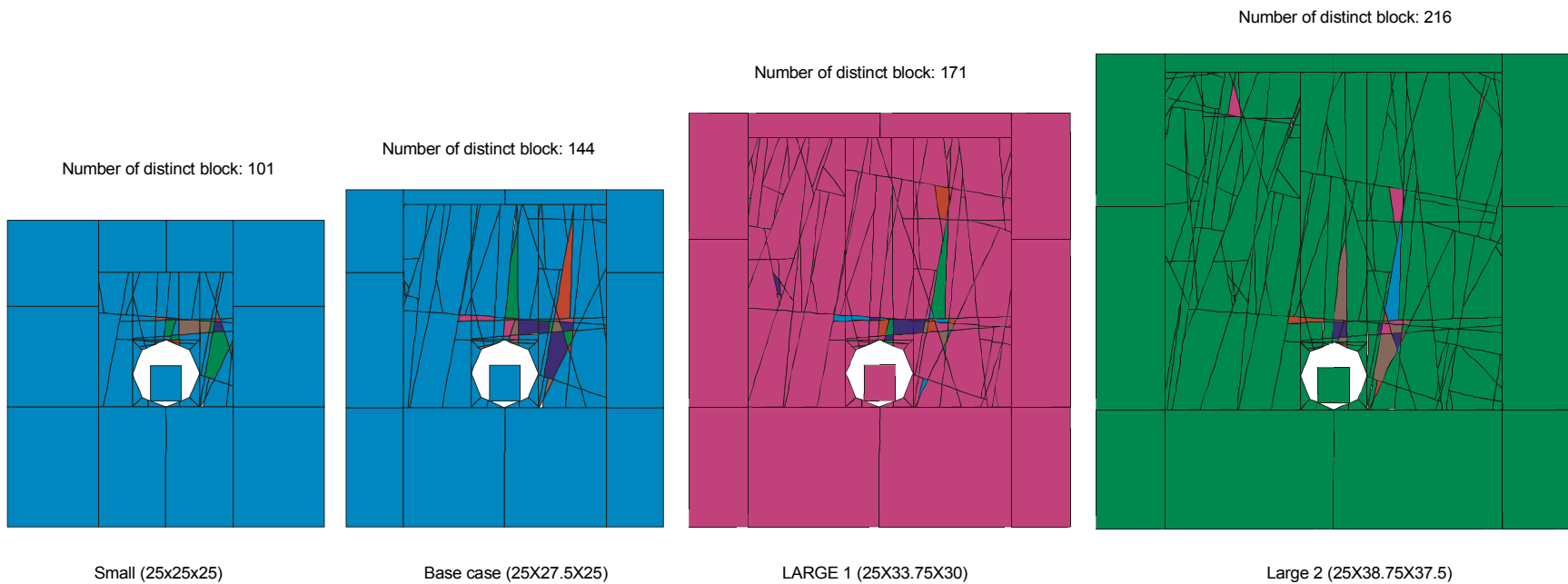


Figure 84. Cross-Section of the Four Model Dimensions Selected for Sensitivity Study

### 6.3.1.6.5 Block Deletion

As described in Section 6.3.1.1, a drip shield block anchored at the invert is included in the model to record the information of the locations and relative velocities for the rockfall impact. An algorithm was placed to delete the fallen block after the impact. The deletion is to facilitate the recording of all possible rockfall on the drip shield. If the blocks are not deleted for the heavy rockfall cases, the drip shield will be covered with fallen rocks so that some of the rockfall at the later part of seismic shaking will not directly impact the drip shield. The simulations without deletion of the rock block after the impact are presented in this section.

Figures 85 and 86 shows two cases in which block deletion algorithm is not included. As expected, with the fallen blocks piled on the drip shield, the blocks on top do not directly impact the drip shield. Table 29 compares the results for rockfall prediction with and without the block deletion algorithm. Much less rockfall for the case without block deletion is predicted. The effect of blocks not directly impacting the drip shield will be mainly the dead load added onto the drip shield. The accumulation of dead load on top of the drip shield for the fallen rock is addressed in Section 6.4.2.

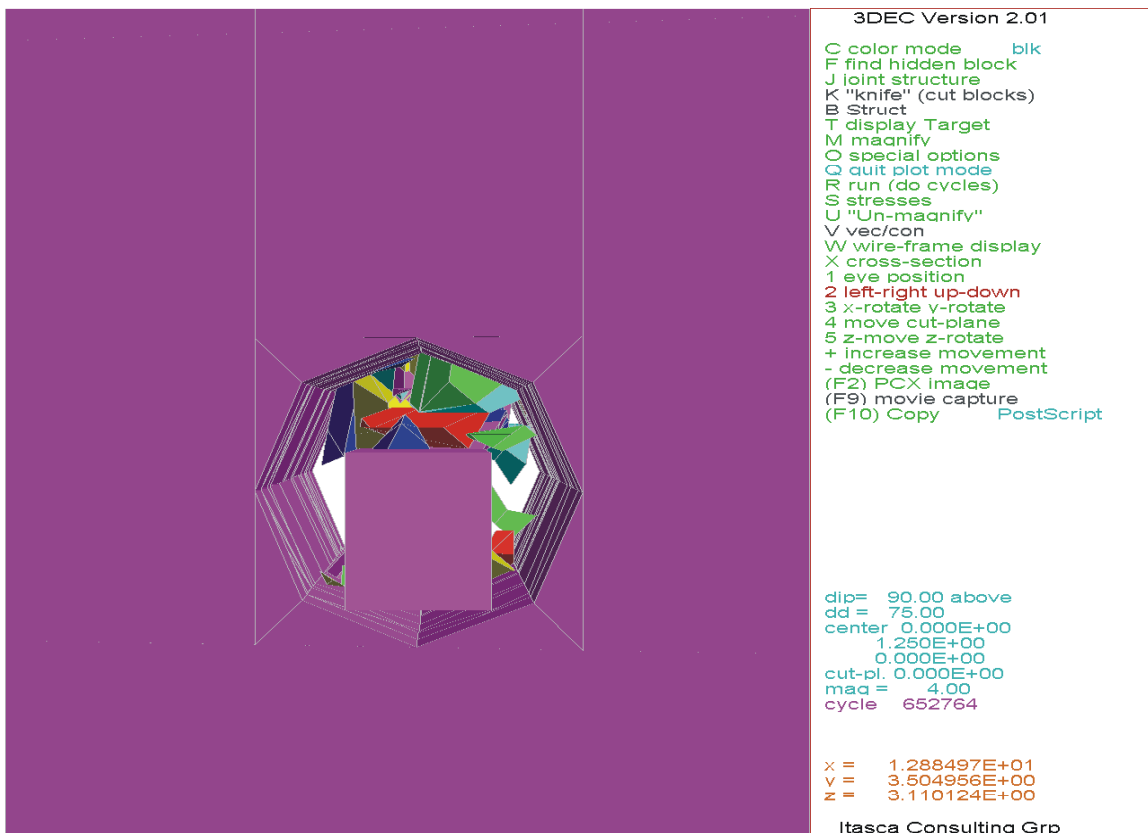


Figure 85. Blocks Accumulated Above the Drip Shield Without Implementing Block Deletion Algorithm, Fracture Modeling Region #8,  $1 \times 10^{-6}$  Ground Motion Set #14

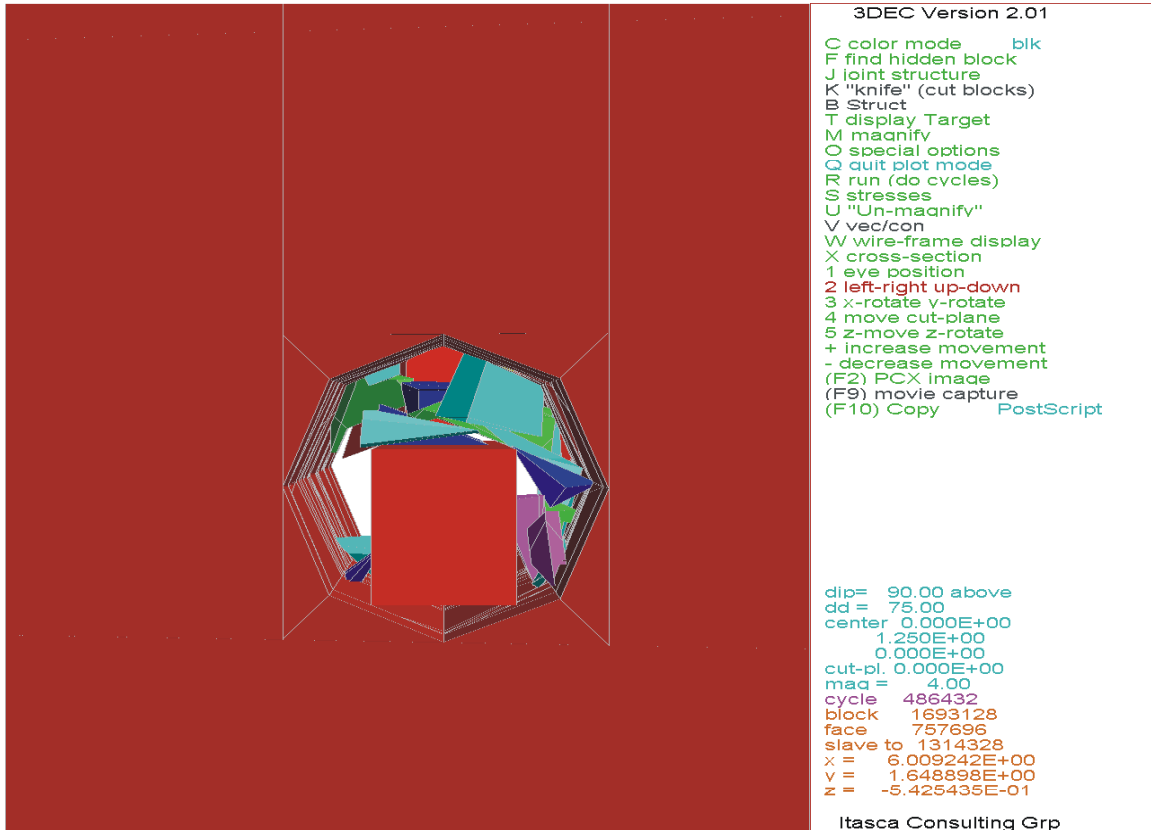


Figure 86. Blocks Accumulated Above the Drip Shield Without Implementing Block Deletion Algorithm, Fracture Modeling Region #16,  $1 \times 10^{-6}$  Ground Motion Set #2

Table 29. Predicted Rockfall With and Without Block Deletion After Impact

Fracture Modeling Region	$1 \times 10^{-6}$ ground motion	With Block Deletion		Without Block Deletion	
		Number of Blocks	Rockfall Volume (m <sup>3</sup> )	Number of Blocks	Rockfall Volume (m <sup>3</sup> )
8	14	39	40.75	16	16.41
16	2	21	14.11	14	8.16

## 6.3.2 Consideration of Intensely Fractured Zone

### 6.3.2.1 Introduction

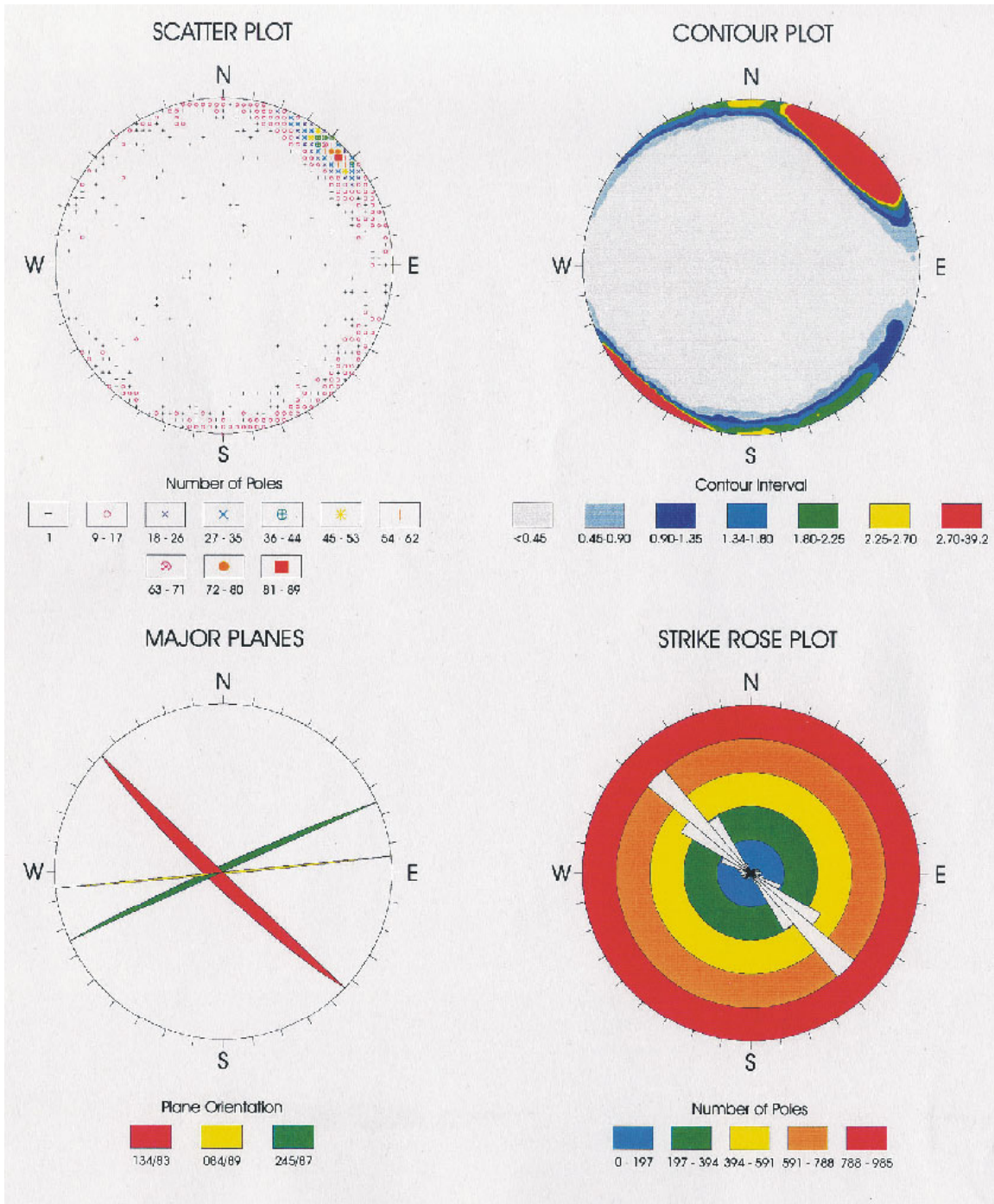
An intensely fractured zone is observed at ESF main loop Stations 42+00 to 51+50 with approximately 1000-m length. A description of this fracture zone is provided in *Geology of the Main Drift - Station 28+00 to 55+00, Exploratory Studies Facility, Yucca Mountain Project, Yucca Mountain, Nevada* (Albin et al. 1997, p. 58):

The fracture zone between Sta. 42+00 and 51+50 is a zone of intense Set 1 fracturing. This zone appears to be strata bound within the Tptpmn. The zone does not crop out on the surface. Down-hole video from drill hole SD-12, located 39.4 m west of tunnel Sta. 46+49, shows a similar zone of intensely fractured rock only within the Tptpmn. The Main Drift in the area of the fracture zone is parallel to the Ghost Dance Fault and is approximately 100 m west of and in the hanging wall of the fault. It is not known whether the fracture zone is continuous across the Ghost Dance fault as only limited information exists east of the Main Drift.

According to Albin et al. (1997), the two likely hypotheses for the origin of this zone are tectonic and/or cooling of the ash-flow sheet. Figures 87 and 88 show the intensely fractured rock mass with a predominant joint set of 134/83 (strike/dip). Set 2 and 3 fractures are sparse compared to Set 1 fractures. The mean and median joint spacing for the predominant Set 1 fractures was calculated to be 0.24 m and 0.12 m, respectively.



Figure 87. Photo Showing the Intensely Fractured Zone in ESF Main Drift



Source: CRWMS M&O 1998a, p. II-66

Figure 88. Fracture Analysis for the Intensive Fracture Zone

### 6.3.2.2 Numerical Modeling

A 3DEC analysis, which is used for rockfall modeling of the nonlithophysal jointed rock mass, is not suitable for such highly fractured rock. A three-dimensional continuum analysis with ubiquitous joint model (FLAC3D analysis) was adopted to account for the highly fractured and anisotropic nature of the rock mass in this zone. The ubiquitous joint model is ideal for conditions with one predominant fracture set in the rock mass.

Figure 89 shows a 25-m cube FLAC3D model constructed for the analysis. To simplify the model, the tunnel axis was oriented parallel to the y-axis and the input fracture orientation was adjusted based on the coordinate system shown in Figure 89. The intact rock deformation properties and joint strength properties used in the model are identical to the 3DEC base-case model presented in Table 7. A typical modeling sequence was simulated with initial consolidation and tunnel excavation. The lateral and bottom boundaries were fixed at the direction normal to the boundary surface, whereas the in situ static pressure was applied to the top boundary for the consolidation and excavation stages. Both the preclosure seismic motion ( $1 \times 10^{-6}$  seismic ground motion set 1) were applied to the model with free-field boundary condition imposed. These analyses do not include thermal loading.

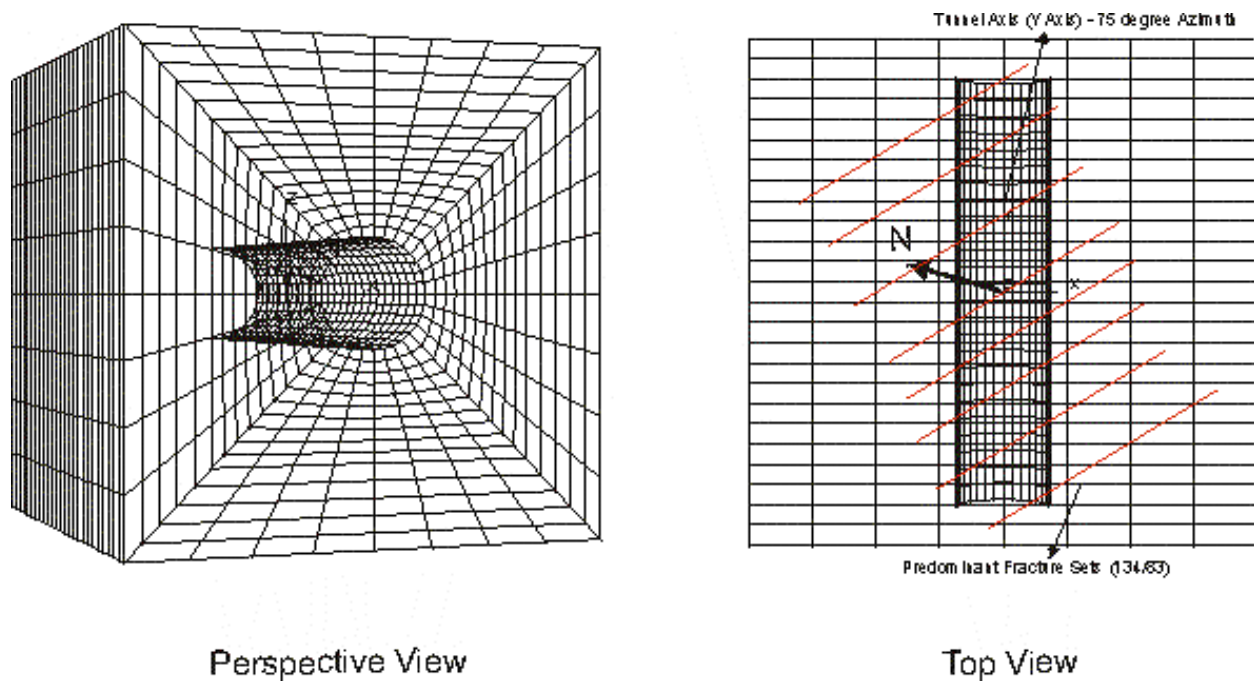


Figure 89. FLAC3D Model Mesh and Fracture Orientation

Figures 90 to 92 show the yield state, in-plane shear stress contours, and principal stress tensor for the preclosure seismic analysis after approximately 34 seconds of shaking. The same set of figures for the postclosure seismic analysis is presented in Figures 93 to 95. Yielding is confined within an element around the opening for the preclosure analysis as shown in Figure 90. The drift appears to be stable for the entire duration of seismic shaking in this case. However, extensive yielding is observed in the model region for the postclosure seismic analysis. The extensile stresses imposed by the large amplitude of seismic motion exceed the in situ compressive stress on the ubiquitous joint planes, tensile and shear failure is observed at these planes. The stress path of shear and normal stresses at the roof projected onto the predominant joint plane are presented in Figures 96 and 97 for the preclosure and postclosure analysis, respectively. Perturbation of stresses is minor in the preclosure case, whereas large stress variation is observed in the postclosure case. The stress states at the predominant joint plane reach the Mohr-Coulomb failure envelope under the postclosure seismic motion as shown in Figure 97.

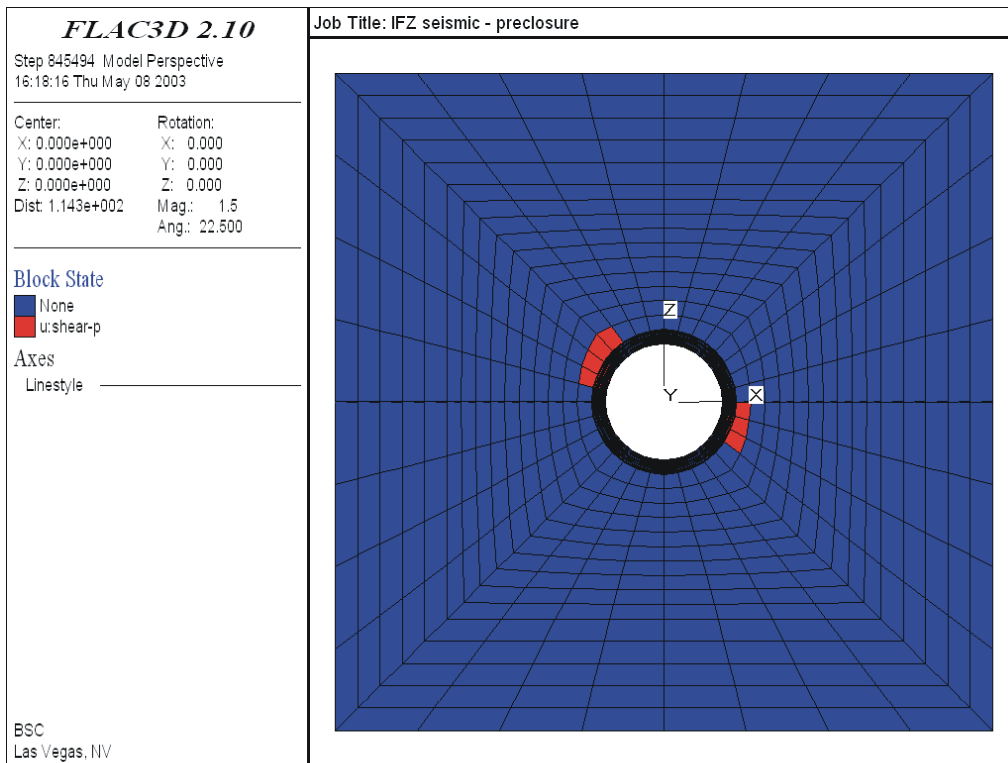


Figure 90. Yield State Prediction - Preclosure Ground Motion at 28 Seconds

# Drift Degradation Analysis

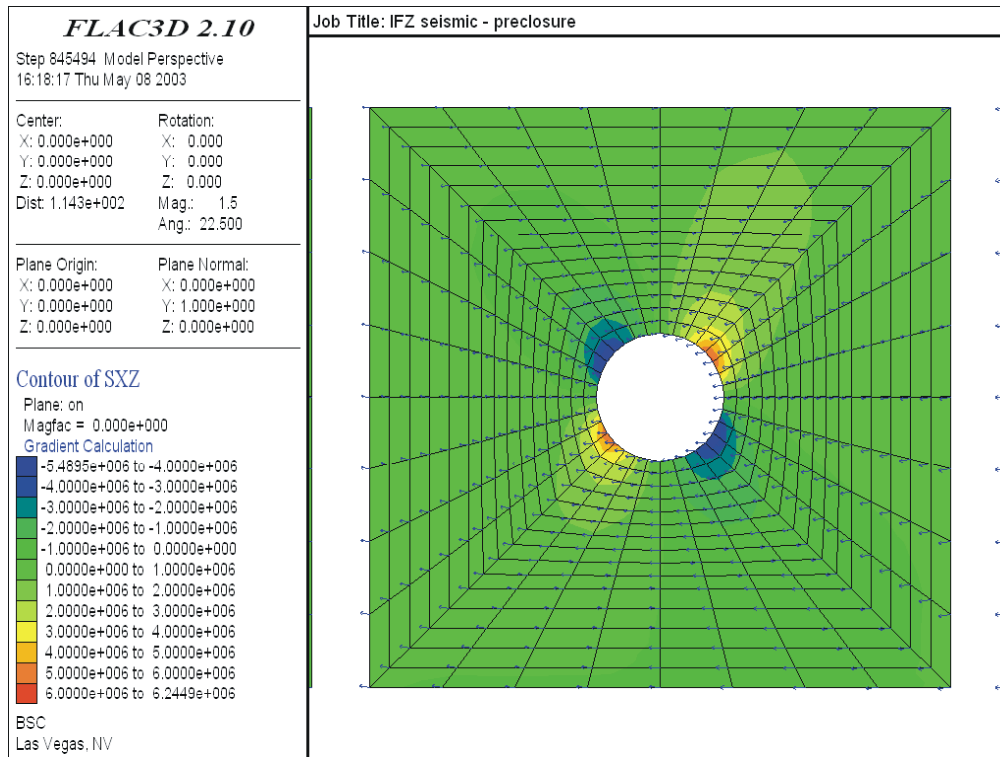


Figure 91. In-Plane Shear Stress Contours - Preclosure Ground Motion at 28 Seconds

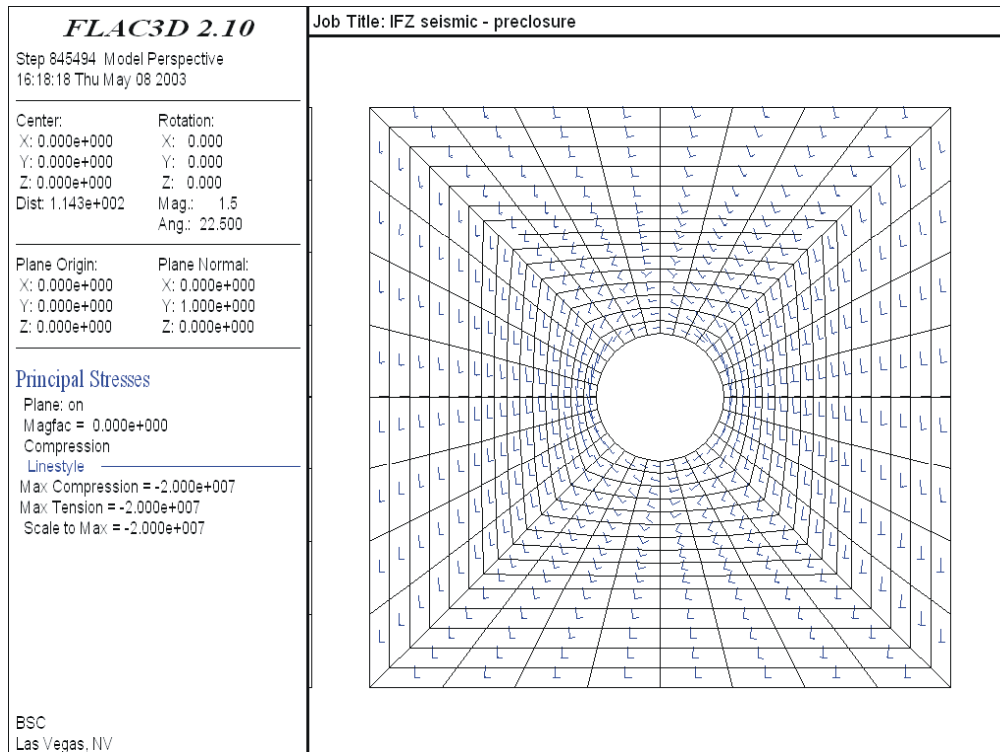


Figure 92. Principal Stress Tensor - Preclosure Ground Motion at 28 Seconds

# Drift Degradation Analysis

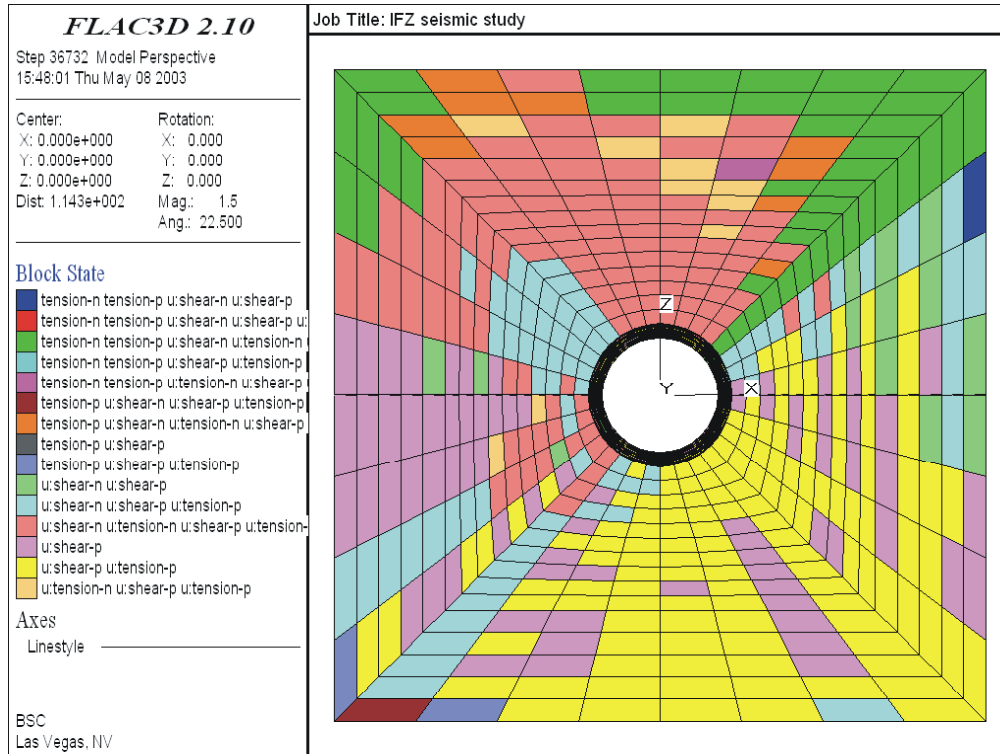


Figure 93. Yield State Prediction - Postclosure Ground Motion at 2 Seconds

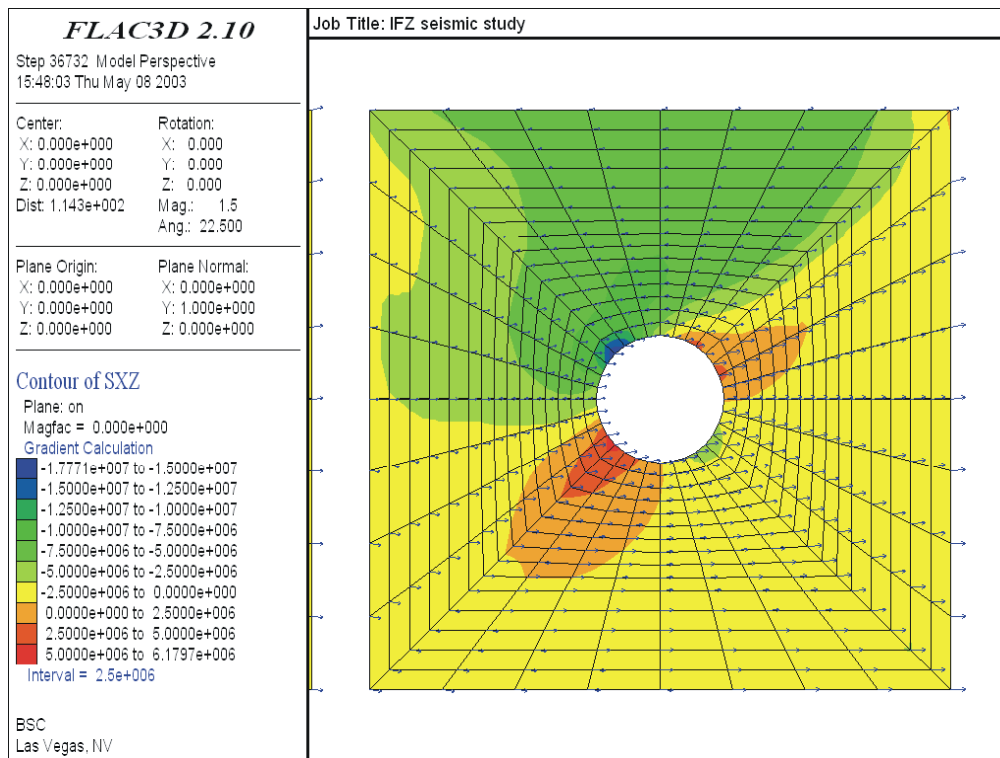


Figure 94. In-Plane Shear Stress Contours - Postclosure Ground Motion at 2 Seconds

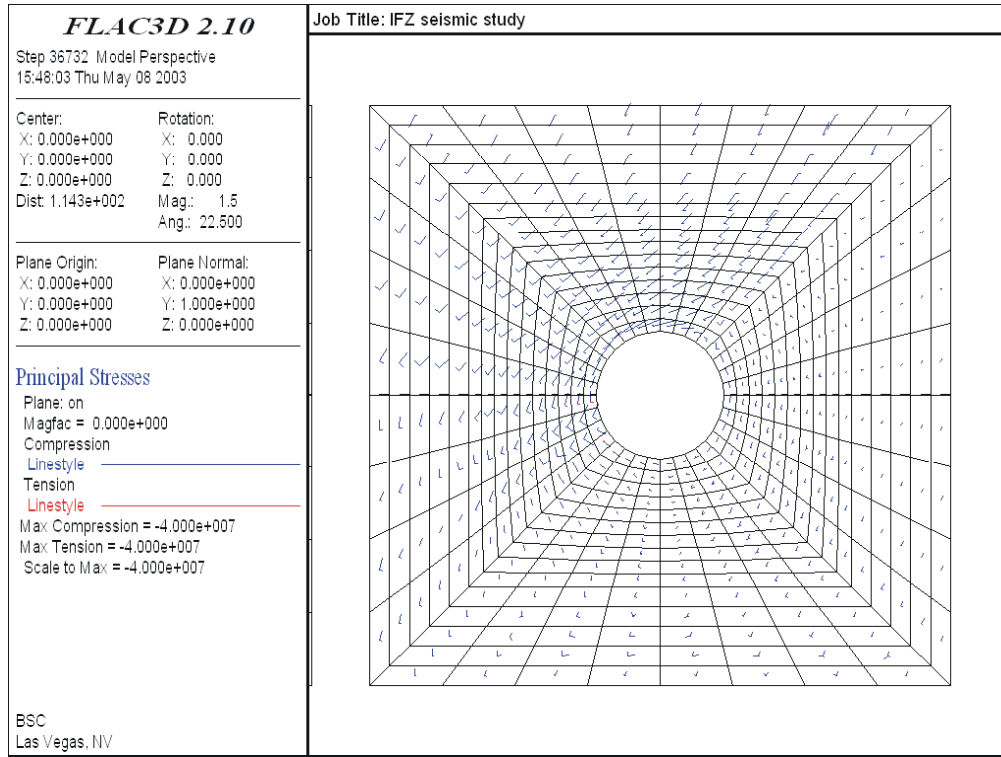


Figure 95. Principal Stress Tensor - Postclosure Ground Motion at 2 Seconds

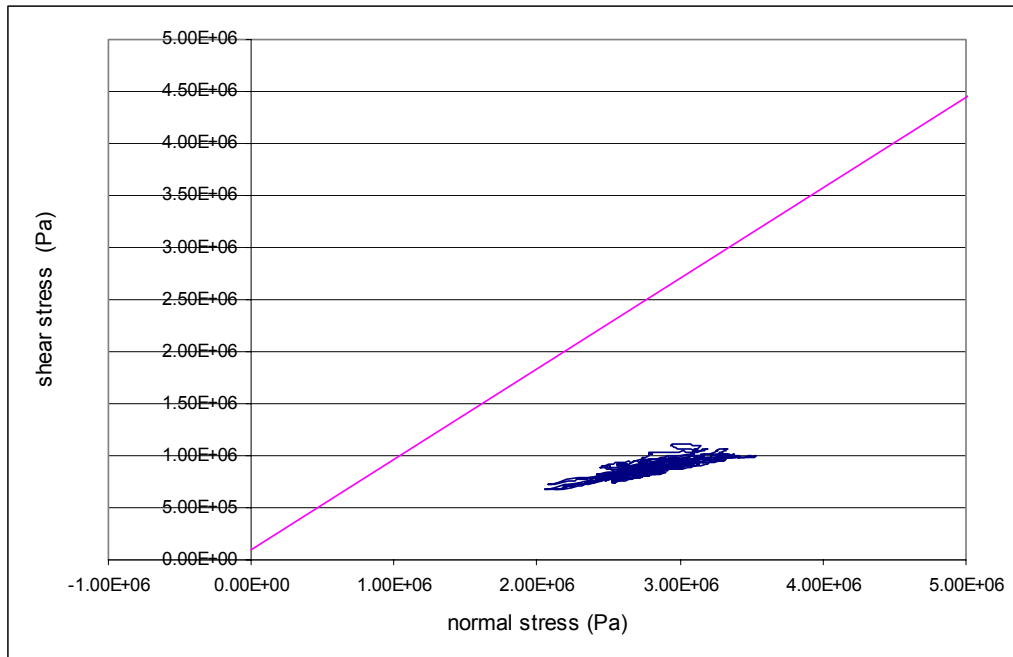


Figure 96. Stress Path at Roof Under Preclosure Seismic Motion

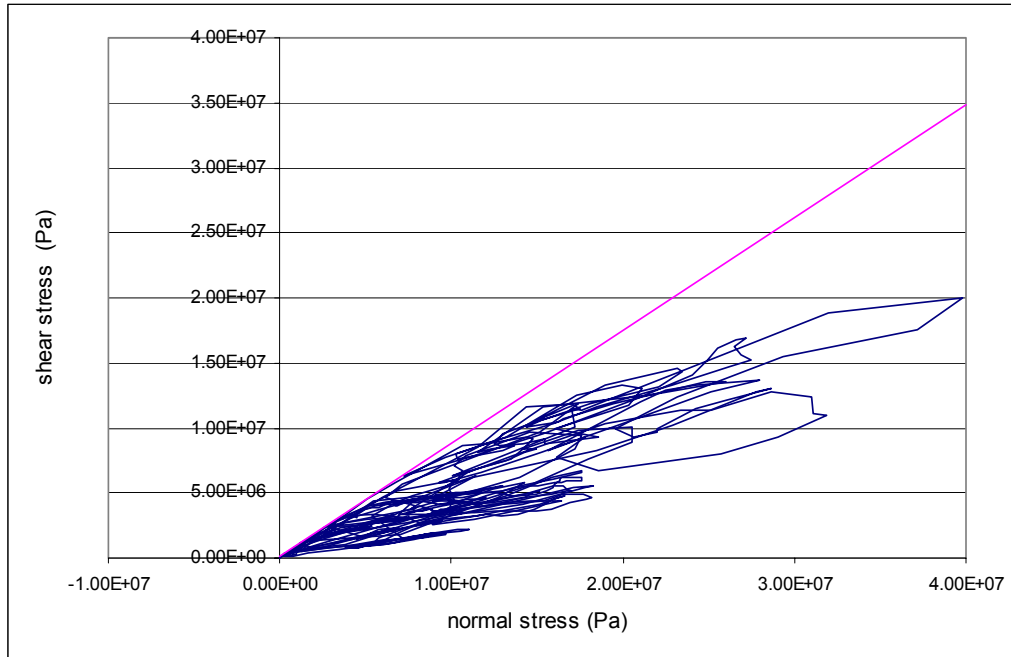


Figure 97. Stress Path at Roof Under Postclosure Seismic Motion

The ubiquitous joint model used in the analysis considers through-going joints in the model region. However, rock bridges do exist and will provide additional strength to resist the extensile and shear strains induced by the seismic motions. The prediction of yielding in the model region for the postclosure ground motion is therefore conservative. Based on the FLAC3D analysis results presented in this section and the spalling type of failure predicted in Section 6.3.1.6, extensive failure around the drift opening is likely.

### 6.3.3 Impact of Small-Scale Fractures on Rockfall in Nonlithophysal Units

Small-scale fractures were mapped in six 6-m panels (DTN: GS990908314224.009) as described in Section 6.1.4.1. Two of the six panels are located in the Tptpmn unit (Stations 11+15 and 11+30). The small-scale fracture data in these two panels are used in this study to determine their impact to block formation. The ranges of fracture traces mapped in these two panels are tabulated in Table 30 and presented in Figure 98. As shown in Figure 98, the fracture trace length distributions are the typical negative exponential nature with the concentration in the range of 10 cm to 20 cm. The fractures with trace lengths longer than 1 m only account for less than 20 percent of all the fractures mapped in these two panels.

It is not practical to incorporate all the small trace length fractures into a distinct block code, such as 3DEC used in the seismic and thermal analysis presented in Section 6.3.1, due to the extraordinary computational effort. The probabilistic key-block code DRKBA, with an efficient key-block simulation algorithm, is therefore selected to assess the impact of small-scale fractures to rockfall. The assessment is based on static condition with comparison of the results of two cases: (1) including the small-scale fractures and (2) excluding the small-scale fractures.

Table 30. Range of Fracture Traces in Panels 11+15 and 11+30

Trace Length Bin(m)	Frequency	Cumulative %
0	0	.00%
0.1	87	22.25%
0.2	112	50.90%
0.3	53	64.45%
0.4	31	72.38%
0.5	12	75.45%
0.6	9	77.75%
0.7	5	79.03%
0.8	3	79.80%
0.9	7	81.59%
1	8	83.63%
1.1	10	86.19%
1.2	2	86.70%
1.3	6	88.24%
1.4	0	88.24%
1.5	4	89.26%
2	12	92.33%
2.5	9	94.63%
3	7	96.42%
More	14	100.00%

Because the fractures with trace lengths greater than 1 m have already been accounted for in the existing joint data for DRKBA analysis, these fractures included in the 6-m panels were first filtered out. Additionally, fractures with trace lengths less than 15 cm are filtered out to reduce the computational effort for key-block analysis. This criterion is reasonable because the block volume formed by small traces less than 15 cm would be too small to be considered relevant to the damage of waste package or drip shield. The orientation of the remaining small-scale fractures are presented in the fracture pole plot as shown in Figure 99.

### 6.3.3.1 DRKBA Comparative Analysis

For the comparative analysis, the primary excavation is a horizontal 3-m diameter drift trending 75°. The region around the excavation has been modeled with a grid consisting of 2,744,000 nodes. The nodes are spaced 15 cm (0.5 ft) apart, with each node representing 0.0035 cubic meters (0.125 cubic foot) of the rock mass. The smaller size tunnel is used because of the excessive computer memory required for the mesh compatible to 5.5-m diameter drift. Because of the comparative nature of the analysis, and the focus of small-scale fractures in this analysis, the smaller size tunnel is justified.

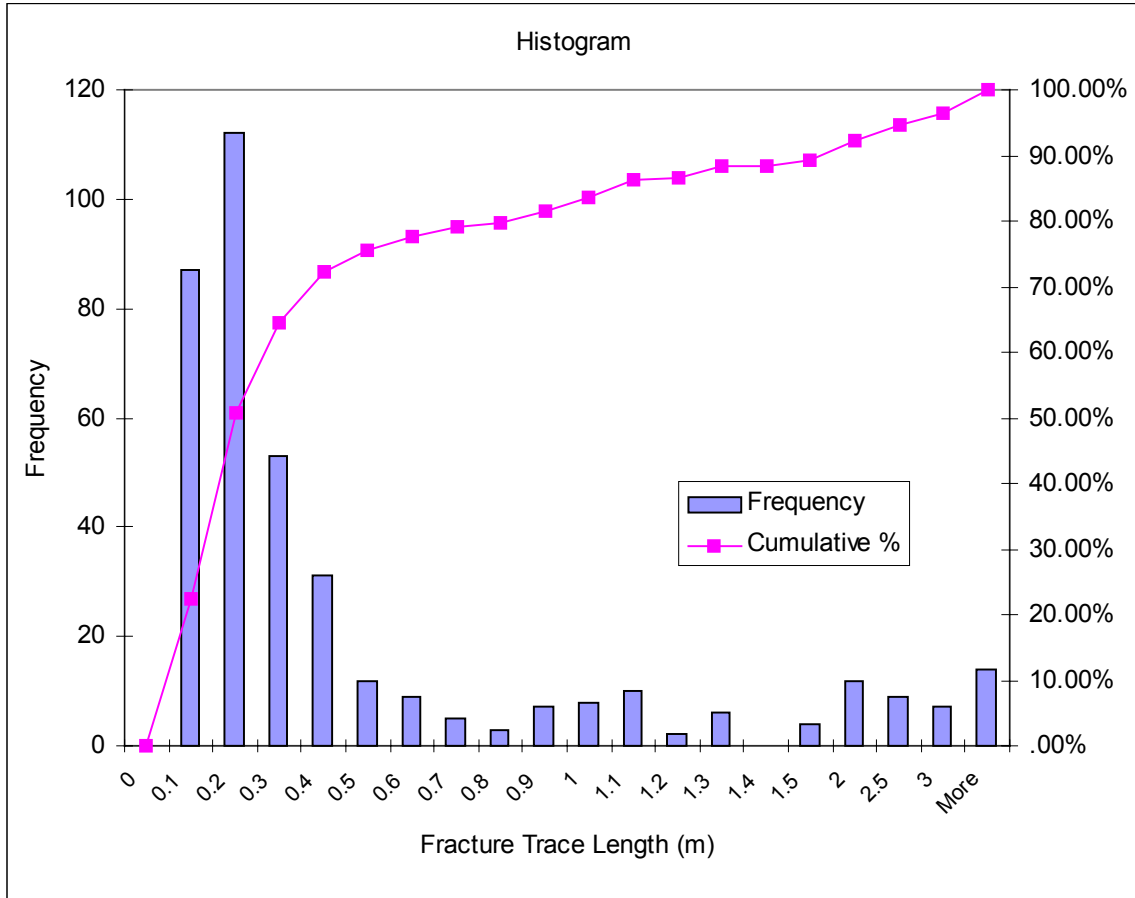


Figure 98. Histogram Fracture Traces in Panels 11+15 and 11+30

For each Monte Carlo simulation, an 18.3-m-long (60-ft) tunnel has been modeled in three-dimensional space. To describe the circumference of the circular tunnel, 18 plane equations were used. In addition, two plane equations were used to describe each end of the tunnel. Random joint patterns are generated with joint centers positioned in three-dimensional space, considering each joint set in sequence for each Monte Carlo simulation. The forming of key blocks is therefore different in each Monte Carlo simulation. A total of 400 Monte Carlo simulations were used in this analysis.

In addition to the four joint sets identified based on the mapped fractures data with trace length greater than 1m (Section 6.1), a random set representing the small-scale fractures is included in the DRKBA analysis for the case considering the small-scale fractures. The required input parameters for each individual joint set and their derivation are provided in Attachment IV. Cohesion and friction angle of the joints are simulated with the bivariate normal distribution. Mean and standard deviation for the cohesion and friction angle are provided in Attachment V. Cohesion values were conservatively reduced, providing increased rockfall (Attachment IV, Section IV.2).

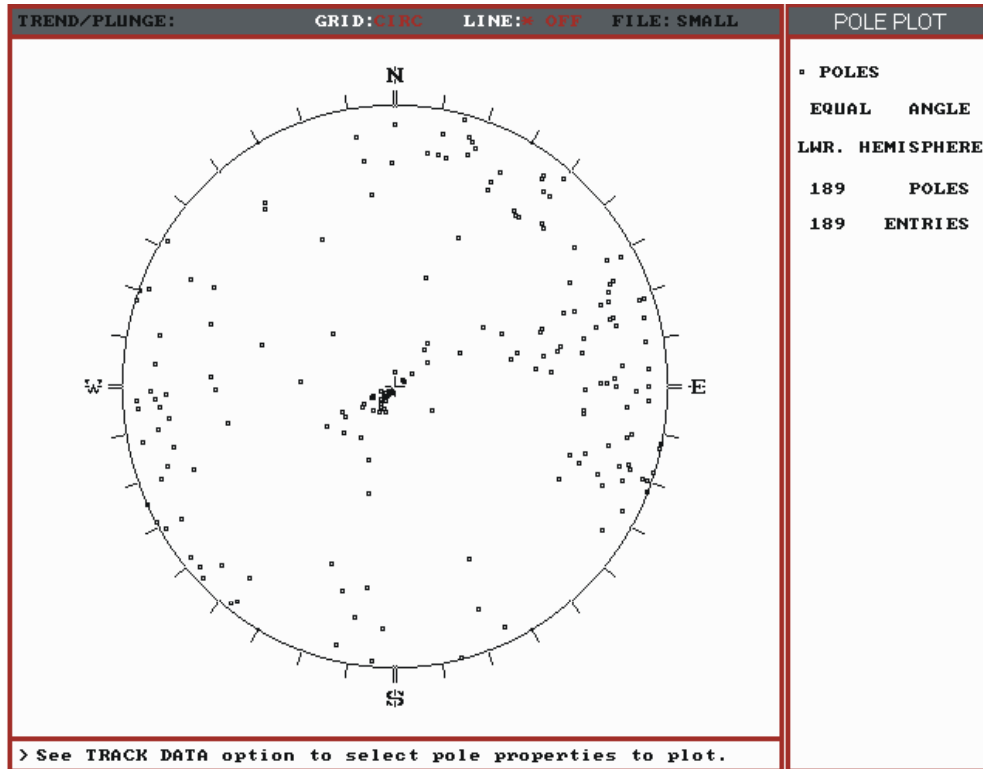


Figure 99. Pole Plots for the Filtered Small-Scale Fractures

### 6.3.3.2 Comparison of Analysis Results

Figure 100 presents the key-block analysis results in the format of cumulative frequency of occurrence for both cases. The cumulative frequencies of occurrence corresponding to 50, 75, 90, 95, and 98 percentile block volume for each unit are listed in Table 31. The maximum block sizes predicted from the analyses are also presented in this table. The block size predicted considering the small-scale fractures is in general smaller than the case without including the small-scale fractures as shown in Table 31. The maximum block predicted is 7.4 cubic meters for the case without small-scale fractures comparing with 3.25 cubic meters for the case including the small-scale fractures. The results also show that by considering the small-scale fractures, more blocks would form. A total of 347 blocks were generated in the case with inclusion of the small-scale fractures, compared to 325 blocks predicted in the case without the small-scale fractures. The results are summarized in Table 32. Approximately 10 percent more blocks are predicted when considering the small-scale fractures. It is therefore concluded that small-scale fractures have a minor impact on key-block development in the nonlithophysal units.

**Impact of Small Scale Fractures to the Block Size Distribution**

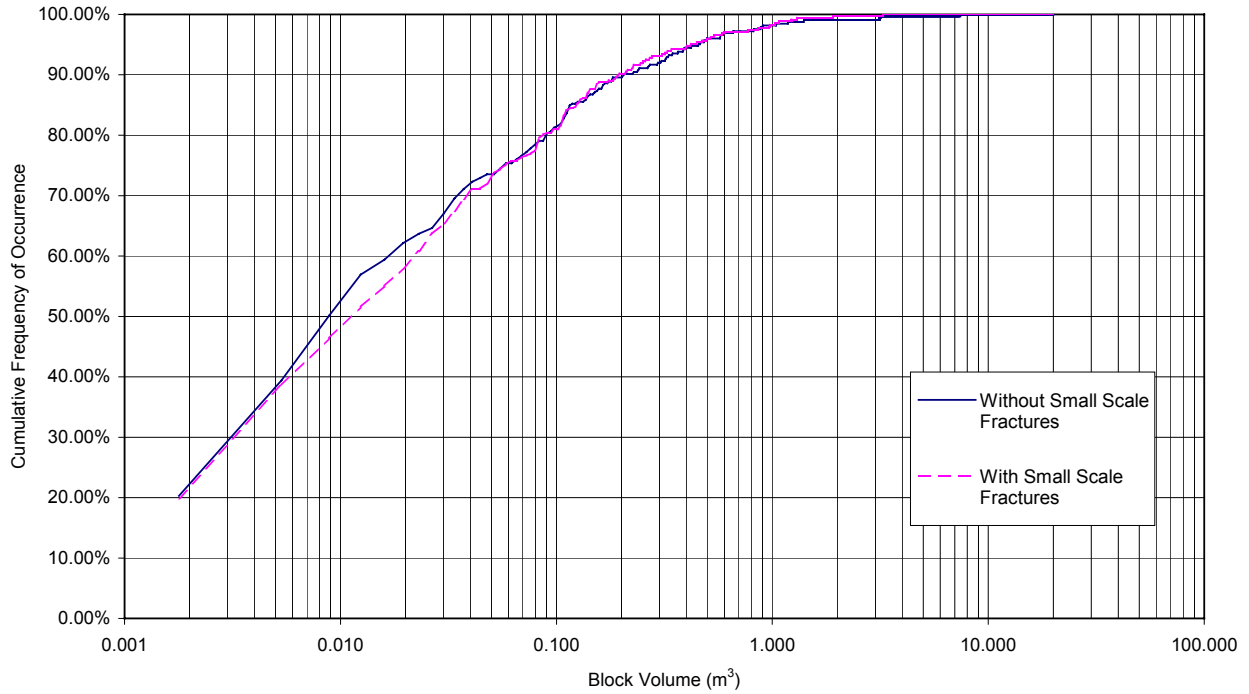


Figure 100. Block Size Distribution Predicted from DRKBA Analyses

Table 31. Block Volume (in cubic meter) Corresponding to Various Levels of Predicted Cumulative Frequency of Occurrence

Cumulative Frequency of Occurrence	Without Small-Scale Fractures	With Small-Scale Fractures
50%	0.01	0.01
75%	0.05	0.05
90%	0.20	0.19
95%	0.45	0.42
98%	0.90	0.97
100%	7.36	3.25

NOTE: Calculation of block volumes documented in Attachment IV (Section IV.11).

Table 32. Summary of Results for DRKBA Comparative Analysis

	Without Small-Scale Fractures	With Small-Scale Fractures
Total Number of Blocks	325	347
Number of Blocks per km	44	47
Total Volume of Blocks (m <sup>3</sup> )	38.0	32.0
Volume of Blocks per km (m <sup>3</sup> /km)	5.2	4.4

NOTE: Calculation of block information is documented in Attachment IV (Section IV.11) and Attachment I (small scale fracture results.xls).

#### 6.3.4 Drift Profile and Block Geometry Prediction in Nonlithophysal Units

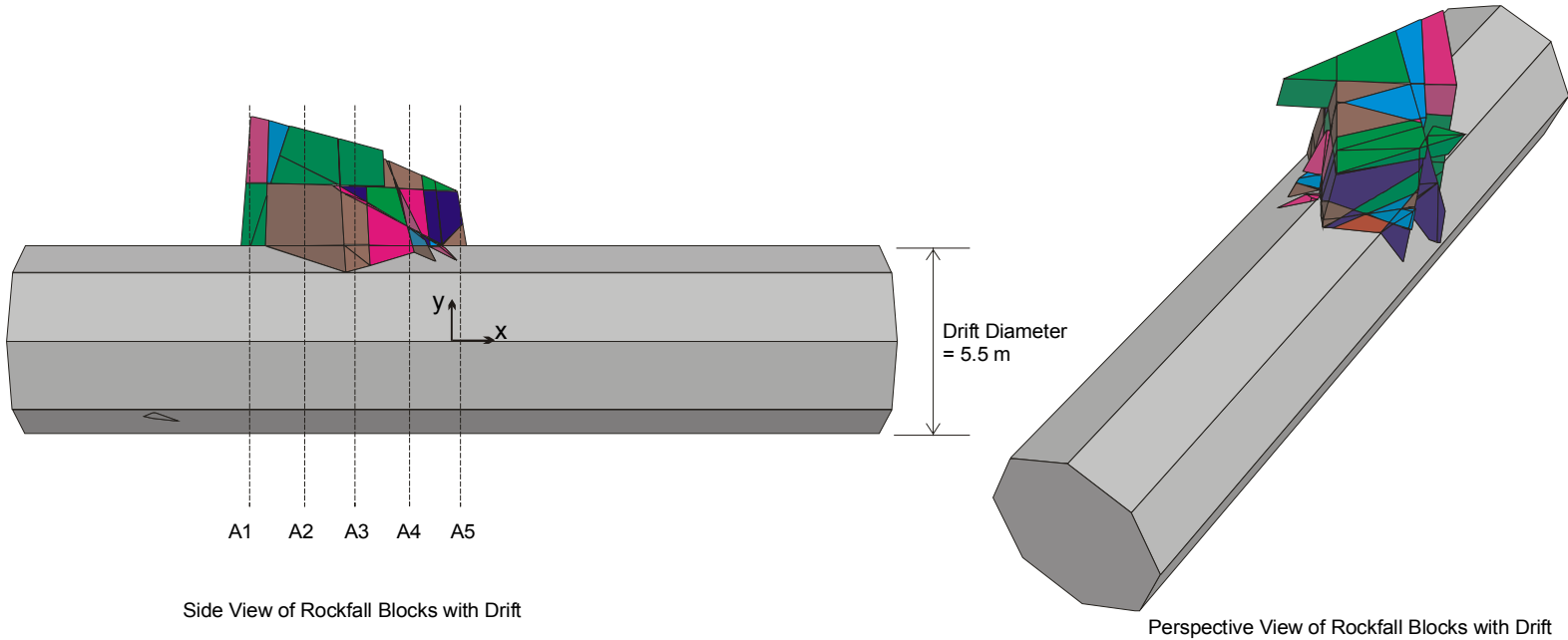
The distinct block approach applied in this analysis has provided an assessment of existing fracture data to determine probable occurrences of rock blocks that would fall onto the drip shield in the absence of ground support. The 3DEC approach considers progressive block failure, such that when an initial rock block fails and is removed, then an additional failure surface may open up allowing other blocks to fall. Progressive block failure continues until the crown becomes geometrically and mechanically stable, and no additional blocks can fall. The final progressive failure surface provides the basis for the drift profile predictions presented in this section.

A statistical distribution of the deteriorated drift profiles is shown in Figures 101 to 105. These profiles were the outcome of the 3DEC analysis with rock mass and opening subject to in situ and seismic loadings. Since the drifts are in general more stable under the thermal loading as shown in Sections 6.3.1.3 and 6.3.1.4, the drift profiles for the cases considering thermal loading are not included.

The selected drift profiles are the worst case profile and 75 percentile profile for the  $1 \times 10^{-6}$  and  $1 \times 10^{-7}$  hazard levels plus the worst case profile for the preclosure consideration ( $5 \times 10^{-4}$  hazard level). The 75 percentile profile is selected as the 75 percentile among all the simulations predicting rockfall for the given hazard level. The 75 percentile profile ranking was based on the total rockfall volume within the simulation. Due to the limited amount of rockfall predicted for the  $5 \times 10^{-4}$  seismic hazard, only the worst case profile is presented. The total rockfall volume and the number of blocks predicted for each simulation presented are listed in Table 33. The profile for each simulation includes the side view and perspective view of drift with predicted fallen blocks. Also included are 4 or 5 cross-sections at the locations indicated in the side view figure. Notice that the fracture pattern for the worst case  $1 \times 10^{-6}$  and  $1 \times 10^{-7}$  hazard levels is the same. The profiles for these two simulations are therefore similar with additional blocks shown on top of the profile for the  $1 \times 10^{-7}$  hazard level case. Spalling may occur for the postclosure level of ground motions as described in Section 6.3.1.6. Additional break up of rock around the opening is likely when subject to postclosure level of ground motions.

The drift profile for the intensely fractured zone can not be directly obtained from the FLAC3D ubiquitous joint model (described in Section 6.3.2) since the model is a continuum. Considering the small yield zone shown in Figure 90 for the preclosure ground shaking, minor spalling is expected along the side wall for preclosure period. However, severe spalling is likely for the seismic shaking due to postclosure ground motions with an extensive yield zone shown in Figure 89. It is estimated that the likely profile for the intensely fractured zone with the postclosure consideration will be similar to Figure 82.

There are many different sizes and shapes of rock blocks predicted to impact the drip shield. Since block geometry information is mainly used for drip shield impact calculations, the geometry of large blocks is provided in this section. Nine blocks were selected, each with a volume greater than the design basis key block of  $2.5 \text{ m}^3$  (6 metric tons) (BSC 2001d). The block geometric information for each individual block is presented in Attachment IX (Figures IX-1 to IX-9).



Side View of Rockfall Blocks with Drift

Perspective View of Rockfall Blocks with Drift

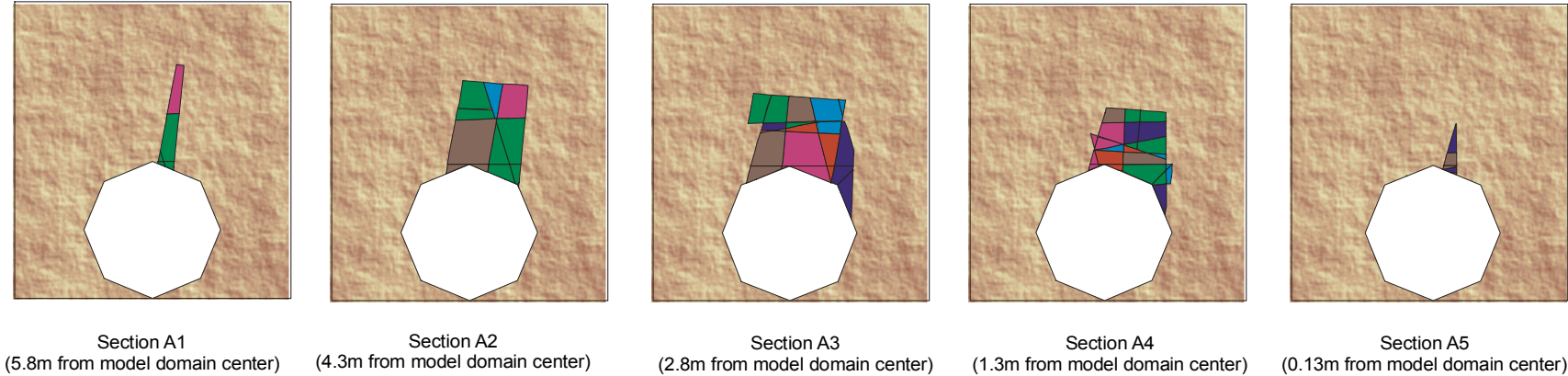


Figure 101. Drift Profile for  $1 \times 10^{-7}$  Hazard Level, Worst Case

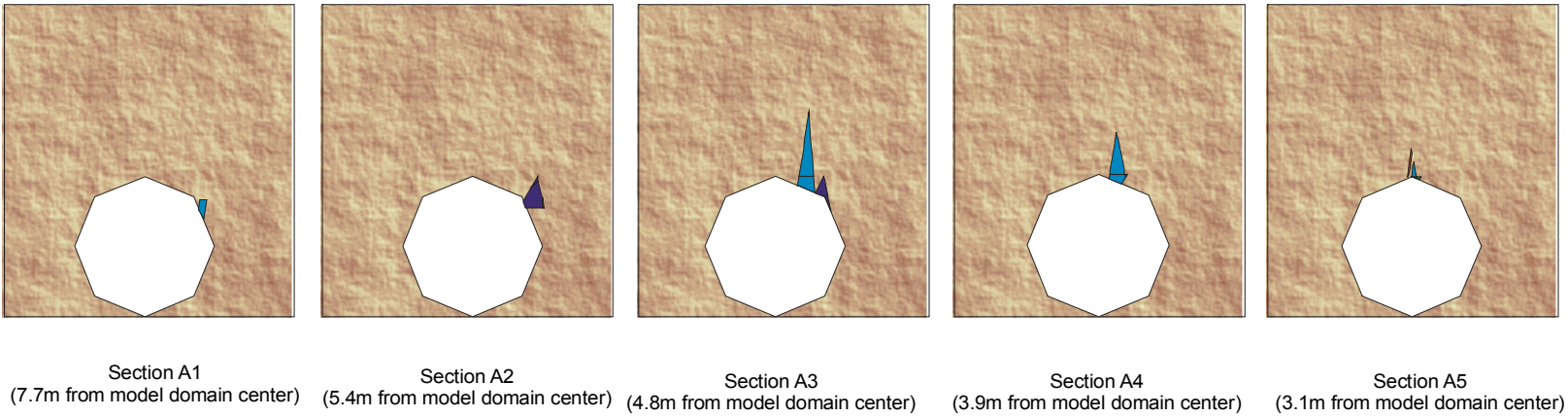
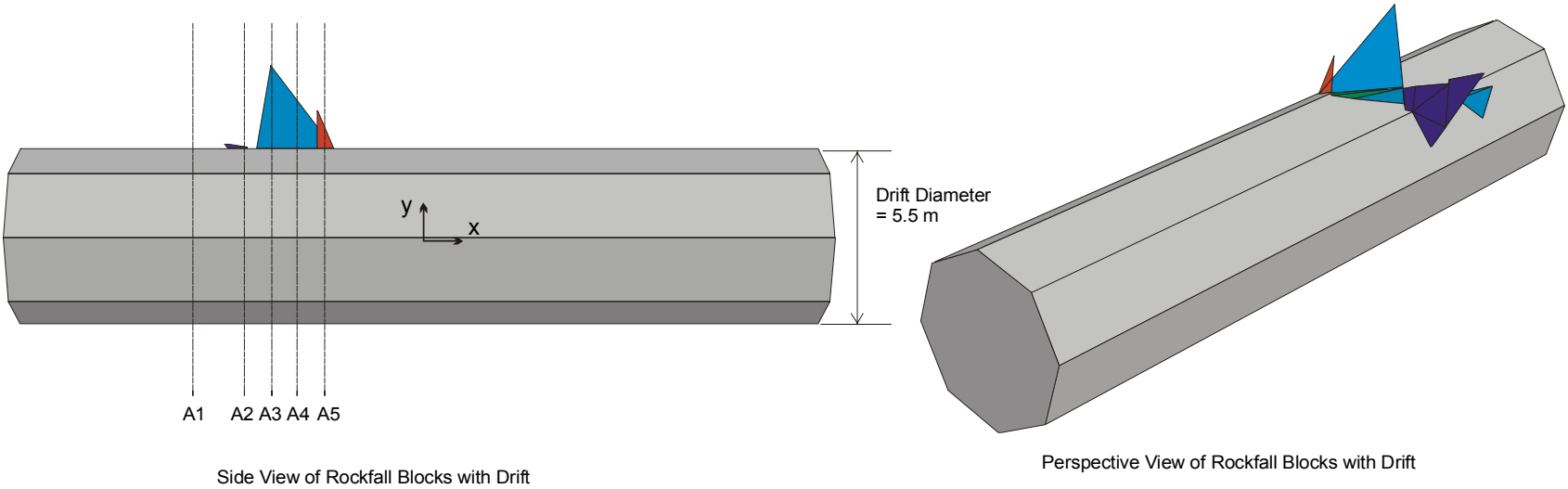
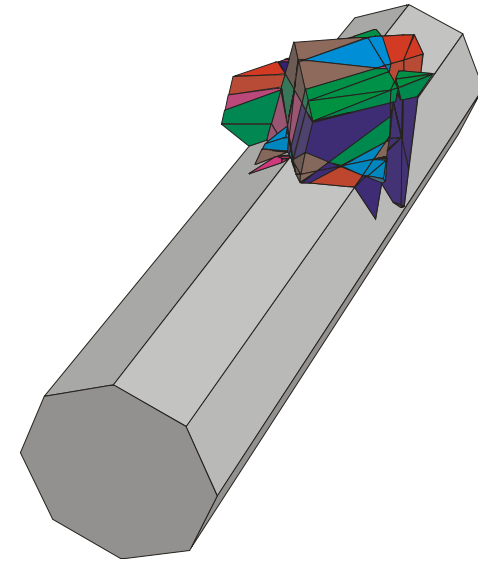
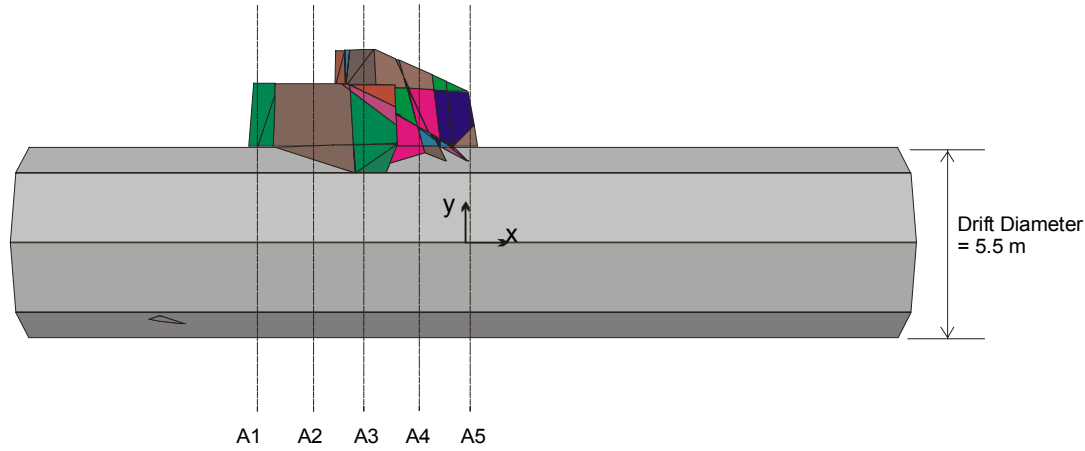
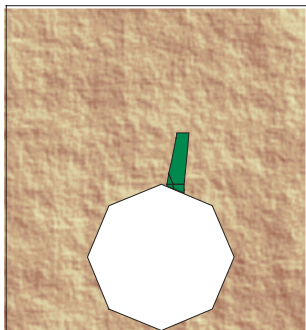


Figure 102. Drift Profile for  $1 \times 10^{-7}$  Hazard Level, 75 Percentile Case

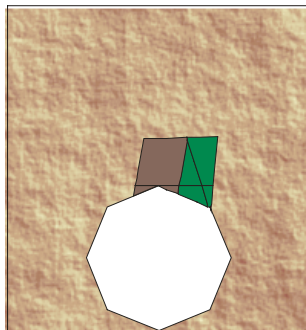


Side View of Rockfall Blocks with Drift

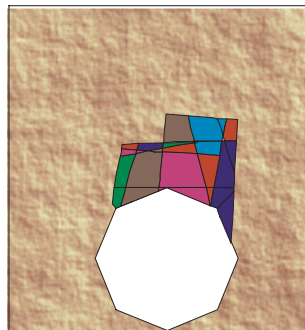
Perspective View of Rockfall Blocks with Drift



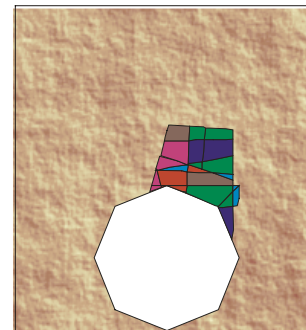
Section A1  
(5.8m from model domain center)



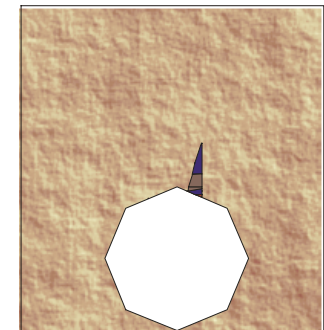
Section A2  
(4.3m from model domain center)



Section A3  
(2.8m from model domain center)

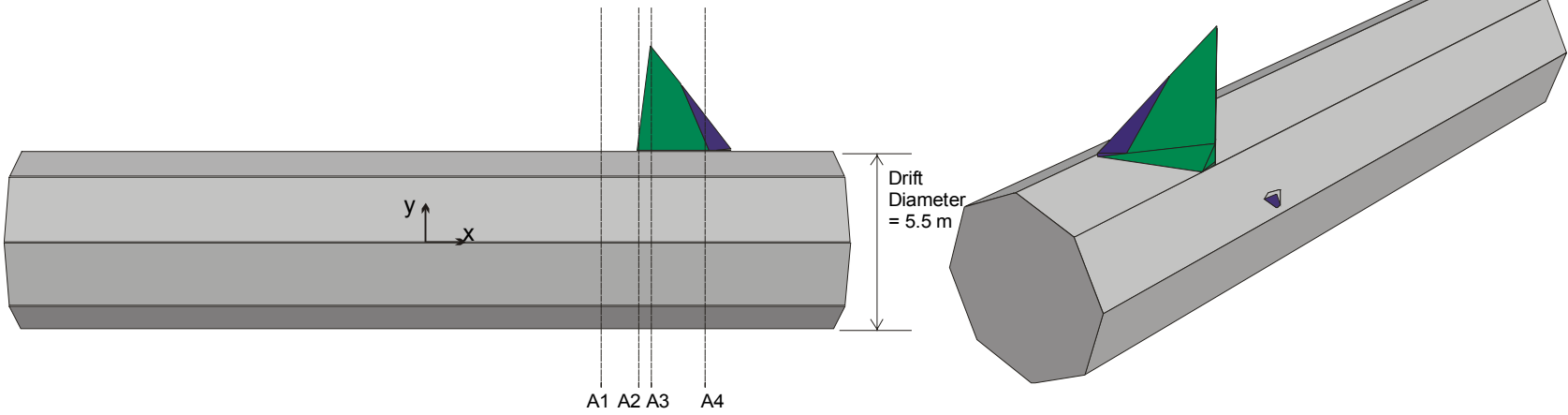


Section A4  
(1.3m from model domain center)



Section A5  
(-0.13m from model domain center)

Figure 103. Drift Profile for  $1 \times 10^{-6}$  Hazard Level, Worst Case



Side View of Rockfall Blocks with Drift

Perspective View of Rockfall Blocks with Drift

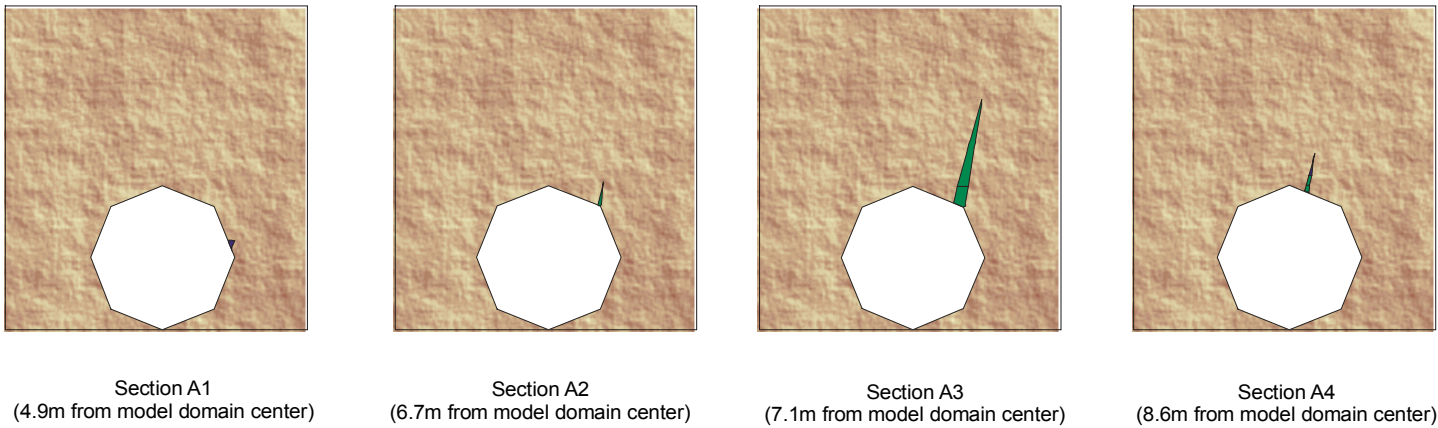
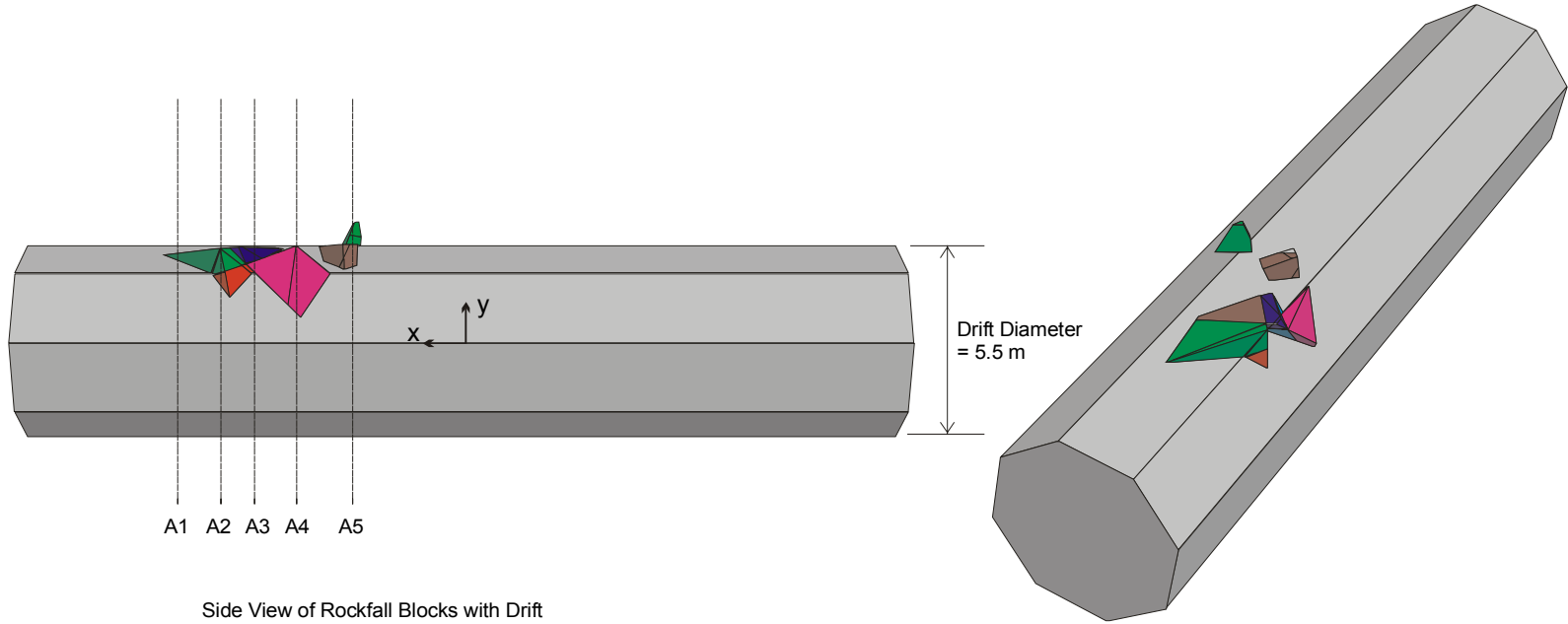
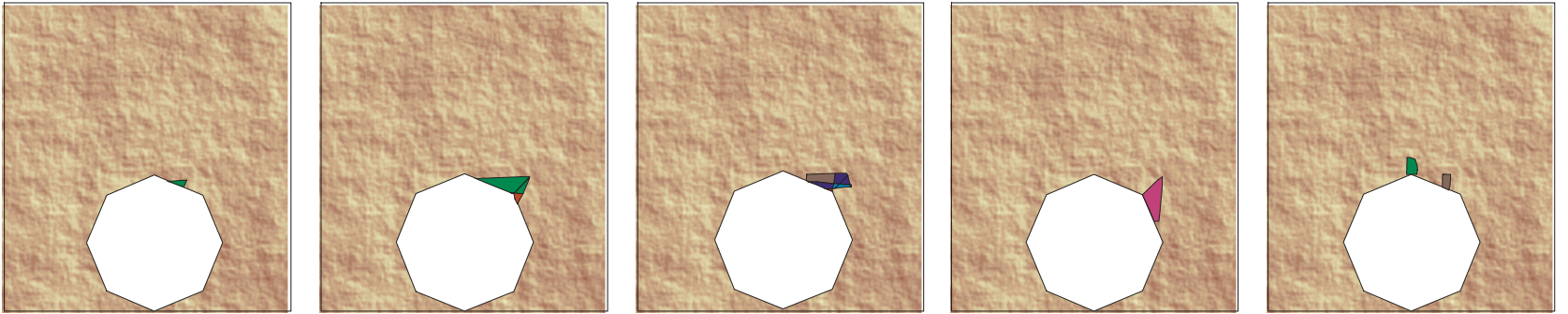


Figure 104. Drift Profile for  $1 \times 10^{-6}$  Hazard Level, 75 Percentile Case



Side View of Rockfall Blocks with Drift

Perspective View of Rockfall Blocks with Drift



Section A1  
(7.9m from model domain center)

Section A2  
(6.7m from model domain center)

Section A3  
(5.9m from model domain center)

Section A4  
(4.6m from model domain center)

Section A5  
(3.1m from model domain center)

Figure 105. Drift Profile for  $5 \times 10^{-4}$  Hazard Level, Worst Case

Table 33. Predicted Number of Rockfall and Volume for the Presented Drift Profile

Simulation	Number of Blocks	Total Volume (m <sup>3</sup> )
1×10 <sup>-7</sup> hazard, worst case profile	46	50.64
1×10 <sup>-7</sup> hazard, 75 percentile profile	5	2.02
1×10 <sup>-6</sup> hazard, worst case profile	44	42.26
1×10 <sup>-6</sup> hazard, 75 percentile profile	3	1.06
5×10 <sup>-4</sup> hazard, worst case profile	14	3.03

#### 6.4 ROCKFALL IN THE LITHOPHYSAL UNITS

Lithophysal units, particularly the lower lithophysal (Ttptll), are characterized by intense fracturing. Joint sets are not as clearly defined as in middle nonlithophysal (Ttptmn) units. Average joint spacing is less than 1 m, and at certain locations this spacing is much smaller, in the order of 0.1 m (as discussed in Section 6.1.4.1). In addition to fracturing on different scales, lithophysal rock mass is characterized by the presence of almost uniformly distributed holes (lithophysae) of varying size (from less than 1-cm to 1-m in diameter). The lithophysae account for up to 30 percent of the rock mass volume (see Section 6.1.4.2 for a detailed discussion on lithophysae). The size of the internal lithophysae structure and fracture spacing is much smaller than the drift size (i.e., 5.5-m diameter). There is no preferred direction in the orientation that would justify introduction of anisotropy. Heterogeneity is considered on the scale of the repository in such a way that the analysis on the drift scale is conducted using different properties of the rock mass to investigate the effect of varying quality of rock mass on drift stability. However, properties within each model are considered homogeneous. Under such conditions, when there is no internal structure in the model, and properties are isotropic and homogeneous, the drift stability analysis is conducted using a two-dimensional model in the plane perpendicular to the drift axis. The model results of rockfall prediction in the lithophysal units (in a cross-section characterized by particular rock mass properties) can be used to provide an estimate of overall rockfall in the lithophysal zone based on the distribution of different rock mass qualities throughout the repository.

The assessment of rock mass properties for lithophysal rock is documented in Attachment V (Section V.4.1). Six categories were developed to represent the range of rock mass properties as summarized in Table 34. The validity of this approach to represent the lithophysal rock mass is discussed in Sections 7.3 and 7.4. Categories 1 through 5 represent variability of rock mass quality throughout the repository level. Category 6 was considered as extremely poor quality of rock on the repository level used for very conservative (i.e., high) predictions of damage and rockfall.

Table 34. Categories of the Lithophysal Rock Mass Selected for Analysis

Category	Unconfined Compressive Strength (MPa)	Estimated Young's Modulus (GPa)	Bulk Modulus, K (GPa)	Shear Modulus, G (GPa)
1	10	1.9	1.07	0.80
2	15	6.4	3.54	2.65
3	20	10.8	6.01	4.51
4	25	15.3	8.48	6.36
5	30	19.7	10.95	8.21
6	6	1.0	0.56	0.42

NOTE: The calculation of rock strength properties is documented in Attachment V (Section V.4.1).

#### 6.4.1 Two-Dimensional Discontinuum Analysis of Lithophysal Rock Mass

The objective of the analysis presented in this section is to predict the amount of rockfall in the emplacement drifts due to: (a) drift excavation, (b) stresses induced by the heat released by the waste, (c) seismic ground motions with different probabilities of occurrence, and (d) strength degradation. The standard approach in geotechnical engineering of solving problems of stability of underground excavation is using models based on continuum mechanics. Such an approach is quite effective if the main interest is stress redistribution around an opening or displacements. However, difficulties are encountered if a continuum model is used for prediction of instability. Continuum models use constitutive models to describe the mechanical behavior of a material. A linearly elastic-perfectly plastic Mohr-Coulomb constitutive model is often used to represent mechanical behavior of a rock mass. Because the material strength of a perfectly plastic Mohr-Coulomb model does not decrease as a function of plastic deformation, the model of a drift will show indications of material yielding (i.e., plastic deformation) in different portions of the model, but will never actually predict the rockfall. It is necessary to use a strain-softening constitutive model, in which strength degrades as a function of deformation after the peak-strength of material has been reached, to have a reasonable prediction of rockfall area. However, the strain-softening model within the framework of continuum mechanics leads to problems of mesh dependency. It was decided, based on all previous considerations, to use the two-dimensional distinct element code, UDEC (Section 3.1), for drift stability analysis. In the UDEC model, the rock mass is represented as an assembly of polygonal, elastic blocks. The entire domain is discretized into blocks using Voronoi tessellations (Itasca 2002). The joints between blocks are considered to be linearly elastic-brittle. The joints between the blocks represent the pre-existing fractures. The elastic behavior of joints is controlled by normal and shear stiffness (joint stiffness is constant). Joints can sustain finite tensile stress as prescribed by tensile strength. The Coulomb slip condition governs the onset of slip as a function of joint cohesion and friction angle. If a joint fails either in tension or shear, tensile strength, friction and cohesion are reset to residual values. This model allows for the formation of joints between blocks, separation and instability (under action of gravity) of portions of rock mass around a drift. No ground support was considered in the analyses. All cases of thermal and seismic loading considered in this section were also analyzed using a continuum, linearly elastic approximation. The analyses were done using the finite difference code FLAC (Section 3.1). The results of the continuum model were used as a reference for easier interpretation of the results from the complex UDEC model.

Additional details for the justification and calibration of the lithophysal rock model are provided in Section 7.7. The calibrated micro properties are listed in Tables 35 and 36, for UDEC models with average block sizes of 0.2 m and 0.3 m, respectively. Note that, if not indicated otherwise, the analysis was done using a block size of 0.3 m.

The geometry of the UDEC model is shown in Figure 106. As indicated, only the region around the drift where inelastic deformation is expected is discretized into Voronoi blocks. The rest of the model is composed of a few large, elastic blocks. However, the resulting stiffness of the discretized portion of the model (i.e., stiffness of blocks and joints together) is the same as the stiffness of the large elastic blocks, which represent far-field behavior.

Table 35. Micro Properties in the Model with 0.2 m Block Size

Category	Friction Angle (deg)	Residual Friction Angle (deg)	Cohesion (MPa)	Tension (MPa)	Normal Stiffness (GPa/m)	Shear Stiffness (GPa/m)	Block Bulk Modulus (GPa)	Block Shear Modulus (GPa)
1	35	15	3.91	1.56	13.40	6.69	13.00	9.75
2	35	15	5.86	2.34	45.10	22.50	43.60	32.80
3	35	15	7.82	3.12	76.20	38.00	73.60	55.40
4	35	15	9.77	3.90	108.00	53.90	104.00	78.50
5	35	15	11.70	4.68	139.00	69.40	134.00	101.00
6	35	15	2.34	0.94	7.05	3.52	6.82	5.13

NOTE: Residual cohesion and tensile strength are zero.

Table 36. Micro Properties in the Model with 0.3 m Block Size

Category	Friction Angle (deg)	Residual Friction Angle (deg)	Cohesion (MPa)	Tension (MPa)	Normal Stiffness (GPa/m)	Shear Stiffness (GPa/m)	Block Bulk Modulus (GPa)	Block Shear Modulus (GPa)
1	35	15	3.83	1.53	9.34	4.67	9.03	6.80
2	35	15	5.85	2.34	31.48	15.72	30.44	22.88
3	35	15	7.94	3.18	53.08	26.57	51.37	38.60
4	35	15	10.09	4.03	74.90	37.60	72.80	54.70
5	35	15	12.30	4.92	97.00	48.40	93.60	70.50
6	35	15	2.30	0.92	4.90	2.50	4.80	3.60

NOTE: Residual cohesion and tensile strength are zero.

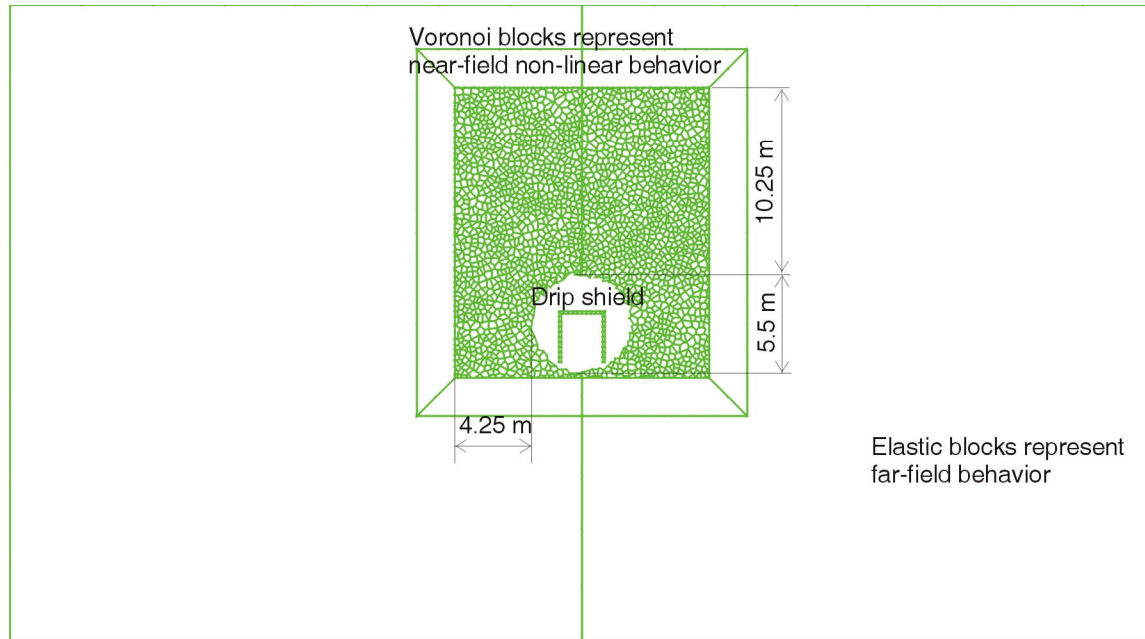


Figure 106. Geometry and Initial Conditions of the UDEC Model

#### 6.4.1.1 Seismic Consideration in Lithophysal Units

Drift stability was analyzed for different conditions of ground motion:

- Ground motion with  $5 \times 10^{-4}$  probability of annual occurrence (preclosure earthquake, DTN: MO0211TMHIS104.002)
- Ground motion with  $1 \times 10^{-6}$  probability of annual occurrence (postclosure earthquake, DTN: MO0301TMHIS106.001).

The ground motions are discussed in detail in Section 6.3.1.2.1. Fifteen ground motions (two horizontal and one vertical component of motion) were considered in the analysis for  $1 \times 10^{-6}$  probability of annual occurrence. Only one ground motion was considered for  $5 \times 10^{-4}$  probability of annual occurrence. Instead of simulating all possible combinations of the 15 cases of ground motion (for  $1 \times 10^{-6}$  probability) with six rock mass categories, only 15 realizations shown in Table 37 were simulated (note that 15 ground motions are numbered 1 through 14 in sequence, and 16). Based on Latin Hypercube sampling (DTN: MO0301SPASIP27.004), realizations from Table 37 are selected as representative of all possible realizations. Combinations in Table 37 include only rock mass categories 1 through 5, as representative of variability of lithophysal rock mass quality on the repository level. Only postclosure ground motion number 1 was considered for rock mass category 6 as an extreme condition. It was planned to conduct simulations of drift stability for ground motions with  $1 \times 10^{-7}$  probability of annual occurrence. However, the results of analyses for  $1 \times 10^{-6}$  probability of annual occurrence (complete collapse of the emplacement drifts) proved such an analysis futile. Because there is just one preclosure ground motion case, it was analyzed for all six rock mass categories.

Table 37. Simulated Combinations of  $10^{-6}$  Ground Motions and Rock Mass Categories

Realization Number	Ground Motion Time History Number	Rock Mass Category Number
1	4	3
2	8	5
3	16	4
4	12	1
5	2	3
6	8	1
7	14	2
8	4	4
9	10	2
10	6	3
11	9	1
12	1	1
13	1	3
14	7	4
15	11	4

DTN: MO0301SPASIP27.004

NOTES: Realization numbers 1 through 15 are from the sampling in the lithophysal zone provided by the source DTN.

An in situ (before excavation) stress state, defined by 7 MPa vertical and 3.5 MPa horizontal stresses, is used throughout the simulations, which is consistent with the 3DEC modeling in Section 6.3. The equilibrium state of the model after excavation of a drift represents the initial condition for the dynamic analysis. This equilibrium state is achieved by performing quasi-static simulation. The geometry and the boundary and initial conditions used in the initial quasi-static simulation preceding the dynamic simulation are illustrated in Figure 107.

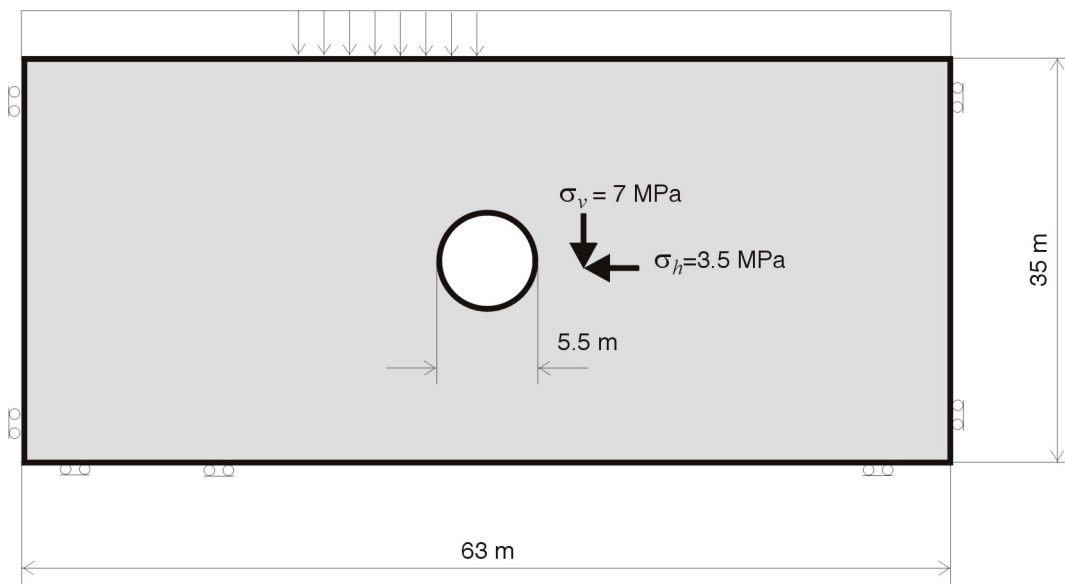


Figure 107. Dynamic Model, Initial and Boundary Conditions: Initial Static Simulation

The boundary conditions as used in the dynamic analysis are illustrated in Figure 108. Quiet boundaries (indicated in Figure 108 as viscous boundaries) were used on all models outside boundaries. These boundaries prevent reflection of outgoing seismic waves back into the model. Quiet boundaries were combined with free-field boundaries on the vertical outside boundaries. The free-field boundaries perform one-dimensional simulation of vertically propagating plane waves representing motion of truncated, semi-infinite medium. They prevent distortion of vertically propagating plane waves along the quiet boundaries. Dynamic loading was applied at the bottom of the model, as propagating vertically upwards. Although the dynamic loading was specified as velocity histories, it was applied at the bottom model boundary as stress boundary condition. However, using formulas developed for plane waves in elasto-dynamics, direct relation between velocity and stress can be established (Itasca 2002, Manuals/3DEC/Optional Features/Section 2: Dynamic Analysis, Section 2.6):

$$\begin{aligned}\sigma_y &= 2\rho C_p v_v \\ \sigma_{xy} &= 2\rho C_s v_h\end{aligned}\tag{Eq. 7}$$

where  $\rho$  is material density;  $C_p$  and  $C_s$  are P and S wave velocity; and  $v_v$  and  $v_h$  are vertical and horizontal velocity component. The factor 2 in Equation 7 is due to quiet boundaries. Figure 109 shows specified component 1 of the horizontal velocity history for ground motion 14. Velocity histories at the bottom and the top of the model, also shown in Figure 109, recorded during the simulation, confirm that the applied stress boundary condition results into the motion, which is exactly the same as the specified velocity boundary condition. Comparison of the velocities at the top and the model (identical histories slightly offset in time) confirms that the free-field boundaries operate correctly.

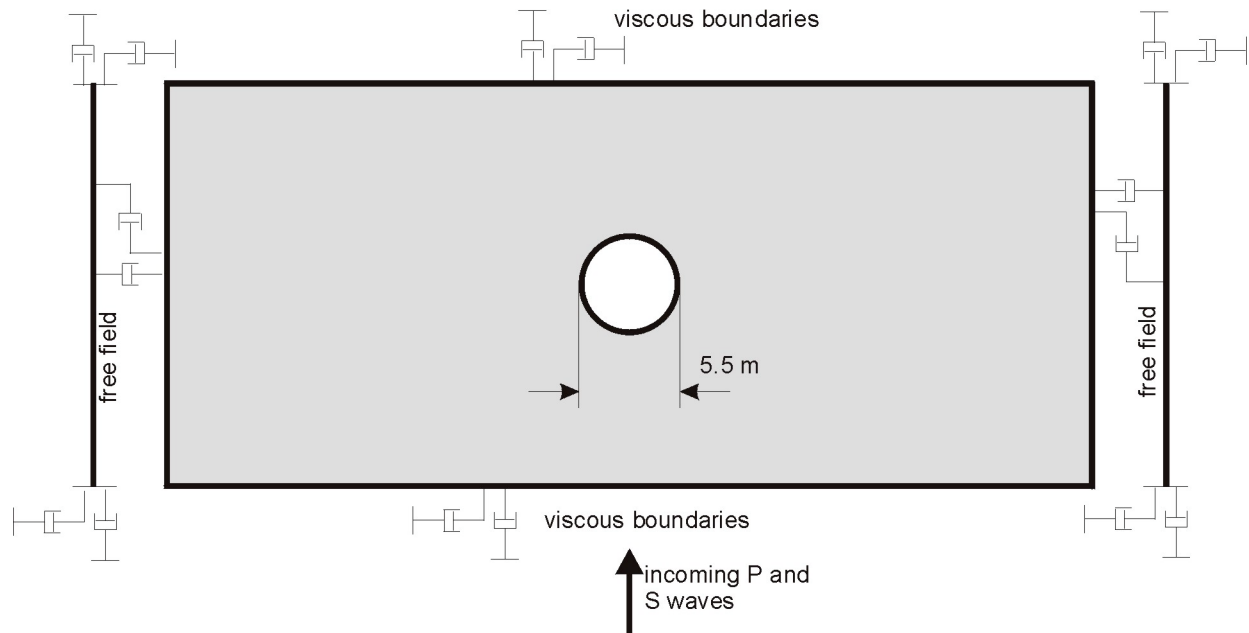
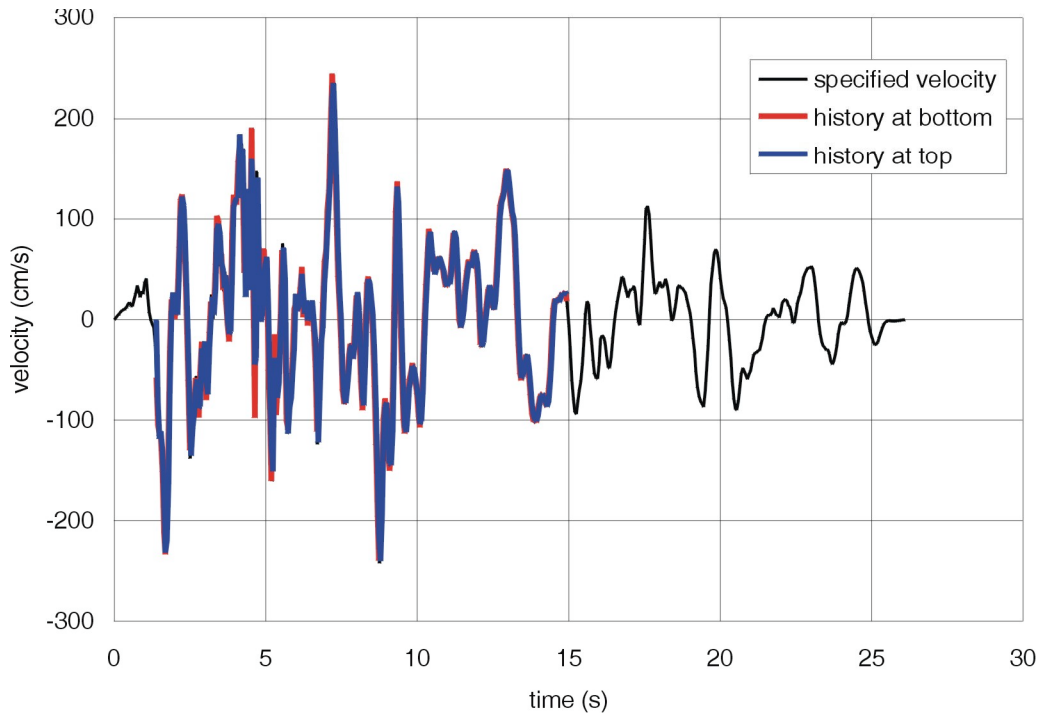


Figure 108. Dynamic Model Boundary Conditions for Dynamic Simulation

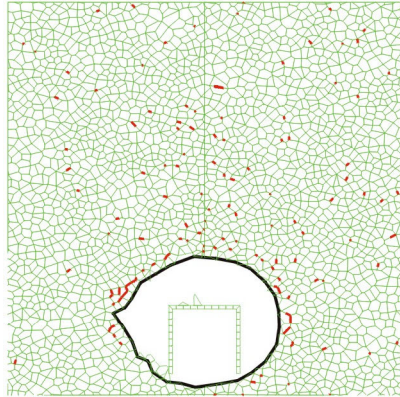
## Drift Degradation Analysis



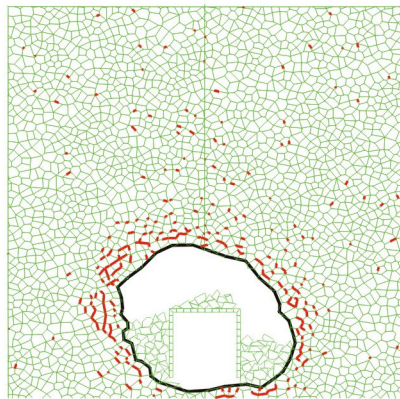
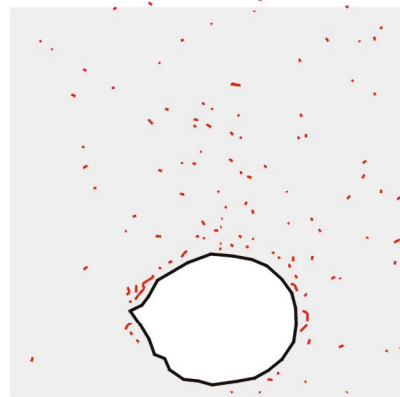
NOTES: The specified horizontal velocity is provided by DTN: MO0301TMHIS106.001. The horizontal velocities recorded at the top and at the bottom of the model coincide with the specified velocity.

Figure 109. Horizontal Velocity, Component 1 for Ground Motion 4

The conducted analyses indicate that ground motion with a probability of an annual occurrence of  $5 \times 10^{-4}$  will not induce any rockfall for rock mass categories 2 through 5. A relatively small amount of rockfall from the drift walls (shown in Figure 110a) is expected for category 1. The amount of rockfall and fracturing of the surrounding rock mass for extremely poor quality of rock (category 6), assuming no ground support, is shown in Figure 110b. The elastic stress paths from the preclosure ground motion simulation for the category 1 rock mass (shown in Figures 111 and 112 in the wall and roof, respectively) and the category 5 rock mass (shown in Figures 113 and 114 in the wall and roof, respectively) indicate that this level of ground motion causes small oscillations of the stress state relative to the initial equilibrium. With the exception of the point on the drift wall located in the category 1 rock mass, all stress states are within the elastic region throughout the duration of the preclosure ground motion. The observed rockfall is a consequence of regions that are above the yield limit after excavation of the drift (i.e., the wall in the category 1 rock mass) being shaken down.



a) category 1



b) category 6

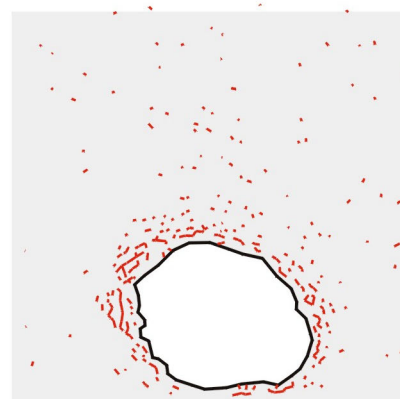


Figure 110. Geometry of the Model after Simulation for Preclosure Ground Motion (Probability  $5 \times 10^{-4}$ ): Rock Mass Categories 1 and 6

Drift Degradation Analysis

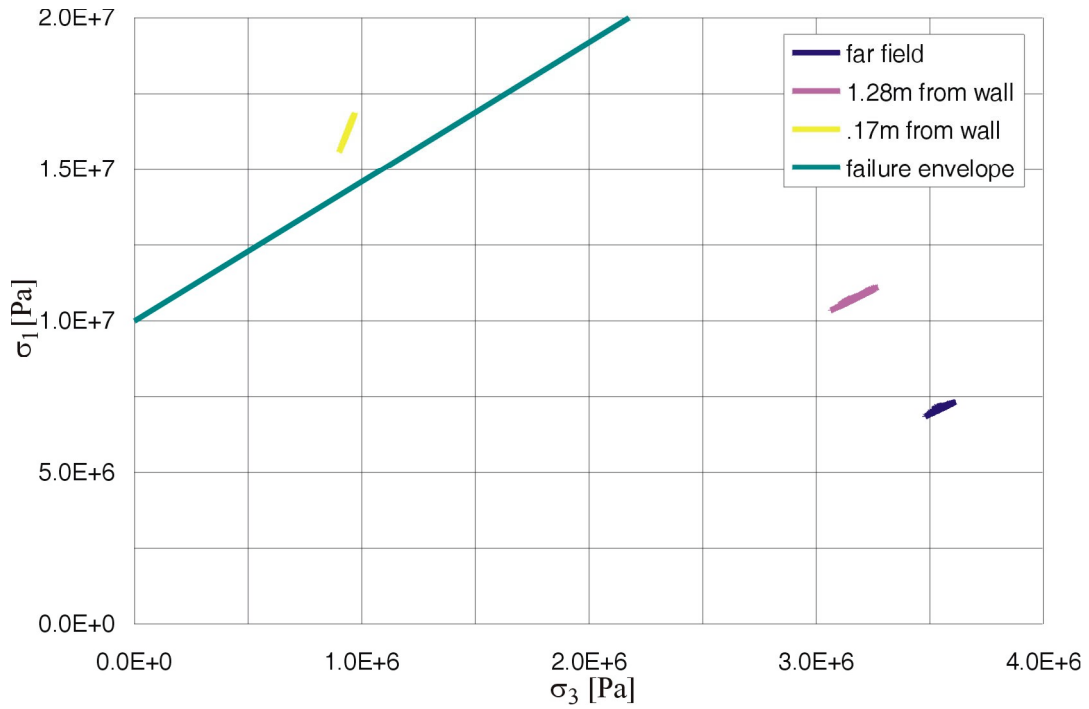


Figure 111. Elastic Stress Paths in the Drift Wall due to Preclosure Ground Motion: Category 1

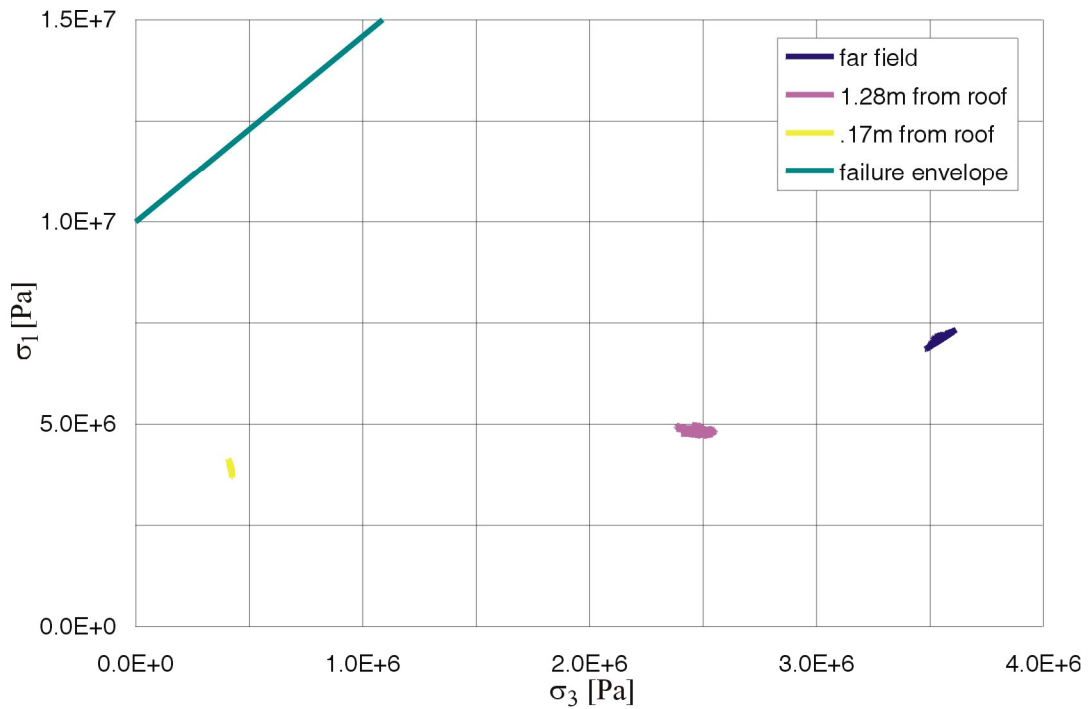


Figure 112. Elastic Stress Paths in the Drift Roof due to Preclosure Ground Motion: Category 1

Drift Degradation Analysis

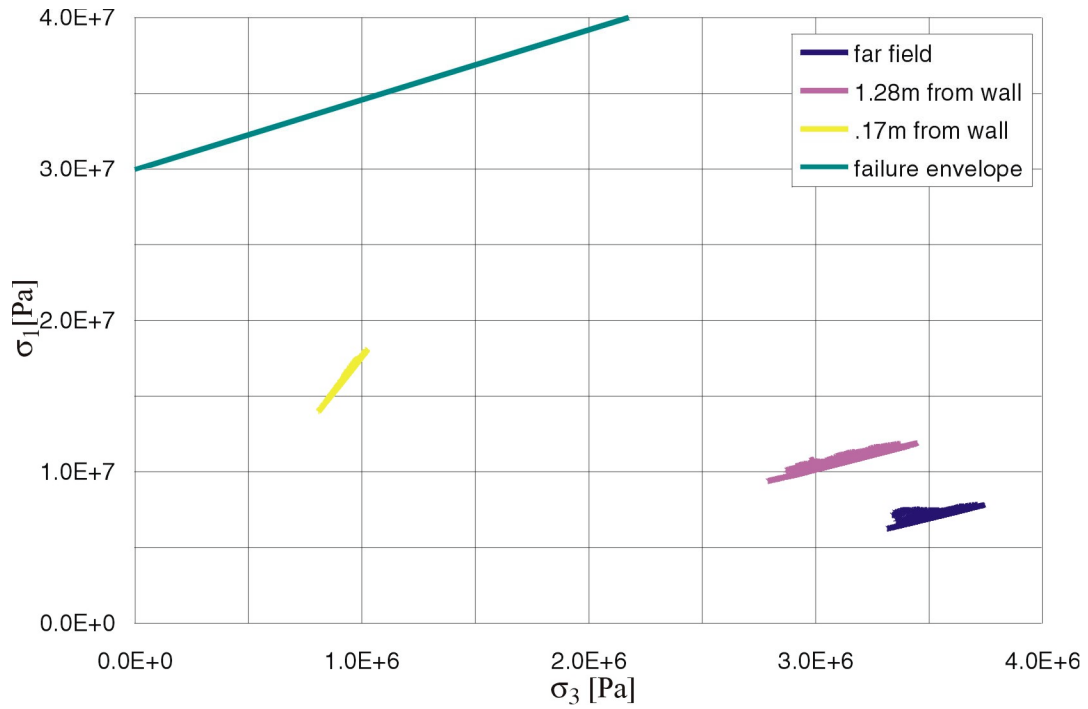


Figure 113. Elastic Stress Paths in the Drift Wall due to Preclosure Ground Motion: Category 5

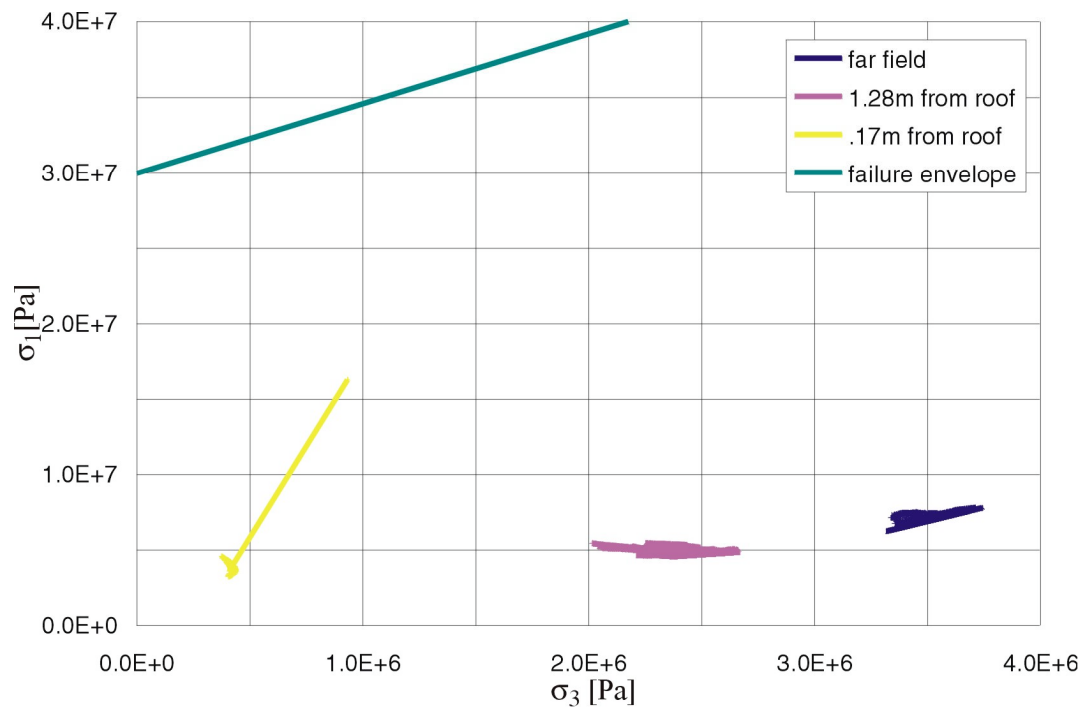


Figure 114. Elastic Stress Paths in the Drift Roof due to Preclosure Ground Motion: Category 5

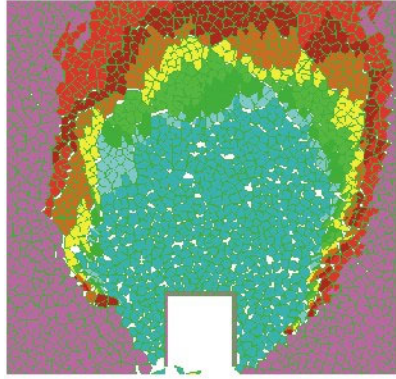
Ground motions with a probability of an annual occurrence of  $1 \times 10^{-6}$  cause complete collapse of the emplacement drifts irrespective of the rock mass category and ground motion case. The model geometries after simulations of realization numbers 1 through 6 from Table 37 are shown in Figure 115. Elastic stress paths (for ground motion case 1) shown in Figures 116 and 117, for the category 1 rock mass, and Figures 118 and 119, for the category 5 rock mass, demonstrate different mechanisms of drift collapse depending on the rock mass quality. In poor quality rock masses (e.g., categories 1 and 6), far-field stress (unaffected by the drift) is mostly elastic during the history of the ground shaking. However, stress amplifications and concentrations around the drift cause intense yielding in tension and shear, which eventually causes the drift to collapse. In the case of better rock mass quality (e.g., category 5), the rock mass fails in the tension even for far-field conditions (away from the drift), and tensile fractures propagate throughout the rock mass. The drift creates an open space into which the loose blocks collapse.

After the drift collapses, the overall bulking of the collapsed material in the model causes complete closure of the drift opening. The resulting pressures of the caved rock mass on the top, left and right side of the drip shield are summarized in Table 38. Detailed results for drip shield pressures are provided in Attachment XVI. The extremely large pressure ( $507.1 \text{ kN/m}^2$ ) on the right side of the drip shield for realization number 10 is a model artifact due to a single block wedged between the lower edge of the drip shield (set as rigid in the analysis) and the still unbroken rock mass. In reality, blocks are not elastic and such a stress would cause its breakage. Deformation of the drip shield would also result in a reduction of lateral pressure.

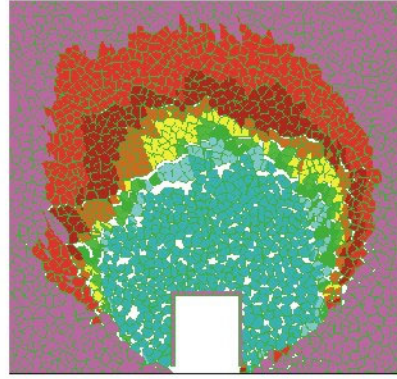
#### **6.4.1.2 Thermal Consideration in Lithophysal Units**

Geometry and boundary conditions used in the model for predictions of thermally induced rockfall are shown in Figure 120. The model does not perform complete thermal-mechanical simulation. Instead, temperature fields calculated with the code NUFT, for  $1.45 \text{ kW/m}$  and 50 years of forced ventilation, are imported into UDEC (thermal calculation described in Section 6.2). Two cases of ventilation efficiency were considered: 90 and 70 percent. Stresses are calculated for each new temperature state based on the temperature increment (from the previous temperature state) and the coefficient of thermal expansion. For all considered cases, the same coefficient of thermal expansion, function of temperature, was used. In order to have gradual evolution of stresses during the simulated time, 45 temperature fields (corresponding to different times after waste emplacements) were considered. For each new temperature field, simulation was conducted in two steps. First, the model was run to the equilibrium elastically (i.e., all unbroken bonds were made infinitely strong). Next, after the model had reached equilibrium, the actual strength was assigned to the unbroken bonds and the model was run again to the equilibrium. The reason for the two-step approach was to reduce the impact of non-gradual stress changes due to incremental changes of temperature state. The entire analysis was conducted considering that rock mass strength does not degrade with time. Any observed damage and rockfall are consequences of the thermally induced stresses only. All three cases of thermal calculation (described in Section 6.2) were considered for the drift stability analysis in lithophysal rock mass: (a) base case (average thermal properties and 90 percent ventilation efficiency); (b) case 2, sensitivity calculation for thermal properties (thermal properties one standard deviation smaller than the average properties); and (c) case 3, sensitivity calculation for the heat removal ratio (average thermal properties and 70 percent ventilation efficiency).

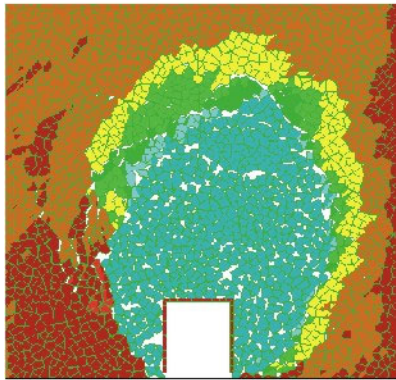
Drift Degradation Analysis



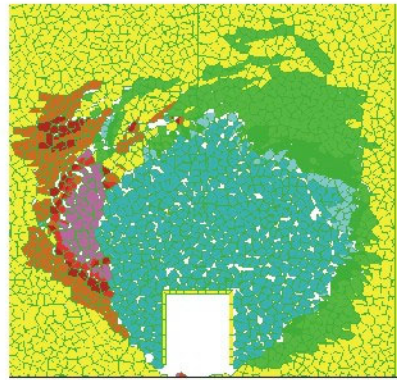
a) realization 1



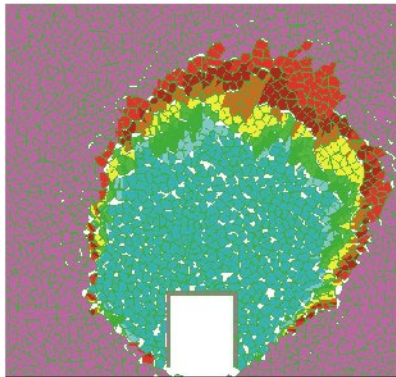
b) realization 2



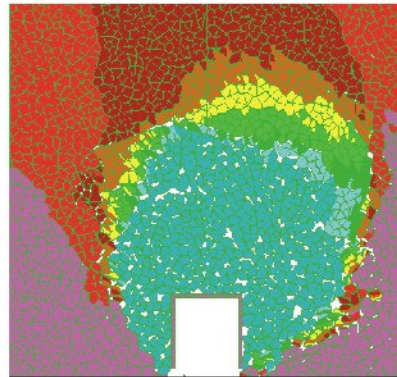
c) realization 3



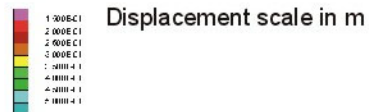
d) realization 4



e) realization 5



f) realization 6



NOTE: Blocks are colored by magnitude of displacement.

Figure 115. Geometry of the Model after Simulations for Postclosure Ground Motions (Probability  $1 \times 10^{-6}$ ): Realizations 1 through 6 from Table 37

Drift Degradation Analysis

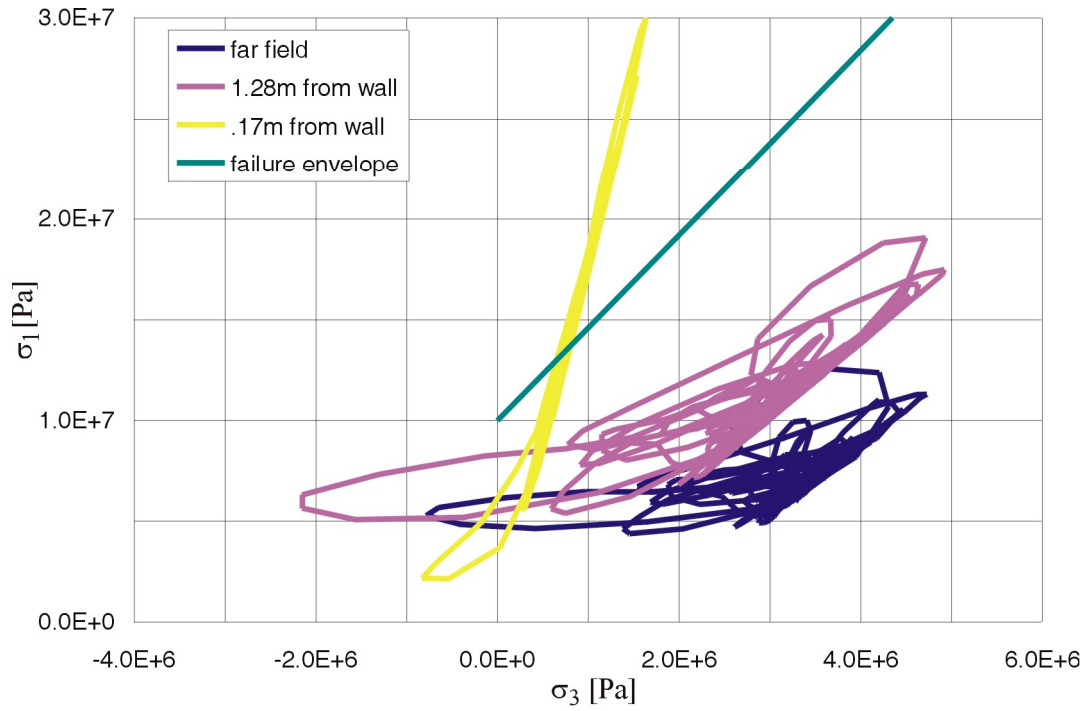


Figure 116. Elastic Stress Paths in the Drift Wall due to Postclosure Ground Motion No. 1: Category 1

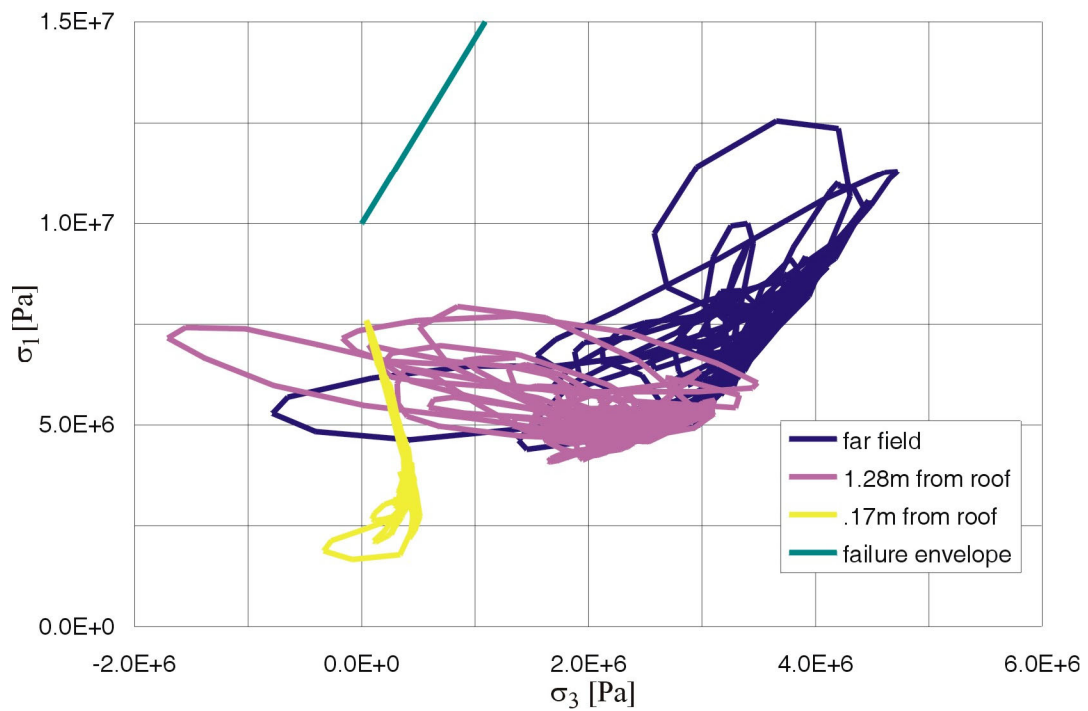


Figure 117. Elastic Stress Paths in the Drift Roof due to Postclosure Ground Motion No. 1: Category 1

Drift Degradation Analysis

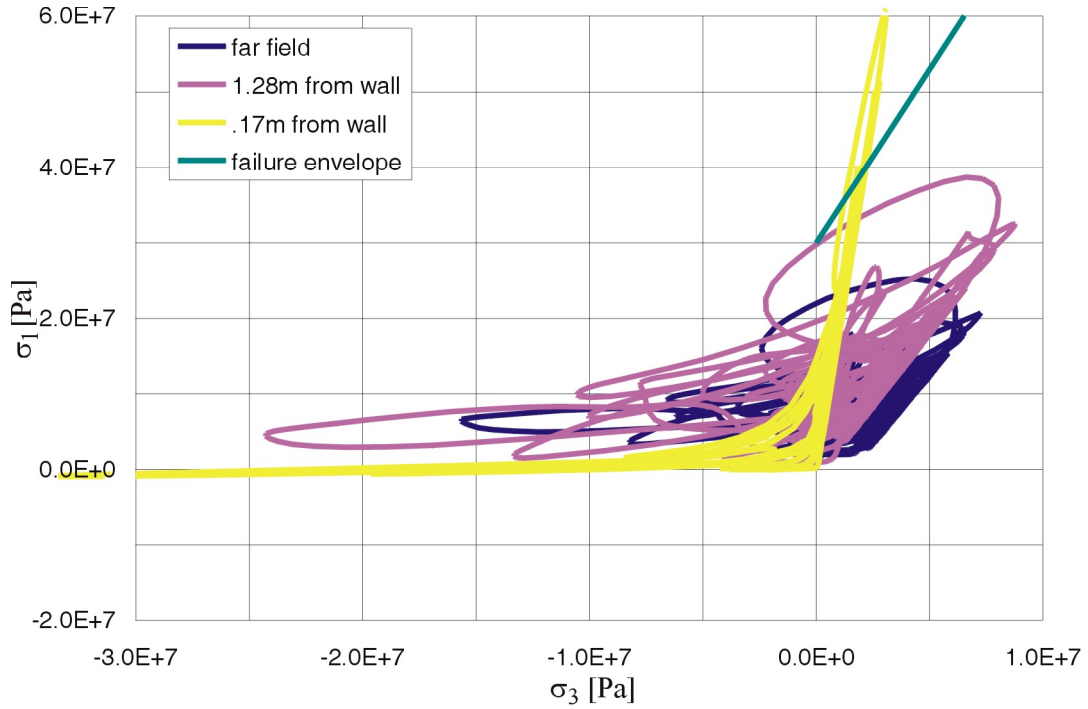


Figure 118. Elastic Stress Paths in the Drift Wall due to Postclosure Ground Motion No. 1: Category 5

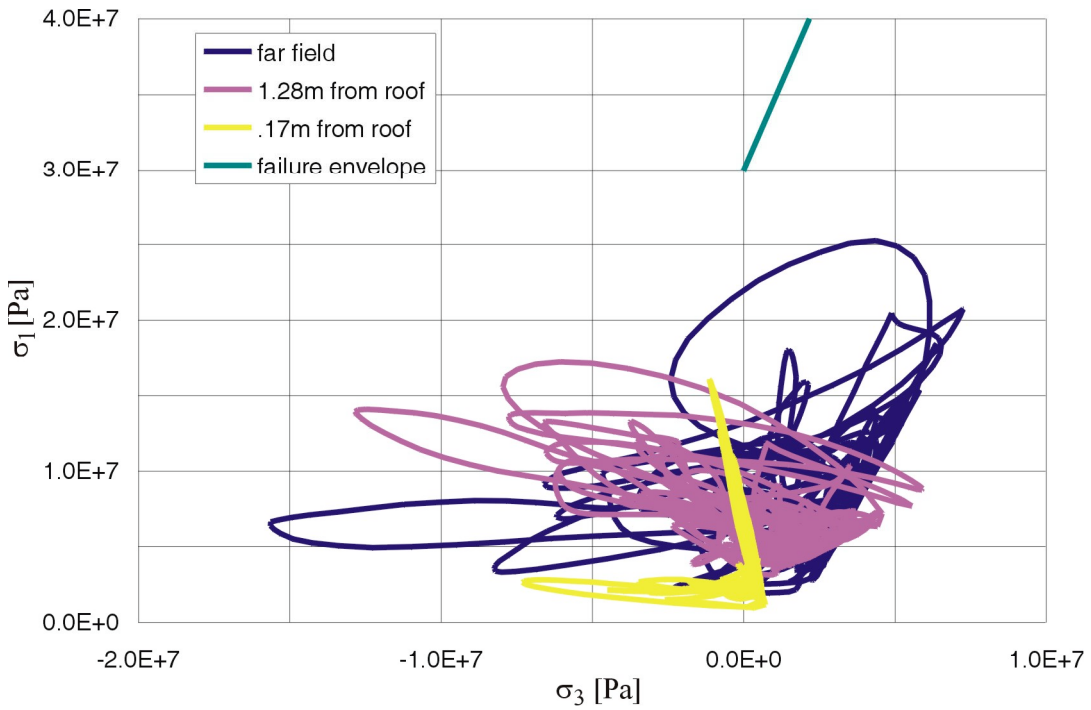


Figure 119. Elastic Stress Paths in the Drift Roof due to Postclosure Ground Motion No. 1: Category 5

Table 38. Summary of Loads on the Drip Shield after Drift Collapse Caused by Postclosure Ground Motion (Probability  $1 \times 10^{-6}$ )

Realization Number	Pressure Left (kN/m <sup>2</sup> )	Pressure Top (kN/m <sup>2</sup> )	Pressure Right (kN/m <sup>2</sup> )	Bulking (kN/m <sup>2</sup> )
1	33.0	263.2	211.1	0.16
2	19.1	147.0	16.5	0.35
3	13.3	197.4	21.9	0.21
4	272.7	317.1	53.5	0.22
5	24.5	154.1	49.7	0.32
6	21.6	89.6	16.8	0.13
7	19.4	168.8	62.2	0.36
8	27.7	161.7	24.8	0.24
9	24.3	92.0	99.4	0.24
10	18.6	161.9	507.1	0.52
11	84.0	150.2	33.2	0.29
12	42.3	292.6	33.7	0.27
13	22.5	163.7	9.0	0.21
14	27.6	167.5	13.8	0.28
15	8.9	146.6	30.9	0.37

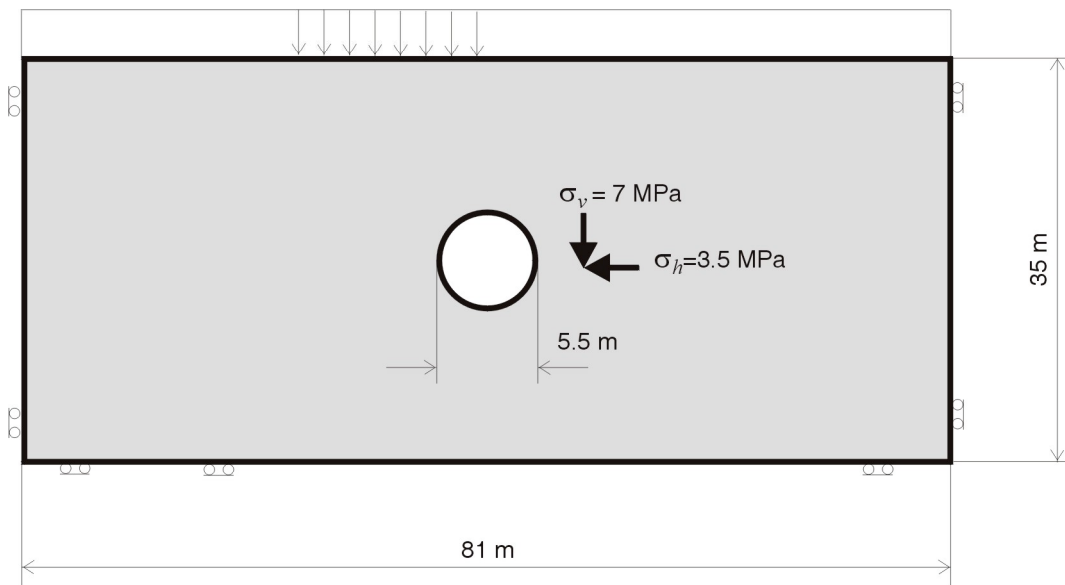


Figure 120. Thermal-Mechanical Model Initial and Boundary Conditions

The simulation was conducted for all six categories of the rock mass. It is observed that the amount of thermally induced rockfall is generally small. The temperature and stress fields for rock mass category 1 with the base-case thermal properties and 90 percent ventilation efficiency are shown in Figure 121. The figure shows the model state after 80 and 10,000 years of heating. There is no significant rockfall or damage induced by heating. Conditions are similar for other rock mass categories. Elastic stress paths during 10,000 years of temperature variation are

shown in Figures 122 and 123, for rock mass category 1 in the wall and roof, respectively, and in Figures 124 and 125, for rock mass category 5 in the wall and roof, respectively. The elastic stress paths confirm the results of the UDEC model. The drift wall in the category 1 rock mass is in the yielding state after drift excavation. Heating does not increase damage significantly (Figure 122). The stress state in the drift roof in category 1 (shown in Figure 123) moves closer to the yield surface during heating, but it still remains elastic. The thermal stress increase in the drift roof in the category 5 rock mass (Young's modulus of 19.7 MPa) moves the stress state barely above the yield surface (Figure 125) during the relatively short period of time when the temperature reaches the maximum, around 80 years after waste emplacement. This is consistent with observation of minor rockfall from the drift roof in rock mass category 5.

The rockfall simulations using temperatures from cases 2 and 3 of the thermal calculation do not show any increase in rockfall compared to the base case.

### 6.4.1.3 Combined Seismic and Thermal Effect in Lithophysal Units

Stability of the emplacement drifts located in the lithophysal rock units was investigated for both thermal and seismic loading conditions independently for both seismic and thermal loading conditions in Sections 6.4.1.1 and 6.4.1.2, respectively. The initial condition for the seismic analysis discussed in Section 6.4.1.1 was in situ stress state perturbed by excavation of the drifts only. An additional analysis, presented in this section, was done to assess the effect of changing thermal stress in the rock mass around the repository after waste emplacement as an initial condition for seismic ground shaking. Using a similar approach as for the nonlithophysal rock (Section 6.3.1.4), stress paths during the regulatory period of 10,000 years were recorded at a number of locations around the drift. Temperatures from the thermal calculations for the base case and the sensitivity calculation for the heat removal ratio (case 3 in Section 6.2) were considered. The critical state was qualitatively determined from those paths, based on locations of stress states along that path relative to the yield surface. The critical state was used as an initial condition for the seismic analysis. Because the ground motion with  $1 \times 10^{-6}$  probability of annual occurrence results in complete drift collapse, it was not of particular interest to investigate the effect of that level of ground motion combined with thermally induced initial stresses. Instead, ground motion with  $5 \times 10^{-4}$  probability of annual occurrence was considered. Since the predicted temperatures are similar for the base case and the sensitivity case 2 at preclosure period, the sensitivity case 2 is not considered for the evaluation of the combined seismic and thermal effect. Rock mass categories 1 and 5 were considered in this analysis.

Stress paths (principal stresses) at 14 different locations around the drifts in rock mass category 1 during the regulatory period of 10,000 years are shown in Figures 126, 127, and 128. A yield condition corresponding to 10 MPa uniaxial compressive strength, and a selected friction angle of  $40^\circ$  is also indicated in the figures. Stress states at two points, almost at the drift springline (shown in Figures 126 and 127), are above the yield surface. Because those stresses are at the points inside the elastic blocks (inelastic behavior of this model is due to inelastic deformation of joints only), it is possible that they lay outside the yielding surface.

Drift Degradation Analysis

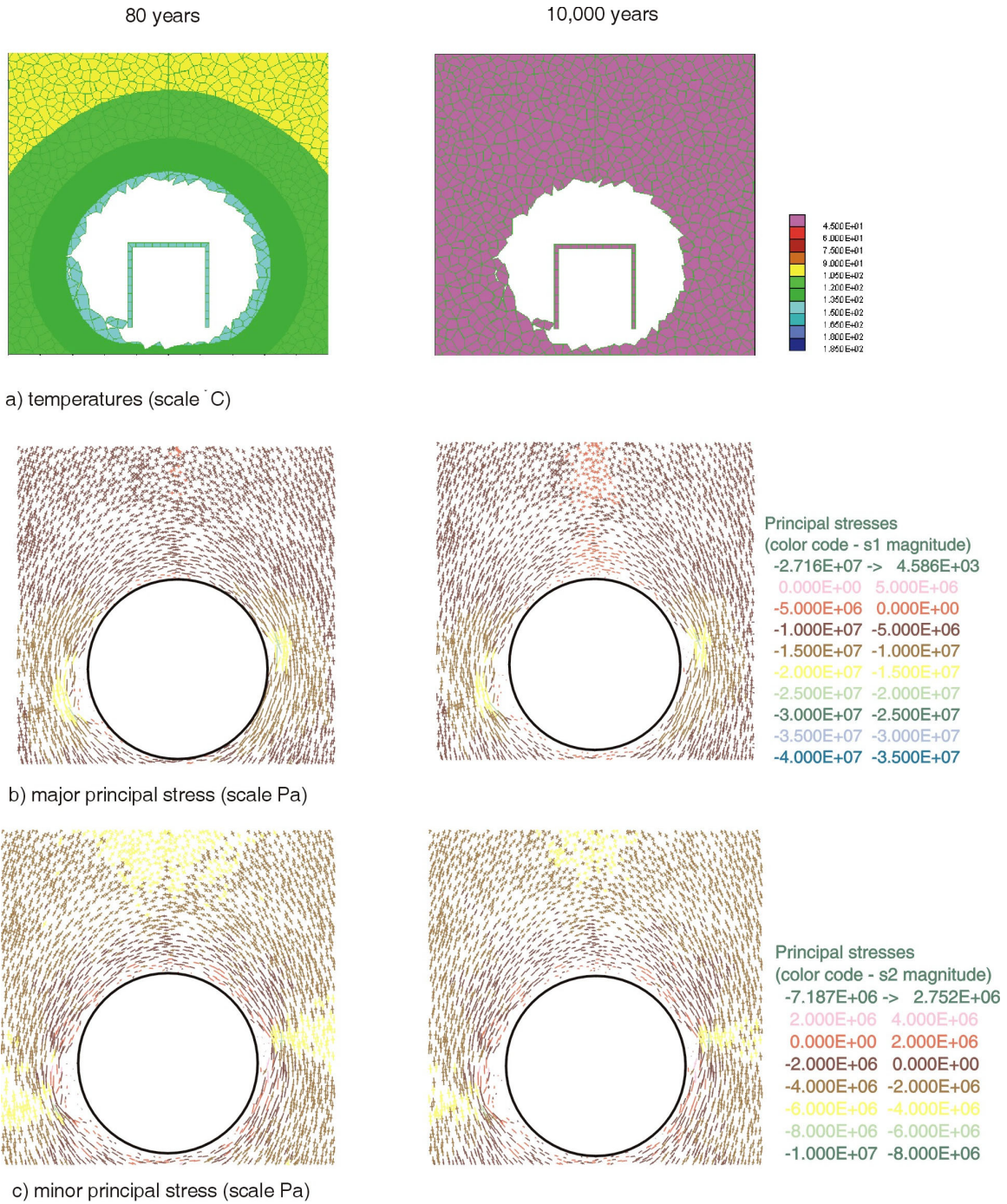


Figure 121. Thermally Induced Rockfall and Stresses After 80 and 10,000 years of Heating in Rock Mass Category 1

Drift Degradation Analysis

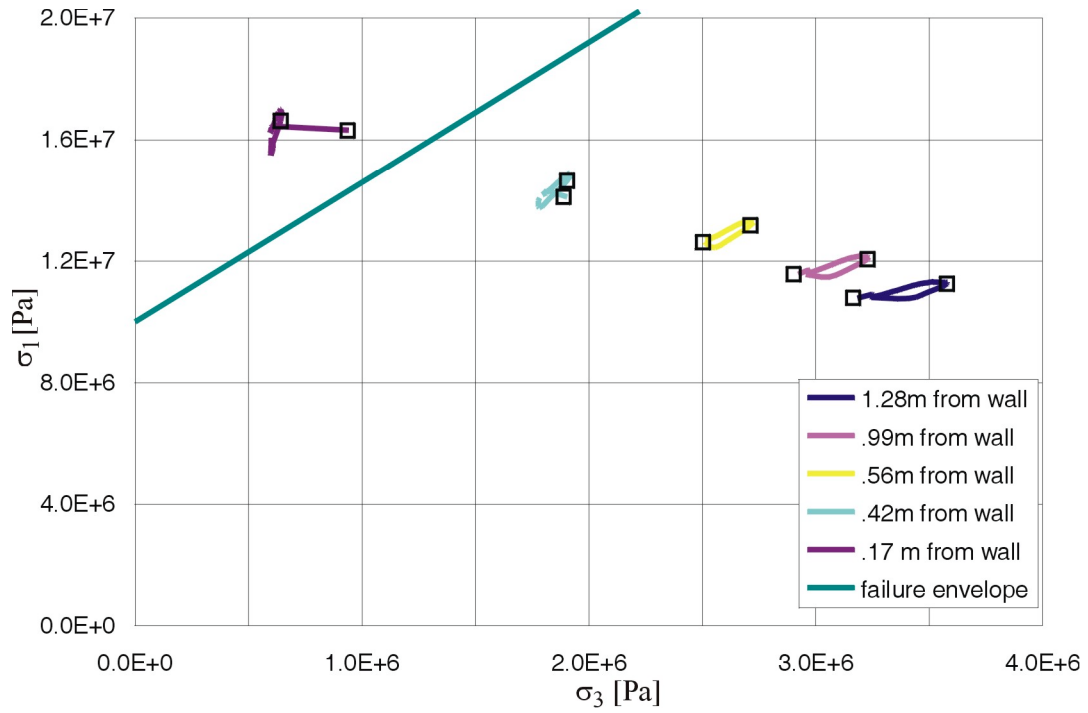


Figure 122. Elastic Stress Paths in the Drift Wall due to Temperature History: Category 1

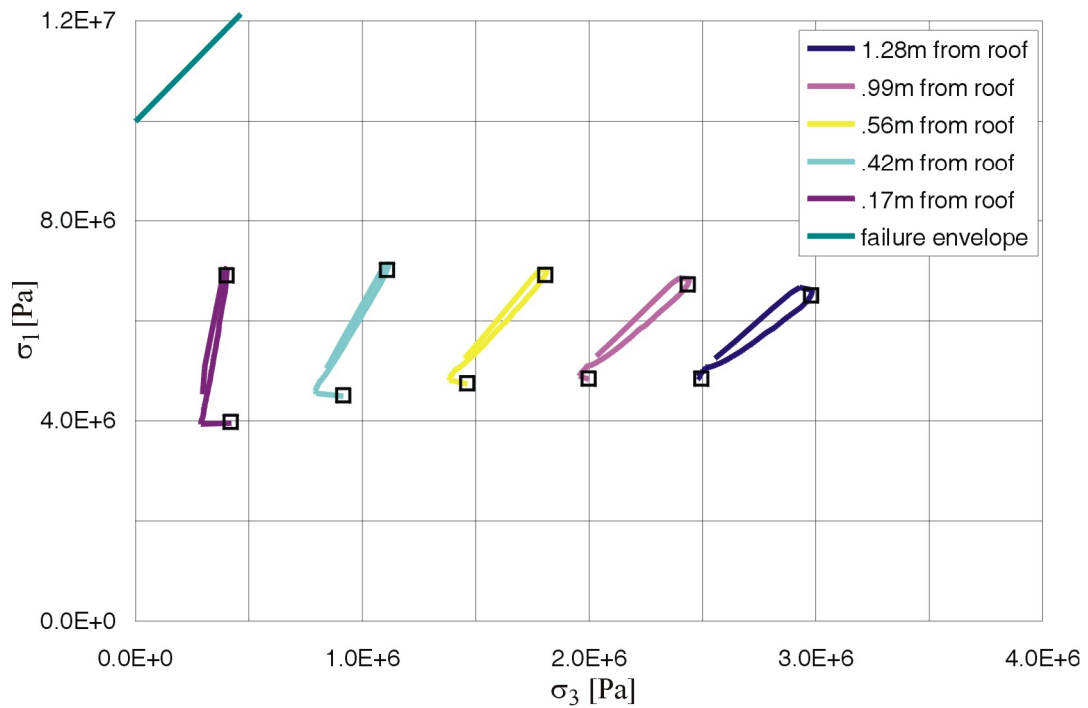


Figure 123. Elastic Stress Paths in the Drift Roof due to Temperature History: Category 1

Drift Degradation Analysis

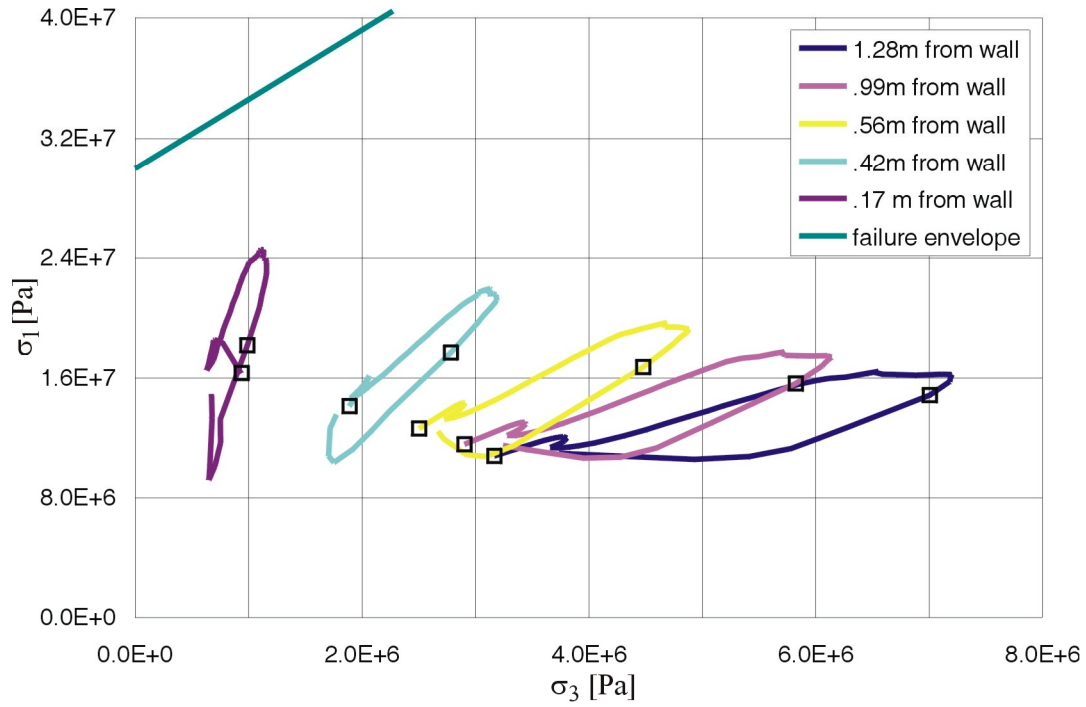


Figure 124. Elastic Stress Paths in the Drift Wall due to Temperature History: Category 5

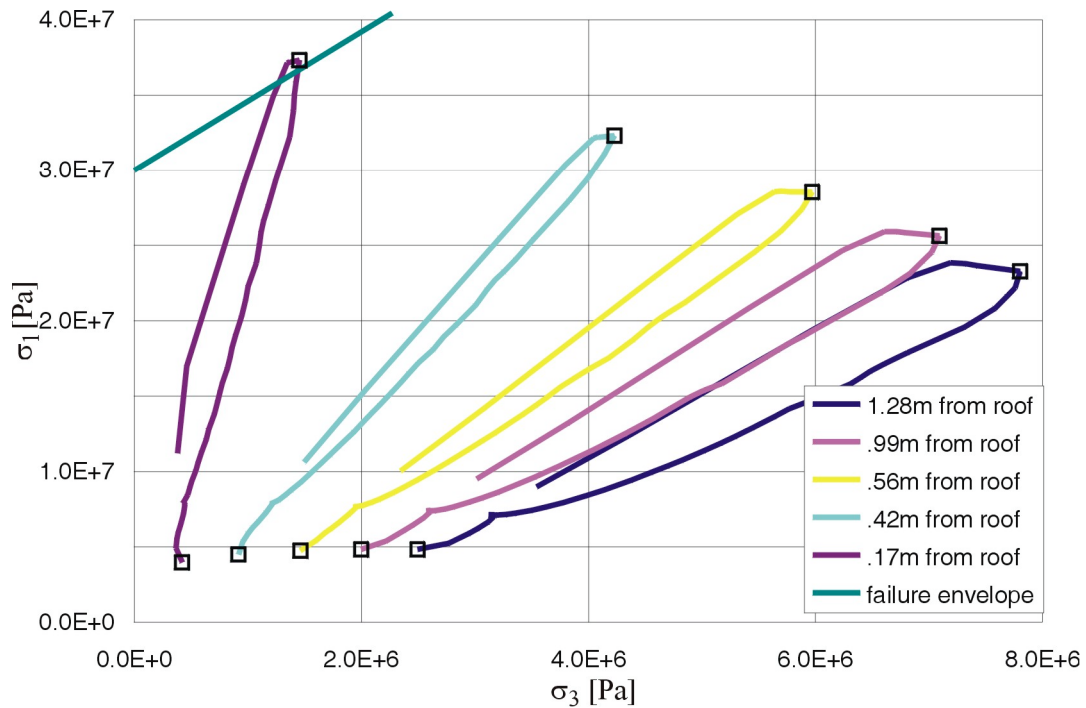


Figure 125. Elastic Stress Paths in the Drift Roof due to Temperature History: Category 5

Drift Degradation Analysis

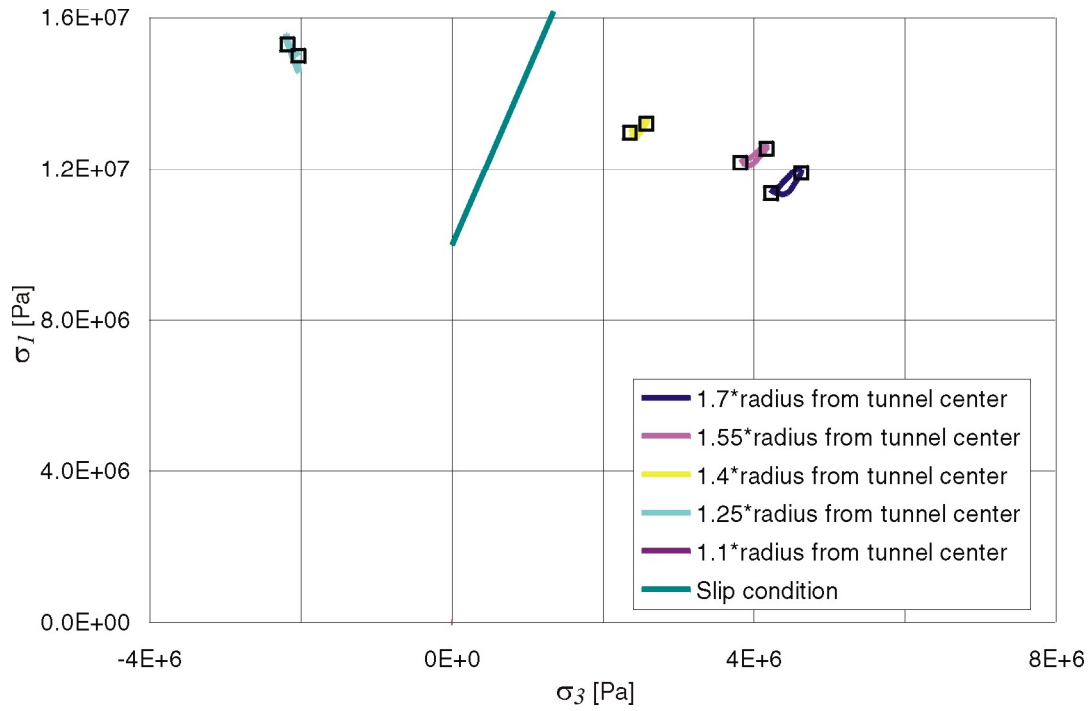


Figure 126. Stress Paths in the Left Drift Wall due to Temperature History: Category 1

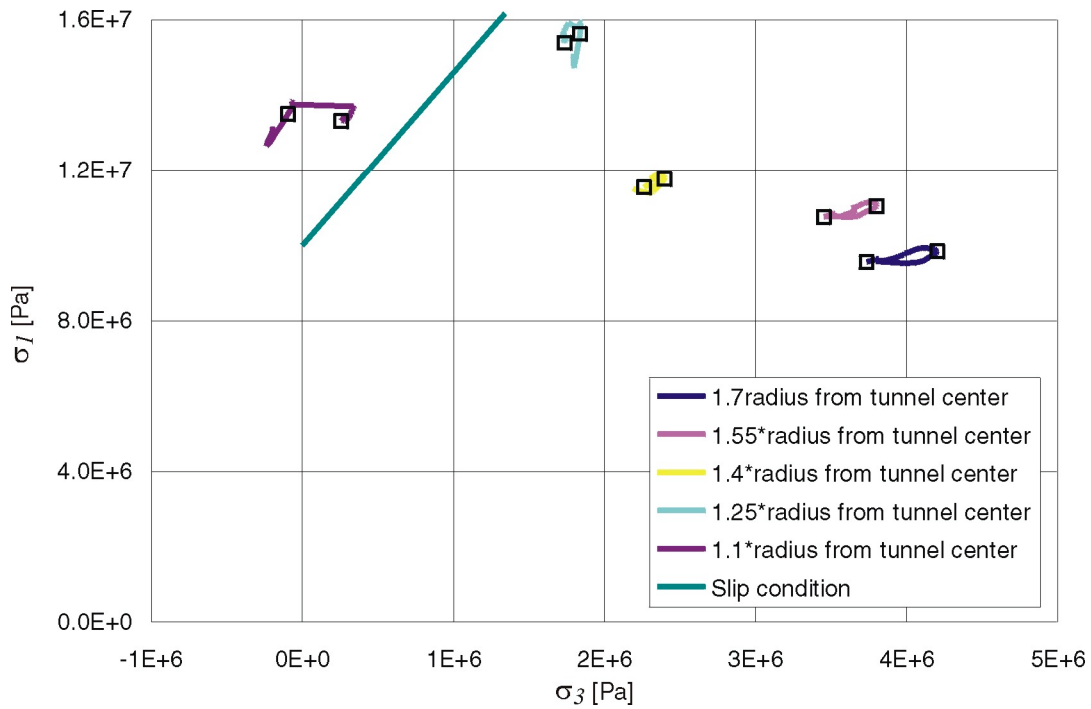


Figure 127. Stress Paths in the Right Drift Wall due to Temperature History: Category 1

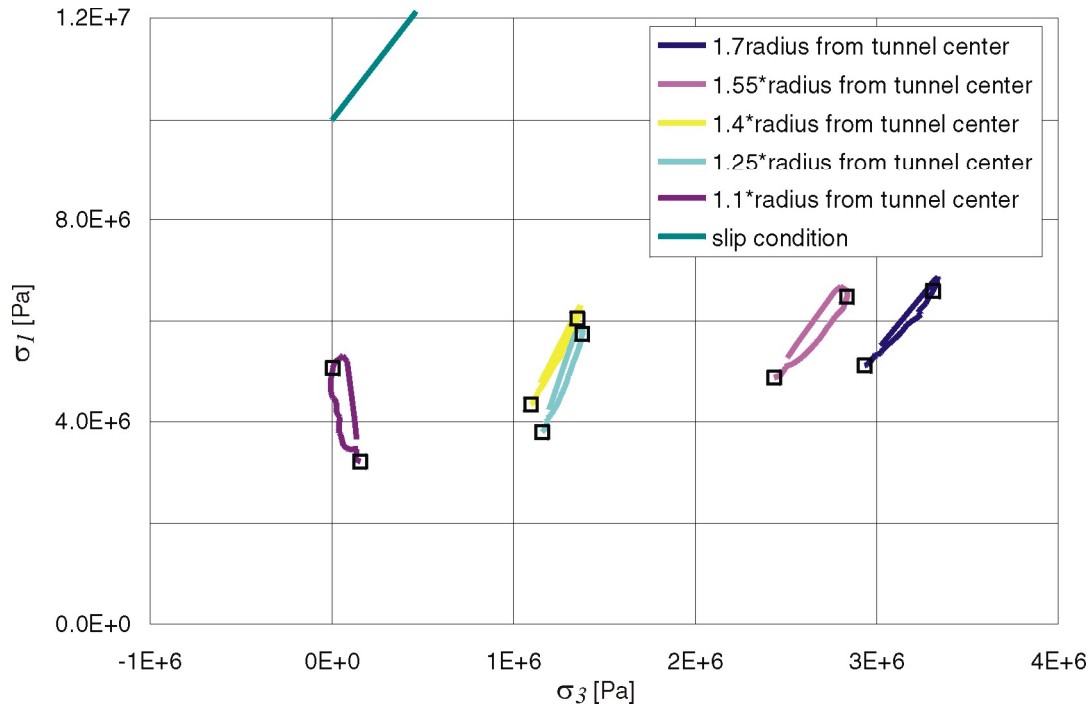


Figure 128. Stress Paths in the Drift Roof due to Temperature History: Category 1

Stress variation due to heating is quite limited in this case, since the stiffness of rock mass is small (i.e., Young's modulus is 1.9 GPa). The initial stress state and the state after 80 years of heating, selected as critical on the stress path, are marked on the plots with the squares.

Seismic analysis after 80 years of heating for rock mass category 1 resulted in an increased rockfall compared to rockfall from the seismic shaking of the rock mass at an in situ stress state (see Figures 129a and 130a). No rockfall is induced in rock mass category 5 in the case of 90 percent ventilation efficiency (Figure 129b), and very little rockfall in the case of 70 percent ventilation efficiency (Figure 130b). The result of an increase in rockfall for lithophysal rock mass category 1 is in an apparent contradiction with the results of the same analysis for the nonlithophysal units. Thermal stresses in the case of nonlithophysal rock resulted in reduced rockfall. However, the mechanism of rockfall is completely different for these two cases. In the case of the nonlithophysal rock mass, rockfall is due to sliding of blocks along the pre-existing joints, and an increase in the initial stress increases confinement on the joints, thereby increasing their resistance to sliding. In the case of the lithophysal rock mass, ground motion with  $5 \times 10^{-4}$  probability of annual occurrence causes rockfall by shaking down already damaged rock mass around the drift. Therefore, the heating induces additional damage (compared to damage caused by drift excavation), which does not necessarily result in a rockfall under static loading conditions, but is shaken down by the  $5 \times 10^{-4}$  ground motion.

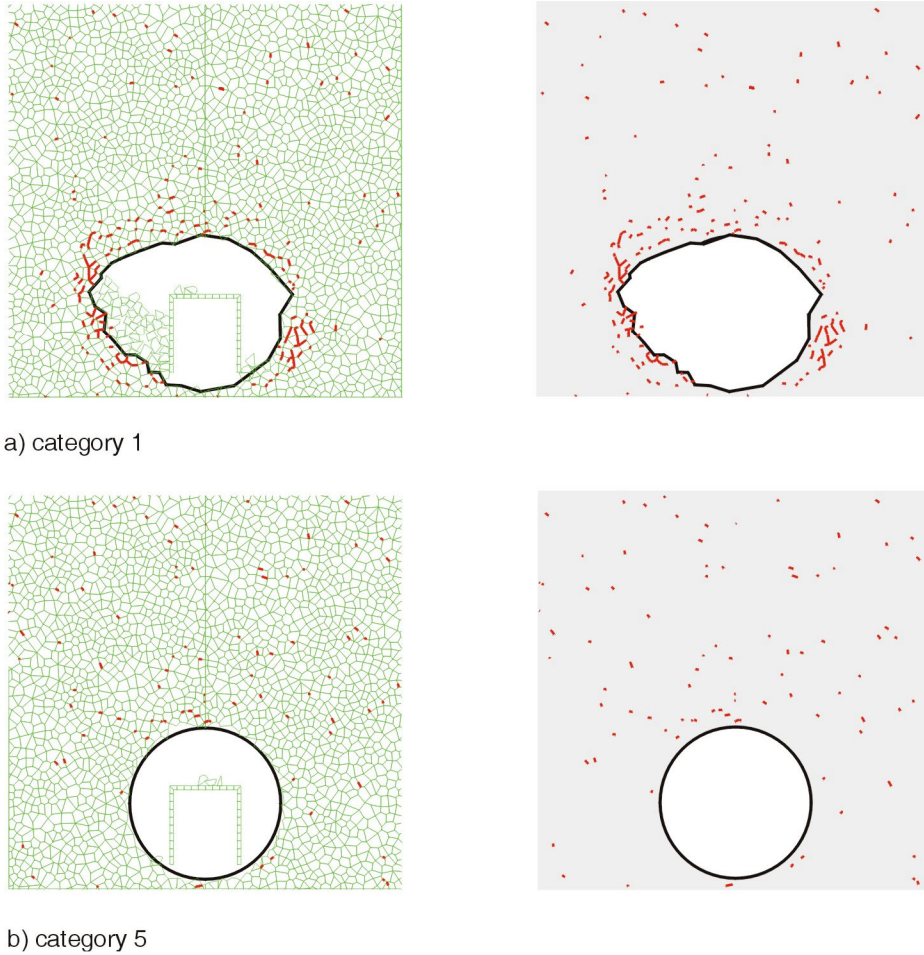


Figure 129. Rockfall and Fractures Induced Around a Drift by Preclosure Ground Motion After 80 Years of Heating in Rock Mass Categories 1 and 5

### 6.4.2 Lithophysal Rock Mass Degradation

Underground and surface excavations, which are designed to be stable after excavation, degrade with time, and some eventually collapse completely. The main reason for these observations is that strength of a rock mass exposed to humidity and temperature of the open atmosphere decays with time when it is loaded to a stress levels higher than 50 to 60 percent of its short-term strength. The rate of strength decay depends, among other parameters, on rock type, stress state, relative humidity and temperature. Stress corrosion is considered the main mechanism causing strength degradation of the rocks (Potyondy and Cundall 2001, Section 3).

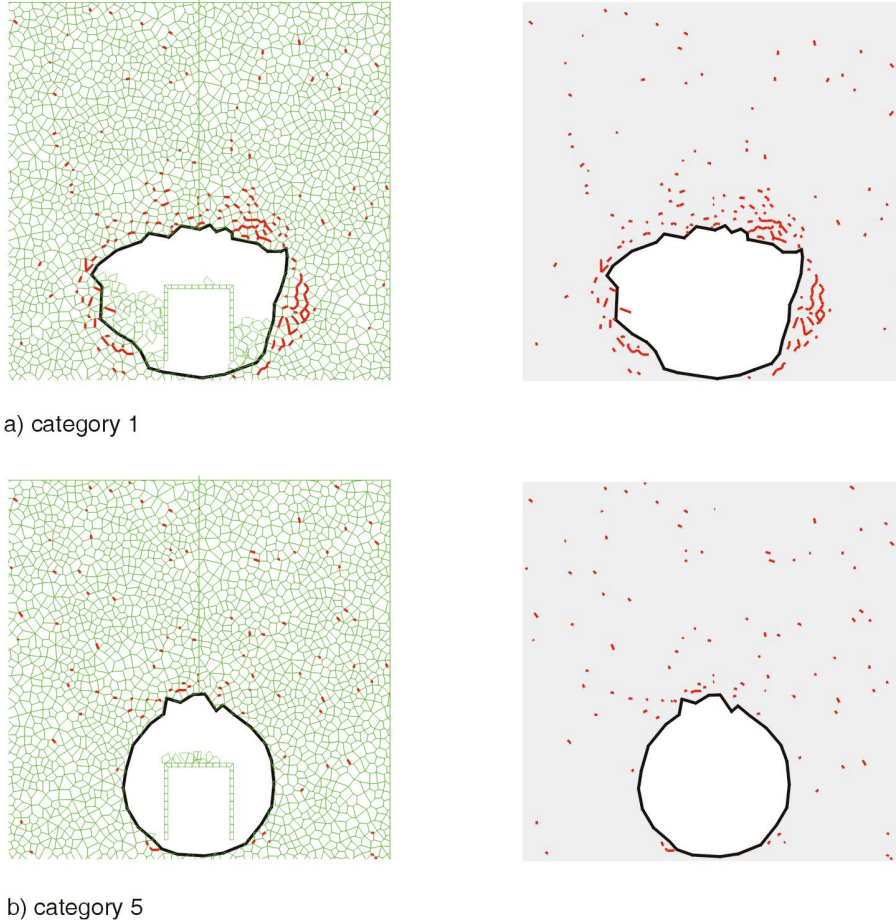


Figure 130. Rockfall and Fractures Induced around a Drift by Preclosure Earthquake after 80 Years of Heating (70 Percent Ventilation Efficiency) in Rock Mass Categories 1 and 5

The emplacement drifts at Yucca Mountain will be stable under currently existing conditions (in situ stresses and rock mass strength) without any ground support. However, it is expected that during the regulatory period of 10,000 years the ground support will completely lose its integrity, and drift degradation will occur due to strength decay of the rock mass. Drift degradation is important issue for the repository design and performance (e.g., drifts have to remain open during the preclosure period; the caved rock will load the drip shields possibly affecting their integrity and performance). Prediction of the rate of drift degradation for the duration of the regulatory period of 10,000 years is extremely difficult task (it requires extrapolation of testing results, which can be done for a period of months or a year, to a period of 10,000 years). Uncertainty in such predictions will be quite large. Although testing and modeling of strength decay of rock mass is recommended, it is reasonable to estimate the extent of caving of the rock mass above the drifts and the loads of the caved rock on the drip shield for the extreme conditions, when the rock mass completely loses its cohesive strength. Cohesion and tensile strength of the rock mass are considered to degrade to zero in the degradation model. Friction angle will likely have very minor change. No change of friction angle is considered in the model. Such an estimate will represent a conservative (i.e., high) upper bound of the load of the caved rock on the drip shield irrespective of the rate of strength decay and the residual strength of the rock mass.

Predictions of drift degradation and the load of the broken rock on the drip shield were done using three different approaches: (a) analytical, (b) numerical, continuum, and (c) numerical, discontinuum. Each of the methods uses certain conditions regarding caving of the rock above the drifts and transfer of the stresses within the broken rock mass. Those conditions make the model results (i.e., cave size and pressures on the drip shield) conservative in each of three approaches (i.e., the conditions result in higher pressures). The level of conservatism is the largest in the analytical results, and the smallest in the approach that represents rock mass as a discontinuum.

#### 6.4.2.1 Bulking

When the rock mass above underground openings collapses it increases volume (i.e., it bulks). During the collapse, either sudden or gradual, rock mass disintegrates in a number of pieces (blocks) which fall separately rotating along the way. When blocks equilibrate after caving, they do not fit together resulting in increased porosity and overall volume. Rock mass of volume  $V$  in the in situ conditions has volume  $V_B$  after caving, where:

$$V_B = (1 + B)V \quad (\text{Eq. 8})$$

where  $B$  is the bulking factor.

Amount of bulking (i.e., the bulking factor,  $B$ ) depends, among other things, on the lithology, pre-existing internal structure (jointing, bedding), and the mechanism of collapse. For example, density of crushed limestone is in the range between 1360 kg/m<sup>3</sup> and 1440 kg/m<sup>3</sup>; while density of the crushed dolomite is in the range between 1280 kg/m<sup>3</sup> and 1600 kg/m<sup>3</sup> (Fruchtbaum 1988). Considering that the specific gravity of limestones and dolomites is approximately 2.6 (Bauer et al. 1991), and using an in situ porosity of 20 percent (Goodman 1980), the in situ density of limestones and dolomites is approximately 2200 kg/m<sup>3</sup>. Consequently bulking of these rocks from in situ state to a crushed state is between 37.5 and 72 percent. Duncan et al. (1980) reported that porosity of the rock fill for dams is between 23 and 36 percent. The rock fill used for dams is crushed to satisfy certain size requirement and is compacted during construction, which leads to reduction of its porosity. It appears from this discussion that bulking factor for the caved rock can be conservatively selected to be in the range between 0.2 and 0.4.

Caving of the underground excavations is a self-limiting process in many situations. At a certain stage of caving, due to bulking, the volume of the caved rock completely fills the volume of the original excavation and the volume occupied by the collapsed rock before onset of collapse. When the cave is completely filled, the broken rock provides the backpressure, which prevents further collapse of the rock mass.

#### 6.4.2.2 Analytical Consideration

It is considered in this approach that the cave above the emplacement drift grows until it becomes filled with the broken rock. The extent of the caved rock is calculated as a function of the bulking factor,  $B$ , considering that the cave stabilizes when it is completely filled with the broken rock. An additional unknown in this approach is the shape of the cave. Two extreme conditions illustrated in Figures 131 and 132 and were considered.

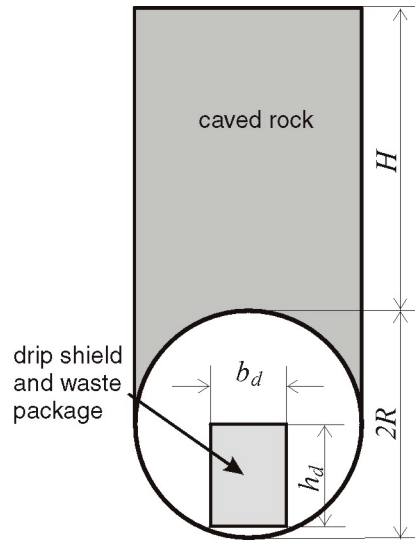


Figure 131. "Piping" Type of Caving Mechanism

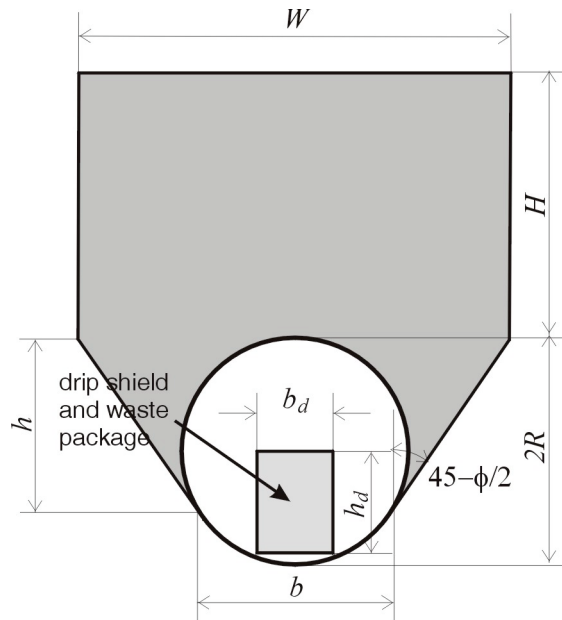


Figure 132. Terzaghi Type of Caving Mechanism

The "piping" mode of roof collapse (shown in Figure 131) is typical for conditions when the rock mass is bedded and there is a relatively large ratio of the span of the excavation to its depth. This type of roof collapse is typical for coal mines (with a bedded shale overburden) using the longwall mining method, and almost always occurs suddenly. Roof piping collapse is not a likely mode of drift collapse for the following reasons:

- None of the rock mass units are layered
- Drifts are relatively deep below the ground surface
- Drift collapse due to strength decay will evolve gradually over a long period of time.

The piping mechanism is considered here as a conservative extreme condition and is a mechanism that results in the largest vertical extent of the cave,  $H$ .

The other extreme condition of the rock mass collapse around the underground opening (shown in Figure 132) corresponds to the limit equilibrium conditions around a shallow tunnel, which Terzaghi (1943) used to calculate the load on the tunnel support. Slip lines extend from the drift walls at an angle of  $45 - \phi/2$  from the vertical direction, where  $\phi$  is the friction angle.

The cave height,  $H$ , is calculated for both cases as a function of the bulking factor,  $B$ . The pressure of the collapsed rock on the drip shield is calculated considering that the rock filling the cave acts on the drip shield as a dead weight. Expressions for the height of the cave are shown in Equations 9 and 10 for the piping and Terzaghi failure mechanisms, respectively, which have been derived based on the consideration of the geometry shown in Figures 131 and 132:

$$\frac{H}{2R} = \frac{1}{2} \left[ \frac{\pi}{2B} - \frac{b_d h_d}{2BR^2} - \left( 1 - \frac{\pi}{4} \right) \right] \quad (\text{Eq. 9})$$

$$\frac{H}{2R} = \frac{\frac{\pi}{B} - \frac{b_d h_d}{BR^2} - \frac{b+W}{2R^2} h + \frac{V_s}{R^2}}{\frac{2W}{R}} \quad (\text{Eq. 10})$$

where  $\frac{b}{R} = 2 \cos\left(\frac{\pi}{4} - \frac{\phi}{2}\right)$

$$\frac{h}{R} = 1 + \sin\left(\frac{\pi}{4} - \frac{\phi}{2}\right)$$

(Eq. 11)

$$\frac{W}{R} = 2 \left\{ \cos\left(\frac{\pi}{4} - \frac{\phi}{2}\right) + \left[ 1 + \sin\left(\frac{\pi}{4} - \frac{\phi}{2}\right) \right] \tan\left(\frac{\pi}{4} - \frac{\phi}{2}\right) \right\}$$

$$\frac{V_s}{R^2} = \frac{3\pi}{4} - \frac{\phi}{2} + 2 \cos\left(\frac{\pi}{4} - \frac{\phi}{2}\right) \sin\left(\frac{\pi}{4} - \frac{\phi}{2}\right)$$

The predictions of the cave height are shown in Figure 133 for the range of bulking factors between 0.2 and 0.4. As expected, the cave height is larger in the case of the piping mechanism than in the case of Terzaghi failure mechanism. The cave height varies (for two considered cases and for the bulking factor in the range between 0.2 and 0.4) between approximately 1 and 2.5 drift diameters.

The vertical pressure of the broken rock on the drip shield is calculated from the following equation, also derived based on the consideration of the geometry shown in Figures 131 and 132:

$$p = (H + R - t) \frac{\rho g}{1 + B} \tag{Eq. 12}$$

where  $t$  is the height of the upper surface of the drift shield above the drift centerline. Calculated vertical pressure on the drip shield as a function of the bulking factor is shown in Figure 134.

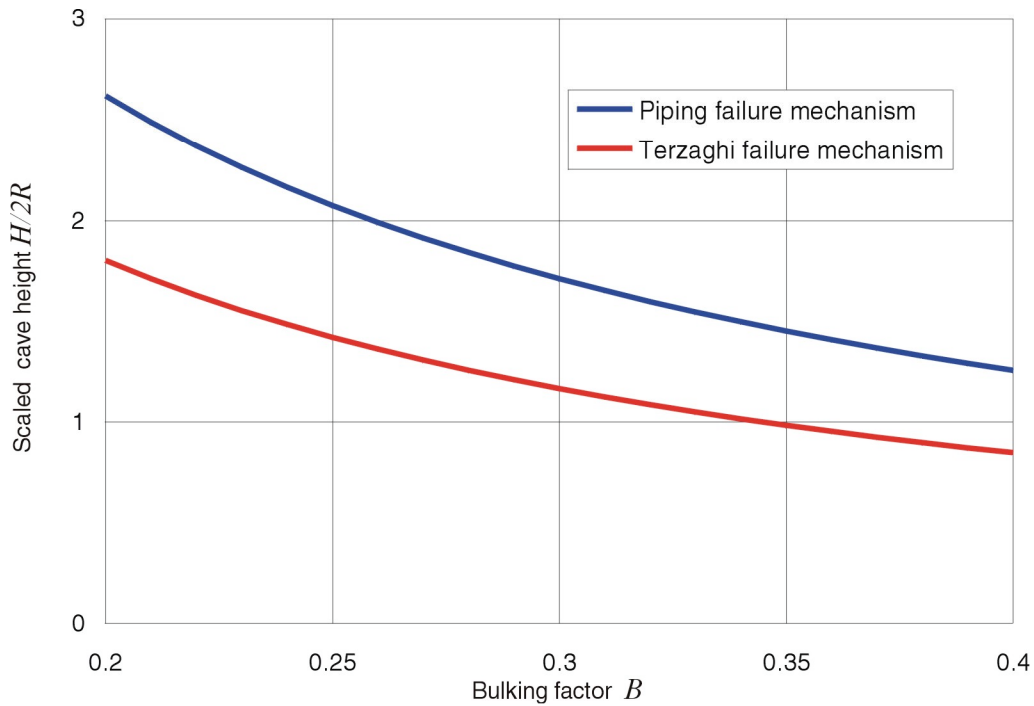


Figure 133. Cave Height as a Function of Bulking Factor: Analytical Solution

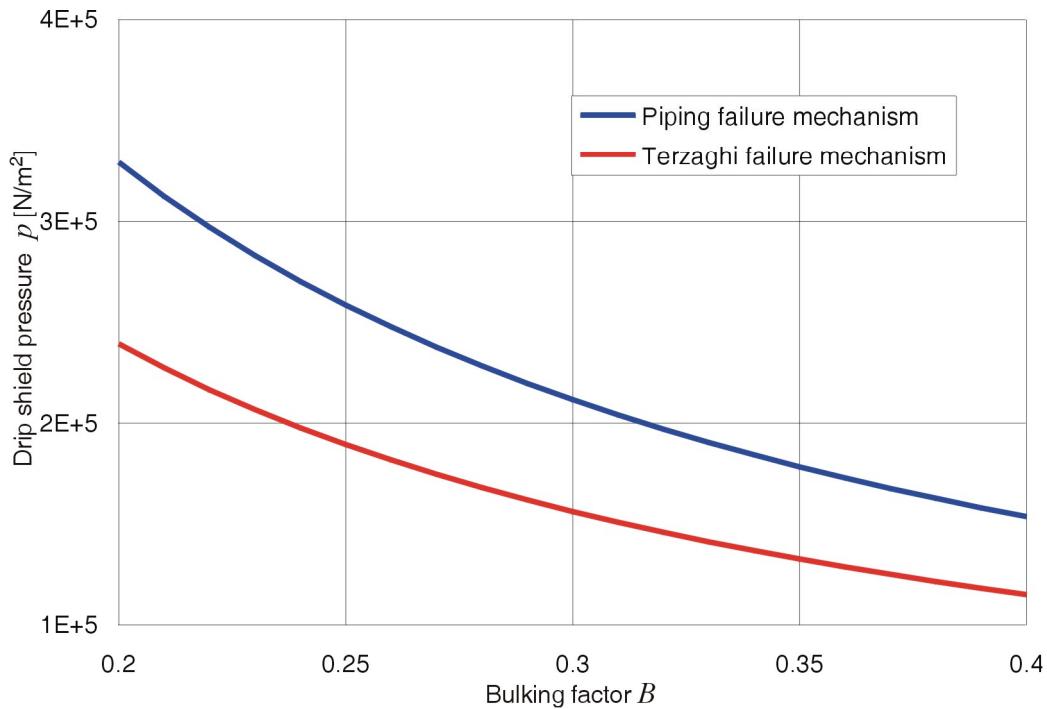


Figure 134. Vertical Load on the Drip Shield as a Function of Bulking Factor: Analytical Solution

### 6.4.2.3 Numerical Continuum Approach

The purpose of the numerical analysis of the drift degradation and estimation of the pressures on the drip shield was to more accurately estimate the shape of the cave formed above the drift, and to account for potential stress arching within the broken rock piled on the top of the drip shield. A simplistic methodology was used. A model of the drift in the rock mass represented as a Mohr-Coulomb material was set using FLAC, a continuum numerical code. “Roller” boundary conditions were used on the vertical and the bottom model boundaries. A stress boundary condition was applied on the top model boundary. The model uses symmetry conditions along the vertical plane through the drift center. The model width was set equal to 10 drift radii. The total model height is either 16 or 25 drift radii, depending on vertical extent of the zone of the caved rock mass. The model bottom boundary is 4.8 radii below the drift center.

The actual strength of the lithophysal rock mass was used in the initial simulation (Table V-9, Category 1, with a friction angle of 40°). Subsequently, cohesion and tensile strength were reduced gradually, in steps. At each stage of strength reduction the model was run until either equilibrium was achieved, or there was clear indication that equilibrium could not be achieved (i.e., the rock mass around the drift was collapsing). Once the collapse was detected (an example is shown in Figure 135), the model simulation was interrupted, and the cave height was calculated based on the bulking factor and the volume of the rock mass within the destabilized region. Again, two limiting mechanisms were considered: 1) piping mechanism (shown in Figure 136, where the caved region is assigned zero cohesion), in which the cave width was limited to the drift width, and 2) Terzaghi mechanism (shown in Figure 137), in which cave width coincides with the width of the destabilized region of the rock mass. Subsequently the drift and the caved region were filled with zones (caved rock selected to have no cohesion or

tensile strength, and density accounting for the bulking), and the model was run to the equilibrium to determine the load on the drift shield.

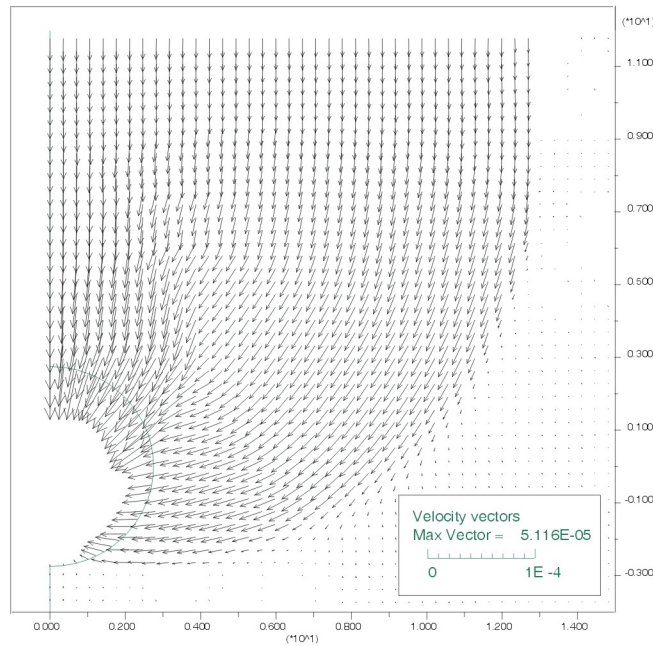


Figure 135. Failure Mechanism of a Deep Tunnel in Cohesionless Material

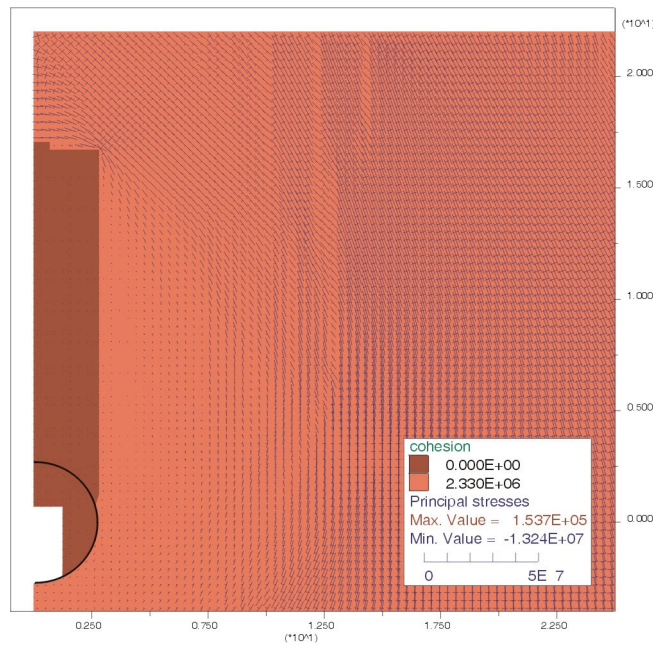


Figure 136. Piping Failure Mechanism Considered in the Continuum Model: Bulking Factor  $B = 0.2$

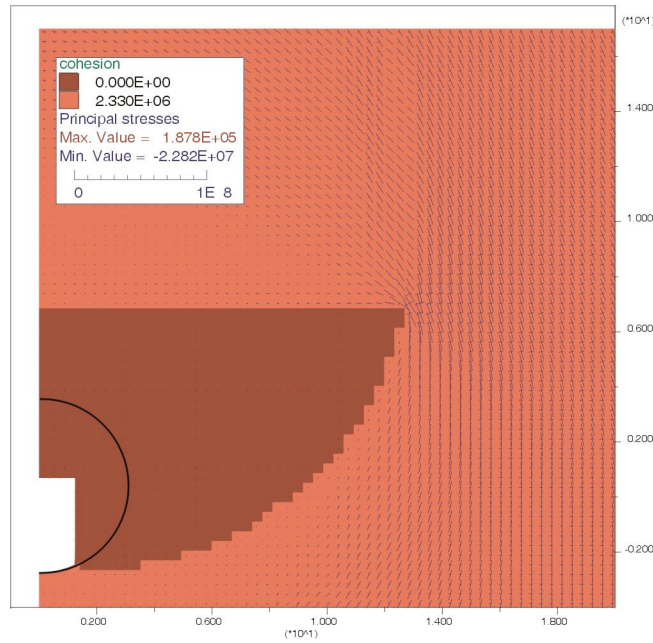


Figure 137. Terzaghi Failure Mechanism Considered in the Continuum Model: Bulking Factor  $B = 0.1$

Clearly, the failure mechanism shown in Figure 135 is not a realistic mechanism of the drift collapse at Yucca Mountain. This mechanism is more typical for the shallow tunnels in a soil-like media where shearing is the predominant mechanism of inelastic deformation. For emplacement drifts, collapse of the rock mass from the roof will occur much before the deep-seated shear failure in the walls can be mobilized.

Results of the continuum analysis of rock pressure on the drip shield as a function of the bulking factor and different failure mechanism types are summarized in Table 39.

Table 39. Summary of Pressures on the Drip Shield Calculated from the Continuum Model

Case	Property Category	Failure Type	Bulking	Pressure (kN/m <sup>2</sup> )	
				Top of Drip Shield	Side of Drip Shield
1	1	Terzaghi	0.1	269.2	47.1
2	1	pipe	0.1	403.3	39.6
3	1	Terzaghi	0.2	203.6	27.3
4	1	pipe	0.2	295.6	28.3
5	1	Terzaghi	0.4	117.9	20.1
6	1	pipe	0.4	161.6	17.8

#### 6.4.2.4 Numerical Discontinuum Approach

It appears that the results of both previously discussed approaches (analytical and continuum) are overly conservative in the predictions of the cavity size and transfer of the load through the caved rock. Consequently, predicted loads on the drip shield are quite large. Therefore, the problem was also solved using UDEC, a two-dimensional discontinuum numerical code. As in Section 6.4.1, the rock mass was represented as an assembly of polygonal blocks of a certain

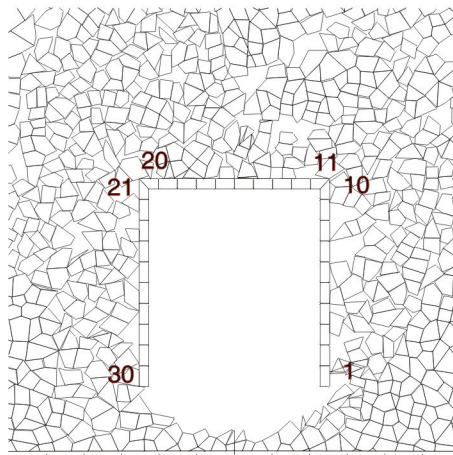
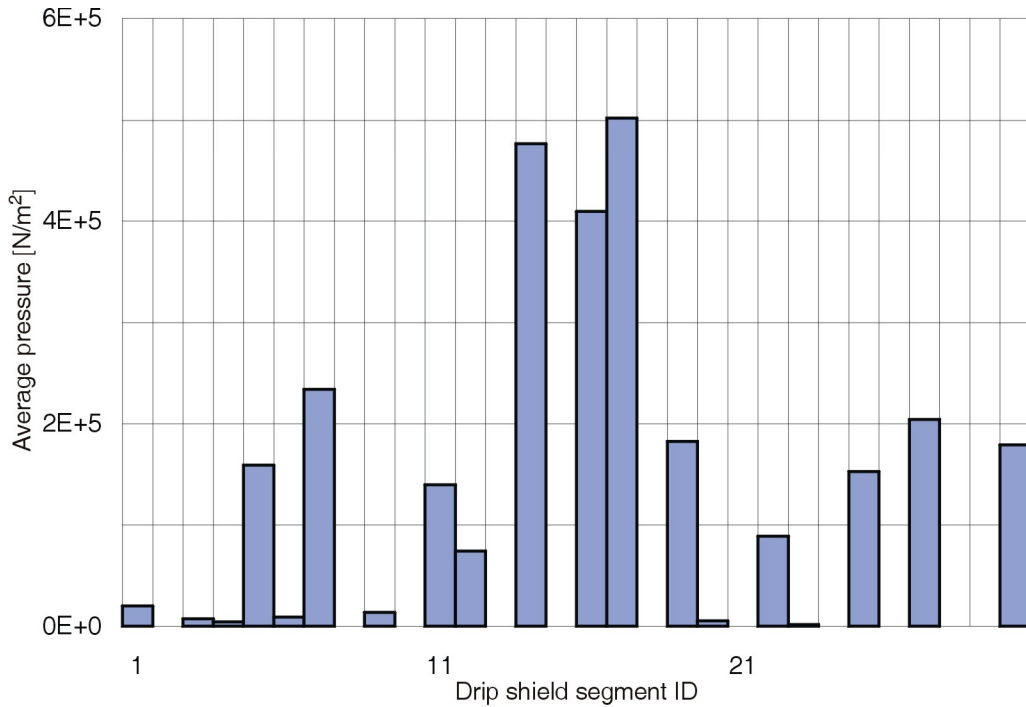
shape (i.e., Voronoi blocks). The size and the shape of the blocks were selected such that it does not influence the results of the model. The same synthetic material as in Section 6.4.1, calibrated to macro properties of the rock mass (micro properties are shown in Tables 35 and 36), is used in the analysis of drift degradation.

The simulations started using the actual material strength. Cohesion and tensile strength were subsequently reduced in steps equal to 20 percent of the initial strength. For each step of strength reduction, the model was run to equilibrium allowing development of fractures and falling of any loose blocks. At the end of the simulation, when cohesion and tensile strength were completely reduced to zero, the model provides an estimate of the maximum extent of the collapsed rock mass and pressures on the drip shield. However, in this model the bulking of the caved rock is not a model parameter but its result. The bulking in reality depends on the size and the shape of the falling blocks, which are predetermined by the size and the shape of the Voronoi blocks in the model. To assure that the model estimates are conservative, the Voronoi block size was selected such that the resulted bulking factor was equal or less than 0.2, the lower bound of the bulking factor expected in rocks (cases 3, 4, and 5 in Table 40). The results of 5 simulated cases are summarized in Table 40. Cases 1 and 2 are for the model with a block size of 0.3 m, for different realizations of the geometry of Voronoi blocks. Cases 3, 4, and 5 are for different realizations of the geometry of 0.2-m large Voronoi blocks. Cases 1 and 2 resulted in a bulking factor of 37 and 30 percent, respectively. These values are within the expected range for the bulking factor of the rock mass, but cannot be considered as conservative. For that reason the analysis was done for a block size of 0.2 m (cases 3, 4 and 5). The resulting 16 to 17 percent bulking is certainly equal or less than the lower bound of bulking factor in rocks, yielding conservative (i.e., higher) estimates of the cave size and the pressure on the drip shield.

Table 40. Summary of Pressures on the Drip Shield Calculated from the Discontinuum Model

Case	Block Size (m)	Pressure (kN/m <sup>2</sup> )			Bulking
		Left Side of Drip Shield	Top of Drip Shield	Right Side of Drip Shield	
1	0.3	105.4	107.3	72.9	0.37
2	0.3	10.4	119.9	220.8	0.30
3	0.2	142.7	172.2	37.7	0.17
4	0.2	62.6	179.2	44.8	0.16
5	0.2	107.8	145.1	49.2	0.17

The pressures listed in Table 40 are averaged over two sides and the top of the drip shield. However the pressures are quite non-uniform as shown in Figure 138 for case 4. Note that the pressures shown in Figure 138 are forces averaged over 30 segments: 10 on each side and 10 on the top of the model. Details of drip shield pressures for each of the cases analyzed are provided in Attachment XVI.



segment IDs

Figure 138. Pressures on the Drip Shield Calculated from the Discontinuum Model: Case 4

The evolution of rockfall and the cave size for case 4 as a function of strength degradation is shown in Figure 139. The model shows that in this case (lithophysal rock mass category 1 with unconfined compressive strength of 10 MPa), the emplacement drift is completely filled with caved rock after 80 percent degradation of the cohesive rock strength (Figure 139e). However, in the case of rock mass category 5, which has an unconfined compressive strength of 30 MPa (three times more than UCS for category 1), after 80 percent of strength degradation (Figure 139b), there will be some rockfall from the walls, but the drifts will, in general, be open.

Drift Degradation Analysis

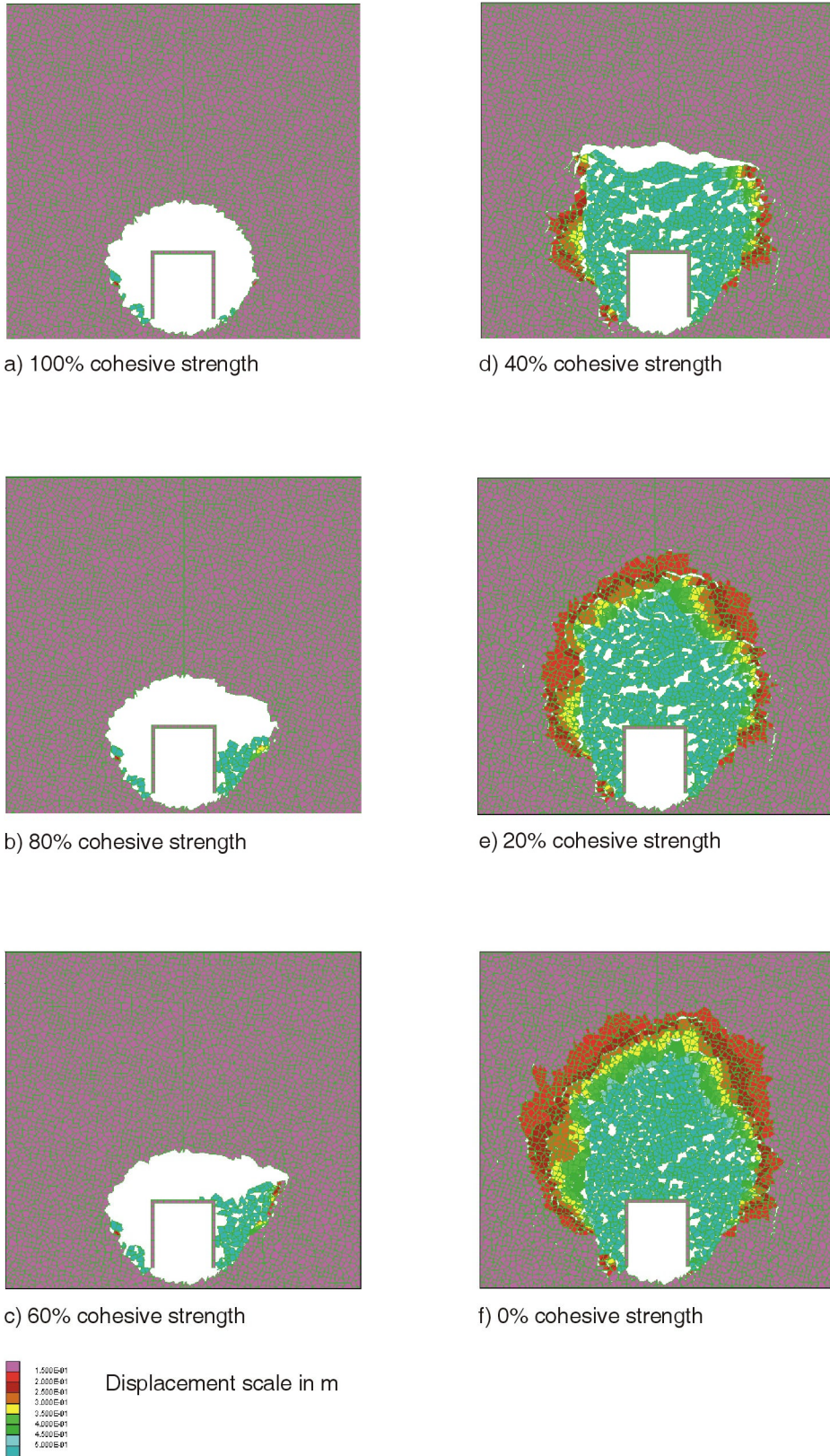


Figure 139. Evolution of the Cave as a Function of the Cohesive Strength: Case 4

To demonstrate that selected block size of 0.2 m (cases 3, 4 and 5) does not effect the size or the shape of the predicted cave, the cave sizes are shown in Figure 140 for all three cases after complete strength degradation. There is certain level of randomness in the results, but the general trend is consistent. The results of average pressures on the drip shield from Table 40 also confirm that variability in the model results, as a function of the realization of the geometry of Voronoi blocks is relatively small.

Arching of stresses in case 4 around and inside the caved rock is shown in Figure 141.

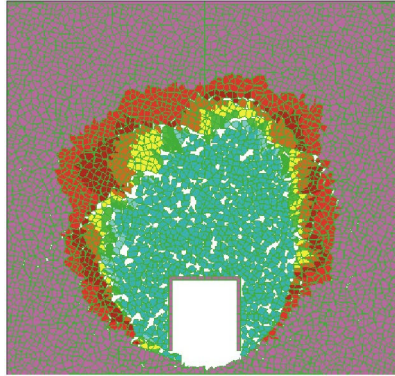
#### **6.4.2.5 Summary of Rock Mass Degradation in Lithophysal Units**

The predictions of pressure of the caved rock on the drip shield by all three modeling approaches are summarized in Figure 142. As expected, analytical model yields the largest loads due to overly conservative conditions. The continuum numerical model accounts more accurately for transfer of load by friction from the caved rock to the surrounding stable rock mass. Consequently predicted loads for small bulking factors and large cavity size are much smaller than analytical predictions. When the bulking factor is large, the height of the cave becomes small. Stress arching cannot be realized within the small column of the cave rock and consequently, prediction between analytical and continuum models are identical. The most accurate approach, using the discontinuum model, does not use an imposed condition about the shape of the caved region. It also correctly accounts for load transfer through the caved rock. The predictions of the pressures on the drip shield using this approach are smaller than the predictions of the analytical and continuum models for all values of the bulking factor.

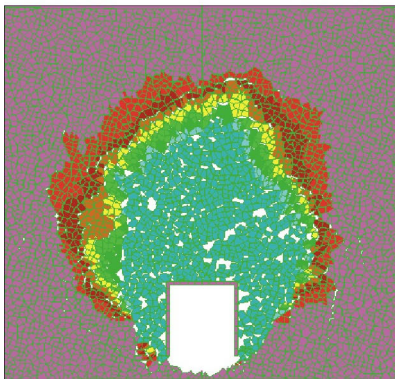
#### **6.4.3 Investigation of Potential Key Blocks in Lithophysal Units**

This section describes the probability of key-block existence, or the possibility that wedge-type failure occurs in the lithophysal units. The general approach used for analyses of wedge-type failure in the nonlithophysal units, as described in Section 6.3.1, is also applied in this study. The three-dimensional discontinuum code 3DEC is used for the mechanical analysis of the jointed rock mass simulated by FracMan. Since small-scale fractures have minor effect on wedge formation as confirmed in Section 6.3.3, only the fractures with trace lengths greater than or equal to 1 m long are included here.

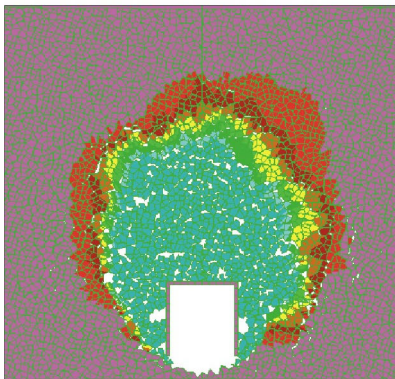
Same as the nonlithophysal base case, a total of 76 fracture modeling regions were selected from the 100-m cube simulated FracMan jointed rock mass for Tptpl unit (Section 6.1). Since the coordinates of the 76 fracture modeling regions selected for the nonlithophysal units were randomly generated, they were also used in the lithophysal units. For conservatism and efficiency, joint strength parameters (cohesion and friction angle) were reduced to 0 to evaluate the probability of key-block existence. With strength parameter values assigned as 0, the predicted rockfall is equivalent to all blocks that are kinematically admissible to fall regardless of the frictional resistance of joint surface.



a) case 3



b) case 4

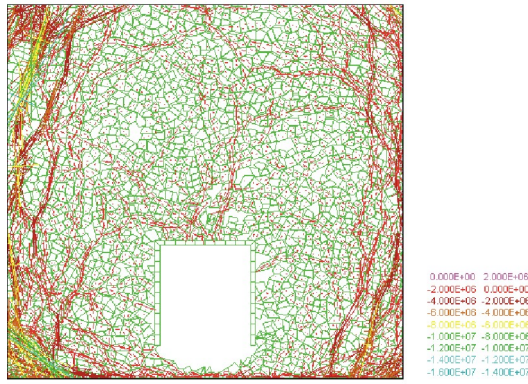
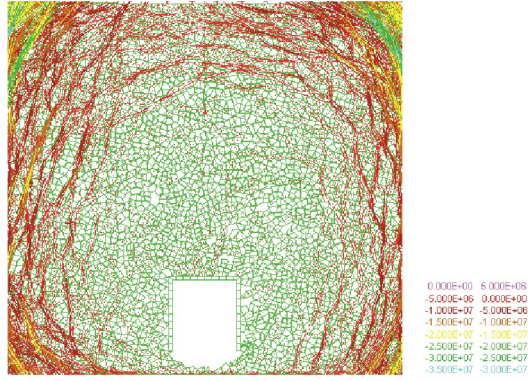


c) case 5



Figure 140. Size and Shape of the Cave for Cases 3, 4, and 5

# Drift Degradation Analysis



Stress scales in Pa

Figure 141. Stresses in the Rock Mass after Caving Shown at Two Scales

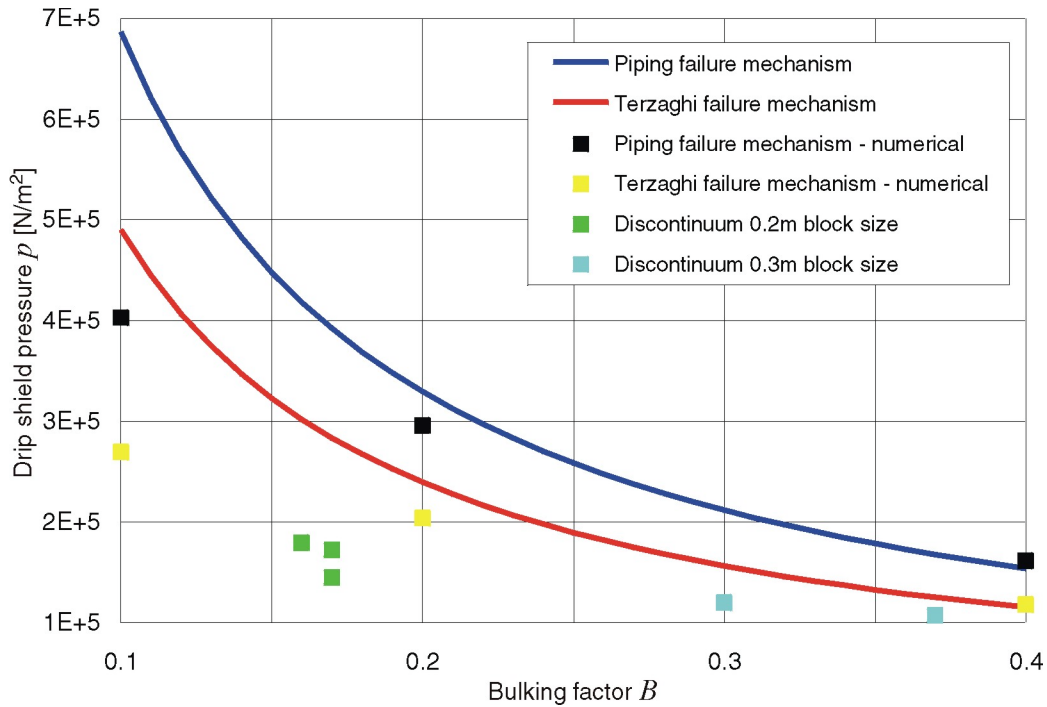


Figure 142. Summary of Vertical Load on the Drip Shield as a Function of Bulking Factor

The summary of the analyses is presented in Table 41. The distinct blocks existing in all simulations amount to only 24. Notice that the distinct blocks are the blocks that exist in the rock mass regardless of whether the blocks are kinematically or mechanically suitable to fall. A typical cross-section of the analysis with prediction of the distinct block is provided in Figure 143. Only two blocks were predicted to fall into the drift with a block volume of approximately 0.15 m<sup>3</sup> (0.36 tonnes) for both. With only two blocks predicted for almost 2 km of drift simulated while using extremely conservative (i.e., low) joint strength properties, the probability of key-block occurrence in lithophysal units is very low.

Table 41. Summary of 3DEC Rockfall Prediction for Lithophysal Units

Runs Completed	76
Number of Simulation Predict No Rockfall	74
Number of Simulation Predict No Distinct Block	61
Total Number of Rockfall	2
Total Volume of Rockfall (m <sup>3</sup> )	0.31
Total Length of Drift Simulated(m)	1900
Number of Blocks per km	1
Volume of Rockfall per km (m <sup>3</sup> /km)	0.16



Figure 143. Cross-Section of a Typical Simulated Lithophysal Rock Mass in 3DEC

#### 6.4.4 Drift Profile Prediction and Degraded Rock Mass Characteristics in Lithophysal Units

The distinct block approach applied in this analysis of lithophysal rock has provided a representation of the rock mass using an assembly of Voronoi blocks as described in Sections 6.4.1 and 7.7. This approach allows for internal fracturing to form and blocks to loosen and fail into the opening as the evolving stress states dictate. Progressive block failure continues until the crown becomes mechanically stable, and no additional blocks can fall. The final progressive failure surface provides the basis for the drift profile predictions presented in this section.

A depiction of worst-case profiles are provided, which are the outcome of UDEC analyses with the rock mass and opening subjected to in situ and seismic loadings. The worst-case drift profile resulting from preclosure ground motion is shown in Figure 110. The worst-case drift profile resulting from  $1 \times 10^{-6}$  postclosure ground motion is shown in Figure 115, which shows complete collapse of the drift opening. The  $1 \times 10^{-7}$  postclosure ground motion also results in complete drift collapse. For the preclosure period, thermally induced rockfall is in general minor due to ventilation.

Attachment XVIII includes the drift profiles for strength category 1 rock with consideration of seismic loading, thermal loading, and strength degradation. A total of 30 scenarios were provided. Attachment XVIII also provides information for degraded rock mass characteristics

around the opening. The information consists of the stress tensor for UDEC zones, aperture change along the joints, and averaged volumetric strain.

## 6.5 UNCERTAINTIES AND LIMITATIONS

The task of predicting and characterizing drift degradation anticipated within repository emplacement drifts throughout the 10,000-year period of compliance for postclosure performance has several inherent uncertainties and limitations. These uncertainties are associated with both the modeling methods and the model inputs. To provide a meaningful assessment of drift degradation, the uncertainties must be identified and adequately represented within the model. The uncertainties associated with modeling methods are addressed with model validation (Section 7). Additionally, a discussion of alternative conceptual models has been provided (Section 6.7), which refutes plausible alternative models, thereby demonstrating that the drift degradation models presented in this report are adequate to account for all uncertainties and limitations.

This section provides a discussion of uncertainties associated with model inputs. The discussion below has been rank-ordered according to importance. That is, the parameters and their associated uncertainty that have the most significant impact on model results are discussed first.

**Joint Geometry Data**—The natural variability of joints within a rock mass represents epistemic uncertainty (i.e., uncertainty due to incomplete knowledge) in the design of structures in rock. The vast amount of joint data collected at the YMP provides a very good representation of the range of joints anticipated at the emplacement drift horizon. The range of joint geometry variability from tunnel mapping has been captured in the rockfall model for nonlithophysal rock through multiple simulations of the rock mass. Section 6.1.6 describes the generation of representative rock volumes using FracMan with the consideration of the natural variability of joints. The representativeness of the FracMan generated rock volume is validated in Section 7.8.2. Section 6.3.1.2.2 documents the random selection of the fracture modeling region in the rockfall analyses to cover the uncertainties associated with joint geometry data. The joint geometry is concluded to be the dominant factor for wedge-type rockfall in nonlithophysal rock. The uncertainty associated with joint geometry data in the rockfall models is assessed to be low.

**Seismic Ground Motion Data**—The seismic time histories used to evaluate rockfall reflect a number of variabilities, including epistemic uncertainty and randomness (aleatoric uncertainty). Epistemic uncertainties (due to incomplete knowledge) in the characterization of seismic sources and median ground motion attenuation, along with randomness in seismic ground motion, were explicitly incorporated into the probabilistic seismic hazard analysis. The mean results of that analysis form the basis for the site-specific ground motions used in this report. At annual probabilities of exceedance lower than about  $1 \times 10^{-6}$ , the mean hazard exceeds the 85th percentile of the hazard uncertainty distribution.

Development of site-specific ground motions incorporates additional epistemic uncertainty in the velocity and dynamic properties of site materials. Observed randomness of site materials is also addressed. Finally, randomness in the spectral content and duration of time histories that produce the same peak ground motion is accommodated in the drift degradation analyses through the use of 15 sets of time histories for each of the two postclosure hazard levels considered. The

earthquake magnitudes and epicentral distances of the recorded strong motion data that form an input to these time histories, reflect the range of magnitudes and distances contributing most strongly to seismic hazard at the site for the given annual probabilities of ground motion exceedance.

While the seismic ground motion inputs developed in this manner fully account for the underlying uncertainties and randomness, the result is that for annual exceedance probabilities of about  $1 \times 10^{-6}$  and lower, some realizations of ground motion are larger than the largest ground motions observed and may not be physically realizable. Nonetheless, these ground motions are consistent with and demonstrate fully the current state of uncertainty and randomness in deriving ground motion inputs for very low annual probabilities of exceedance. Currently lacking a technical basis to limit such ground motions to smaller values, these inputs are used in the analyses supporting TSPA-LA.

**Intact Rock Physical and Mechanical Properties Data**—A sufficient amount of intact rock physical and mechanical properties data has been collected for the nonlithophysal rock units. The epistemic uncertainty associated with this intact data for nonlithophysal rock is assessed to be low. Conversely, the amount of intact rock physical and mechanical properties data for the lithophysal units is limited. The epistemic uncertainty associated with this intact data for lithophysal rock is assessed to be high. To account for this uncertainty in the rockfall model for lithophysal rock, 6 categories of rock properties were included in the model to assess the impact of the ranges in intact properties data. The difference of rockfall prediction for the range of properties considered is provided in Section 6.4.

**Joint Mechanical Properties Data**—The amount of joint mechanical properties data for both the nonlithophysal and lithophysal rock units is limited; therefore, the uncertainty associated with this data is epistemic, and is relatively high. To account for this uncertainty in the rockfall models, sensitivity analyses for the possible range of joint strength parameters, dilation angle, and joint stiffness were conducted and the results are presented in Section 6.3.1.6. Joint mechanical properties appear to have secondary effect on rockfall comparing with joint geometry data.

**Rock Mass Mechanical Properties Data**—Rock mass mechanical properties data for nonlithophysal rock are calculated using rock mass classification data collected from field mapping within the ESF and intact rock properties data collected from laboratory testing. The uncertainties associated with the intact rock properties data are described above. The uncertainties associated with the rock mass classification data are epistemic, and are assessed to be low since an abundance of data has been collected based on established, industry-accepted methods. There is a moderate degree of epistemic uncertainty associated with calculation approach for assessing rock mass properties, since they are based on empirical methods and have an inherent characteristic of imprecision. This uncertainty has been accounted for by using two separate empirical calculation methods and demonstrating that the results are similar. The rock mass properties data are primarily used in the thermal-mechanical calculation to determine stresses within the model as described in Section 6.2, and is a relatively insensitive parameter to the stress calculations.

Rock mass mechanical properties data for lithophysal rock are based on large-diameter uniaxial compression test data and in situ slot test data (Attachment V, Section V.4.1). The epistemic uncertainty associated with this rock mass data for lithophysal rock is assessed to be high. To account for this uncertainty in the rockfall model for lithophysal rock, six categories of rock properties were included in the model to assess the impact of the ranges in rock mass properties data. The difference of rockfall prediction for the range of properties considered is provided in Section 6.4.

**Rock Thermal Properties Data**—A sufficient amount of rock thermal properties data has been collected for the nonlithophysal rock units. The epistemic uncertainty associated with this thermal properties data for nonlithophysal rock is assessed to be low. Conversely, the amount of rock thermal properties data for the lithophysal units is limited. Therefore, the epistemic uncertainty associated with this thermal properties data for lithophysal rock is assessed to be high. Uncertainty assessments are provided in the data source documentation identified in Table 2 and in Attachment V (Section V.5). Sensitivity calculations for thermal properties were conducted with one standard deviation less values used for thermal conductivity and specific heat as described in Section 6.2, Section 6.3.1.3, and Section 6.4.1.2. The sensitivity case results in approximately 23° higher peak temperature comparing with the base case but with minor impact to the rockfall prediction.

**Repository Layout Information**—The repository layout data is based on design information, which is currently in the preliminary design stage. This design information is subject to change before being finalized. The model results documented in this report are applicable for the emplacement drift diameter and emplacement drift alignment provided by repository design and performance assessment information exchange drawings (BSC 2002b; BSC 2003b; BSC 2003c) and Section 5.1.4 and 8.7 of *Underground Layout Configuration* (BSC 2002a). The rockfall models are sensitive to both emplacement drift diameter and alignment, and any change to this design information would require reevaluation.

## 6.6 DRIFT DEGRADATION FEATURES, EVENTS, AND PROCESSES

The development of a comprehensive list of features, events, and processes (FEPs) potentially relevant to postclosure performance of the repository is an ongoing, iterative process based on site-specific information, design, and regulations. The approach for developing an initial list of FEPs, in support of TSPA-SR (CRWMS M&O 2000b), was documented by Freeze et al. (2001). The initial FEP list contained 328 FEPs, of which 176 were included in TSPA-SR models (CRWMS M&O 2000b, Tables B-9 through B-17). To support TSPA-LA, the FEP list was re-evaluated in accordance with Section 3.2 of *The Enhanced Plan for Features, Events, and Processes (FEPs) at Yucca Mountain* (BSC 2002e). Table 42 provides a list of FEPs that are addressed in this model document, and provides specific references to sections within this document.

Table 42. FEPs Addressed by This Model Report

FEP No.	FEP Name	Section Where Disposition is Described	Summary of Disposition in TSPA-LA
1.1.02.00.0B	Mechanical effects of excavation/ construction in EBS	6.1.4 V.4	A partial treatment of this FEP is provided in this report. The results of the rockfall models will be used in a separate analysis of EBS FEPs to determine the include/exclude status of the FEP for TSPA-LA. Specifically, this report provides rockfall models that are based on observation of rock characteristics representing the as-built (post-excavation) condition, so that potential excavation effects, if any, are considered. For example, the field mapping data of geologic features presented in Section 6.1.4 were collected post-excavation in the ESF, and therefore include excavation effects. Similarly, the calculation of rock mass properties in Attachment V (Section V.4) inherently includes these excavation effects. Therefore, the effects of excavation on rock mass response are reflected in the results presented in this report.
2.1.06.02.0A	Mechanical effects of rock reinforcement materials in EBS	5.5	A partial treatment of this FEP is provided in this report. The results of the rockfall models will be used in a separate analysis of EBS FEPs to determine the include/exclude status of the FEP for TSPA-LA. In this model report, no credit is taken for ground support in rockfall models (Section 5.3). Therefore, the consideration of the mechanical effects of rock reinforcement is implicit in the modeling approaches discussed in Sections 6.3 and 6.4. The rockfall models presented in this report (Sections 6.3 and 6.4) provide a bounding scenario in the analysis of the effects of rock reinforcement on drift degradation.
2.1.07.01.0A	Rockfall	6.3 6.4 7.8.4	A partial treatment of this FEP is provided in this report. The results of the rockfall models (i.e., block size distribution data for various seismic hazard levels) have been incorporated into consequence models for the seismic scenario for TSPA-LA to determine the include/exclude status of the FEP. Specifically, this report provides rockfall models that are based on site characterization data. Probabilistic descriptions of rock size and rockfall frequency are provided for use in engineering design analyses (Sections 6.3 and 6.4). The block size distributions and frequency of blocks presented in this report for static (i.e., no seismic) and preclosure ground motion are similar to the block size data developed using the approach in the previous version of this document (Section 7.8.4).
1.2.03.02.0B	Seismic-induced rockfall damages EBS components	6.3 6.4 7.8.4	A partial treatment of this FEP is provided in this report. The results of the rockfall models (i.e., block size distribution data for various seismic hazard levels) have been incorporated into consequence models for the seismic scenario for TSPA-LA to determine the include/exclude status of the FEP. Specifically, this report provides rockfall models that are based on site characterization data. Probabilistic descriptions of rock size and rockfall frequency are provided for use in engineering design analyses (Sections 6.3 and 6.4). The block size distributions presented in this report are similar to the block size distributions developed using the approach in the previous version of this document (Section 7.8.4). However, the frequency of blocks has increased with the larger ground motions used in this report compared to the previous approach (Section 7.8.4).

Table 42. FEPs Addressed by This Model Report (Continued)

FEP No.	FEP Name	Section Where Disposition is Described	Summary of Disposition in TSPA-LA
2.1.07.02.0A	Drift collapse	6.3 6.4 7.8.4	A partial treatment of this FEP is provided in this report. The results of the rockfall models (i.e., block size distribution data for various seismic hazard levels) have been incorporated into consequence models for the seismic scenario for TSPA-LA to determine the include/exclude status of the FEP. Also, drift profile results will be included into seepage abstraction models for TSPA-LA. Specifically, this report provides rockfall models that are based on site characterization data, including joint geometry and rock strength data, coupled with anticipated thermal stresses and seismic ground motion. Based on the analyses presented in this report (Section 6.3 and 6.4), minor degradation or collapse of drift is anticipated for the static (i.e., no seismic) case and during the preclosure period. The mechanical degradation or collapse of drift predicted for the static case and during the preclosure period is similar to the results from the previous approach using DRKBA (Section 7.8.4).
1.2.03.02.0A	Seismic ground motion damages EBS components	6.3 6.4	A partial treatment of this FEP is provided in this report. The results of the rockfall models (i.e., block size distribution data for various seismic hazard levels) have been incorporated into consequence models for the seismic scenario for TSPA-LA to determine the include/exclude status of the FEP. Specifically, this report provides rockfall models that are based on site characterization data, including joint geometry and rock strength data, coupled with anticipated thermal stresses and seismic ground motion. Based on the analyses presented in this report (Section 6.3 and 6.4), postclosure ground motion levels are sufficient to produce collapse of drifts in the lithophysal rock units (which represent approximately 75% of the emplacement drifts). Minor to moderate degradation or collapse of drift is anticipated in the nonlithophysal rock units throughout the regulatory period for postclosure performance.
2.1.11.07.0A	Thermal expansion/stress of in-drift EBS components	6.2	A partial treatment of this FEP is provided in this report. The results of the rockfall models will be used in a separate analysis of EBS FEPs to determine the include/exclude status of the FEP for TSPA-LA. Specifically, this report provides rockfall models that include the potential impact of thermally induced stress changes in the rock mass (Section 6.2). The effects of thermally induced stress changes on drift degradation are documented in Sections 6.3.1.3 (nonlithophysal rock) and 6.4.1.2 (lithophysal rock).

## 6.7 DOCUMENTATION OF ALTERNATIVE CONCEPTUAL MODELS

Alternative conceptual models are based on assumptions and simplifications that are different from those employed in the base-case models (i.e., the rockfall model for nonlithophysal rock (Section 6.3) and the rockfall model for lithophysal rock (Section 6.4)). An important reason for considering alternative conceptual models is to help build confidence that changes in modeling assumptions or simplifications will not change conclusions regarding subsystem and total system performance. Conceptual model uncertainty results from sparse observational data and a lack of available information to corroborate or refute plausible alternative interpretations of the subsystem and the processes occurring within the subsystem.

The alternative conceptual models considered in this analysis of drift degradation are summarized in Table 43.

Table 43. Alternative Conceptual Models Considered

Alternative Conceptual Model	Key Assumptions	Screening Assessment and Basis
Continuum model of lithophysal rock	Lithophysae and fractures are smeared into the elements in the equivalent continuum representation of the rock mass. Rock damage is expressed as element yielding following the selected failure criterion.	The continuum model, such as FLAC or FLAC3D, is capable of modeling the material yielding behavior with elasto-plastic constitutive model. Yielding occurs when the stress state within the element reach the strength criterion specified by the constitutive law, the yielding of elements in the continuum, however, is not equivalent to rockfall. To estimate the extent of rockfall based on the depth of yielding could be too conservative. Therefore, this alternative conceptual model is excluded from further evaluation.
Continuum model of nonlithophysal rock	Fractures are smeared into the elements in the equivalent continuum representation of the rock mass. Element contains the weak plane information for potential shear slipping.	The compliant joint model (Chen 1987) is capable of analyzing jointed media behavior with fractures smeared into the elements. The model includes a continuum approximation based on average discontinuous displacements across joint planes within a representative elementary volume. The model also includes a material constitutive description based on linear elastic matrix material behavior and nonlinear normal and shear joint behavior between joint planes. The continuum model provides global rock mass response with predominant weak plane orientation, but can not predict wedge-type failure. Therefore, this alternative conceptual model is excluded from further evaluation.
Hudson and Priest (1979) model of nonlithophysal rock for estimating block size distribution	All joint planes are assumed to be perfectly planar, persistent, and extend throughout the rock volume of interest. The distribution of joint spacing values along a line are assumed to be of negative exponential form.	The approach to determine block size distribution using the Hudson and Priest approach has been documented by <i>Preliminary Block Size Calculation</i> (CRWMS M&O 1998b, Section 5.3). This approach provides a generalized statistical representation of the joint geometry. In particular, the assumption of continuous joints is not consistent with the discontinuous joints observed in the ESF. Since joint geometry is a primary factor in the assessment of block development, the generalized approach by Hudson and Priest does not provide the level of detail required to accurately model drift degradation. Therefore, this alternative conceptual model is excluded from further evaluation.

## 6.8 RESOLUTION OF KEY TECHNICAL ISSUES

The NRC is conducting an ongoing review of the information provided by the YMP activities to allow early identification and resolution of potential licensing issues. The NRC has identified several key technical issues (KTIs) and associated sub-issues, along with acceptance criteria for resolution of the issue. The drift degradation analysis provides information that is directly related to the KTI on Repository Design and Thermal-Mechanical Effects (NRC 2002). To provide a clear understanding of the technical issues, a NRC/DOE Technical Exchange and Management Meeting on Repository Design and Thermal-Mechanical Effects was held in February of 2001. As a result of this meeting, a number of agreements between the NRC and DOE were formally adopted (Reamer and Williams 2001), outlining the plan for resolution of the technical issues. The agreement items addressed in this report are presented verbatim as follows:

- **RDTME 3.04**—Provide in the Design Parameter Analysis Report (or some other document) site-specific properties of the host rock, as a minimum those included in the NRC handout, together with the spatial and temporal variations and uncertainties in such properties, as an update to the information contained in the March 1997 Yucca Mountain Site Geotechnical Report. The DOE will: (1) evaluate the adequacy of the currently available measured and derived data to support the potential repository licensing case and identify areas where available data may warrant additional field measurements or testing to reduce uncertainty. DOE will provide a design parameters analysis report (or other document) that will include the results of these evaluations, expected to be available to NRC in FY 2002; and (2) acquire data and/or perform additional analyses as necessary to respond to the needs identified in 1 above. The DOE will provide these results prior to any potential license application.
- **RDTME 3.05**—Provide the Rock Mass Classification Analysis (or some other document) including the technical basis for accounting for the effects of lithophysae. The DOE will provide a rock mass classification analysis (or other document), including the technical basis for accounting for the effects of lithophysae, expected to be available to NRC in FY 2002.
- **RDTME 3.10**—Provide technical basis for the assessment that two-dimensional modeling for emplacement drifts is considered to be adequate, considering the fact that neither the in-situ stress field nor the principle fracture orientation are parallel or perpendicular to emplacement drift orientation. The DOE will provide the technical bases for the modeling methods used in ground control analysis in a revision to the Ground Control for Emplacement Drifts for SR, ANL-EBS-GE-000002 (or other document) supporting any potential license application. This is expected to be available to NRC in FY 2003.
- **RDTME 3.15**—Provide field data and analysis of rock bridges between rock joints that are treated as cohesion in DRKBA modeling together with a technical basis for how a reduction in cohesion adequately accounts for thermal effects. The DOE will provide clarification of the approach and technical basis for how

reduction in cohesion adequately accounts for thermal effects, including any additional applicable supporting data and analyses. Additionally, the adequacy of the cohesion reduction approach will be verified according to the approach described in Subissue 3, Agreement 22 [RDTME 3.19], of the Repository Design and Thermal-Mechanical Effects Technical Exchange. This will be documented in a revision to the Drift Degradation Analysis, ANL-EBS-MD-000027, expected to be available to NRC in FY 2003.

- **RDTME 3.16**—Provide a technical basis for the DOE position that the method used to model joint planes as circular discs does not under-represent the smaller trace-length fractures. The DOE will analyze the available small trace-length fracture data from the Exploratory Studies Facility and Enhanced Characterization of the Repository Block, including their effect on block development. This will be documented in a revision to the Drift Degradation Analysis, ANL-EBS-MD-000027, expected to be available to NRC in FY 2003.
- **RDTME 3.17**—Provide the technical basis for effective maximum rock size including consideration of the effect of variation of the joint dip angle. The DOE will provide the technical basis for effective maximum rock size including consideration of the effect of variation of the joint dip angle. This will be documented in revisions to the Drift Degradation Analysis, ANL-EBS-MD-000027, and the Rockfall on Drip Shield, CAL-EBS-ME-000001, expected to be available to NRC in FY 2003.
- **RDTME 3.19**—The acceptability of the process models that determine whether rockfall can be screened out from performance assessment abstractions needs to be substantiated by the DOE by doing the following: (1) provide revised DRKBA analyses using appropriate range of strength properties for rock joints from the Design Analysis Parameters Report, accounting for their long-term degradation; (2) provide an analysis of block sizes based on the full distribution of joint trace length data from the Fracture Geometry Analysis Report for the Stratigraphic Units of the Repository Host Horizon, including small joints trace lengths; (3) verify the results of the revised DRKBA analyses using: (a) appropriate boundary conditions for thermal and seismic loading; (b) critical fracture patterns from the DRKBA Monte Carlo simulations (at least two patterns for each rock unit); (c) thermal and mechanical properties for rock blocks and joints from the Design Analysis Parameters Report; (d) long-term degradation of rock block and joint strength parameters; and (e) site-specific ground motion time histories appropriate for post-closure period; provide a detailed documentation of the analyses results; and (4) in view of the uncertainties related to the rockfall analyses and the importance of the outcome of the analyses to the performance of the repository, evaluate the impacts of rockfall in performance assessment calculations. DOE believes that the Drift Degradation Analysis is consistent with current understanding of the Yucca Mountain site and the level of detail of the design to date. As understanding of the site and the design evolve, DOE will: (1) provide revised DRKBA analyses using appropriate range of strength properties for rock joints from a design

parameters analysis report (or other document), accounting for their long-term degradation; (2) provide an analysis of block sizes based on the full distribution of joint trace length data from the Fracture Geometry Analysis for the Stratigraphic Units of the Repository Host Horizon, ANL-EBS-GE-000006, supplemented by available small joint trace length data; (3) verify the results of the revised DRKBA analyses using: (a) appropriate boundary conditions for thermal and seismic loading; (b) critical fracture patterns from the DRKBA Monte Carlo simulations (at least two patterns for each rock unit); (c) thermal and mechanical properties for rock blocks and joints from a design parameters analysis report (or other document); (d) long-term degradation of joint strength parameters; and (e) site-specific ground motion time histories appropriate for post-closure period. This will be documented in a revision to the Drift Degradation Analysis, ANL-EBS-MD-000027, expected to be available to NRC in FY 2003. Based on the results of the analyses above and subsequent drip shield calculation revisions, DOE will reconsider the screening decision for inclusion or exclusion of rockfall in performance assessment analysis. Any changes to screening decisions will be documented in analyses prior to any potential license application.

The contribution toward fulfillment of these agreement items provided by this model report is identified in Table 44.

Table 44. Repository Design and Thermal-Mechanical Effects Key Technical Issue Agreement Items Addressed in This Model Report

Agreement Item	Approach and Section Reference	Status of Agreement
RDTME 3.04	Geotechnical data to support the drift degradation analyses documented in this report are identified in Section 4, Section 7, and Attachment V. Discussions of data adequacy are provided throughout Sections 6, 7, and 8. Newly acquired data from lithophysal rocks have been used to develop the lithophysal rockfall model, including data from laboratory compression testing on large-diameter cores, and from in situ flatjack (slot) compression testing in the ESF main loop and ECRB Cross-Drift.	The data and information provided in this model report contributes to the closure of this agreement.
RDTME 3.05	The technical basis for accounting for the effects of lithophysae is presented in Section 6.4. The validity of this approach is discussed in Sections 7.3 and 7.4.	The data and information provided in this model report contributes to the closure of this agreement.
RDTME 3.10	<p>The assessment of an appropriate approach to model the rock mass is a function of the specific repository host rock type: lithophysal or nonlithophysal rock (Section 7.1).</p> <p>For nonlithophysal rock, jointing controls the mechanical response, which is generally anisotropic in nature. Therefore, two-dimensional modeling of nonlithophysal rock is not realistic for rockfall modeling, and a three-dimensional modeling approach must be used.</p> <p>Conversely, lithophysal rock is characterized by the presence of more-or-less uniformly distributed voids (lithophysae) of varying size. Additionally, in the Tptpl, short trace length interlithophysae fracturing exists. Under these conditions, the representation of lithophysal rock as a homogeneous, isotropic rock mass is appropriate. Therefore, in models of drift stability, the use of a two-dimensional model in the plane perpendicular to the axis is adequate.</p>	The data and information provided in this model report are intended to fully address the requirements of this agreement.
RDTME 3.15	Additional clarification of the approach and technical basis for how reduction in cohesion adequately accounts for thermal effects in the DRKBA analyses is provided in Attachment IV. However, the DRKBA analyses now provide a confirmatory role in the assessment of drift degradation. The drift degradation analyses are primarily conducted using UDEC and 3DEC, in which thermal loads have been explicitly modeled (Sections 6.3 and 6.4). The adequacy of the methods to account for thermal effects on drift degradation are validated in Section 7.8.	The data and information provided in this model report are intended to fully address the requirements of this agreement.
RDTME 3.16	The available small trace-length fracture data have been analyzed and included in this report, documenting their effect on block development (Section 6.3.3).	The data and information provided in this model report are intended to fully address the requirements of this agreement.
RDTME 3.17	The approach for determining the effective maximum rock size has been revised in this model report. The approach of varying the joint geometry input to UNWEDGE is no longer applied. The maximum rock size and shape is taken directly from the 3DEC output, which includes the variation in joint strike, dip, spacing, and persistence. The variation of joint geometry parameters is based on field mapping data from the ESF, which has been input into the rockfall model (Sections 6.1.6 and 6.3).	The data and information provided in this model report are intended to fully address the requirements of this agreement.

Table 44. Repository Design and Thermal-Mechanical Effects Key Technical Issue Agreement Items Addressed in This Model Report (Continued)

Agreement Item	Approach and Section Reference	Status of Agreement
RDTME 3.19	<p>(1) In this revision of this model report, the DRKBA analyses provide a confirmatory role in the assessment of drift degradation. The primary analyses for degradation of nonlithophysal rock is provided using 3DEC (Section 6.3), while lithophysal rock is analyzed using UDEC (Section 6.4). An appropriate range of joint strength properties has been applied as documented in Section 6.3.1.6. Long-term degradation has been accounted for as documented in Section 6.3.1.5.</p> <p>(2) An analysis of block sizes based on the full distribution of joint trace length data has been included in this report (Sections 6.1.4 and 6.1.6), including the available small joint trace length data (Section 6.3.3).</p> <p>(3) As indicated above, the DRKBA results now provide a confirmatory role in the assessment of drift degradation. 3DEC has replaced DRKBA as the primary code for analyzing structural block development in the nonlithophysal rock units. The 3DEC and DRKBA results are in good agreement (Section 7.8.4).</p> <p>(a) Appropriate boundary conditions for thermal and seismic loading have been included in 3DEC as documented in Section 6.3.1.1.</p> <p>(b) A total of 76 fracture patterns have been analyzed, which were drawn from the same fracture population used in the DRKBA analyses (Section 6.3.1.1).</p> <p>(c) Thermal and mechanical properties for rock blocks and joints are available in the Technical Data Management System as documented in Section 4.1.</p> <p>(d) Long-term degradation of joint strength has been included as documented in Section 6.3.1.5.</p> <p>(e) Site-specific ground motion time histories appropriate for postclosure period have been modeled as documented in Section 6.3.1.2.</p>	<p>The data and information provided in this model report are intended to fully address the requirements of this agreement.</p>